Experimental and numerical analysis of a pivoted cylinder subjected to vortex-induced vibrations

By:

Daniel Alejandro Mella Vivanco

A thesis submitted in partial fulfilment of the requirements for the degree of Doctor of Philosophy

THE UNIVERSITY OF SHEFFIELD
FACULTY OF ENGINEERING
DEPARTMENT OF CIVIL AND STRUCTURAL ENGINEERING

MARCH 2021

Dedicated to my family,
for all their love and support.

Abstract

This thesis presents and discusses the results of two investigations. The first involves studying wake dynamics along the span of a pivoted cylinder undergoing vortex-induced vibrations (VIV) and its relationship with the structural response. This experiment used planar Particle Image Velocimetry and image-based tracking techniques to measure the wake and cylinder response at different flow velocities. The second investigation assesses the accuracy of a two-dimensional representation of the first experimental study using RANS models based on the $k - \omega$ turbulence model. A prior experiment of a bottom-fixed cylinder undergoing VIV was performed to analyse its variable amplitude condition in preparation for the pivoted cylinder case.

The pivoted cylinder results showed maximum amplitudes of approximately half and two times its diameter along and perpendicular to the flow direction, respectively. Similar to the bottom-fixed cylinder, the maximum response was achieved when the cylinder motion and vortex shedding frequencies were equal (i.e., synchronised) to the natural frequency of the structure in water, and when this equivalence was preserved along the cylinder span. At higher flow velocities, a desynchronised region appeared at the water surface, different from the previously observed bottom-up desynchronisation of the bottom-fixed cylinder. Wake measurements closer to the water surface had a broader wake width, higher momentum transference, and higher vortex strength compared to lower water depths. The local response along the cylinder span could not fully explain these differences.

The numerical model reached amplitudes that were 40% lower than the experimental results. Moreover, bistable responses were observed in the upper branch and not in the experimental results. The tested numerical model was insufficient to account for the three-dimensional component of the pivoted cylinder. Additional research is needed to understand the cylinder-wake dynamics of the pivoted cylinder, especially related to its synchronisation-desynchronisation process, to improve the prediction capabilities of two-dimensional numerical models.

Acknowledgements

Firstly, I wish to express my sincere gratitude to Professor Luca Susmel for his supervision and personal guidance. He took an active role in my research, encouraging discussions, and giving thoughtful and constructive criticism. He really helped me to stay focused on my research goals and to finish this thesis in a reasonable amount of time.

Secondly, I would like to express my gratitude to Professor Wernher Brevis. His advice and encouragement played a critical role in this research project. His support through difficult times meant a lot to me.

Thirdly, I would like to thank all my friends and colleagues I made along my PhD adventure.

Finally, I want to thank my family for their encouragement and support. I feel as we went through this PhD together.

Contents

List of Figures

List of Tables

Nomenclature

α	Diffusion parameter
β^*	$k-\omega$ turbulence model coefficient
β_1	$k-\omega$ turbulence model coefficient
β_2	$k-\omega$ turbulence model coefficient
$\mathbf{\Phi}_i$	Spatial mode. $i=[1,2,...]$
$\Delta_{a,b,c}$	Distance between adjacent mesh elements
Δ_t	Time step
δij	Kronecker delta function. $\delta_{ij}=1$ when $i=j$
γ	$k-\omega$ turbulence model coefficient
λ	QUICK scheme parameter
μ	Dynamic viscosity
μ_t	Dynamic Turbulent viscosity
∇	Gradient function
ν	Kinematic viscosity
ν_t	Kinematic Turbulent viscosity
ω	Dissipation per unit of kinetic energy
ϕ	Phase angle between the lift and displacement
ϕ_{xy}	Phase angle between the streamwise and crossflow motion
ρ	Water density
$\sigma_{\omega 1}$	$k-\omega$ turbulence model coefficient

$\sigma_{\omega 2}$	$k-\omega$ turbulence model coefficient
σ_{k1}	$k-\omega$ turbulence model coefficient
σ_{k2}	$k-\omega$ turbulence model coefficient
τ_f	Diffusion coefficient
FB-error	Forward-Backward tracking error
θ	Cylinder rotation regarding its rest position
θ_{m}	Maximum cylinder rotation regarding its rest position
$\tilde{\omega}$	Intensity diffusion parameter
ε_i	Relative modal value. $i=[1,2,...]$
φ	Scalar quantity (e.g. velocity)
ζ	Structural damping
A	Area
a_1	$k-\omega$ turbulence model parameter
a_{c}	Inflow acceleration
A_{f}	Face area of a mesh element
A_{o}	Free decay test parameter
A_{w}	Cross-sectional area of the flow
A_{x}	Maximum structural amplitude in the streamwise direction
A_{y}	Maximum structural amplitude in the crossflow direction
B_{o}	Free decay test parameter
B_{r}	Blockage ratio
C	Stuctural damping of an elastically mounted cylinder
C_{D}	Drag force coefficient
C_{eq}	Structural stiffness of a pivoted cylinder. Gravitational and Buoyance moments included
C_{F}	Three-dimensional force correction

C_{L}	Lift force coefficient
$CD_{k\omega}$	$k-\omega$ turbulence model coefficient
D	Diameter of the cylinder
d	Normalised boundary distance
dt_{camera}	Time step between two images
dt_{laser}	Time step between laser pulses
F_1	First blending function of the $k-\omega$ turbulence model
F_2	Second blending function of the $k-\omega$ turbulence model
f_{cx}	Main streamwise oscillation frequency
f_{cy}	Main crossflow oscillation frequency
f_{c}	Main oscillation frequency
F_{D}	Drag force
F_{L}	Lift force
f_{na}	Natural frequency measured in air
f_{nw}	Natural frequency measured in still water
F_{r}	Froude number
f_{vs}	Vortex shedding frequency
f_{x}	Streamwise oscilation frequency
f_{y}	Crossflow oscilation frequency
g	Gravitational acceleration
g_{r}	Growth rate in the radial direction within the O-grid mesh region
H_{RK_i}	Runge-Kutta fourth order coefficient. $i = [1, 2, 3, 4]$
H_{w}	Water depth
$H_{\mathrm{y+}}$	Height of the first mesh element around the cylinder
I^*	Inertia ratio

I_{f}	Displaced fluid moment of inertia
I_{s}	Structural moment of inertia
K	Stuctural stiffness of an elastically mounted cylinder
$k-\omega$	Turbulence model
$k-\varepsilon$	Turbulence model
K_{eq}	Total stiffness of a pivoted cylinder. Gravitational and Buoyance moments included
K_{s}	Structural stiffness of a pivoted cylinder. Gravitational moment included
L	Length of the cylinder
L_{f}	Vortex formation length
L_{RK_i}	Runge-Kutta fourth order coefficient
m^*	mass ratio
M_{a}	Added mass
M_{f}	Displaced fluid mass
M_{i}	Total moment on the cylinder. $i=[x,y]$
M_{s}	Structural mass
N_{c}	Number of mesh elements around the cylinder
N_{e}	Total number of mesh elements
N_{face}	Nummber of faces in a mesh element
N_{L}	Number of mesh layers around the cylinder
n_{m}	Manning coefficient
P_1	Initial tracking target location
P_2	Final tracking target location
P_k	Production term in the $k-\omega$ turbulence model
P_w	Wetter perimeter
R_{e}	Reynolds number

R_w	Hydraulic radius
S_f	Water channel friction slope
S_o	Water channel slope
S_t	Strouhal number
S_φ	Source term of the $k-\omega$ turbulence model
S_{ij}	Strain tensor mean rate
t	time
t_a	acceleration time
t_end	Starting time of the stable simulation phase
t_ini	Time within the initial simulation phase
U	Time-averaged streamwise velocity
u'	Fluctuating component of the streamwise velocity
U_in	Bulk inflow velocity
$U_{\mathrm{r\_end}}$	Reduced velocity at the stable simulation phase
$U_{\mathrm{r\_ini}}$	Reduced velocity at the initial simulation phase
U_r	Reduced velocity replacing f_nw to f_c
U_r	Reduced velocity
u_i	flow velocity component. $i = [1, 2, 3]$
V	Time-averaged crossflow velocity
v'	Fluctuating component of the crossflow velocity
W_f	Water channel width
x, y, z	Cartesian coordinate system
y_wall	Height of the first mesh element around a body

Chapter 1

Introduction

This section outlines the motivation of this thesis, its objectives and original contributions published or presented in peer-reviewed journals and conferences.

1.1 Motivation

Fluid-Structure Interactions (FSI) is a multidisciplinary field related to body displacements or deformations subjected to internal or external flows. Technological advancements in material properties, construction techniques, and engineering design have led to slender and more flexible structures susceptible to vibrations triggered by surrounding fluid flows. A commonly observed phenomenon that stands out in these cases is Vortex-Induced Vibrations (VIV), which refers to the constant feedback between the vortex shedding behind a body and its structural response [111]. Under certain conditions, structures subjected to VIV experience large oscillations when the vortex shedding and structural vibration frequencies coincide [10]. This phenomenon is commonly referred to as lock-in or synchronisation. VIV is an important contributor to fatigue damage and structural stability in several engineering structures, such as marine risers, bridges, towers, masts, heat exchanger tubes, submerged floating tunnels, to name a few. Key topics related to this classic problem has been summarised in numerous reviews (see, for example, [4, 24, 89, 111]).

The complexity of VIV is summarised as an ”inherently non-linear, self-governed or self-regulated, multi-degree-of-freedom” phenomenon [89]. Consequently, a significant portion of the current research body has been built around simplified cylindrical models. These models involve elastically mounted cylinders forced or free to vibrate perpendicular to the flow direction and subjected to a range of uniform flows. Results and insights from these studies have been critical to understanding, predicting and controlling VIV, and have been the foundation in most design codes and commercial Software. Still, lower fatigue life of up to one order of magnitude can be estimated when the results of these simplified models are applied to complex VIV configurations, such as marine risers [69]. In recent years, experimental VIV studies have included complex configurations commonly found in engineering problems, such as variable-amplitude responses, several modes of vibration, free stream turbulence, and sheared flows. These experiments have limited applicability, are often time-consuming, difficult to scale and require costly measurement equipment. As an example, offshore structures with aspect ratios (length-to-diameter) of $\mathcal{O}(10^3)$ are commonly subjected to turbulent ocean currents with Reynolds numbers R_e (characteristic length: structural diameter) between $\mathcal{O}(10^5)$ and $\mathcal{O}(10^6)$. Scaling these conditions in an experimental setting requires specialised equipment with inflow velocities that are difficult to achieve.

Numerical models based on the Reynolds-Averaged Navier-Stokes (RANS) equations offer an attractive alternative to experimental research. These models are usually preferred due to their lower computational costs, lower grid resolution, and less demanding time step requirements. Nevertheless, the non-linear fluid-body interaction and the hysteretic nature of VIV impose significant restrictions regarding its numerical simulation. A common assumption is that the inherently three-dimensional VIV can be represented as an equivalent two-dimensional model. Previous studies indicated that these representations are restricted to low Reynolds numbers, where $R_e < 2 \times 10^2$ is considered the upper threshold for two-dimensional and laminar vortex shedding regime [88]. Still, recent numerical studies based on two-dimensional RANS models successfully simulated the main features (maximum cylinder amplitude, main oscillation frequency, total hydrodynamic forces, phase angle, among others) of elastically mounted rigid cylinders undergoing VIV [35, 105, 117]. The Reynolds number in these simulations ranged between 1×10^3 and 1×10^4, and the structural response reached amplitudes of at least one cylinder diameter. The adequacy of the two-dimensional representation seems to be associated with the synchronisation between the vortex shedding and the cylinder oscillation frequency. This phenomenon enhances two-dimensionality and seems to be strong enough to offset the three-dimensional instabilities of the flow.

Cylinders with variable amplitude along their span and subjected to VIV are an interesting problem on their own. In particular, the linear response variability along the span of a pivoted cylinder promotes complex structural responses dependant on the three-dimensional body-wake interaction. As described before, two-dimensional numerical models have successfully extracted the main VIV features on cylinders with high amplitude responses and above the laminar vortex shedding regime. Still, their application is mainly restricted to rigid cylinders under uniform flow conditions, and little consideration has been paid to their use on variable amplitude cylinders, such as the pivoted configuration. How do changes in the wake dynamics along a pivoted cylinder affect its structural response? Can two-dimensional models extract the main features of a pivoted cylinder, considering their three-dimensional body-wake interaction? This thesis addresses these questions by analysing the experimental case of a pivoted cylinder subjected to VIV and its two-dimensional representation using RANS models. Firstly, an initial experiment related to a bottom-fixed cylinder subjected to VIV was conducted. Its main goal was to acquire experience with the experimental equipment, calibration system, and data analysis. Moreover, its variable amplitude condition along the structural span provided important insights in preparation for the pivoted cylinder case. Secondly, the structural response and wake dynamics along the span of a pivoted cylinder undergoing VIV were analysed across a range of open-channel flows. Lastly, a two-dimensional model was developed based on the pivoted cylinder experimental condition. The numerical model's limitations, capabilities, and accuracy were evaluated by comparing its results with the experimental pivoted cylinder in terms of displacements and oscillation frequencies.

1.2 Objectives

This thesis analyses the experimental case of a pivoted cylinder subjected to VIV and its numerical representation through two-dimensional RANS models. The Reynolds number in the experiments ranged between 2.5×10^3 and 5.8×10^3. The wake and cylinder motion was measured using Particle Image Velocimetry (PIV) and image-based tracking techniques. The wake dynamics, emphasising its variability along the structural span, and cylinder responses were analysed across a range of open-channel flows. A two-dimensional model was developed based on the experimental conditions and the pivoted configuration. The numerical models' limitations, capabilities, and accuracy were evaluated by comparing their cylinder responses and oscillation frequencies with the experimental results. An initial experiment related to a bottom-fixed cylinder subjected to VIV was conducted. Its main goal was to acquire experience with the experimental equipment, calibration system, and data analysis. Moreover, its variable amplitude condition along the structural span provided important insights in preparation for the pivoted cylinder case. In particular, the relationship between wake dynamics and structural response as the cylinder reaches its maximum amplitude and then desynchronises at higher flow velocities. The main objectives of this thesis are

- Measure and characterise the body-wake interaction along the span of a bottom-fixed cylinder subjected to VIV. Important insights were gained in preparation for the pivoted cylinder experiment. In particular, the relationship between wake dynamics and structural response as the cylinder reaches its maximum amplitude and then desynchronises at higher flow velocities.

- Analyse how changes in the wake dynamics along the span of a pivoted cylinder subjected to VIV affect its structural response. Particular emphasis on the body-wake interaction as the cylinder achieves its maximum response are analysed.
- Determine the accuracy and possible limitations of two-dimensional RANS models to simulate the response of a pivoted cylinder subjected to VIV.

1.3 Organization of this thesis

Chapter 2: Literature review
This chapter highlights the main experimental and numerical studies related to cylinders subjected to VIV. Firstly, a summary of the vortex shedding process and associated hydrodynamic forces of a flow around a stationary cylinder is presented. Secondly, a description is given of the main governing parameters, results and insights of simplified models undergoing VIV. These concepts are compared to VIV studies based on complex configurations, such as variable-amplitude responses and inflow conditions. Lastly, an overview of the latest numerical VIV studies related to two-dimensional RANS models is presented.

Chapter 3: Experimental methods
This chapter describes the experimental setup for the bottom-fixed and pivoted cylinders. The experimental equipment, mounting, calibration, measurement, and data processing from raw flow images to flow velocity fields are provided. Different verification processes are detailed to minimise and quantify the measurement error. Additionally, a general description of the flow velocity under open-channel conditions is given.

Chapter 4: Numerical methods
A description of the theory and numerical techniques for two-dimensional RANS models are given in this chapter. The governing flow equations and turbulence modelling are first introduced. Only the Shear Stress Transport $k - \omega$ model is described due to its successful application in previous VIV studies. The spatial and temporal discretisation techniques used in the numerical model are described within the context of Ansys Fluent, the Computer Fluid Dynamic Software used in this thesis. Lastly, this chapter describes the cylinder model and its fluid-structure coupling mechanism.

Chapter 5: VIV on bottom-fixed cylinder
This chapter analyses the wake dynamics and structural response of a bottom-fixed

cylinder subjected to a range of open-channel flows. The cylinder response was characterised in terms of maximum amplitude and oscillation frequency. Different statistics were used to characterise and study the spanwise wake dynamics as the cylinder reaches its maximum amplitude and then desynchronises at higher flow velocities.

Chapter 6: VIV on pivoted cylinder
This chapter analyses the wake dynamics and structural response of a pivoted cylinder subjected to a range of open-channel flows. The cylinder response was characterised in terms of maximum amplitude and oscillation frequency. The wake dynamics were analysed by measuring one plane along the cylinder span and two planes at different water depths. Different statistics were calculated to characterise and study the spanwise wake dynamics as the cylinder reaches its maximum amplitude.

Chapter 7: Numerical model. Pivoted cylinder
This chapter analyses the limitations, capabilities and accuracy of two-dimensional RANS models to simulate the response of a pivoted cylinder subjected to VIV. The inflow and structural characteristics of the experimental pivoted cylinder in Chapter 6 were used as input for the numerical model. The numerical model was first validated by simulating a low mass-damping two degree-of-freedom cylinder [41]. Then, the influence of the inflow conditions that trigger a high-response state was analysed. These inflow conditions were critical to ensuring a high-response state in the simulations. Finally, the numerical model of the pivoted cylinder was compared to its experimental counterpart in terms of displacements and oscillation frequencies.

Chapter 8: Conclusions
This chapter summarizes the main contributions of this thesis and discusses several gaps and recommendations for future work.

1.4 Publications and presentations

Some of the work presented in this thesis has been published in two peer-reviewed journals and two international conferences

- **Mella, D. A., Brevis W., Susmel L.** ”Single cylinder subjected to vortex-induced vibrations: estimating cyclic stresses for fatigue assessment”, 1st Virtual European Conference on Fracture (2020).

- **Mella, D. A., Brevis W., Susmel L.** ”Spanwise wake development of a bottom-fixed cylinder subjected to vortex-induced vibrations”, Ocean Engineering. (2020); 218: 108280.
- **Mella, D. A., Brevis W., Higham J. E., Racic, V., Susmel L.** ”Image-based tracking technique assessment and application to a fluid–structure interaction experiment”, Proceedings of the Institution of Mechanical Engineers, Part C: Journal of Mechanical Engineering Science (2019); 233: 5724 – 5734.
- **Mella, D. A., Brevis W.** Image-based techniques applied to a fluid-structure interaction experiment (Uso de técnicas basadas en imágenes aplicado a un caso de interacción fluido-estructura). XXVIII Latin american conference of Hydraulics (2018).

Chapter 2

Literature review

2.1 Introduction

Vortex-induced vibrations (VIV) is a non-linear, self-regulated, multi-degree-of-freedom (DOF) phenomenon [89] sustained by the constant interaction between vortex shedding and body motion [111]. VIV is an important contributor to fatigue damage and structural instability in numerous engineering applications, such as marine risers, bridges, towers, masts, heat exchanger tubes, submerged floating tunnels, to name a few. Thus, an extensive research body has been developed towards its understanding, prediction, and control. Key topics related to this problem have been summarised in several reviews (see, for example, [4, 24, 89, 111]).

This chapter highlights the main experimental and numerical studies related to VIV on cylinders within the scope of this thesis. Firstly, the vortex shedding process is introduced by analysing a stationary cylinder subjected to uniform flows. Secondly, fundamental concepts and main governing parameters are described by analysing cases of cylinders undergoing VIV and restricted to move perpendicular to the flow direction (one degree-of-freedom). These results are contrasted with cases of VIV under complex configurations, such as variable-amplitude responses, mounting systems, and inflow conditions. Lastly, the accuracy and capabilities of several numerical studies based on two-dimensional RANS models are highlighted. Details related to the theory and numerical techniques used to model cylinders undergoing VIV are described in Chapter 4.

2.2 Flow around a stationary cylinder

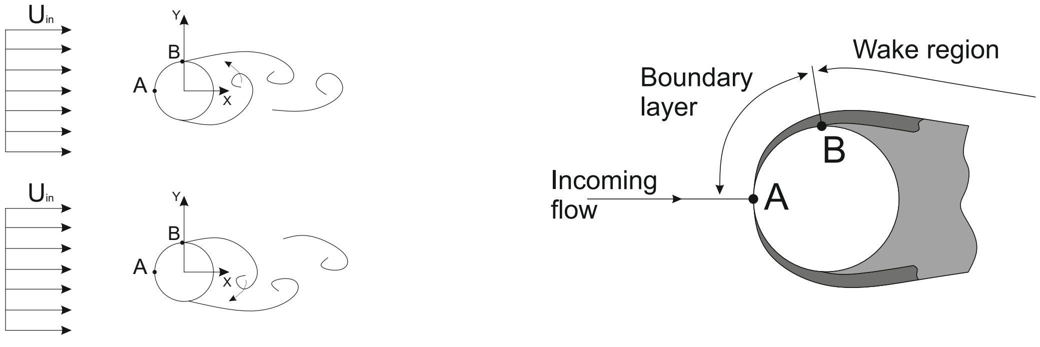

(a)

(b)

Figure 2.1: Fluid flow around a two-dimensional fixed cylinder. a) Temporal evolution of the wake. b) Wake development close-up

The case of a fluid flow around an obstacle and its structural influence has been a topic of interest for several decades. Despite the rich literature related to this case, most findings remain in the ”the empirical, descriptive real of knowledge” [87]. Figure 2.1 shows a two-dimensional cylinder placed in a uniform flow. The flow moves from left to right along the x-axis or the streamwise direction. The y-axis or crossflow direction is perpendicular to the flow and the cylinder axis. The z-axis (out-of-plane in Figure 2.1a) or spanwise direction refers to the axis of the cylinder at rest. This coordinate system is used throughout this thesis unless stated otherwise. The flow dynamics around a cylinder are governed by the Reynolds number R_e [110]. Here, $R_\mathrm{e} = U_\mathrm{in}D/\nu$, where U_in is the bulk inflow velocity, D is the cylinder diameter, and ν corresponds to the kinematic viscosity. Other parameters, such as surface roughness [34], flow turbulence [70], and aspect ratio (length-to-diameter) [74], can also influence the flow dynamics as the ideal case shown in Figure 2.1 approximates real-world applications.

The flow dynamics around a stationary cylinder were classified several decades ago as a function of R_e [86] and are constantly being updated as more information is gathered [113]. At $R_\mathrm{e} < 5$, the flow remains attached to the cylinder surface, and a steady laminar wake is formed. The solid-fluid interface slows down the nearby flow as a function of the fluid viscosity. The region affected by this interaction is called the boundary layer (Figure 2.1b). At a Reynolds number between $5 < R_\mathrm{e} < 40$, the adverse pressure gradient at the cylinder rear end is strong enough to detach the boundary layer (point B in Figure 2.1b), developing two stable counter-rotating vortices behind the cylinder. The stability of this configuration breaks between $48 \lesssim R_\mathrm{e} \lesssim 49$ [78], and a new configuration called vortex shedding is reached. This flow is characterised by the constant formation, growth, and advection of vortices from each side of the body [26]. The timing or frequency of vortex shedding can be expressed as a function of the Strouhal number, $S_{\mathrm{t}} = (f_{\mathrm{vs}}D)/U_{\mathrm{in}}$, where f_{vs} is the shedding frequency. The vortex shedding maintains a laminar state up to $R_{\mathrm{e}} < 200$. At higher Reynolds numbers, a systematic transition from a laminar to a turbulent state takes place, starting from the far wake up to the boundary layer. Firstly, a subcritical regime between $3 \times 10^2 < R_e < 3 \times 10^5$, characterised by a turbulent wake and a laminar boundary layer separation. Here, the Strouhal number remains relatively constant at 0.2 [75]. The experiments of this thesis are classified within this regime. Secondly, a critical regime between $3 \times 10^5 < R_e < 3.5 \times 10^5$, with a turbulent boundary layer separation. Thirdly, a supercritical and upper transition regimes between $3.5 \times 10^5 < R_e < 4 \times 10^6$, where the boundary layer transitions from a laminar to a turbulent state at one side of the cylinder. Lastly, at $R_e > 4 \times 10^6$, the flow transitions to a transcritical regime with a completely turbulent boundary layer at both sides of the cylinder.

The process of vortex shedding generates fluctuating pressures and viscous forces on the body. Under certain circumstances, this dynamic loading leads to structural vibrations that change the pressure distribution around the cylinder. This feedback system between the wake and body motion is referred to as vortex-induced vibrations [111]. A laminar vortex shedding regime ($R_{\mathrm{e}} < 200$) is not expected to vary in the spanwise direction. Thus, its characterisation (wake and hydrodynamic force) can be achieved by means of two-dimensional models (e.g., [78, 80]) or by extrapolating a single two-dimensional measurement along the cylinder span. Flow instabilities arise at higher R_{e} as the wake becomes turbulent [113]. The associated fluid forces undergo notable changes as the wake transition to a three-dimensional state. Numerical models tend to include this variability at the expense of significant increments in computational power. On the other hand, experimental studies use external means (e.g., [97]) or increase the number of measurements in the spanwise direction (e.g., [61]) to minimise or incorporate the three-dimensionality of the flow. Independent of the wake complexity, its characterisation is often based on the following statistical parameters: streamwise and crossflow forces, base pressure, vortex length and strength, boundary layer separation point, and vortex shedding frequency. Moreover, mean and fluctuating flow velocities and Reynold stresses can be linked to the previously mentioned parameters (e.g., [118]). This research project analyse these first and second-order statistics of the wake and its relationship to the cylinder response. Furthermore, the resultant forces in the streamwise and crossflow direction, commonly called drag and lift forces, are critical for the tested numerical model. The non-dimensional form of these forces is

$$C_{\mathrm{D}} = \frac{1}{2} F_{\mathrm{D}} \rho A U_{\mathrm{in}}^2 \tag{2.1}$$

$$C_\mathrm{L} = \frac{1}{2} F_\mathrm{L} \rho A U_\mathrm{in}^2 \tag{2.2}$$

where F_D and F_L are the drag and lift force, respectively, and A is the characteristic area of the body.

The foundation of VIV is derived in part from the fundamentals behind an incident flow on a stationary cylinder. Nevertheless, structural vibrations in VIV significantly change the vortex shedding process compared to the stationary cylinder case. The drag and lift forces of an elastically mounted cylinder subjected to VIV can increase up to three and five times compared to its stationary condition [49]. Structural vibrations can occur at $R_\mathrm{e} = 20$ [19], which is significantly lower than the Reynolds number associated to the onset of vortex shedding [78]. The Strouhal relationship is no longer valid in VIV since the body motion leads the vortex shedding (Section 2.3.1).

It is important to describe a mathematical technique frequency used in fluid dynamics. A certain quantity can be decomposed as the sum of its expected value and its fluctuations. The total variable φ is decomposed as the sum

$$\varphi = \overline{\varphi} + \varphi' = \overline{\varphi} + \tilde{\varphi} + \varphi'' \tag{2.3}$$

where $\overline{\varphi}$ is the time-averaged variable, while the fluctuating value φ' is further decomposed into a large-scale periodic component $\tilde{\varphi}$ and a residual random part φ''. This technique is later used to analyse the mean and fluctuating velocity of the wake and extract large-scale coherent patterns from a highly modulated cylinder response.

2.3 Vortex-Induced Vibrations

2.3.1 One degree-of-freedom cylinders

This section starts with an analysis of the classical VIV experiments of Feng [20] and Khalak and Williamson [47]. Both studies analysed the response of an elastically mounted cylinder subjected to a range of low turbulence flows. Each cylinder had similar structural damping and was restricted to move in their crossflow direction. Despite these similarities, Figure 2.2 shows significant differences in terms of maximum crossflow amplitudes A_y and main oscillation frequencies f_c. Khalak and Williamson's cylinder achieved a 74% higher maximum crossflow amplitude, and its range of significant body motion was four times higher compared to Feng's results. The range of reduced velocities U_r, where the vortex shedding frequency f_vs is equal to f_c, is commonly referred to as lock-in or synchronisation. Here, $U_\mathrm{r} = U_\mathrm{in}/(f_\mathrm{nw} D)$,

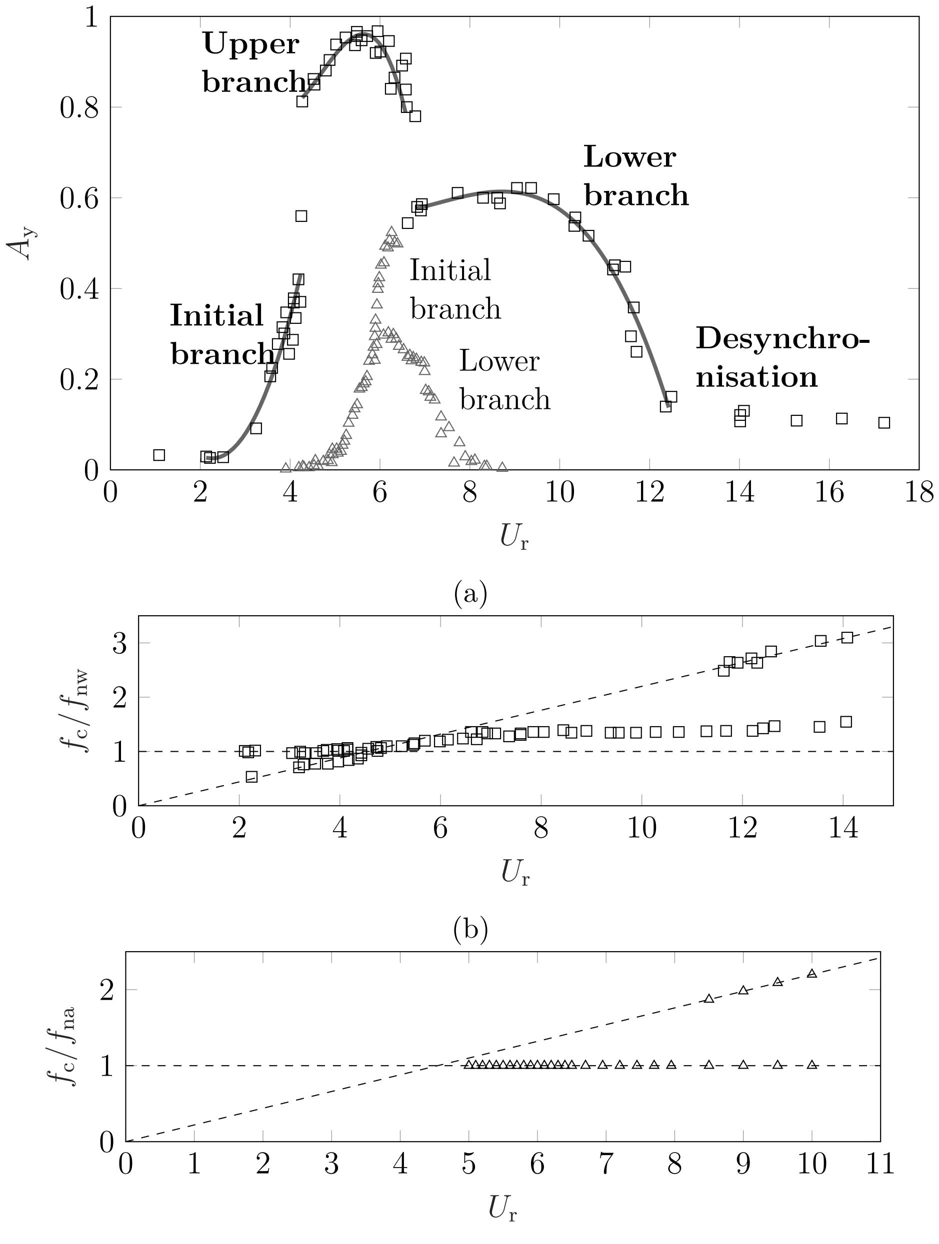

(a)

(b)

(c)

Figure 2.2: Comparison between two elastically mounted cylinders undergoing VIV. □: [47] ($m^* = 2.4$) vs △: [20] ($m^* = 248$). a) Maximum crossflow amplitude. b) Crossflow oscillation frequency [47]. c) Crossflow oscillation frequency [20]

where f_{nw} is the natural frequency of the cylinder measured in still water. Throughout the synchronisation range in Feng's experiment, f_{vs} and f_{c} were equal to the natural frequency of the cylinder measured in air f_{na}. On the other hand, a clear departure from this equivalence is observed in Khalak and Williamson's results (Figure 2.2b vs Figure 2.2c). These differences can be explained by analysing the theoretical case of a two-dimensional cylinder subjected to VIV. An in-depth formulation can be found in [3]. Consider the equation of motion of a one degree-of-freedom cylinder subjected to a time-dependent lift force

$$M_{\mathrm{s}}\ddot{y} + C\dot{y} + Ky = F_{\mathrm{L}} \tag{2.4}$$

where M_{s}, C and K are the cylinder mass, structural damping, and stiffness, respectively. In the region of high-amplitude cylinder responses, F_{L} and y can be approximated as a sinusoidal function

$$y = \tilde{Y}\sin(2\pi f_{\mathrm{c}} t) \tag{2.5}$$

$$F = \tilde{F}_{\mathrm{L}}\sin(2\pi f_{\mathrm{c}} t + \phi) \tag{2.6}$$

where $\tilde{Y}$ and $\tilde{F}$ are the displacement and force amplitudes respectively, and ϕ is the force-displacement phase angle. Substituting Eq. (2.5) and (2.6) into Eq. (2.4), the oscillation frequency and maximum amplitude response in non-dimensional form are

$$\frac{f_{\mathrm{c}}}{f_{\mathrm{na}}} = \left[1 - \left(\frac{\tilde{C}_{\mathrm{L}}}{4\pi^2}\right)\cos\phi\left(\frac{1}{m^*}\right)\left(\frac{U_{\mathrm{in}}}{f_{\mathrm{na}}D}\right)^2\left(\frac{\tilde{Y}}{D}\right)^{-1}\right]^{-1/2} \tag{2.7}$$

$$\frac{\tilde{Y}}{D} = \frac{\tilde{C}_{\mathrm{L}}}{8\pi^2}\sin\phi\left(\frac{1}{m^*\zeta}\right)\left(\frac{U_{\mathrm{in}}}{f_{\mathrm{na}}D}\right)^2\left(\frac{f_{\mathrm{na}}}{f_{\mathrm{c}}}\right) \tag{2.8}$$

The natural frequency in air f_{na} is used here to keep the original formulation [3]. The important non-dimensional parameters governing this theoretical model are: the mass ratio m^*, equal to the ratio between the oscillating mass M_{s} and its displaced fluid mass M_{f}; damping ratio ζ, defined as a percentage of the structural critical damping; reduced velocity U_{r}; frequency ratio $f_{\mathrm{c}}/f_{\mathrm{na}}$; amplitude ratio $\tilde{Y}/D$, and phase angle ϕ. In addition, the lift coefficient is affected by the structure and all the fluid parameters that have an influence in the vortex shedding process (Section 2.2). The phase angle plays an important role in Eq. (2.7) and (2.8). It defines the regions of positive energy transfer between the fluid forces and cylinder motion [112]. Moreover, the cylinder oscillates at a lower frequency than f_{na} when $0° \leq \phi \leq \pi/2$, while $f_{\mathrm{c}} > f_{\mathrm{na}}$ if $\pi/2 \leq \phi \leq \pi$ [3]. The mass-damping $m^*\zeta$ parameter has an inverse relationship with the maximum response amplitude. As an experimental

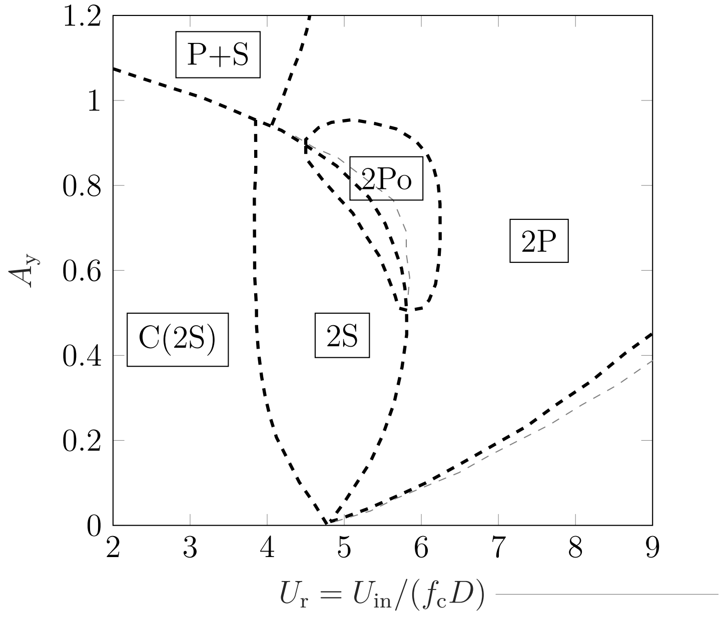

Figure 2.3: Vortex mode map of an elastically mounted cylinder forced to vibrate at different frequencies and amplitudes. Partial reproduction of Figure 3 in [71]

example, $A_y \approx 0.95D$ ($m^* = 2.4$ [47]) and $A_y \approx 0.53D$ ($m^* = 248$ [20]). The relative effects between m^* and ζ were analysed using an elastically mounted one degree-of-freedom cylinder subjected to VIV [48]. The results showed that $m^*\zeta$ was directly related to the maximum cylinder response, while the synchronisation range was mainly controlled by m^*. Equation (2.7) shows that $f_c \approx f_{vs} \approx f_{na}$ for high m^* cylinders, whereas $f_c \approx f_{vs}$ is not necessarily equal to f_{na} for structures with low m^*. This departure can be explained in terms of the added mass M_a, related to the acceleration of all the fluid particles set in motion as the cylinder oscillates [102]. The additional inertial force given by M_a decreases the natural frequency of the system, allowing the vortex-body synchronisation to persist over a broader range of U_r. Still, the cylinder will eventually desynchronise as M_a decreases on-average and the reduced velocity increases [102]. The added mass effect diminishes for higher m^* cylinders due to its smaller contribution relative to the structural mass. Thus, as shown in Figure 2.2c for Feng's cylinder, the relationship $f_c \approx f_{vs} \approx f_{na}$ persists over the synchronisation range.

Figure 2.2a shows that the cylinders of Feng [20] and Khalak and Williamson [47] experience different responses across their respective synchronisation ranges. In particular, Feng's cylinder exhibited two distinct responses called the initial and lower branch. At the beginning of the initial branch ($U_r \leq 4.5$), f_{vs} differed from f_c and low cylinder responses were observed. As U_r increased and f_{vs} approached the main oscillation frequency of the cylinder, A_y rapidly grew up to a maximum value of $0.53D$ at $U_r \approx 5.5$. Then, the maximum amplitude decreased significantly to

$A_\mathrm{y} \approx 0.3D$ as the cylinder transitioned between the initial to the lower branch. This transition was hysteretic, i.e. the cylinder response depended on the time history of the incoming flow velocity [20]. A_y kept decreasing at higher U_r until a negligible value was reached at $U_\mathrm{r} \approx 8$. Considering a Strouhal number $S_\mathrm{t} \approx 0.2$, then

$$S_\mathrm{t} = \frac{f_\mathrm{sv} D}{U_\mathrm{in}} = \frac{f_\mathrm{sv}}{U_\mathrm{r} f_\mathrm{nw}} \rightarrow \frac{f_\mathrm{sv}}{f_\mathrm{nw}} \approx 1 \rightarrow U_\mathrm{r} \approx 5 \tag{2.9}$$

approximately marks the beginning of the synchronisation range.

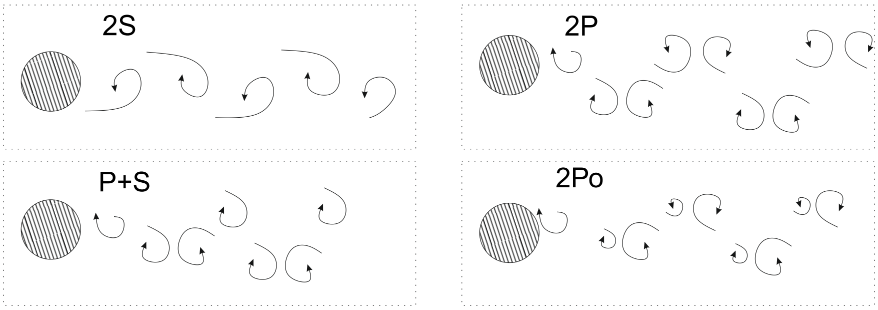

Figure 2.4: Vortex modes commonly found in one degree-of-freedom cylinders undergoing VIV

An additional branch called the upper branch was observed in the low m^* cylinder of Khalak and Williamson (see Figure 2.2a). The initial to upper branch transition occurred when f_c approached f_nw and is associated with changes in the vortex shedding timing [28]. Within the upper branch, A_y reached a maximum value of $0.95D$, while f_c increased with U_r due to the added mass effect. As the oscillation frequency approached f_na, the cylinder amplitude jumped to the lower branch. This transition was associated with a drastic change in the phase angle between the fluid force and the cylinder displacement [28]. The maximum amplitude and oscillation frequency in the lower branch remained approximately constant at $A_\mathrm{y} \approx 0.62D$ and $f_\mathrm{c}/f_\mathrm{nw} = 1.4$, respectively. At higher flow velocities, the cylinder and vortex shedding desynchronise ($f_\mathrm{c} \neq f_\mathrm{vs}$), and A_y rapidly decreased towards $0.1D$.

The experiments in Figure 2.2 showed different structural responses and oscillation frequencies across a range of reduced velocities. Due to the intrinsic relationship between the fluid flow and structural motion, it is expected to observe significant changes in the vortex dynamics as well. A classical VIV experiment forced a one degree-of-freedom cylinder to vibrate at different amplitudes and oscillation frequencies [112]. The Reynolds number was maintained between $3 \times 10^2 \leq R_e \leq 1 \times 10^3$. The vortex pattern was observed at each prescribed amplitude-frequency pair, and a vortex map was built. The results showed four characteristic vortex patterns: 2S (two single vortices per cycle), C(2S) (2S vortex mode but vortices coalesce downstream), 2P (two pairs of vortices at every oscillation), and P+S (single and a pair of vortices per half-cycle of body motion). Flow visualisation techniques were used to relate each response branch with a particular vortex pattern. The vortex shedding in the initial branch follows the 2S mode, while the 2P vortex pattern dominates the upper and lower branch [28]. Later, a high-resolution version of the previous vortex map found a new 2Po mode in the amplitude range associated with the upper branch [71]. This new vortex pattern is composed of a weaker vortex in each pair of vortices per cycle. Part of the high-resolution vortex map is reproduced in Figure 2.3 and Figure 2.4 shows a sketch of the previously described vortex patterns.

2.3.2 Two degree-of-freedom cylinders

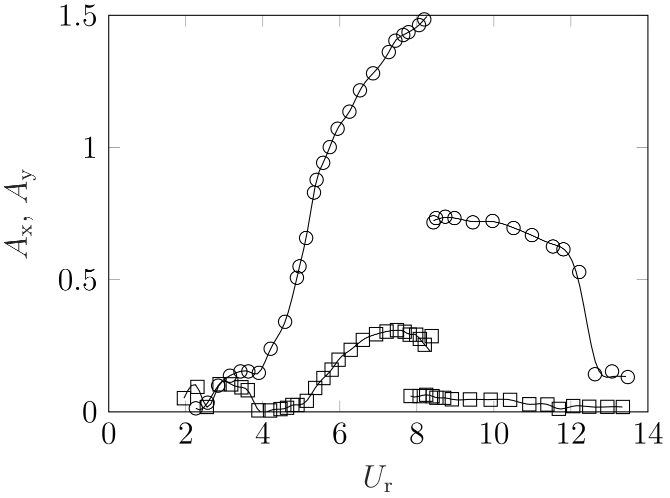

(a) ○: A_y. □: A_x

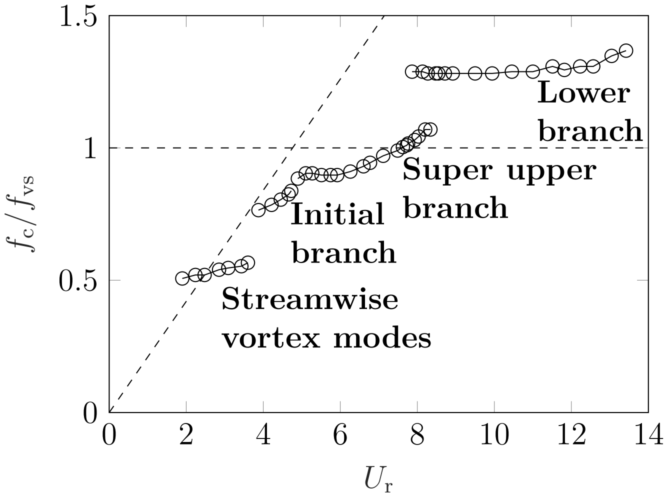

(b)

Figure 2.5: Response of a low mass-damping two degree-of-freedom cylinder undergoing VIV. $m^* = 2.6$ and $\zeta = 0.0036$ [41]. a) Maximum crossflow and streamwise response. b) Crossflow oscillation frequency

Although extremely insightful in understanding the fundamentals of VIV, the results described in the previous section are rarely found in practical situations. Streamwise and crossflow vibrations (two degree-of-freedom), variable amplitude across the span of the cylinder, multiple modes of vibration, among others, are typical conditions where VIV plays a critical role in the structural design. Moreover, the governing parameters in VIV have an intrinsic variability that plays a role in fatigue failure prediction [59].

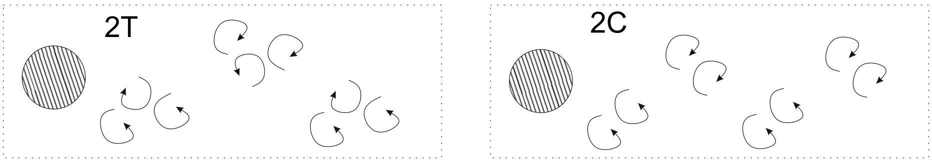

Figure 2.6: Vortex modes found in two degree-of-freedom cylinders

The high-resolution vortex map (Figure 2.3) predicted the maximum response and vortex patterns of a free-vibration elastically mounted cylinder after carefully matching the experimental conditions [71]. Nevertheless, free-vibration responses have an intrinsic random component not reproducible in forced-vibration experiments [71]. An experimental study simultaneously tested a two degree-of-freedom bottom-fixed cylinder and a one degree-of-freedom elastically mounted rigid cylinder [23]. Both structures had similar similar dimensions, m^*, and ζ. The bottom-fixed cylinder exhibited a higher maximum crossflow amplitude ($1.15D$ vs $0.9D$) and a broader synchronisation range compared to the rigid cylinder. The effects of allowing an additional degree-of-freedom on an elastically mounted rigid cylinder have shown to be quite significant and dependant on m^* [41]. The additional degree-of-freedom had a small impact in cylinders with $m^* > 6$. However, at lower m^*, significant changes in terms of maximum cylinder amplitude and vortex pattern were observed. Figure 2.5 shows the maximum amplitude in the streamwise A_{x} and crossflow A_{y} direction, and crossflow oscillation frequency ($f_{\mathrm{c}} = f_{\mathrm{y}}$) for a two degree-of-freedom cylinder with $m^* = 2.6$ [41]. Figure 2.5b only shows f_{y} since $f_{\mathrm{x}} = 2f_{\mathrm{y}}$ across U_{r}. The wake exhibited two characteristic vortex patterns between $1.8 \leq U_{\mathrm{r}} \leq 2.8$, the streamwise symmetric and antisymmetric vortex patterns. These modes are associated with a significant streamwise motion relative to its crossflow counterpart. As U_{r} increases, the oscillation frequency jumped to $f_{\mathrm{c}}/f_{\mathrm{vs}} \approx 0.75$ and the cylinder transitioned to the initial branch. The maximum amplitude experienced a rapid growth per U_{r} and a second jump to a high-amplitude region called super-upper branch occurred. The transition between branches occurred at $f_{\mathrm{c}} \approx 0.9f_{\mathrm{nw}}$, which is 10% lower compared to the initial-upper branch transition for one degree-of-freedom cylinders [28, 47]. Within the super-upper branch, the cylinder achieved a maximum amplitude of $A_{\mathrm{x}} \approx 0.3D$ and $A_{\mathrm{y}} \approx 1.5D$. Moreover, a new vortex mode called 2T (two triplet of vortices per body oscillation) was observed (Figure 2.6). The cylinder jumped from the super-upper to the lower branch as f_c approaches f_na. This hysteretic transition coincided with a jump in the phase angle between the lift force and the crossflow displacement [41]. The lower branch had similar characteristics found in one degree-of-freedom cylinders. The cylinder exhibited a reasonable constant maximum amplitude and oscillation frequency from $U_\mathrm{r} \approx 8$ to $U_\mathrm{r} \approx 12$, where the vortex-cylinder entered a desynchronised (non-lock-in) state.

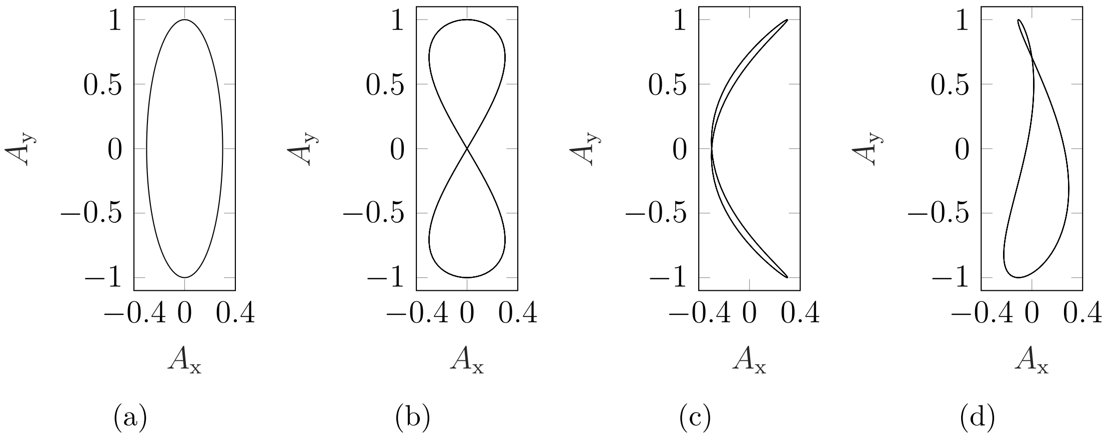

Figure 2.7: Examples of two degrees-of-freedom cylinder trajectories. a) Elliptical [62]. b) Eight [41]. c) Crescent [41]. d) Combination between (a) and (b) [44]

One intrinsic characteristic of two degrees-of-freedom cylinders undergoing VIV is the relationship between their streamwise and crossflow vibrations. Experiments on cables subjected to a range of uniform and sheared flows showed a quadratic relationship between the two response directions in their synchronised and desynchronised range [100]. This quadratic relationship influenced the trajectory traced by the cable. Two degree-of-freedom cylinders subjected to VIV also showed distinct trajectories, ranging from an elliptical-type, eight-type, or a combination of both depending on the structural coupling between the streamwise and crossflow motion [51, 52]. Cylinders with high structural coupling are characterised by an equal oscillation frequency in the streamwise and crossflow direction, tracing an elliptical-type trajectory (Figure 2.7a). On the other extreme, the streamwise vibration frequency of low structural coupling cylinders is approximately double its crossflow counterpart, and an eight-type trajectory is traced (Figure 2.7b). An intermediate structural coupling is, thus, associated with a combination between eight- and elliptical-type trajectories (see Figure 2.7d).

The incoming flow condition plays a significant role in VIV. Sheared flows, characterised by a linear variation of the flow velocity along the cylinder span, incoming turbulence intensity, and the number of potentially excited modes, are necessary to estimate the occurrence of synchronisation on multi-modal cylinders undergoing VIV [99]. Flows with high shear fraction impact the correlation length along the span of the cylinder, influencing its pressure distribution and enhancing flow three-dimensionality. These changes have been shown to decrease the maximum cylinder amplitude alongside an increment in the response modulation [40, 89]. Previous studies on the effects of free-stream turbulence on fixed square-shaped structures showed a positive relationship between peak forces and turbulent intensity [15]. However, a negative relationship was found when a squared-shaped structure was subjected to VIV [16]. The Reynolds number is more significant than previously thought. Using a variable magnetic eddy-current system, a series of experiments controlled the structural damping while maintaining a constant R_{e} on a one degree-of-freedom cylinder [53]. The results showed a direct relationship between R_{e} and the maximum cylinder response. Similarly, another study tested a one degree-of-freedom elastically mounted cylinder under systematic changes of ζ at $5 \times 10^2 \leq R_{\mathrm{e}} \leq 3.3 \times 10^4$ [31]. The results showed that the maximum amplitude not only depended on $m^*\zeta$ (see [48]) but also on R_{e}. Additionally, the researchers successfully collapsed the maximum cylinder response of a large number of studies against $m^*\zeta$ when the Reynolds number was taken into account. Important differences were observed when the Reynolds number was increased above the upper range of the subcritical regime. Experiments of an elastically mounted cylinder at $4 \times 10^4 \leq R_{\mathrm{e}} \leq 6 \times 10^6$ showed maximum amplitudes of $1.9D$ even with high structural damping ratios and a distinct influence of R_{e} on the synchronisation range [82].

A group of researchers examined cylinders with nonuniform amplitudes along their structural span to represent a more realistic engineering model. The simplest case of nonuniform amplitude is given by a pivoted configuration, characterised by a linear amplitude response along its span. Pivoted cylinders are generally mounted on a small rod-shaped pin fixed to a base. The pin acts as a pivot point, allowing the cylinder to vibrate like a pendulum in any direction perpendicular to its axis. Flow movements towards the free surface have been observed in a one degree-of-freedom pivoted cylinder undergoing VIV. This phenomenon is due to stronger vortices in regions of higher response amplitudes [103]. The inertia ratio I^*, defined as the ratio between the inertia of the solid mass around the pivot point and its displaced fluid inertia, and the inertia-damping parameter $I^*\zeta$ have a significant influence on the range of synchronised responses and maximum tip amplitude, respectively [21]. It is important to mention that I^* is equivalent to m^* when the cylinder is fully submerged in the fluid medium. Two degree-of-freedom pivoted cylinders with high $I^*\zeta$ have shown good agreement in terms of maximum amplitudes with one degree-of-freedom elastically mounted cylinders ([21] vs [28]) and in terms of vortex modes when compared to the vortex map predictions ([21] vs [71, 112]). This last result is supported by a subsequent study on a high $I^*\zeta = 0.139 - 0.0318$ pivoted cylinder undergoing VIV [62]. The observed 2S, 2Po, and 2P modes and associated amplitude branches agreed well with the vortex map [71] predictions, except for the predicted 2P mode as the cylinder desynchronises with the vortex shedding. As the inertia-damping ratio decreases, the pivoted cylinder exhibits typical initial-upper-lower branches commonly observed in low $m^*\zeta$ elastically mounted cylinders [17]. Nevertheless, at a sufficiently low $I^*\zeta$, two degree-of-freedom pivoted cylinders can reach peak crossflow amplitudes of approximately $1.5D$, develop a new vortex mode called 2C (two co-rotating vortices per half-cycle), and exhibit the simultaneous existence of two vortex modes along the span [21]. Figure 2.6 shows a sketch of the 2C vortex mode. Testing the boundaries of low structural parameters, a group of researchers analysed a two degree-of-freedom pivoted cylinder with $m^* = 0.45$ [57]. This tested mass ratio was below its theoretical limit of $m^* = 0.5$ [21], where the amplitude responses reach a maximum value and the synchronisation range extends to infinity [28]. The results showed an upper branch that extended up to the maximum tested U_r with no observable lower branch. Unlike previous two degree-of-freedom experiments, the cylinder achieved a significantly higher maximum streamwise amplitude of $A_\mathrm{x} \approx 2.5D$ compared to $A_\mathrm{y} \approx 2D$. Moreover, the vortex pattern in the upper branch was the P+S mode, which is unusual for two degree-of-freedom elastically mounted cylinders.

Similar to the uniform amplitude cylinder case, pivoted cylinders are affected by multiple structural and flow parameters. Shear flows on one degree-of-freedom pivoted cylinders increase the synchronisation range and promote secondary stable responses [2]. A characteristic beating behaviour was observed in the initial, and upper branches of a one degree-of-freedom pivoted cylinder undergoing VIV. This behaviour was explained by a small frequency mismatch between vortex shedding and cylinder oscillation frequencies [17, 103]. Comparison between bottom-fixed and pivoted cylinders at low aspect ratio (length-to-diameter less than two) showed higher amplitude responses at higher aspect ratios and the disappearance of the lower branch at low aspect ratios [27]. Moreover, amplitude differences due to the cylinder mounting (bottom-fixed vs pivoted) were minimised when a modal form factor was introduced [27]. The streamwise motion of a pivoted cylinder involves oscillations at the natural frequency and its first harmonics, whereas the crossflow motion locks onto the natural frequency in the synchronisation region. Thus, the pivoted cylinder can potentially exhibit elliptical-type (e.g. [62]) and eight-type (e.g. [21]) trajectories depending on its structural coupling between streamwise and crossflow motion [51, 52].

The majority of the research on VIV has been concerned with cylinders restricted to move in the crossflow direction. The number of studies related to the more practical case of two degree-of-freedom cylinders is comparatively low. Within this small subset, the case of a pivoted cylinder has received the attention of a small number of researchers. New vortex modes, hybrid vortices along the cylinder span, trajectory patterns, among other characteristics, show that the pivoted configuration has interesting dynamics observed in several engineering problems, such as marine piles and articulated ocean columns. Previous studies quantified the wake topology and structural response of a pivoted cylinder using a single two-dimensional PIV measurement [57, 62]. Although their results were insightful, the wake dynamics along the cylinder span could only be indirectly analysed. A classical study related to a two degree-of-freedom pivoted cylinder subjected to VIV performed multiple two-dimensional PIV measurements along the cylinder span [21]. This study focused on vortex mode characterisation rather than quantifying their associated wake dynamics at different cylinder responses. This research project explores this gap by investigating how changes in the wake dynamics along the span of a pivoted cylinder undergoing VIV affect its structural response. The wake and cylinder motion was measured using Particle Image Velocimetry (PIV) and image-based tracking techniques. The wake dynamics, emphasising its variability along the structural span, and the cylinder response were analysed across a range of open-channel flow velocities.

2.4 Numerical modelling of VIV

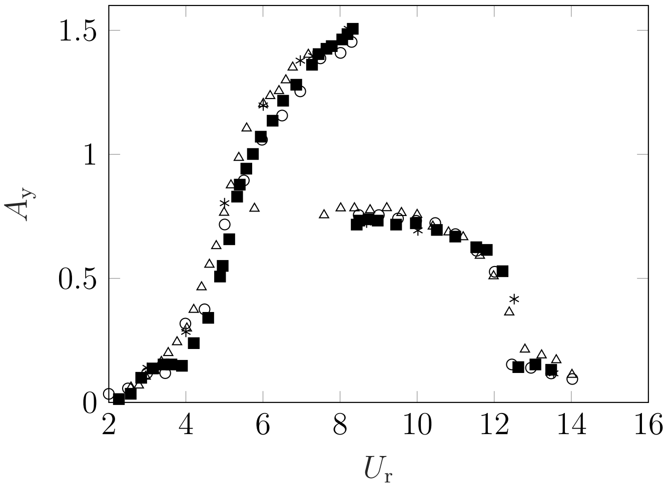

Figure 2.8: Maximum crossflow amplitude comparison between different numerical studies of a low mass-damping two degree-of-freedom cylinder. Experimental case, ■: [41]. Numerical simulations, ○: [35], △: [45], *: [105]

Computational Fluid Dynamics (CFD) is a design tool widely used in industry and research to simulate physical problems in a range of disciplines, such as fluid-structure interactions. Significant efforts are currently being made to predict the complex nature of VIV. Most numerical models consider three components: the fluid flow with its range of turbulent scales, the structural properties, and the solid-fluid interaction. The challenges of these models are mainly associated with the computational power needed to simulate the full range of turbulent scales as the flow interacts with the structure. This challenge dramatically increases considering that VIV depends on the time history of the inflow conditions ([7, 20, 89]). The numerical methods commonly used to solve the fluid flow in VIV problems are divided into three categories: Direct Numerical Simulations (DNS), Large Eddy Simulations (LES), and Reynolds-Average Navier Stokes (RANS) models. DNS solves the full range of turbulent scales. LES applies different filters to separate the small and large turbulent scales. The small scales are simulated, while the larger ones are directly solved. RANS models solve the time-averaged equations of the fluid motion. The turbulence scales are completely modelled using a turbulence model. Despite DNS and LES models solving the full or partial turbulent scales, RANS models are preferred due to their low computational costs, lower grid resolution, and less stringent time step requirement.

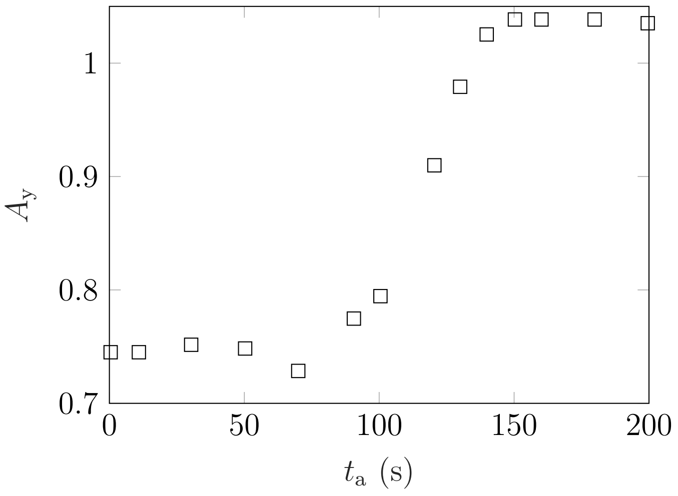

Figure 2.9: Maximum crossflow amplitude at different acceleration times. Source: [45]

Numerical models based on the solution of the RANS equations describe the statistical evolution of a flow in a given system. Due to a greater number of unknowns than equations, additional information is needed. This problem is solved by the inclusion of turbulence models, which are a set of equations obtained through experimentation or mathematical derivation that predict the effects of turbulence in a flow. Several turbulence models have been developed, each with their advantages, disadvantages and limitations. The accuracy of different turbulent models was compared against two-dimensional PIV measurements of a flow around a stationary cylinder at $R_e = 4 \times 10^4$ [98]. Compared to the Spalart–Allmaras, Realisable

$k - \epsilon$ and Wilcox $k - \omega$, the Shear Stress Transport (SST) $k - \omega$ achieved higher accuracy in terms of velocity, vorticity, and shear stresses estimation. The higher accuracy of the SST $k - \omega$ against other popular turbulence models was also demonstrated in cases of a flow around a stationary cylinder at $R_\mathrm{e} = 2.5 \times 10^5$ [1] and in three-dimensional models of a flow around axis turbines [63]. In the context of VIV, several researchers successfully extracted the main features (maximum cylinder amplitude, main oscillation and vortex frequencies, total hydrodynamic forces, vortex modes, phase angle, among others) in one [50, 117] and two [35, 45, 105, 106] degree-of-freedom cylinders using the SST $k - \omega$ model. Figure 2.8 shows some of the impressive results achieved by these numerical models. The SST $k - \omega$ [67, 68] is a hybrid two-equation eddy-viscosity model that uses a blending function to transition between the $k - \omega$ model near solid surfaces and the $k - \epsilon$ model outside the boundary layer. Despite the overall good performance and accuracy of the SST $k - \omega$ model, several numerical studies have shown difficulties to reach the maximum experimental responses in the upper branch of low mass-damping ratio cylinders [25, 32, 77]. In recent years, the use of two-dimensional RANS models on complex VIV configurations improved considerably after carefully matching the numerical and experimental conditions. A numerical study showed the importance of the Reynolds number R_e and how this parameter must be proportional to U_r to accurately simulate the response of a one degree-of-freedom cylinder undergoing VIV [104]. In addition, the inflow conditions on the cylinder response have been a critical component in the correct simulation of VIV. The cylinder response of a one degree-of-freedom cylinder [47] was simulated under three different inflow conditions: constant velocity and gradual increment/decrement of the inflow velocity up to the desired value followed by a period of constant velocity [33]. The simulation captured the beginning of the upper branch under increasing velocity conditions. Nevertheless, the cylinder response transitioned back to the lower branch at an earlier U_r compared to the experimental results [33]. The same inflow scheme was tested for a two degree-of-freedom cylinder simulation [115]. The model successfully captured the super-upper branch under a gradual increment in the flow velocity. Specifically, the inflow velocity started at $U_\mathrm{r} = 2$ and increased at a constant normalised acceleration a_c of 0.025. This parameter is defined as

$$a_\mathrm{c} = \frac{U_{\mathrm{r\_end}} - U_{\mathrm{r\_ini}}}{f_\mathrm{nw} t_\mathrm{a}} \tag{2.10}$$

where $U_{\mathrm{r\_ini}}$ is the initial or starting reduced velocity, $U_{\mathrm{r\_end}}$ is the final reduced velocity, and t_a is the acceleration time from $U_{\mathrm{r\_ini}}$ to $U_{\mathrm{r\_end}}$.

A numerical study analysed the discrepancies of previous numerical models to capture the high-amplitude responses observed in Jauvtis and Williamson's cylinder and proposed two improvements [45]. Firstly, a modified version of the $k - \omega$ was developed. This new turbulence model achieved a higher performance compared to the standard SST $k-\omega$ for a fixed cylinder between $5\times10^3 \leq R_\mathrm{e} \leq 1\times10^6$. Secondly, the researchers studied the influence of t_a (a_c) on the cylinder response (Figure 2.9). Overall, the maximum crossflow response increased towards its experimental value as t_a (a_c) increased (decreased). The researchers concluded that a minimum acceleration time of 150 seconds was needed to trigger the maximum amplitudes observed in the supper-upper branch. Using the modified SST $k - \omega$ turbulence model and considering a minimum acceleration time of 150 seconds, the numerical model achieved good agreement in oscillation frequency, maximum displacement, lift and drag forces, phase angle, and vortex modes. Moreover, the numerical model captured the complex 2T vortex mode characteristic of the super-upper branch. Other researchers were able to capture most of the super-upper branch by slowly increasing the flow velocity and maintaining a constant $R_\mathrm{e}/U_\mathrm{r}$ (see Figure 2.8). These numerical studies used the SST $k - \omega$ model, indicating that most of the improvements shown in [45] were due to imposing a proper normalised acceleration on the inflow velocity.

This section has shown the significant progress from two-dimensional RANS models to extract the main features of cylinders subjected to VIV. Still, their application is mostly restricted to rigid cylinders subjected to uniform flows, and little consideration has been paid to their use on variable amplitude cylinders, such as the pivoted configuration. Can two-dimensional models extract the main features of a pivoted cylinder, considering their three-dimensional body-wake interaction? This research project aims to explore this gap by investigating the experimental case of a pivoted cylinder subjected to VIV and its two-dimensional representation using numerical RANS models. A two-dimensional model was developed based on the experimental conditions and the pivoted configuration. The numerical model's limitations, capabilities, and accuracy were evaluated by comparing its results with the experimental pivoted cylinder in terms of displacements and oscillation frequencies.

Chapter 3

Experimental methods

3.1 Introduction

This chapter introduces the experimental equipment and methods used to characterise the incoming flow, wake and structural response of a cylinder subjected to VIV. Firstly, a general description of each experimental component and their respective setup are given. Secondly, the process of obtaining data from images used for flow velocity fields and structural motion are detailed alongside their respective measurement errors. Thirdly, several tests on the cylinder integrity and linear-elastic behaviour were described. Lastly, the incoming open-channel flow was broadly characterised.

3.2 Experimental equipment

3.2.1 Water channel

The recirculating water channel shown in Figure 3.1 has dimensions of 17.5 m length and 0.5 m width. The side and bottom of the flume were covered using clear cast acrylic sheets, leaving an effective width of 486 mm. The longitudinal slope was fixed at 0.001 m/m by adjusting two hydraulic presses underneath the flume. The water depth was fixed at the measurement zone by adjusting a control gate located at the end of the flume. A remotely controlled valve regulated the incoming flow rate. A maximum flow rate of 33.1 l/s was achieved when this valve was fully opened. The experiments were performed at 10.5 m downstream of the inlet. Specific dimensions of the water channel are shown in Figure 3.2.

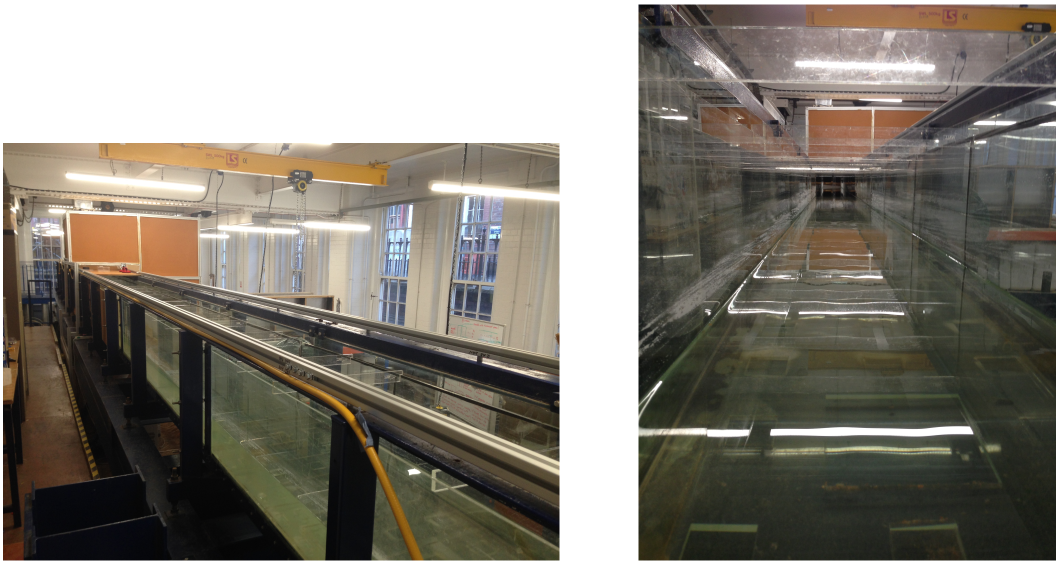

(a) (b)

Figure 3.1: Photos of the recirculating water channel. a) Outside view. b) Inside view

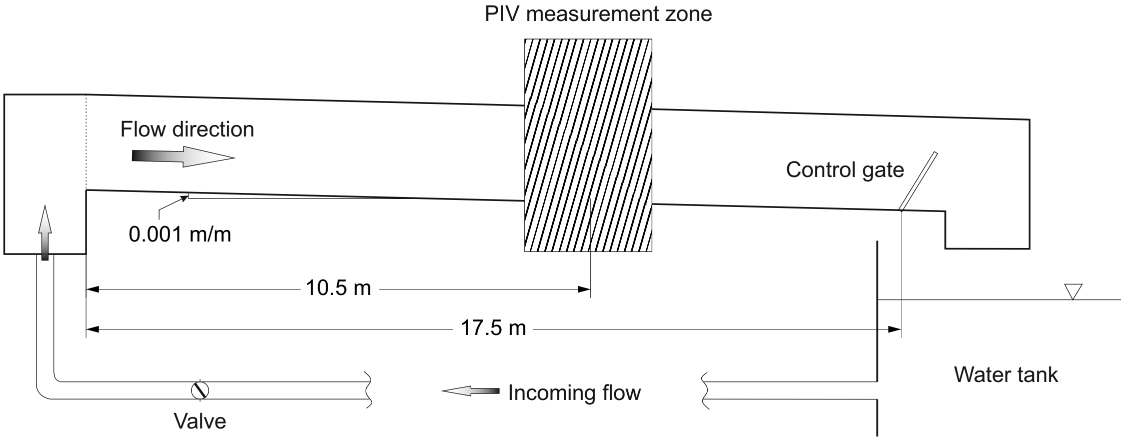

Figure 3.2: Sketch (not scaled) and dimensions of the recirculating water channel

3.2.2 Cylinder configuration

This section describes the materials and mounting process for the bottom-fixed and pivoted cylinders.

Bottom-fixed cylinder

Figure 3.3 shows a bottom-fixed cylinder made of clear cast acrylic. This material has a density of 1.19 g/cm^3 and an elastic modulus of 3200 MPa. The cylinder had a 5 mm diameter and 501 mm total length, reduced to an effective length of 491 mm after the mounting process. A 10 mm hole was drilled in an acrylic base of 165 mm width. The cylinder was inserted into the acrylic base, and its connection was chemically welded to ensure a fixed end. Figure 3.3b shows the cylinder-base

(a) (b)

Figure 3.3: Bottom-fixed cylinder. a) Rest position. b) Cylinder-base welded connection

connection 24 hours after the acrylic weld was applied. The other end is free to vibrate in the streamwise (x-axis) and crossflow (y-axis) direction. The spanwise (z-axis) direction lies along the axis of the cylinder at rest.

Experiments related to the bottom-fixed cylinder undergoing VIV (Chapter 5) maintained a fixed water depth of $H_\mathrm{w} = 347$ mm. Thus, $m^* = 1.41$. A frequency analysis on a free decay test (Section 3.4.1) showed that the natural frequency (first structural mode) measured in air and in water ($H_\mathrm{w} = 347$ mm) were $f_\mathrm{na} = 6.4$ Hz and $f_\mathrm{nw} = 5.3$ Hz, respectively. Moreover, a decaying exponential curve fit on the same free decay test showed that ζ was approximately 4% in air and 7.6% in water. These dynamic parameters were not affected by the direction of the unidimensional displacement.

Pivoted cylinder

The pivoted configuration of Figure 3.4 is composed of a silver pin and a clear cast acrylic tube connected through a rigid plug. The pin of 1.6 mm diameter and 160 mm length was made from a silver-based brazing alloy (38% of silver), characterised by a density of 9.1 g/cm^3 and tensile strength of 450 MPa (specifications in compliance with ISO 17672:2016 Ag 138). The clear cast acrylic tube had a diameter of 20 mm, four millimetre thickness and 300 mm length. The plug was composed of a rigid acrylic disk between two high-density rubber disks. The total height and weight of the plug were 15 mm and 5 g, respectively. The plug was fixed on the silver pin and fitted inside the acrylic tube. A 1.6 mm hole was drilled in an acrylic base of 165 mm width. The pin was inserted into the acrylic base, and its connection was

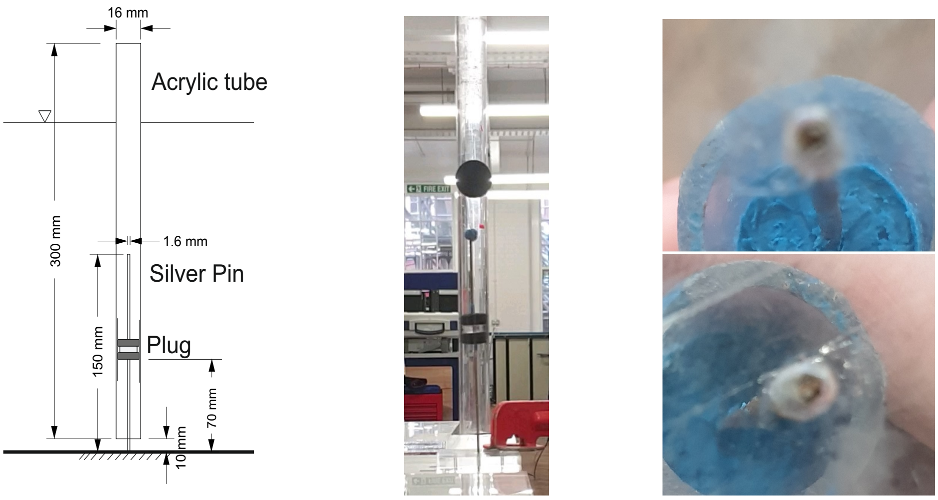

(a) (b) (c)

Figure 3.4: Pivoted cylinder. a) Sketch (not scaled) and dimensions. b) Prototype. Rest position. c) pin-base connection

chemically welded to ensure a fixed end. Figure 3.4c shows the fixed end 24 hours after the acrylic weld was applied on the pin-base connection. The other end is free to vibrate in the streamwise (x-axis) and crossflow (y-axis) direction. The spanwise (z-axis) direction lies along the axis of the cylinder at rest. The distance between the acrylic tube and the bottom of the flume was 10 mm, whereas the distance between the plug and the bottom of the flume was 70 mm (Figure 3.4a).

Experiments related to the pivoted cylinder undergoing VIV (Chapter 6) maintained a fixed water depth of $H_{\mathrm{w}} = 255$ mm. It is important to mention that, while the cylinder was being subjected to VIV, an air-filled region inside the acrylic tube and below the plug (Figure 3.4a) was observed throughout the experiments. This air-filled region was maintained until the cylinder was removed from the measurement zone. Under these conditions, $I^* = 1.82$ and $m^* = 1.5$. The small difference between I^* and m^* is explained by an incomplete submerge condition (water depth lower than the cylinder length). A frequency analysis on a free decay test (Section 3.4.1) showed that the natural frequency (first structural mode) measured in air and in water ($H_{\mathrm{w}} = 347$ mm) were $f_{\mathrm{na}} = 1.88$ Hz and $f_{\mathrm{nw}} = 1.64$ Hz, respectively. Moreover, a decaying exponential curve fit on the same free decay test showed that ζ was approximately 0.39% in air and 0.64% in water. These dynamic parameters were not affected by the direction of the unidimensional displacement.

3.2.3 Particle Image Velocimetry

Particle Image Velocimetry is an optical and non-intrusive measurement technique used to estimate the velocity field and other related fluid properties. Figure 3.5a

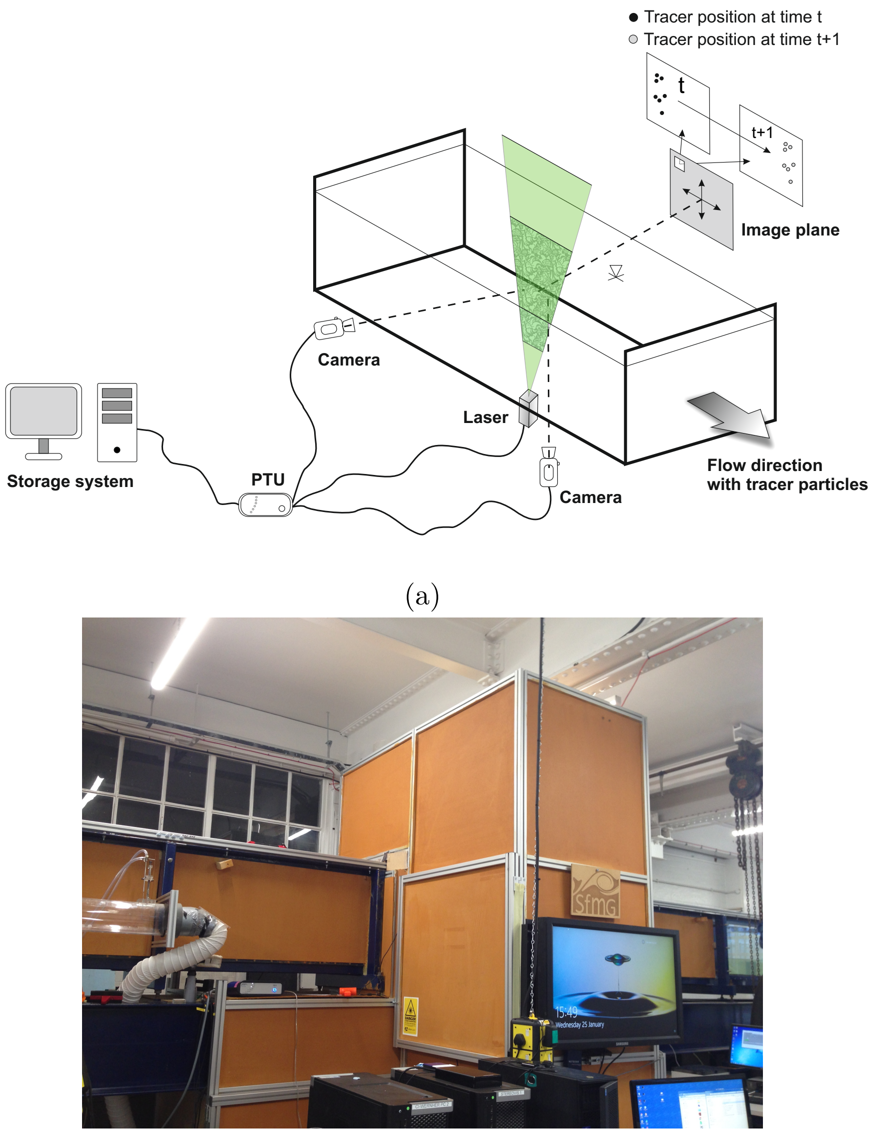

(a)

(b)

Figure 3.5: PIV experimental setup. a) Sketch. Example of a vertical (xz-axis) plane measurement. b) Measurement zone

shows a sketch of a typical PIV setup. The flow is seeded with particles, called tracers, capable of moving with the local flow velocity. A laser-based system illuminates the tracers while their position is captured using a recording device. The recorded flow images are transferred into a storage unit. These raw flow images are corrected, pre- and post-processed, to calculate their flow velocity field.

The PIV system used in this research consisted on a double-pulse 532 nm wavelength Nd:YAG compact laser (Figure 3.6a), three MX 4M high-speed cameras (Figure 3.6b), a set of LaVision calibration plates, and a Programmable Time Unit (Figure 3.6c) that configures the camera and laser trigger time. The company LaVision provided the PIV system. Their proprietary Software Davis 8.3 was used to configure the system and pre- and post-process the raw flow images into velocity

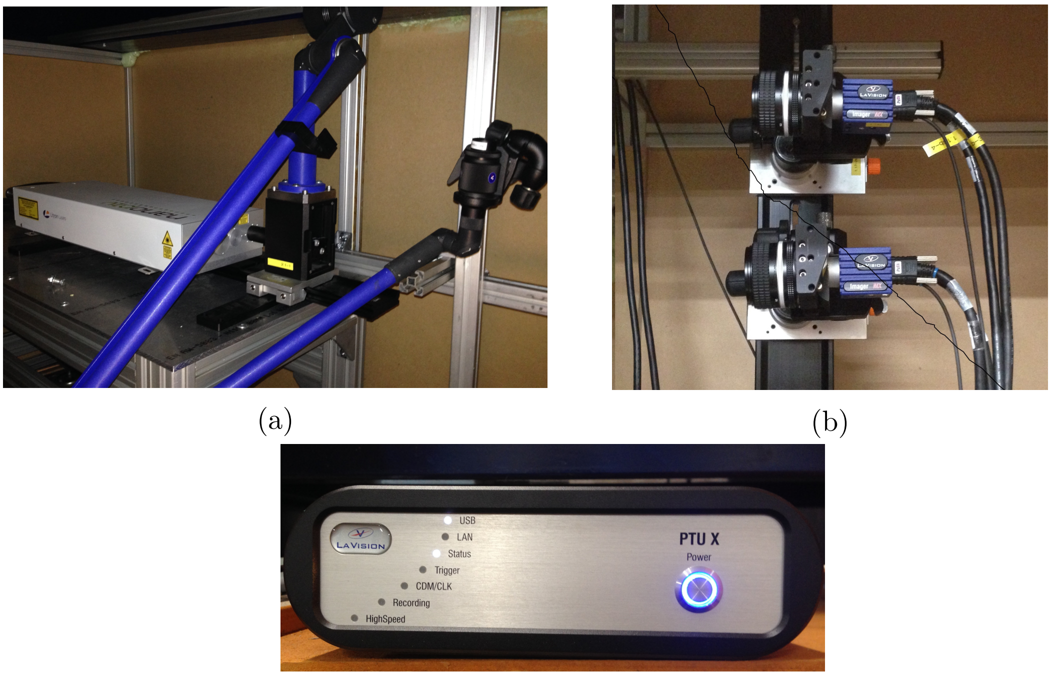

(a) (b)

(c)

Figure 3.6: Components of the LaVision PIV system. a) Double-pulse Nd:YAG compact laser. b) MX 4M cameras. c) Programmable Time Unit

fields. The laser system had a maximum power output and frequency of 100 mJ per pulse, respectively. The light emitted from the laser box travelled inside a mobile guiding arm and exited through a divergence lens towards the measurement region. The laser sheet covered a wide planar zone of five millimetres thickness, from which two-dimensional measurements were taken (Figure 3.5a). The MX 4M cameras had a four Megabyte Pixel resolution with a maximum acquisition frequency of 100 Hz. Each camera had a double-frame or double-exposure mode, where two images are taken with a short delay between exposures. A summary of this double-frame mode is given as follows. Each pixel in an image has a light-sensitive and a masked area for the exposure, accumulation, storage, transfer and conversion of voltage into an analogue video signal. The light-sensitive region receives the information and transfers it to the masked area. This information is then sequentially converted until all the voltage data is stored and a digital image is formed. As the information of the first exposure is being read and stored, the light-sensitive area accumulates light from the second exposure. Figure 3.7 shows a sketch of the synchronisation process between a double-pulse laser and a camera in a double-frame mode. dt_{camera} and dt_{laser} are the time step between images and laser pulses, respectively. The first exposure receives the light of the first laser pulse. As the collected voltage is being read out, the second exposure receives the light of the second pulse. Two images separated by dt_{camera} are generated at each time step. Since dt_{camera} is usually lower than the acquisition frequency, velocity fields calculated using double-frame measurements

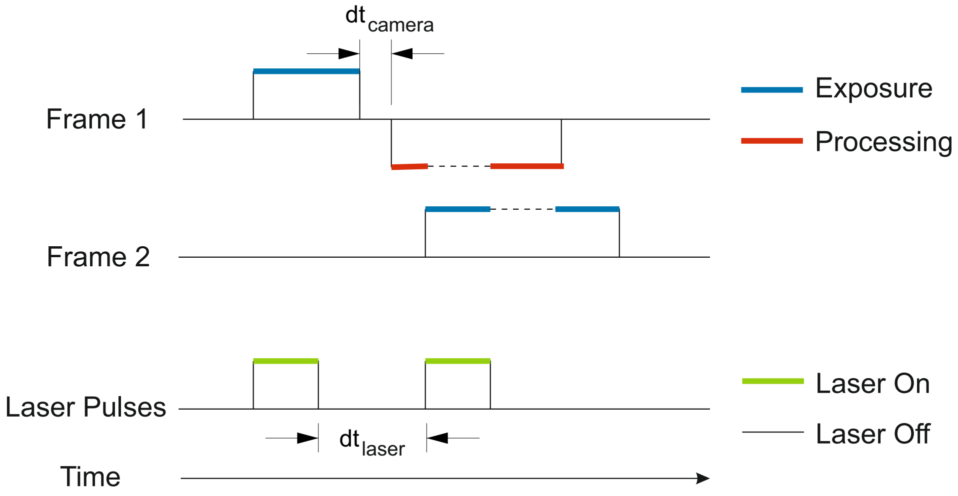

Figure 3.7: Double-pulse laser and camera in double-frame mode timing

are significantly more accurate than their single-frame counterpart. Nevertheless, the double-frame mode requires a higher storage and processing time due to the greater number of images taken per second.

(a) Source: www.vestosint.com (b)

Figure 3.8: a) White Polyamide 12. b) Calibration plate LaVision 058-5

The tracers used for the measurements consisted on white Polyamide 12 (Figure 3.8a) with a mean particle size and a density of 100 µm and 1.06 g/cm^3, respectively. These tracers were selected due to their average spherical shape, strong light scattering, and good buoyancy. Previous studies used Polyamide 12 for flow characterisation around obstacles [5, 37]. The calibration process establishes a relationship between Pixel to real-world coordinates and corrects the raw flow images from small optical distortions, such as water-air light refraction and camera-object perspective angle. Two calibration plates were used for this: model LaVision 309-15 for flow visualisation purposes and model LaVision 058-5 for cylinder motion tracking. Both calibration plates have dot patterns as markers with a square-shaped grid arrangement (Figure 3.6b). The LaVision 309-15 model is a square-shaped plate with 309 mm width. The markers have a distance and diameter of 15 mm and three millimetres, respectively. The LaVision 058-5 model is a square-shaped plate with 58 mm width. The markers have a distance and diameter of five and one millimetres, respectively.

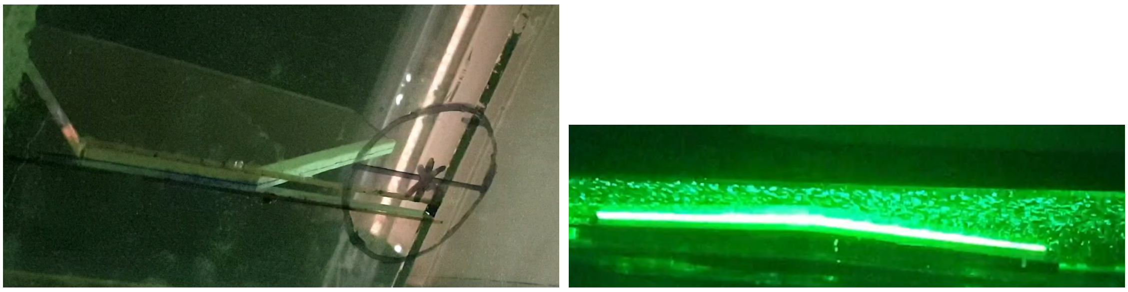

(a) (b)

Figure 3.9: Laser orientation process. a) Inclined square-shaped acrylic sheet placed in the measurement plane. b) Laser illuminates the acrylic sheet

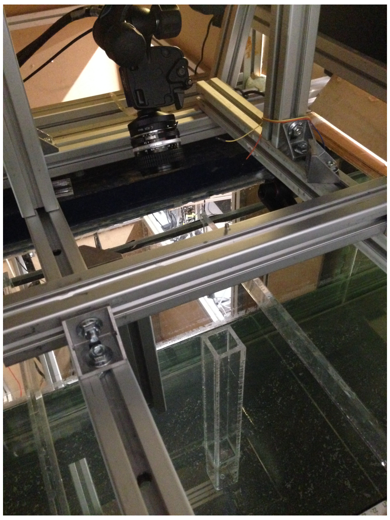

Figure 3.10: Testing the camera position for structural motion tracking

The mounting and setup process of the PIV system is described as follows

- The position of the camera and laser were easily adjusted and fixed by sliding and screwing them over aluminium rails (see Figures 3.6a and 3.6b). Initially, the laser was mounted and oriented towards the desired measurement plane. Likewise, the cameras were mounted and oriented perpendicular to the laser plane. These initial mounting positions are corrected as the experimental setup progresses.
- The laser orientation and thickness were adjusted by controlling its divergence lens. For this, an inclined square-shaped acrylic sheet was mounted in the measurement plane and used as a reference (Figure 3.9a). The water level was raised until the acrylic structure was fully covered. The laser was turned

on at a low-power level, and its orientation was systematically adjusted until the light sheet completely illuminated the side of the acrylic structure (Figure 3.9b). This process ensured a straight measurement plane. The laser sheet thickness was corrected until a convergent light of five millimetres width was achieved. The laser sheet maintained an aperture angle of 24° throughout the measurements, ensuring wide coverage of the wake region behind the cylinder. The laser position was fixed after these adjustments were completed.

- A calibration plate model LaVision 309-15 was placed in the measurement plane. A mounting system on aluminium rails ensured a proper alignment between the calibration markers and the laser sheet. The water level was raised until the calibration plate was fully covered. The position and lens of the cameras were adjusted until the boundaries of the markers were clearly defined. An external light source was evenly distributed on the calibration plate, and 20 images were taken. The average of these images was used to correlate the markers' image position with their real-world location. More details of this process are given in Section 3.3.2. The cameras were fixed to their final position after the calibration process was completed.
- The water channel was emptied, and the cylinder was placed in the measurement area. An additional MX 4M camera, synchronised with the PIV system, was mounted above the cylinder and pointed towards its free end (Figure 3.10). This camera was individually calibrated using the calibration plate LaVision model 058-5.
- Before recording the cylinder motion and wake, a few tests were conducted to configure different parameters, such as acquisition frequency, dt_{laser}, dt_{camera}, and measurement time. More details are given in Section 3.3.3. Specific parameters for each experiment can be found in Chapters 5 and 6.

3.3 Measurements and Verification

3.3.1 Increasing velocity conditions

It is common knowledge that cylinders subjected to VIV exhibit hysteretic behaviour near branch transitions [73]. Specifically, different cylinder responses are observed depending on the inflow conditions, which encloses increasing or decreasing velocity with their respective rate of change per unit of time [89]. Increasing velocity conditions generally lead to higher responses in low $m^*\zeta$ cylinders [12, 81, 92]. Thus, this condition was used in both experiments (bottom-fixed and pivoted cylinder) and is explained as follows. The flow rate was first initially increased up to a certain value. Then, a minimum of 30 minutes was permitted to elapse, ensuring that any transient effect was dissipated. After measuring the flow and cylinder response, the flow rate was increased to a new value, a minimum of 30 minutes elapsed, and a new measurement was taken. This process was repeated until the maximum flow rate of the experimental facility was reached. Throughout this process, the water depth was fixed at the measurement zone.

3.3.2 Calibration process

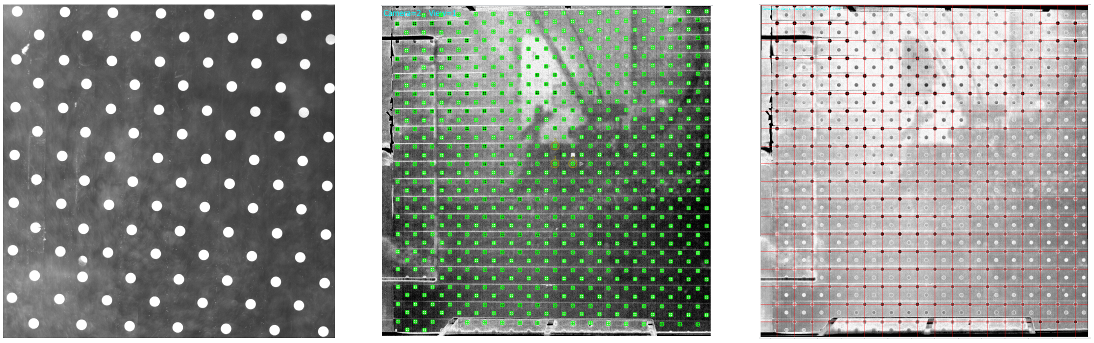

(a) (b) (c)

Figure 3.11: Flow velocity field calibration process. Calibration plate LaVision 309-15 model. a) Raw image. b) Marker detection. c) Corrected image

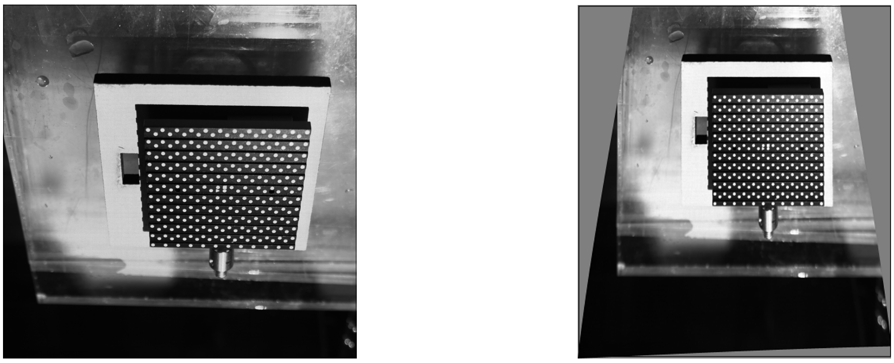

(a) (b)

Figure 3.12: Cylinder motion calibration process. Calibration plate LaVision 058-5 model. a) Raw image. b) Corrected image

The calibration process corrects the raw images from optical distortions and establishes a correspondence between Pixel and real-world coordinates. Figure 3.11a shows a raw image of the LaVision 309-15 calibration plate slightly tilted to the right. This image corresponds to the average of 20 images taken at a low acquisition frequency of 10 Hz. Thus, reducing background noise and improving marker edge definition. These markers were automatically detected using Davis 8.3, as seen in Figure 3.11b. Then, the image was corrected using a third-order polynomial function (Figure 3.11c). The parameters of the polynomial function are used to calibrate each raw flow image before extracting their corresponding velocity field. The same process is applied for the structural motion (Figure 3.12), in which each raw image of the cylinder free end is corrected before tracking its corresponding position. Davis 8.3 quantifies the correction error as the average deviation between the corrected image and an ideal grid. The Davis 8.3 manual [56] recommends an error lower than one Pixel for a two MegaPixel camera. Cameras with higher Pixel resolution allow larger Pixel errors. Errors of 0.4 Pixels or lower were considered acceptable in this thesis.

3.3.3 PIV measurements

This section discusses relevant aspects to accurately capture the flow dynamics around a cylinder. Most of the parameters were adjusted according to the Davis 8.3 manual [56].

The density and resolution of tracers play a fundamental part in their detection and correlation. The particle size was maintained between two and four pixels [79]. The particle density was increased until at least one tracer per 20 pixels was observed. The average distance travelled by the tracers between exposures was maintained at five pixels. These parameters were adjusted through different means. The tracer pixel resolution was changed by adjusting the camera-object distance. The density of the tracers was increased by manually adding more seeding particles. Finally, the tracers' average travel distance was achieved by adjusting dt_{camera}. Davis 8.3 iteratively finds the optimal dt_{camera} until the desired travelled distance of five pixels was achieved. This iterative process was repeated every time the flow rate was increased.

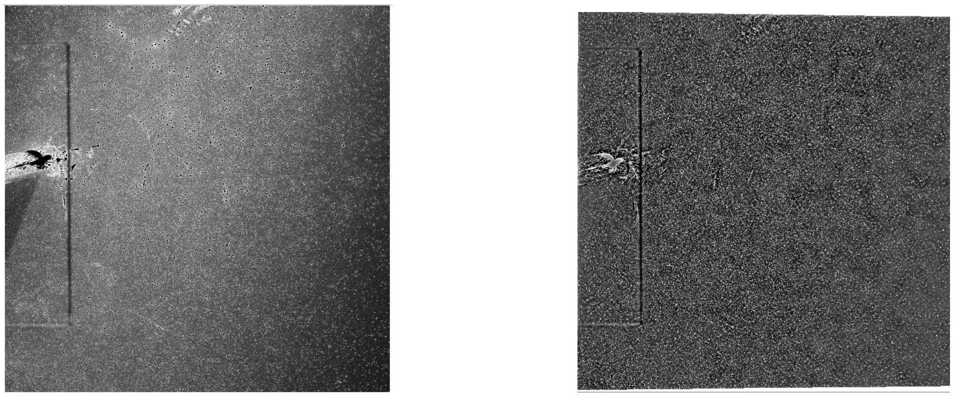

(a) (b)

Figure 3.13: Filter effect on raw flow images. a) Raw image. b) Filtered image

A number of pre-processing techniques are available in Davis 8.3 to improve the tracer resolution and visualisation. In this work, two filters were applied: a sliding background removal and an intensity normalisation object filter. The first filter removes intensity variations in the image background without affecting the pixel intensity of the tracers. The second filter normalises the intensity value of the tracers within a window. Figure 3.13 shows the raw and corrected flow image after applying a sliding background removal and an intensity normalisation window size of 10 and eight pixels, respectively.

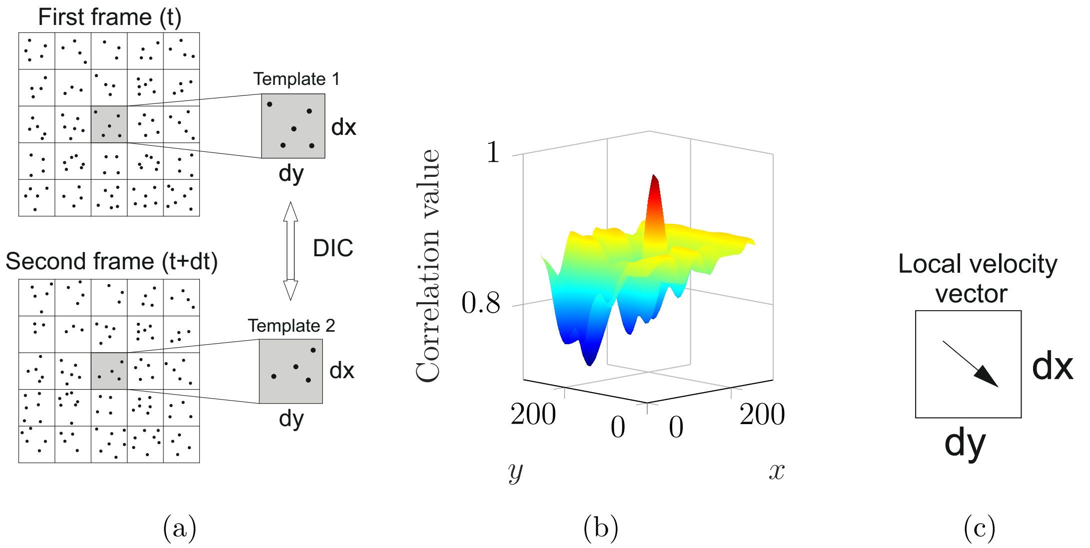

(a) (b) (c)

Figure 3.14: Digital Image correlation applied to corrected flow images. a) Template configuration between consecutive images. b) Correlation map. c) Resultant local velocity vector

Davis 8.3 estimates the position between groups of tracers using an iterative multi-pass multi-grid approach [90] based on the Digital Image Correlation (DIC) technique. DIC uses correlation functions to quantify the similarity between a region around a target (called interrogation window or template) and an image. Figure 3.14 summarises the systematic application of DIC to two consecutive flow images. Each image is subdivided in templates and compared as shown in Figure 3.14a. The correlation function is systematically calculated as the template of the first image is shifted around the template of the second image. This process generates a correlation map per template (Figure 3.14b). The position of the highest correlation peak corresponds to the most probable displacement of the group of tracers within the template. The local velocity vector is then calculated as the ratio between the local flow displacement and the acquisition time between images. The fundamentals of DIC can be found in Appendix A.1. The interrogation window size plays a critical role in the tracking accuracy. The template size must be large enough to maintain a minimum number of tracers. On the other hand, large interrogation window sizes average out the small scale structures of the flow. An interrogation window size that contains an average of at least ten tracers was considered [46].

Davis 8.3 uses different techniques to improve the correlation between the template and flow image. A multi-pass approach uses larger interrogation window sizes as an initial guess to improve the correlation between smaller interrogation window sizes. Subpixel accuracy was achieved by fitting a Gaussian function on the maximum correlation and its nearby values. Thus, the final position of the template was not restricted to an integer pixel position. Finally, the resolution of the measurements was increased by overlapping nearby interrogation windows.

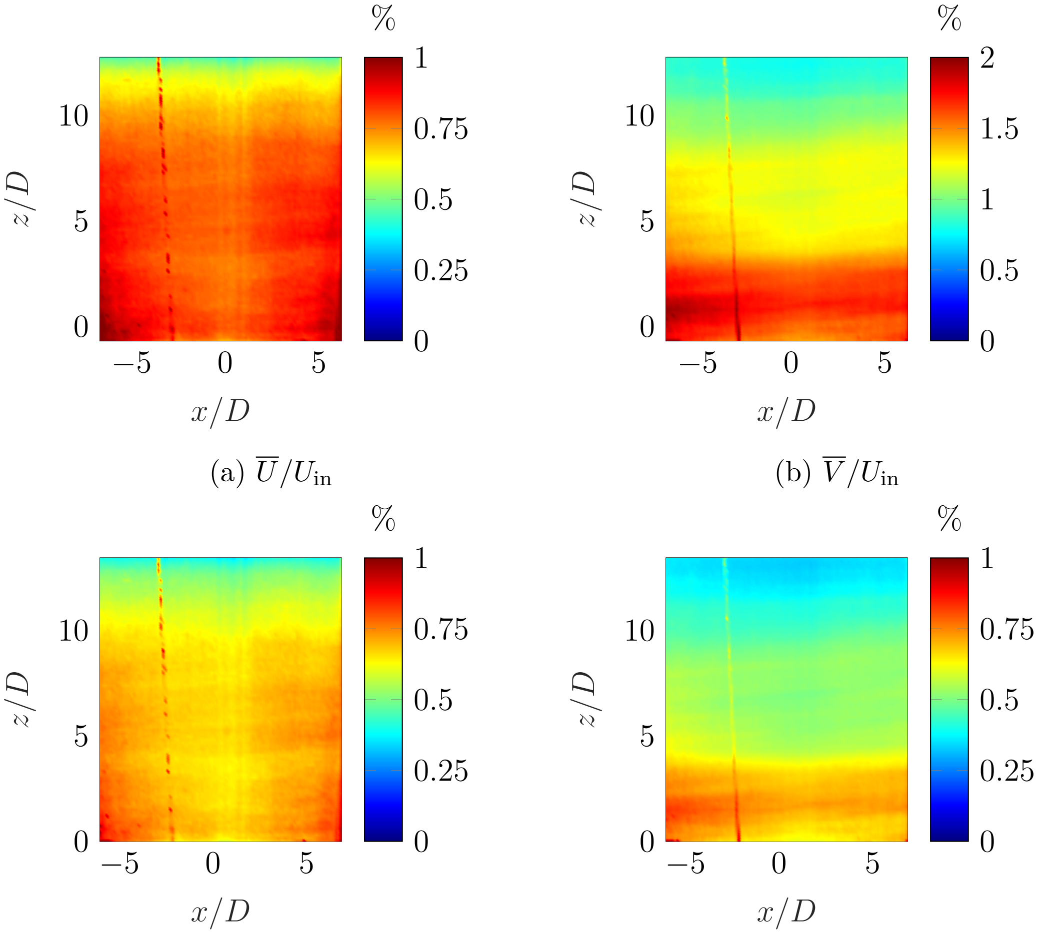

(a) $\overline{U}/U_{\text{in}}$ (b) $\overline{V}/U_{\text{in}}$

(c) $\text{rms}(u')/U_{\text{in}}$ (d) $\text{rms}(v')/U_{\text{in}}$

Figure 3.15: Uncertainty of the free stream flow at the maximum tested inflow velocity ($U_{\text{in}} = 0.29$ m/s). Time-averaged (a,b) and root-mean-square (c,d) uncertainty. Streamwise (a,c) and spanwise (b,d) uncertainty velocity components. Uncertainty was normalised by U_{in}. Spatial dimensions were normalised by the pivoted cylinder diameter $D = 20$ mm

Davis 8.3 uses a post-processing local uncertainty method [109] to measure the error associated with the velocity field. Considering two consecutive flow images, the second image is dewarped back onto the first image using the calculated velocity field. Ideally, this comparison matches perfectly, and a symmetric correlation map is obtained. In an experimental environment, differences between images result in

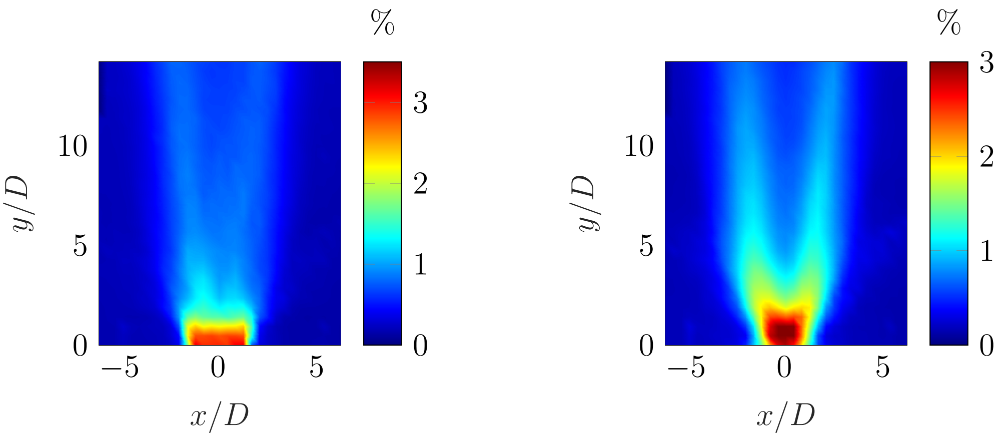

(a) $\overline{U}/U_{\text{in}}$ (b) $\overline{V}/U_{\text{in}}$

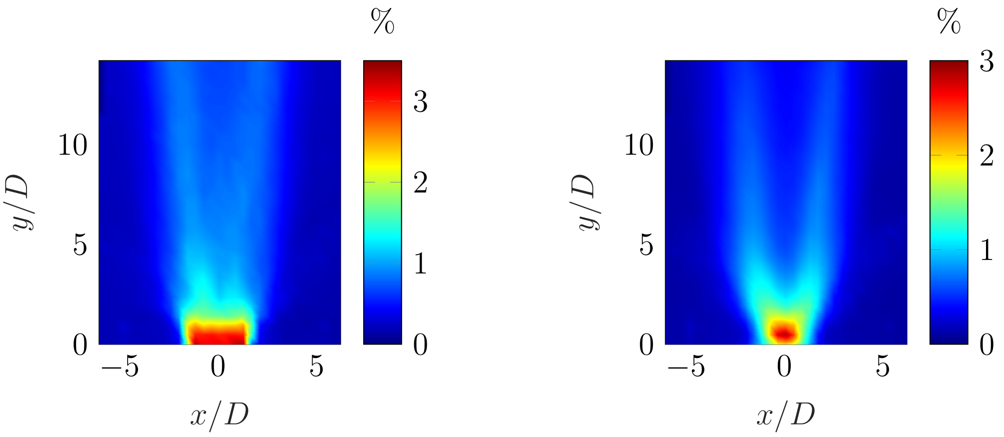

(c) $\text{rms}(u')/U_{\text{in}}$ (d) $\text{rms}(v')/U_{\text{in}}$

Figure 3.16: Uncertainty of the wake behind a pivoted cylinder measured at 20.2 cm from the flume's bed and at the maximum tested inflow velocity ($U_{\text{in}} = 0.29$ m/s). Time-averaged (a,b) and root-mean-square (c,d) uncertainty. Streamwise (a,c) and crossflow (b,d) uncertainty velocity components. Uncertainty was normalised by U_{in}. Spatial dimensions were normalised by the pivoted cylinder diameter $D = 20$ mm

a non-symmetric correlation peak. The contribution of each pixel to the cross-correlation peak shape is used to estimate the uncertainty of the measurement. An uncertainty analysis was performed under extreme experimental PIV conditions, which involve high inflow velocities and high-velocity gradients. Figures 3.15 and 3.16 show the uncertainty of the velocity field under two flow conditions, free stream flow measured at the flume's centreline (Figure 3.15) and wake behind a pivoted cylinder measured at 20.2 cm from the flume's bed (Figure 3.16). The inflow velocity on both conditions was $U_{\text{in}} = 0.29$ m/s. The coordinate system was centred around the cylinder position at rest. A small region of outliers is observed between $x \approx 3D$ and $x \approx 5D$ (Figure 3.15), generated by laser refraction in the measurement region. These outliers did not influence the data analysis process since they were upstream of the cylinder position. Overall, the uncertainty of the velocity field under free flow and wake conditions had an upper limit of 1% and 3.5% under free stream and wake conditions, respectively.

3.3.4 Structural motion tracking

Measurements of the wake and cylinder response were taken in a synchronised manner. The flow images were processed and converted to flow velocity fields as described in Section 3.3.3. The recordings of the cylinder were processed independently, calibrating the raw images (Section 3.3.2) and using tracking techniques to estimate the location of the structure across images. The MX 4M camera placed above the cylinder free end (Figure 3.10) provided high-resolution images (2048x2048 pixels) at acquisition frequencies of up to 100 Hz. These characteristics allowed to capture the cylinder motion at several times the maximum oscillation frequencies of both cylinders (6.4 Hz for the bottom-fixed cylinder and 1.88 Hz for the pivoted cylinder). Thus, the structural motion was properly captured in both experiments and deviations from the true cylinder position are expected to originate from the tracking technique accuracy.

Experiments were conducted to analyse the accuracy and capabilities of two commonly used tracking techniques: digital image correlation and the Lukas-Kanade optical flow technique. An in-depth description of the experiment and results can be found in Appendix A. A computer-controlled shaker was used as a benchmark case to create a one-dimensional oscillatory target motion. Three target frequencies were recorded. The measurements obtained with a low-cost digital camera were compared to a high-precision motion tracking system. The comparison was performed under changes in image resolution, target motion and sampling frequency. Overall, the Lucas-Kanade technique showed superior accuracy when it is able to track the target. Nevertheless, it has an important dependency on the relative pixel value (intensity gradients) of the initial target point, which makes it difficult to achieve its higher accuracy. This dependency can be minimised through the implementation of the Forward-Backward tracking failure technique [43] without depending on additional external measurements.

The structural motion was estimated using the Lucas-Kanade and Forward-Backward techniques (Appendix A.3.5, code implementation can be found in Appendix D.2.1). This last method is based on the fact that the tracking of an object from the spatial position P_1 to P_2 in time is equivalent to its tracking between P_2 and P_1 backwards in time. In an experimental setting, P_1 and the final location tracked from P_2, defined as P_1', will be different. The Euclidean difference between P_1 and P_1' is defined as FB-error and is a measure of the tracking technique accuracy. The Forward-Backward technique has been shown to effectively find the initial target

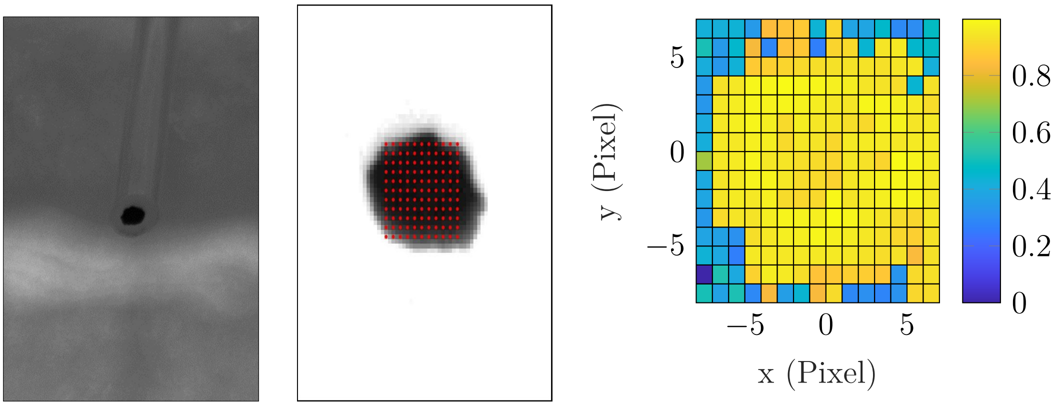

(a) (b) (c)

Figure 3.17: Motion tracking process. a) Cylinder raw image. b) Pre-processed image with 256 initial target points. c) FB-error distribution. $1 - \text{FB-error}/max(\text{FB-error})$

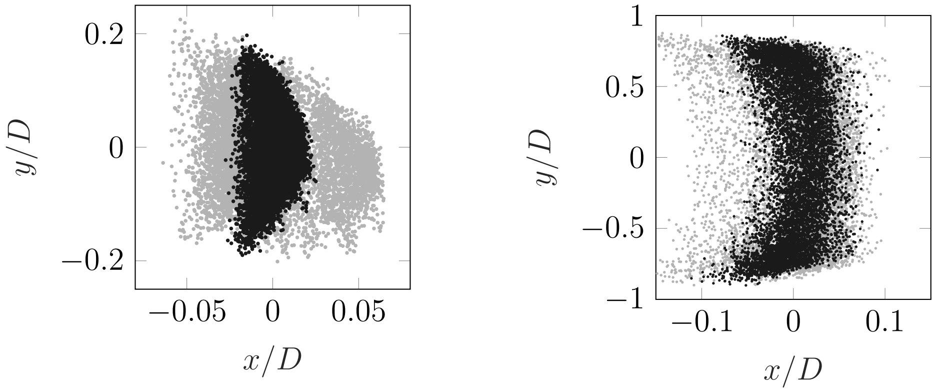

(a) Flow rate: 15 l/s

(b) Flow rate: 23 l/s

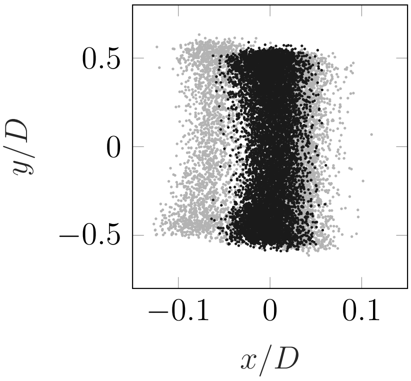

(c) Flow rate: 33 l/s

Figure 3.18: Comparison between the Lucas-Kanade technique with the Forward-Backward implementation (black) and a tracking result with a 99th FB-error percentile (grey). The mean streamwise displacement was removed to facilitate the comparison

points that maximise the accuracy of the Lucas-Kanade technique [66]. Recordings of the bottom-fixed cylinder subjected to three flow rates of 15, 23, and 33 l/s were used to quantify the error associated with the tracking technique. The oscillation frequency of 5.3 Hz and 5 mm diameter of the bottom-fixed cylinder imposed higher difficulties for motion tracking compared to the pivoted cylinder experiment. Each recording was taken at 70 Hz for two minutes (additional information can be found in Chapter 5). Figure 3.17a shows a raw image of the cylinder free end. The image intensity values were adjusted to minimise background noise and increase the intensity gradients of the target. An evenly spaced square grid of 256 initial target points with one Pixel separation was placed on the target (Figure 3.17b). After applying the Lucas-Kanade technique on each grid point, their associated FB-error were calculated. Figure 3.17c summarises the accuracy of the tracking technique per grid point, where the 95th percentile had a FB-error of approximately $0.01D$. Figure 3.18 shows the results obtained after implementing the Forward-Backward technique and one initial tracking point associated with the 99th FB-error percentile (lowest tracking accuracy). Significant differences in displacement are observed in the streamwise direction, where its response is up to 19 times smaller than its crossflow motion. These results show that the tracking technique can track the cylinder position with a FB-error of $0.01D$.

3.4 Cylinder behaviour

3.4.1 Free decay test

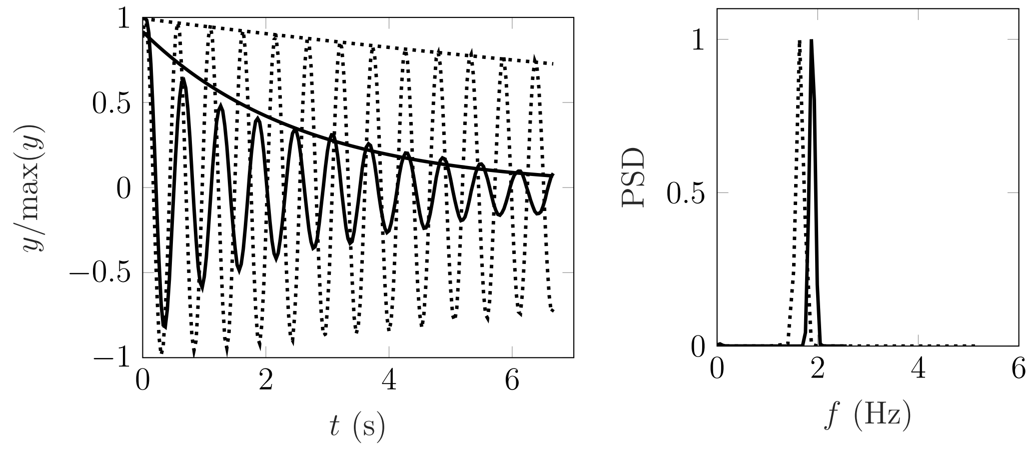

(a) (b)

Figure 3.19: Free decay test. Cylinder response in air (dashed line) and water (black line). a) Cylinder crossflow motion with logarithmic decay fit curves. b) Frequency content of the crossflow response

Free decay tests are commonly used in VIV to determine a structure's damping ratio and natural frequency. Changes in these dynamic properties can be used to detect plastic deformations or losses in structural integrity. Thus, a linear-elastic response can be assumed if these dynamic properties are maintained after subjecting the structure to a series of displacements. In the context of this research project, a free decay test consists of imposing a unidimensional displacement to the cylinder free end. The structure is released while recording its response. This process was repeated five times in the crossflow and streamwise direction each. The cylinder response was estimated using image-based tracking techniques (Section 3.3.4). The main oscillation frequency was calculated through a Power Spectral Analysis. The damping ratio was obtained by fitting the following equation

$$A(t) = A_\mathrm{o} \exp(-B_\mathrm{o} t) \tag{3.1}$$

using the peak amplitude response data. $A(t)$ is the maximum displacement in the streamwise or crossflow direction, A_o and B_o are the parameters of the model. Assuming a logarithmic decay response fitted in the least square sense, $\zeta = B_\mathrm{o}/2\pi f_{\mathrm{na,nw}}$. Figure 3.19 shows the pivoted cylinder response in air and still water, alongside their oscillation frequencies and logarithmic decay responses. As expected, the motion history in air has a higher oscillation frequency and lower damping compared to its response in water.

3.4.2 Bottom-fixed cylinder

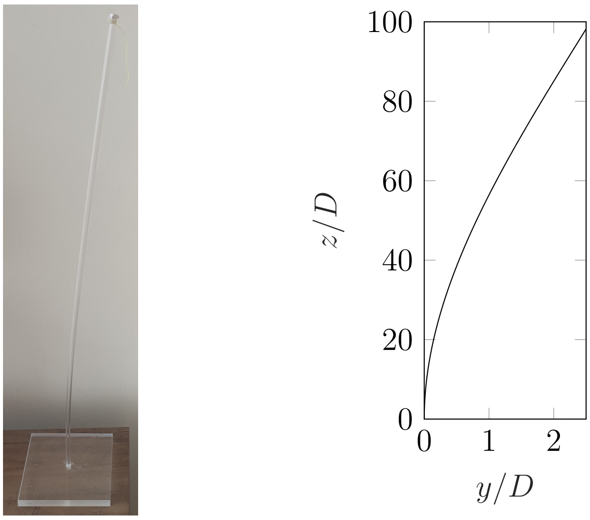

(a) (b)

Figure 3.20: Bottom-fixed cylinder deflected shape. a) Photo of the structure under an arbitrary load applied at its free end. b) Deflected shape of (a) along the cylinder span

The bottom-fixed cylinder in Figure 3.20 behaves as a cantilever structure with a non-linear deflected response along its span. Assuming a linear-elastic response, the position of the bottom-fixed cylinder subjected to an arbitrary displacement was modelled using the Software Ansys Structural (Release 18.1). Figure 3.20b shows this deflected shape under a maximum experimental displacement of $2.5D$ (Section 5.3.1). The associated inclination angle up to the water surface (H_w = 347 mm) was 2.1°. The independence principle states that VIV is driven by the flow component normal to the cylinder surface and that the perpendicular (axial) component is negligible [9]. This principle is valid for inclination angles of less than 20° [9, 96, 114]. Applying the independence principle when the cylinder reaches its maximum inclination angle, the component of the hydrodynamic force normal to the cylinder surface is only 0.1% lower compared to its magnitude. Thus, the maximum inclination angle is expected to have negligible effects on the wake and cylinder response.

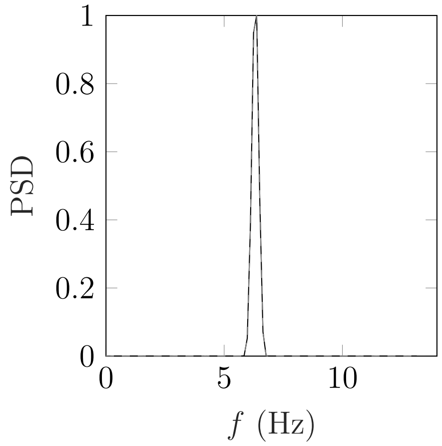

Figure 3.21: Frequency content of the crossflow cylinder response before (black) and after (dashed grey) 60 hours of high-amplitude responses

The endurance of the fixed end and the linear-elastic response condition were tested by subjecting the bottom-fixed cylinder for long periods of VIV. Specifically, high amplitudes of $A_\mathrm{y} \approx 0.7D$ at $U_\mathrm{r} \approx 5$ (Section 5.3) were maintained in six sessions of 10 hours each. A free decay test was conducted before and after the experiments. Figure 3.21 shows no difference in frequency content after long periods of high-amplitude oscillations. Thus, the fixed end did not degrade its condition over time, and the cylinder maintained a linear-elastic response.

3.4.3 Pivoted cylinder

The response of the pivoted cylinder is given by the behaviour of its individual components. The complex hydrodynamic forces on the acrylic tube are transferred to the silver pin through the rigid plug. This force path implies that, while the acrylic tube interacts with the fluid flow, the structural resistance is given entirely

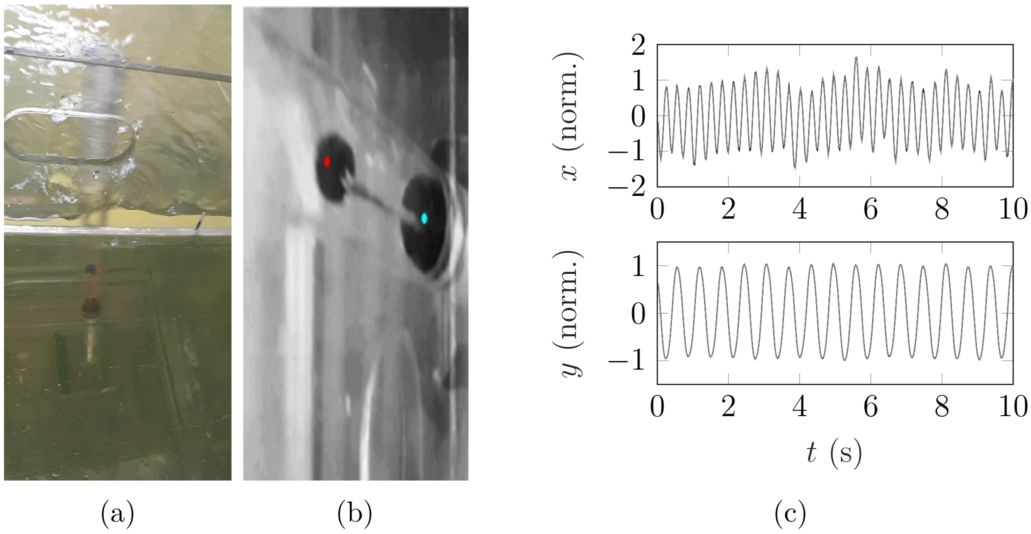

Figure 3.22: Pivoted cylinder monolithic response test. a) Raw image of the recording. b) Pre-processed image for tracking c) Streamwise (up) and crossflow (down) response of the pin (black) and plug (grey). Responses were normalised by their maximum amplitude

by the silver pin. Thus, it is important to prevent relative displacements between components under experimental conditions. A prototype was placed inside the flume and subjected to VIV. An acrylic box was fixed behind the cylinder while touching the water surface to minimise optical distortions and have a clear view of the silver pin and plug. Markers were previously placed on the acrylic tube and pin (Figures 3.4b and 3.22b) to simultaneously track their responses. The cylinder response was recorded at 70 Hz for 300 seconds. Figure 3.22c shows the motion history of the pin and plug in the streamwise and crossflow direction. Each response was normalised by their maximum position for comparison. Negligible differences are observed near peak amplitudes, which can be attributed to the tracking technique accuracy (Section 3.3.4). Overall, there is a clear correspondence between the pin and plug responses, which supports the monolithic behaviour of the pivoted cylinder.

The endurance of the fixed end and the linear-elastic response condition were tested by subjecting the pivoted cylinder for long periods of VIV. The pivoted cylinder was subjected to high-amplitude oscillations at $U_\mathrm{r} \approx 7.42$ (Section 6.3.1). Responses of $A_\mathrm{y} \approx 2.1D$ were maintained in six sessions of 10 hours each. Relative displacements in the plug connection were detected by observing plastic deformations of plasticine added on top and underneath the plug. Pictures taken before and after the experiments (Figure 3.23) showed no observable deformation on the plasticine after 60 hours of high-amplitude vibrations. Then, a free decay test was conducted, and the results were compared to a previously performed free decay test. Figure 3.21 shows no difference in terms of frequency content before and after the experiment. Thus, the fixed end did not degrade its condition over time, and the

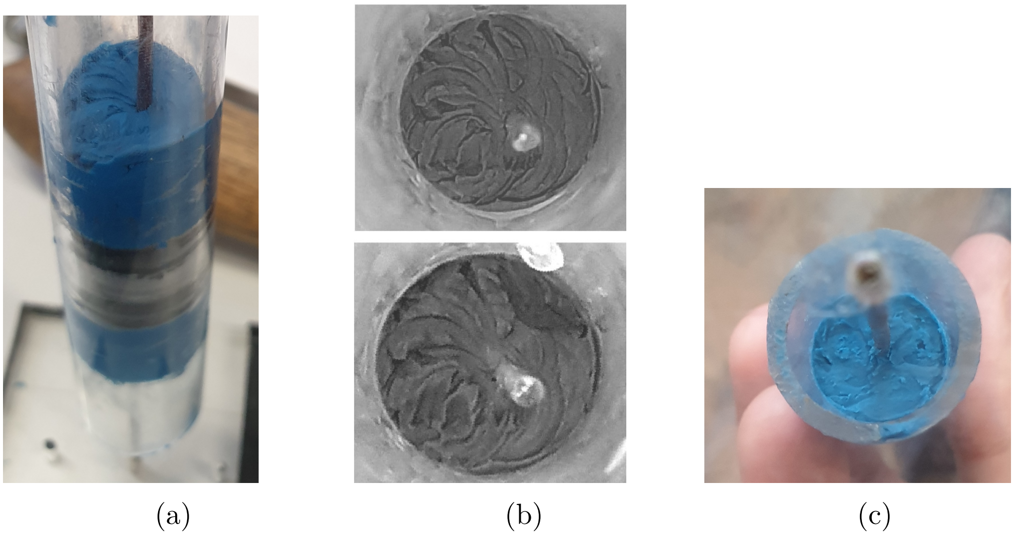
(a) (b) (c)

Figure 3.23: Pivoted cylinder endurance test. a) side view. b) top view before (up) and after (down) 60 hours of high-amplitude vibrations. c) fixed end and bottom pin-plug connection after endurance test

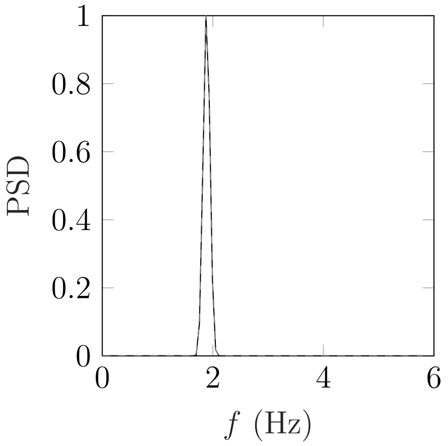

Figure 3.24: Frequency content of the crossflow cylinder response before (black) and after (dashed grey) 60 hours of high-amplitude responses

cylinder maintained a linear-elastic response.

Similarly to the bottom-fixed cylinder (Section 3.2.2), the maximum response of the pivoted cylinder under experimental conditions (Section 6.3.1) led to an inclination angle of $\theta = 7.8^{\circ}$ regarding its rest position. Applying the independence principle at this extreme condition, the component of the hydrodynamic force normal to the cylinder surface is only 1% lower compared to its magnitude. Thus, the maximum inclination angle is expected to have a small effect on the cylinder response. Overall, the tested pivoted configuration maintained a linear-elastic condition with no degradation on its fixed end and between components. These characteristics are critical to ensure that the experimental responses can be represented as a spring-mass-damping model (Section 4.3.2).

3.5 Open-channel flow considerations

The water channel described in Section 3.2.1 has been used throughout this research project. As such, important elements related to open-channel flows must be taken into consideration.

The theory of open-channel flows indicates that a uniform flow with a certain boundary shear stress, flow depth and mean inflow velocity is uniquely related to a combination of flume slope, bed sediment, and flow rate [14]. The experiments in this research project were performed under a fixed flume slope and bed sediment conditions while the flow rate was systematically increased. Thus, the uniform flow condition is not met, and the experimental flow is expected to gradually vary in terms of water depth and mean velocity along the channel length. Under a small slope assumption, the equation for a gradually varied flow can be written as

$$\frac{dh}{dx} = \frac{S_\mathrm{o} - S_\mathrm{f}}{1 - F_\mathrm{r}^2} \tag{3.2}$$

where dh/dx is the rate of change of water depth along the channel length, S_o and S_f are the flume and friction slopes respectively, and F_r is the Froude number. This last parameter is defined as

$$F_\mathrm{r} = \frac{U_\mathrm{in}}{\sqrt{gH_\mathrm{w}}} \tag{3.3}$$

where g is the gravitational acceleration constant and H_w is the water depth. Equation 3.5 shows that changes in water depth (or specific energy) occur when $S_\mathrm{o} \neq S_\mathrm{f}$, i.e. when there is a difference between the rates at which gravitational forces drive the flow and friction retards it. The local friction slope can be obtained from Manning's equation assuming the same rate of energy loss in an equivalent normal flow

$$S_\mathrm{f} = \frac{n_\mathrm{m}^2 U_\mathrm{in}^2}{A_\mathrm{w} R_\mathrm{h}^{4/3}} \tag{3.4}$$

where n_m is the Manning coefficient (equal to 0.011 for smooth surfaces [14]), A_w is the cross-sectional area of the flow, $R_\mathrm{h} = A_\mathrm{w}/P_\mathrm{w}$ is the hydraulic radius, and P_w corresponds to the wetted perimeter. Considering the maximum flow rate, flume slope, and water depth at the measurement plane, $F_\mathrm{r} = 0.11$ and $F_\mathrm{r} = 0.17$ for the bottom-fixed and pivoted cylinder experiments, respectively. Moreover, S_f is two and nine times higher than the flume's slope for the bottom-fixed and pivoted cylinder experiments, respectively. Thus, the experimental flow is subcritical with a decreasing water depth as the flow moves downstream. All the experiments were performed at the same location (10.5 metres downstream of the inlet), and the water depth was fixed at the measurement zone. Thus, the cylinder is subjected to the same inflow condition on average as long as the flow rate remains constant.

Another aspect of open-channel flows is related to their frictional resistance, which results in a non-uniform vertical (xz-axis) velocity profile. The law of the wall expresses a vertical velocity profile as a function of the incoming flow velocity, water depth position, and mean shear stresses. In general, the flow velocity increases parabolically from zero at the bottom of the water channel to a maximum value near the surface. This characteristic vertical velocity profile is expected to have an influence on the wake dynamics along the cylinder span and in VIV. Due to the different tested experimental conditions, the analysis of the vertical velocity profile is provided in Chapters 5 and 6 for the bottom-fixed and pivoted cylinder experiments, respectively.

When a flow is confined within walls, the blockage ratio $B_\mathrm{r} = W_\mathrm{f}/D$, where W_f is the flume's width, can have a significant impact in the vortex shedding process. It is important to mention that the blockage ratio does not take into account the cylinder amplitude. Thus, the blockage-amplitude ratio, defined as the maximum crossflow amplitude A_y divided by the blockage ratio, is also considered here. Numerical simulations of a one degree-of-freedom cylinder between $100 \leq R_\mathrm{e} \leq 150$ observed negligible differences in vibration responses when $B_\mathrm{r} > 4$ [94]. Experiments on a one degree-of-freedom elastically mounted cylinder at $R_\mathrm{e} = 4 \times 10^3$ showed a maximum amplitude difference of 2.2% when the $B_\mathrm{r} = 20$ and $B_\mathrm{r} = 7.5$ cases were compared [31]. Numerical simulations on a two degree-of-freedom cylinder between $1 \times 10^3 \leq R_\mathrm{e} \leq 1.5 \times 10^4$ showed that the effects of walls on VIV are small when $B_\mathrm{r} \geq 10$ [116]. The amplitude-blockage ratio in all these studies imposes an upper limit between between 11% [116] and 14.5% [94].

The cylinders tested in this research project have a blockage ratio of 97.2 and 24.3 for the bottom-fixed and pivoted cylinders, respectively. Based on these parameters, the walls of the flume were expected to have negligible influence on VIV. Still, the maximum amplitude of the pivoted cylinder ($A_\mathrm{y} = 2.1D$) and its associated amplitude-blockage ratio of 8.6% impose a critical condition that must be analysed independently. A compilation of previous studies related to pivoted cylinders undergoing VIV (Section 6.3.1) considered a range of experimental blockage ratios between 47.2 [51] and 10.7 [2], and amplitude-blockage ratios between 8.9% [57] and 2.4% [51]. The tested pivoted cylinder is within the upper end in terms of amplitude-blockage ratio, comparable with a two degree-of-freedom pivoted cylinder with $A_\mathrm{y} = 2D$ [57]. Thus, the amplitude-blockage ratio of the pivoted cylinder indicate a slight influence of the lateral walls on VIV.

Chapter 4

Numerical methods

4.1 Introduction

This chapter describes the theory and numerical techniques used for the two-dimensional RANS model. The governing flow equations and turbulence modelling are first described as a general introduction to RANS models. Out of the several turbulence models commonly used in industry and research, only the Shear Stress Transport $k - \omega$ model is described due to its successful application in previous VIV studies (Section 2.4). The spatial and temporal discretisation techniques used in the numerical model are described within the context of Ansys Fluent [22], the Computer Fluid Dynamic Software used in this thesis. Lastly, the cylinder equation of motion and its fluid-structure coupling implementation are described.

4.2 Mathematical flow models

4.2.1 Governing equations

Given the absence of body forces and free-surface effects, the motion of a Newtonian incompressible fluid particle can be expressed by the following set of equations

$$\frac{\partial u_i}{\partial x_i} = 0 \tag{4.1}$$

$$\frac{\partial u_i}{\partial t} + u_j \frac{\partial u_i}{\partial x_j} = -\frac{1}{\rho}\frac{\partial p}{\partial x_i} + \nu \frac{\partial^2 u_i}{\partial x_j \partial x_j} \tag{4.2}$$

where $i = [1, 2, 3]$ and $j = [1, 2, 3]$ refer to the Cartesian components of the flow velocity u, ρ is the fluid density, p is the fluid pressure, ν is the kinematic viscosity. Equation 4.1 is derived from the mass conservation principle, which states that the rate of mass within a control volume is equal to the difference between the rate of mass into and out of the control volume. Equation 4.2 is commonly referred to as the Navier-Stokes or momentum equations and are the result of applying Newton's second law to a control volume.

4.2.2 Turbulence modelling

The solution of the Navier-Stokes equations using numerical models can be broadly classified into three categories: Direct Numerical Simulations (DNS), Large Eddy Simulations (LES), and Reynolds-Average Navier-Stokes (RANS) models. DNS solves the full range of turbulent scales. LES applies different filters to separate the small and large turbulent scales. The small scales are simulated, while the larger ones are directly solved. RANS models solve the time-averaged Navier-Stokes equations with complete modelling of the turbulence scales. As explained in Chapter 2, RANS models are commonly used in industry and research due to their low computational costs, lower grid resolution, and a less stringent time step requirement. The time-averaged version of Eq. 4.1 and 4.2 is expressed as

$$\frac{\partial \overline{u_i}}{\partial x_i} = 0 \tag{4.3}$$

$$\frac{\partial \overline{u_i}}{\partial t} + \frac{\partial \overline{u_i u_j}}{\partial x_j} = -\frac{1}{\rho}\frac{\partial \overline{p}}{\partial x_i} + \nu \frac{\partial^2 u_i}{\partial^2 x_j} - \frac{\partial \overline{u_i' u_j'}}{\partial x_j} \tag{4.4}$$

where the velocity and pressure were decomposed in their time-averaged and fluctuating components (see Section 2.2), and $\rho u_i' u_j'$ is referred to as Reynolds stress tensor. Given the greater number of unknowns than equations, Equation 4.3 and 4.4 are solved by means of turbulence models. One common assumption behind these models is based on the Boussinesq eddy viscosity conjecture [91], which relates the Reynolds stress tensor to the mean velocity gradients. The mathematical expression of the Boussinesq model is

$$\overline{u_i' u_j'} = -\nu_t \Big(\frac{\partial \overline{u_i}}{\partial x_j} + \frac{\partial \overline{u_j}}{\partial x_i} \Big) + \frac{2}{3} k \delta_{ij} = -2\nu_{\mathrm{t}} S_{ij} - \frac{2}{3} k \delta_{ij} \tag{4.5}$$

where $\nu_{\mathrm{t}} = \mu_{\mathrm{t}}/\rho$ is the turbulent viscosity, k is the turbulent kinetic energy, S_{ij} corresponds to the mean rate of the strain tensor, and $\delta_{ij} = 1$ when $i = j$.

Several studies suggest the use of the SST $k - \omega$ turbulence model due to its accuracy to capture the main features in flows around stationary cylinders [1, 63, 98] and in one [50, 117] and two [35, 45, 105, 106] degree-of-freedom cylinders subjected to VIV. More details can be found in Chapter 2.4. The SST $k - \omega$ [67, 68] combines the robustness and accuracy of the $k-\omega$ model in the inner parts of the boundary layer (near-wall regions) and switches to the free stream independent $k-\epsilon$ model in the rest of the fluid domain. This switch avoids the sensitivity problem of the $k-\omega$ to the free stream turbulent properties [67]. It also avoids the low performance of the $k-\epsilon$ model in regions with strong adverse pressure gradients and significant flow separation [85]. The SST $k-\omega$ is based on two transport equations, one for the turbulent kinetic energy k, and the other for the dissipation per unit of kinetic energy ω. The transport equation for k is given by

$$\frac{\partial \rho k}{\partial t} + \frac{\partial}{\partial x_j}(\rho \overline{u_j} k) = P_{\mathrm{k}} - \beta^* \rho \omega k + \frac{\partial}{\partial x_j}\left[(\mu \sigma_{\mathrm{k}} \mu_t)\frac{\partial k}{\partial x_j}\right] \tag{4.6}$$

where β^* and σ_{k} are constant of the model, and $P_{\mathrm{k}} = \mu_{\mathrm{t}} S^2$ is the production term for incompressible flows. The growth of turbulence in stagnating regions is limited by $\tilde{P}_{\mathrm{k}} = min(P_{\mathrm{k}}, 10\beta^* k\omega)$. The transport equation for ω is given by:

$$\begin{aligned} \frac{\partial \rho \omega}{\partial t} + \frac{\partial}{\partial x_j}\left[\rho u_j \omega - (\mu + \sigma_\omega \mu_{\mathrm{t}} \frac{\partial \omega}{\partial x_j})\right] &= \gamma \rho S^2 - \beta \rho \omega^2 \\ &+ 2(1-F_1)\frac{\rho \sigma_\omega}{\omega}\frac{\partial k}{\partial x_j}\frac{\partial w}{\partial x_j} \end{aligned} \tag{4.7}$$

where β and σ_ω are constant of the model. The blending function F_1 in Eq. 4.7 allows to transition between the $k-\omega$ and $k-\epsilon$ models and is defined as

$$F_1 = tanh\left\{\left\{min\left[max\left(\frac{\sqrt{k}}{\beta^* \omega y_{\mathrm{wall}}}, \frac{500\nu}{y_{\mathrm{wall}}^2 \omega}\right), \frac{4\rho\sigma_{\omega 2} k}{CD_{\mathrm{k}\omega} y_{\mathrm{wall}}^2}\right]\right\}^4\right\} \tag{4.8}$$

where $CD_{k\omega} = max(2\rho\sigma_{\omega 2}\frac{1}{\omega}\frac{\partial k}{\partial x_i}\frac{\partial \omega}{\partial x_j}, 1 \times 10^{-10})$ and y_{wall} is the distance to the nearest wall. Away from a surface, $F_1 = 0$ and the $k-\epsilon$ model is active. Inside a boundary layer, $F_1 = 1$ and the model switches to $k-\omega$. The turbulent viscosity is defined as:

$$\nu_t = \frac{a_1 k}{max(a_1 \omega, SF_2)} \tag{4.9}$$

where F_2 is a second blending function defined by

$$F_2 = tanh\left[\left[max\left(\frac{2\sqrt{k}}{\beta^{*}\omega y_{wall}}, \frac{500\nu}{y_{wall}^{2}\omega}\right)\right]^{2}\right] \tag{4.10}$$

The constant of this models are: $\beta^{*} = 0.09$, $\gamma = 5/9$, $\beta_1 = 3/40$, $\beta_2 = 0.0828$, $\sigma_{\omega 1} = 0.5$, $\sigma_{\omega 2} = 0.856$, $\sigma_{k1} = 0.85$, $\sigma_{k2} = 1$, and $a_1 = 0.31$ [68].

4.2.3 Spatial discretisation

The numerical model was developed in Ansys Fluent [22], a Computer Fluid Dynamic Software based on the Finite Volume Method (FVM) with a cell-centred formulation. The fluid domain is partitioned into subdomains or control volumes, such as hexahedral (three-dimensional) or quadrilaterals (two-dimensional) elements. The flow equations on each control volume are numerically integrated to construct a set of algebraic equations for a given discrete variable, such as velocity, pressure, and temperature. These discrete equations are written as

$$\frac{\partial \rho\phi}{\partial t}V + \sum_{f}^{N_{\text{face}}} \rho_f \vec{u}_f \varphi_f \cdot \vec{A}_f = \sum_{f}^{N_{\text{face}}} \tau_f \nabla\varphi_f \cdot \vec{A}_f + S_\varphi V \tag{4.11}$$

where φ is a scalar property within a control volume V with a face area A_f and a number of faces N_{face}, S_φ is a source term of φ, and the face velocity $\vec{u}_f$ and diffusion coefficient τ_f are integrated over a number of faces N_{face}. Ansys Fluent stores discrete values φ at the centre of each element. Thus, different numerical schemes are used to obtain its corresponding face values φ_f. This work used the following schemes: Body Force Weighted, the Quadratic Upwind Interpolation for Convection (QUICK), and the first and second-order upwind schemes. More information about each numerical scheme can be found in [22, 101].

First-order upwind scheme

First-order interpolation technique. The face value of a scalar quantity φ_f is equal to its cell centre value φ.

Second-order upwind scheme

Second-order accuracy scheme. φ_f is estimated through a Taylor series expansion from its element-centre value,

$$\varphi_f = \varphi + \nabla\varphi \cdot \vec{r} \tag{4.12}$$

where $\nabla\varphi$ is the gradient of the cell-centre scalar quantity in the upstream element, and $\vec{r}$ is the displacement vector from the centroid of the upstream element to its corresponding face centroid.

Quadratic upwind interpolation for convection

The Quadratic Upwind Interpolation for Convection (QUICK) is based on a weighted average of the second-order upwind and central interpolation schemes. In Ansys Fluent, φ_f is given by

$$\begin{aligned} \varphi_f = \lambda\left(\frac{\Delta_c}{\Delta_b+\Delta_c}\varphi_B+\frac{\Delta_b}{\Delta_b+\Delta_c}\varphi_C\right)+ \\ (1-\lambda)\left(\frac{\Delta_a+2\Delta_b}{\Delta_a+\Delta_b}\varphi_B-\frac{\Delta_b}{\Delta_a+\Delta_b}\varphi_A\right) \end{aligned} \tag{4.13}$$

where Δ is the element length for three consecutive cells (A, B and C), and φ_f is the scalar value at the face between elements B and C. $\lambda = 1$ results in a central second-order interpolation, while $\lambda = 0$ converges to a second-order upwind scheme. The QUICK scheme is used on quadrilateral and hexahedral elements where the upstream and downstream faces can be identified. Ansys Fluent sets $\lambda = 1/8$. On unstructured or hybrid meshes, $\lambda = 0$ and the second-order upwind scheme is used.

4.2.4 Temporal discretisation

Each term in Eq. 4.11 must be integrated over a time step Δ_t for transient simulations. The implicit time evolution of φ is given by

$$\frac{\varphi_{t+\Delta_\mathrm{t}}-\varphi_t}{\Delta_\mathrm{t}} = F(\varphi_{t+\Delta_\mathrm{t}}) \tag{4.14}$$

where F is any spatial discretisation scheme, and $\varphi_{t+\Delta_\mathrm{t}}$ is the discrete scalar at a future time step. The second-order implicit formulation for a scalar variable φ is given by

$$\frac{3\varphi_{t+\Delta_\mathrm{t}}-4\varphi_t+\varphi_{t-\Delta_\mathrm{t}}}{2\Delta_\mathrm{t}} = F(\varphi) \tag{4.15}$$

This equation is solved iteratively at each time step. The implicit formulation is unconditionally stable regarding the time step size. Nevertheless, a Courant number below one is maintained (i.e. distance travelled by a fluid particle is lower than the element size) as recommended for the SST $k-\omega$ turbulence model. The Courant number is defined in Ansys Fluent as

$$CFL = max\left(\frac{u_1\Delta_{\mathrm{t}}}{\Delta x}, \frac{u_2\Delta_{\mathrm{t}}}{\Delta y}, \frac{u_3\Delta_{\mathrm{t}}}{\Delta z}\right) \tag{4.16}$$

where Δx, Δy, and Δz are the element length in the (x, y, z) direction.

4.2.5 Gradients and pressure-velocity coupling

Some discretisation techniques require calculating the gradient of a scalar quantity ($\nabla\varphi$). Here, the Green-Gauss Node-Based algorithm is used. This method is based on the Green-Gauss theorem applied to a scalar variable at the centre of an element. The discrete form of this method is given by

$$(\nabla\varphi)_{cell\_centre} = \frac{1}{V}\sum_{f}^{N_{\mathrm{face}}} \overline{\varphi_f} A_f \tag{4.17}$$

where the sum is over all the faces of an element. The face value $\overline{\varphi}_f$ is the average of the nodal values on the face

$$\overline{\varphi}_{\mathrm{face\_nodes}} = \frac{1}{N}\sum_{n}^{N_{\mathrm{face\_nodes}}} \overline{\varphi}_n \tag{4.18}$$

where $N_{\mathrm{face\_nodes}}$ is the number of nodes in a particular face.

The discretisation of the momentum equation requires the interpolation of the pressure and velocity from their cell-centre to their respective face values. The Pressure Staggering Option (PRESTO) scheme is used to estimate the pressure field, while a procedure similar to [83] is used for the velocity field [22]. The discretisation of the flow equations shows a pressure-velocity dependence. This relationship is addressed by ensuring a pressure field that satisfies the momentum and mass conservation equation at each element. For this, the Semi-Implicit Method for Pressure-Linked Equations Corrected (SIMPLEC) scheme is used. Figure 4.1 shows a flow chart of this numerical scheme. A pressure field is guessed or estimated using the flow values from a previous time step. The discretised momentum equations are solved using the estimated pressure field, and an initial velocity field is obtained. This information is used to correct the pressure field and mass fluxes at each element's face. The velocity field is updated to account for the new pressure field. This process is repeated until convergence of the flow parameters is reached.

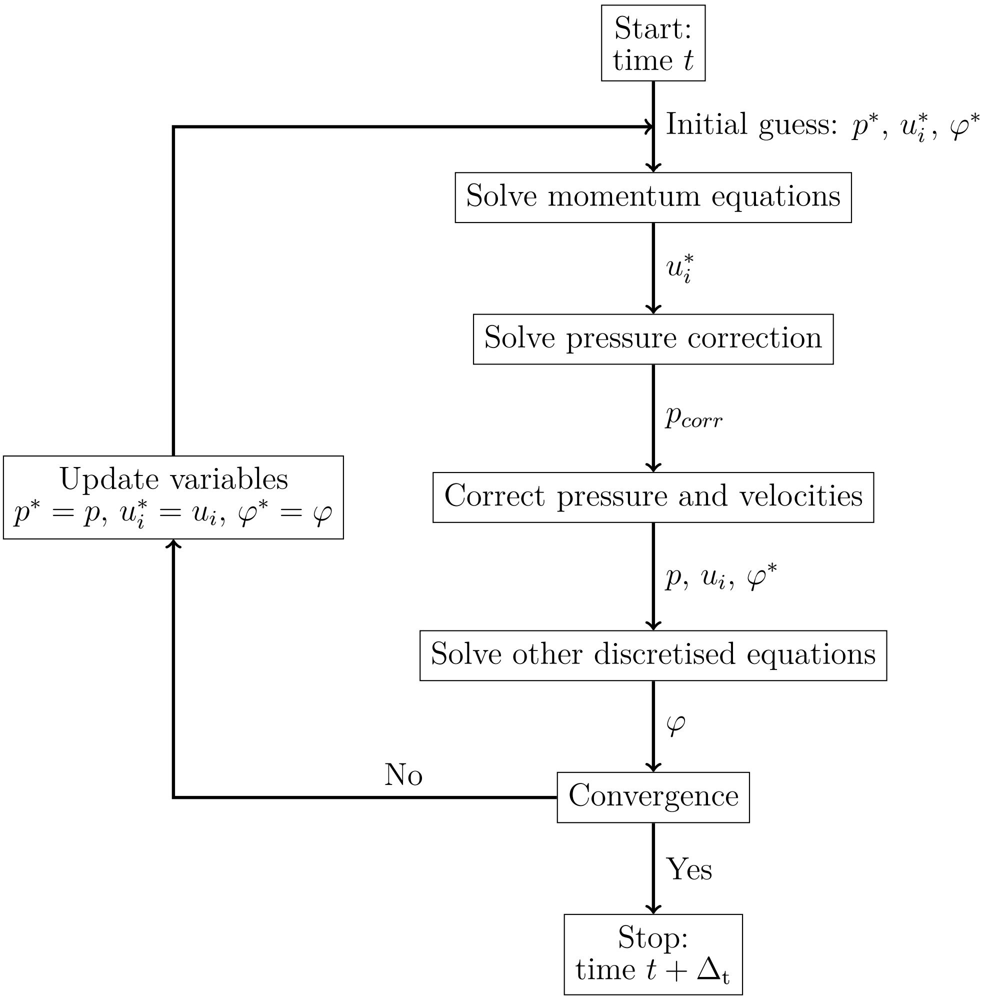

Figure 4.1: Semi-Implicit Method for Pressure-Linked Equations flow chart

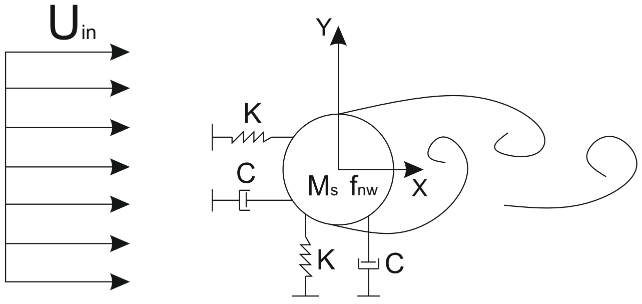

Figure 4.2: Mass-spring-damping model of a two degree-of-freedom elastically mounted cylinder

4.3 Structural models

4.3.1 Elastically mounted cylinder

The elastically mounted cylinder is modelled as a mass-spring-damping system (Figure 4.2). The flow moves from left to right along the x-axis or the streamwise direction. The y-axis or the crossflow direction is perpendicular to the flow and the cylinder axis. The z-axis (out-of-plane in Figure 4.2) or spanwise direction refers to the axis of the cylinder at rest. The corresponding two-dimensional equations are given by

$$M_{\mathrm{s}}\ddot{x} + C\dot{x} + Kx = F_{\mathrm{D}} \tag{4.19}$$

$$M_{\mathrm{s}}\ddot{y} + C\dot{y} + Ky = F_{\mathrm{L}} \tag{4.20}$$

where M_{s}, C, and K are the structural mass, damping and stiffness per unit of length, respectively. F_{D} and F_{L} are calculated as the sum of the normal and shear forces in the streamwise and crossflow direction, respectively. The added mass is not included in Eq. 4.19 and 4.20 since the fluid forces (from which the added mass effect manifest) are explicitly calculated from the flow equations [89]. The structural properties per unit of length are given by

$$M_{\mathrm{s}} = \frac{1}{4}m^{*}\pi D^{2}\rho \tag{4.21}$$

$$C = 4\zeta\pi f_{\mathrm{na}}M_{\mathrm{s}} \tag{4.22}$$

$$K = 4\pi^{2}f_{\mathrm{na}}^{2}M_{\mathrm{s}} \tag{4.23}$$

These parameters are replaced in Eq. 4.19 and 4.20

$$M_{\mathrm{s}}\ddot{x} + 4\pi f_{\mathrm{na}}\zeta M_{\mathrm{s}}\dot{x} + 4\pi^{2}f_{\mathrm{na}}^{2}M_{\mathrm{s}}x = F_{\mathrm{D}} \tag{4.24}$$

$$M_{\mathrm{s}}\ddot{y} + 4\pi f_{\mathrm{na}}\zeta M_{\mathrm{s}}\dot{y} + 4\pi^{2}f_{\mathrm{na}}^{2}M_{\mathrm{s}}y = F_{\mathrm{L}} \tag{4.25}$$

Equation 4.24 and 4.25 are solved using the Runge-Kutta fourth-order algorithm. This method has been used successfully in two degree-of-freedom cylinders subjected to VIV [115]. Considering the crossflow response as an example, Eq. 4.25 is expressed as

$$\frac{dy(t)}{dt} = \dot{y}(t) \tag{4.26}$$

$$\frac{d\dot{y}(t)}{dt} = \frac{F_{\mathrm{L}}}{M_{\mathrm{s}}} - 4\pi f_{\mathrm{na}}\zeta\dot{y} - 4\pi^{2}f_{\mathrm{na}}^{2}y \tag{4.27}$$

The Runge-Kutta fourth-order method solves Eq. 4.26 and 4.27 in a discrete manner as

$$y(t_{\mathrm{n+1}}) = y(t_{\mathrm{n}}) + \frac{\Delta_{\mathrm{t}}}{6}(H_{\mathrm{RK}_1} + 2H_{\mathrm{RK}_2} + 2H_{\mathrm{RK}_3} + H_{\mathrm{RK}_4}) \tag{4.28}$$

$$\dot{y}(t_{\mathrm{n+1}}) = \dot{y}(t_{\mathrm{n}}) + \frac{\Delta_{\mathrm{t}}}{6}(L_{\mathrm{RK}_1} + 2L_{\mathrm{RK}_2} + 2L_{\mathrm{RK}_3} + L_{\mathrm{RK}_4}) \tag{4.29}$$

where

$$H_{R\mathrm{K}_1} = \dot{y}(t_{\mathrm{n}}) \tag{4.30}$$

$$H_{\mathrm{RK}_2} = \dot{y}(t_{\mathrm{n}}) + \frac{\Delta_{\mathrm{t}}}{2}L_{\mathrm{RK}_1} \tag{4.31}$$

$$H_{\mathrm{RK}_3} = \dot{y}(t_{\mathrm{n}}) + \frac{\Delta_{\mathrm{t}}}{2}L_{\mathrm{RK}_2} \tag{4.32}$$

$$H_{\mathrm{RK}_4} = \dot{y}(t_{\mathrm{n}}) + \Delta_{\mathrm{t}}L_{\mathrm{RK}_3} \tag{4.33}$$

$$L_{\mathrm{RK}_1} = \frac{F_{\mathrm{L}}(t_{\mathrm{n}})}{M_{\mathrm{s}}} - 4\pi f_{\mathrm{na}}\zeta\dot{y}(t_{\mathrm{n}}) - 4\pi^2 f_{\mathrm{na}}^2 y(t_{\mathrm{n}}) \tag{4.34}$$

$$L_{\mathrm{RK}_2} = \frac{F_{\mathrm{L}}(t_{\mathrm{n}})}{M_{\mathrm{s}}} - 4\pi f_{\mathrm{na}}\zeta(\dot{y}(t_{\mathrm{n}}) + \frac{\Delta_{\mathrm{t}}}{2}L_{\mathrm{RK}_1}) - 4\pi^2 f_{\mathrm{na}}^2(y(t_{\mathrm{n}}) + \frac{\Delta_{\mathrm{t}}}{2}H_{\mathrm{RK}_1}) \tag{4.35}$$

$$L_{\mathrm{RK}_3} = \frac{F_{\mathrm{L}}(t_{\mathrm{n}})}{M_{\mathrm{s}}} - 4\pi f_{\mathrm{na}}\zeta(\dot{y}(t_{\mathrm{n}}) + \frac{\Delta_{\mathrm{t}}}{2}L_{\mathrm{RK}_2}) - 4\pi^2 f_{\mathrm{na}}^2(y(t_{\mathrm{n}}) + \frac{\Delta_{\mathrm{t}}}{2}H_{\mathrm{RK}_2} \tag{4.36}$$

$$L_{\mathrm{RK}_4} = \frac{F_{\mathrm{L}}(t_{\mathrm{n}})}{M_{\mathrm{s}}} - 4\pi f_{\mathrm{na}}\zeta\,(\dot{y}(t_{\mathrm{n}}) + \Delta_{\mathrm{t}}L_{\mathrm{RK}_3}) - 4\pi^2 f_{\mathrm{na}}^2\big(y(t_{\mathrm{n}}) + \Delta_{\mathrm{t}}H_{\mathrm{RK}_3}\big) \tag{4.37}$$

H_{RK_i} and L_{RK_i} $(i = [1, 2, 3, 4])$ are the Runge-Kutta coefficients, and Δ_{t} is the time step size.

4.3.2 Pivoted cylinder

Figure 4.3 shows a representation of the pivoted cylinder tested in Chapter 6. This configuration and mounting system is similar to previous pivoted cylinder studies [103]. The structure pivots around $(x, y, z) = (0, 0, 0)$, corresponding to the structure's fixed end. The experimental results showed a maximum free end displacement of $2.25D$ at the maximum flow velocity (Chapter 6). The associated inclination angle regarding the cylinder rest position was $\theta = 7.8°$, from which the approximation $tan(\theta) \approx \theta$ is valid. Moreover, the tested configuration had a high aspect ratio (length-to-diameter) of 15.5. These characteristics allowed to linearise the equation of motion of a pivoted cylinder by balancing the moments with respect to the pivot point. The equation of motion for a pivoted cylinder [21] is written as

$$I_{\mathrm{s}}\ddot{\theta}_i(t) + c_{\mathrm{eq}}\dot{\theta}_i(t) + k_{\mathrm{eq}}\theta_i(t) = M_i(t) \tag{4.38}$$

where I_{s} is the structural moment of inertia, c_{eq} and k_{eq} are the equivalent structural

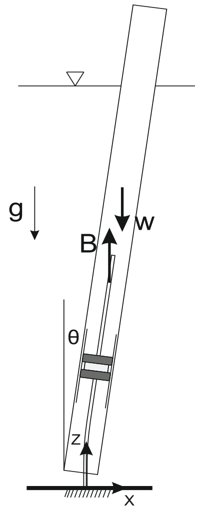

Figure 4.3: Model of a two degree-of-freedom pivoted cylinder. W: weight. B: buoyancy. The flow moves from left to right along the streamwise direction (x-axis). The crossflow direction (y-axis) is perpendicular to the flow and the cylinder axis. The spanwise direction (z-axis) refers to the axis of the cylinder at rest

damping and stiffness respectively, and M_i is the forcing moment in the $i = [x, y]$ direction. The moment of inertia around the pivot point was approximated as $I_\mathrm{s} \approx M_\mathrm{s}L^2/12$ with an error of 4% compared to its equivalent model in Ansys Structural 18.1. The equivalent stiffness is given by

$$k_\mathrm{eq} = k_\mathrm{s} + \frac{g}{2}\left(M_\mathrm{f}H_\mathrm{w} - M_\mathrm{s}L\right) \tag{4.39}$$

were k_s is the structural stiffness, and g is the gravitational acceleration constant. The second and third terms of Eq. 4.39 are the opposite weight and buoyancy moments acting on the centroid of the solid and displaced fluid mass, respectively. The natural frequency measured in water is a function of the equivalent stiffness and the moment of inertia. A free decay test performed under the same experimental conditions can be used to calculate the natural frequency of the structure and determine its equivalent stiffness [51]

$$k_\mathrm{eq} = k_\mathrm{s} + \frac{g}{2}\left(M_\mathrm{f}H_\mathrm{w} - M_\mathrm{s}L\right) = 4\pi^2 f_\mathrm{nw}^2(I_\mathrm{s} + I_\mathrm{a}) \tag{4.40}$$

$$c_\mathrm{eq} = 2\zeta\sqrt{k_\mathrm{s} + \frac{g}{2}\left(M_\mathrm{f}H_\mathrm{w} - M_\mathrm{s}L\right)} = 4\pi f_\mathrm{nw}\zeta(I_\mathrm{s} + I_\mathrm{a}) \tag{4.41}$$

where $I_\mathrm{a} = C_\mathrm{a}I_\mathrm{f}$ is the added inertia. Replacing Equations 4.40 and 4.41 in Eq. 4.38, the pivoted cylinder model can be written as

$$\ddot{\theta}_i + 4\pi f_{\mathrm{nw}}\zeta\dot{\theta}_i + 4\pi^2 f_{\mathrm{nw}}^2\theta_i = \frac{M_i}{1 + C_{\mathrm{a}}I^*} \tag{4.42}$$

Furthermore, approximating the inclination angle to $\theta_i \approx (x, y)/L$ at the cylinder free end ($tan(\theta) \approx \theta$ as shown before), Eq. 4.42 is rearranged (e.g. in the crossflow direction) as

$$\ddot{y} + 4\pi f_{\mathrm{nw}}\zeta\dot{y} + 4\pi^2 f_{\mathrm{nw}}^2 y = \frac{M_y L}{1 + C_{\mathrm{a}}I^*} \tag{4.43}$$

Eq. 4.43 is similar to the equation of motion of an elastically mounted cylinder (Eq. 4.25) except to the right-hand term related to the total forcing moment.

4.4 Coupling mechanism

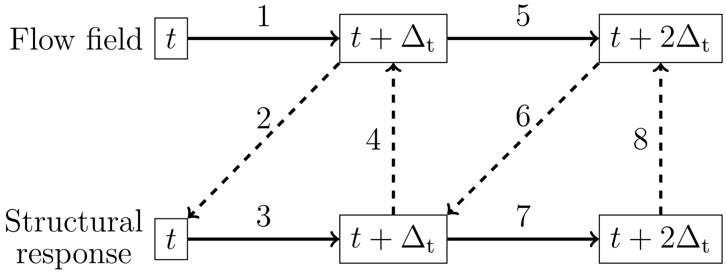

Figure 4.4: Flow chart of the coupling process across time steps [35]

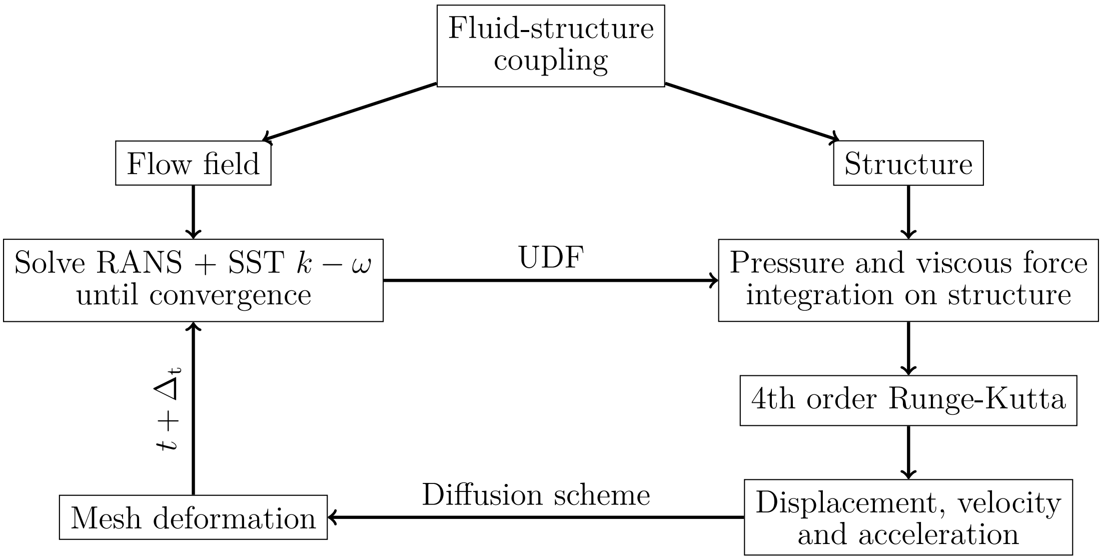

Figure 4.5: Flow chart of the coupling process within a time step

A staggered approach with dynamic mesh deformation was used to couple the cylinder and fluid motion. Figure 4.4 shows the coupling process across time, while Figure 4.5 summarises the fluid-cylinder interaction within a time step. The RANS equations with the SST $k - \omega$ turbulence model are iteratively solved until a converge criteria is achieved. Then, the cylinder's total pressure and viscous forces are extracted using a User Defined Function (UDF, Appendix D.2.2). Equation 4.24 and 4.25 are solved using the Runge-Kutta fourth-order method to obtain the cylinder displacement, velocity and acceleration. As the cylinder updates its position, the nearby mesh adapts following a diffusion-based smoothing scheme [22, 36]. A diffusion equation governs the mesh motion

$$\nabla(\tilde{\omega}\nabla\vec{u}) = 0 \tag{4.44}$$

where $\tilde{\omega}$ is the diffusion coefficient, and $\vec{u}$ is the mesh displacement velocity. The boundary condition in Eq. 4.44 is given by the cylinder motion within a time step. Equation 4.44 describes how the mesh motion diffuses into the interior of the flow domain. The parameter $\tilde{\omega}$ controls the intensity of the diffusion, defined as

$$\tilde{\omega} = \frac{1}{d^{\alpha}} \tag{4.45}$$

where d is a normalised boundary distance and α is the diffusion parameter. $\alpha = 0$ ($\tilde{\omega} = 1$) yields a uniform diffusion throughout the mesh. $\alpha > 0$ preserves regions near the moving boundary, while regions away from the cylinder absorb the mesh motion.

Chapter 5

VIV on bottom-fixed cylinder

5.1 Introduction

This chapter analyses the wake dynamic and structural response of a bottom-fixed cylinder subjected to a range of open-channel flows. Its main goal was to acquire experience with the experimental equipment, calibration system, and data analysis. Moreover, the variable amplitude along the bottom-fixed cylinder span provides important insights in preparation for the pivoted cylinder case of Chapter 6. In particular, the relationship between wake dynamics and structural response as the cylinder reaches its maximum amplitude and then desynchronises at higher flow velocities.

5.2 Experimental setup

5.2.1 Instrumentation and measurements

The experimental setup in Figure 5.1 consists of a recirculating water channel, a bottom-fixed cylinder made of clear cast acrylic, and the laser-based LaVision PIV

Bulk velocity (cm/s)	R_e	U_r	Water slope (m/m)
8.95	448	3.38	0.00055
10.67	534	4.03	0.00035
11.86	593	4.5	0.00012
13.7	685	5.15	0.00007
16.01	801	6.04	-0.00048
19.86	993	7.5	-0.00129

Table 5.1: Relevant hydraulic parameters of the experimental conditions. Water depth $H_\mathrm{w} = 347$ mm fixed at the measurement zone (10.5 m from the inlet). Flume's slope fixed at 0.001 m/m

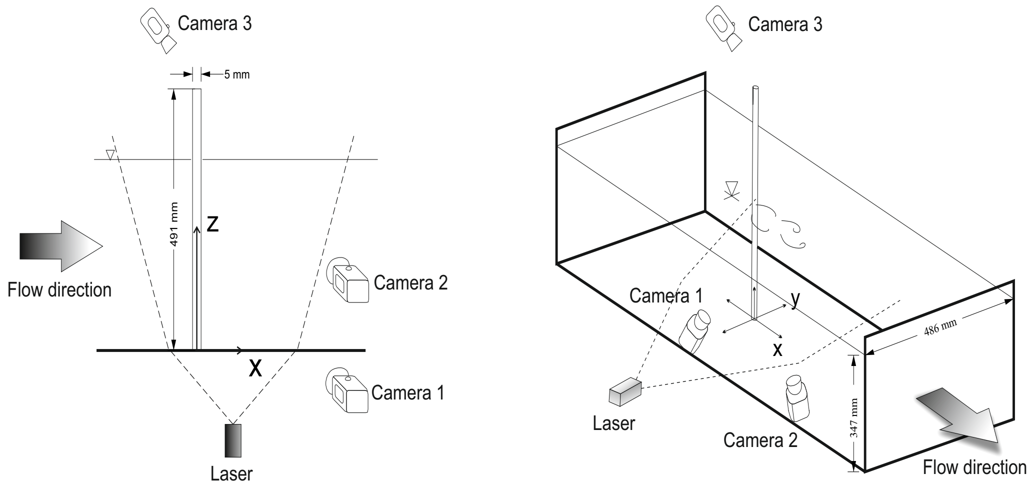

(a) (b)

Figure 5.1: Experimental setup of a bottom-fixed cylinder undergoing VIV. Coordinate system: streamwise (x-axis) and crossflow (y-axis) directions. The spanwise direction (z-axis) lies along the span of the cylinder at rest. a) PIV vertical (xz-axis) plane. b) PIV horizontal (x-axis) plane

system. Details of each equipment were described in Chapter 3. The flume maintained a fixed longitudinal slope of 0.001 m/m and a water depth $H_{\mathrm{w}} = 347$ mm throughout the experiments. The cylinder of diameter $D = 5$ mm and 491 mm length was placed 10.5 m downstream from the flume's entrance. Additional information on the cylinder mounting process and behaviour can be found in Chapters 3.2.2 and 3.4.2. As a summary, the two degree-of-freedom cylinder had an aspect ratio (length-to-diameter) equal to 98.2, mass ratio $m^* = 1.41$, and a low blockage ratio of 97.2 (blockage ratio effects were discussed in Chapter 3.5).

The PIV system used two MX 4M cameras to record the wake behind the cylinder. Simultaneously and synchronised, a third MX 4M camera recorded the cylinder free end response. Each recording was taken at 70 Hz for two minutes. The measurements were taken under increasing velocity conditions (Chapter 3.3.1), from $U_{\mathrm{r}} = 3.38$ up to $U_{\mathrm{r}} = 7.5$. Other relevant hydraulic parameters are summarised in Table 5.1. The flume and water slope differed at different flow velocities as expected from gradually varied open-channel flows (Chapter 3.5). A positive (negative) water slope indicates a systematic increment (decrement) of the water depth as the flow moves downstream. Still, all the experiments were performed at the same location (10.5 metres downstream of the inlet), and the water depth was fixed at the measurement zone. Thus, the cylinder is subjected to the same inflow condition on average as long as the flow rate remains constant (Chapter 3.5). The wake was characterised by measuring one vertical plane across the cylinder centreline and four horizontal planes at $(x, y, z) = (x, y, [20, 34, 52, 60]D)$. Figures 5.1a and 5.1b show the experimental setup of a vertical and horizontal PIV measurement, respectively. The velocity field was calculated from the raw flow images using a multi-pass cross-correlation approach (Chapter 3.3.3). An initial interrogation window of 64x64 pixels with two passes, followed by a 32x32 pixels window with three passes were used. The Universal Outlier detection [108] algorithm was used to remove vectors with small correlation values and replace them using a 5x5 pixel smoothing window. The overlap was set to 75% between interrogation windows, leaving a maximum spatial resolution of 0.39 mm for the horizontal PIV planes and 0.93 mm for the vertical PIV plane. The cylinder response images were calibrated and its motion estimated following the procedure described in Chapters 3.3.2 and 3.3.4. Details of the image-based tracking technique can be found in Appendix A.

A free decay test (Chapter 3.4.1) was performed using a PS3 Eye Camera. The video recordings were taken at 165 Hz with a 320x240 pixel resolution. A frequency analysis showed that $f_{\mathrm{na}} = 6.4$ Hz and $f_{\mathrm{nw}} = 5.3$ Hz on the first structural mode. A decaying exponential curve fit on the cylinder response showed that ζ was approximately 4% in air and 7.6% in water. These dynamic parameters were not affected by the direction of the unidimensional displacement. The free decay test was repeated after all the experiments were completed without degradation of the cylinder dynamic properties. Thus, a linear-elastic response was assumed.

5.2.2 Inflow characterisation

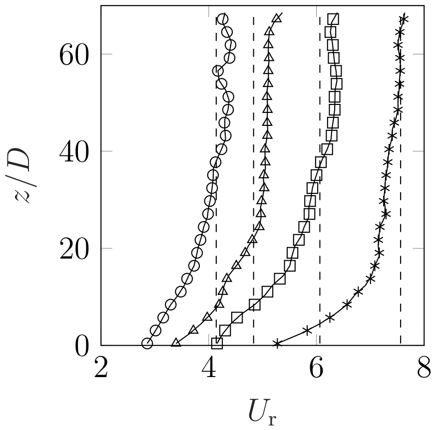

Figure 5.2: Time-averaged velocity profile measured at the flume's centreline. ○: $U_{\mathrm{r}} = 4.03$. △: $U_{\mathrm{r}} = 5.15$. □: $U_{\mathrm{r}} = 6.04$. $*$: $U_{\mathrm{r}} = 7.5$. Dashed lines: bulk velocity

A broad characterisation of open-channel flows in the context of this research project was provided in Chapter 3.5. Figure 5.2 shows the time-averaged velocity profile of the free stream flow. Dashed lines indicate the bulk velocity U_{in} (flow rate divided by the flow cross-sectional area). The velocity profile resembles a parabolic distribution as expected from open-channel flows. Approximately 90% of the average incoming reduced velocity was achieved at $z = 12.7D$ for the minimum reduced velocity and decreased to $z = 7.2D$ at the maximum tested velocity. Considering the $z = 12.7D$ case, the flume's frictional resistance reduces the mean velocity profile over the lowest 18.4% water depth region. This interaction has a direct impact on the wake dynamics of that region, as shown in Section 5.3.3. Still, a small influence on the structural response is expected due to the low forcing moment of that region on the cylinder fixed end. The maximum difference between the bulk velocity and the mean velocity at the measurement zone was 4.4%. Since the mean velocity of the vertical velocity profile varied as a function z, the bulk velocity was used as a normalisation parameter.

5.3 Results

5.3.1 Cylinder response and modal decomposition

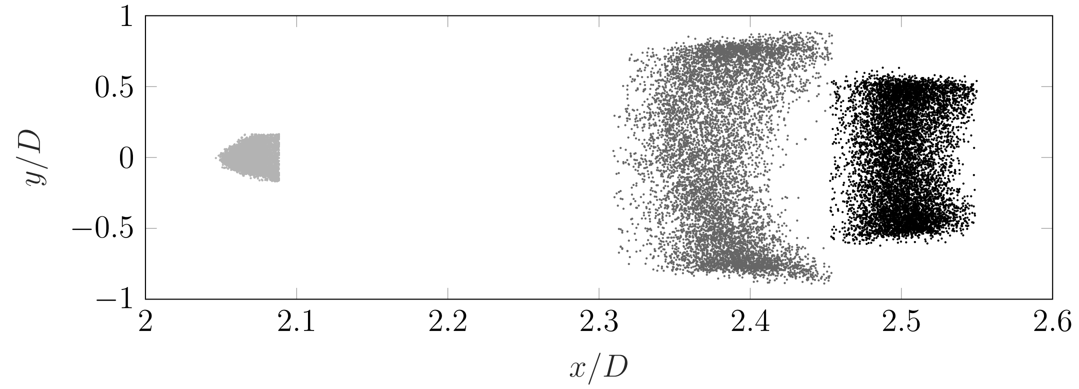

(a) U_r. ●: 3.38. ●: 5.15. ●: 7.5

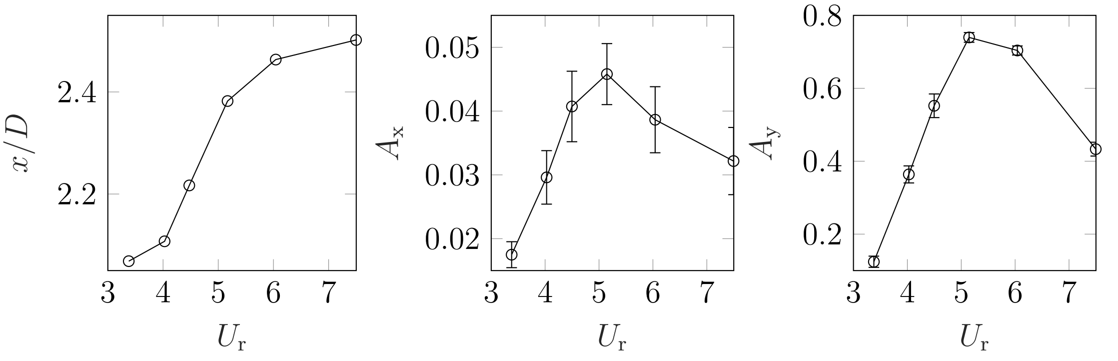

(b) (c) (d)

Figure 5.3: Cylinder free end response at $4.5 \times 10^2 \leqslant \mathrm{R_e} \leqslant 1 \times 10^3$. a) Cylinder motion examples. b) Mean streamwise position. Maximum displacement in the (c) crossflow and (d) streamwise direction. Error bars represent one standard deviation around the maximum displacement

Figure 5.3 summarises the cylinder response in the streamwise and crossflow direction. Figure 5.3a shows the cylinder spatio-temporal position at $U_\mathrm{r} = [3.38, 5.15, 7.5]$.

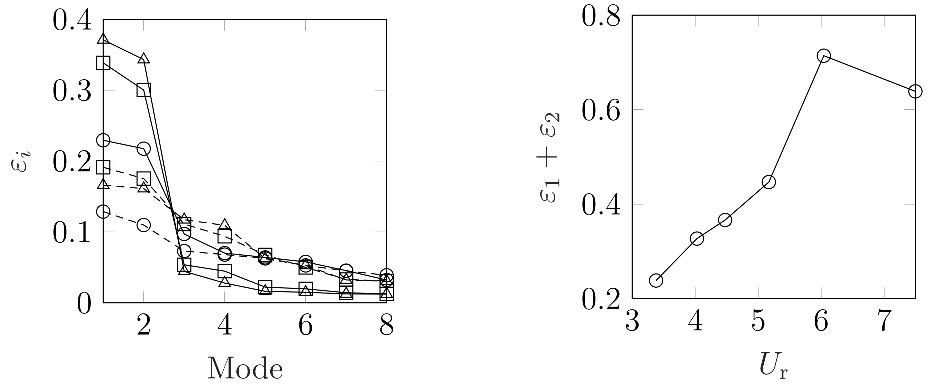

(a) U_r. -⊖-: 3.38, -△-: 4.03, -⊟-: 4.5.
—⊖—: 5.15, —△—: 6.04, —⊟—: 7.5

(b)

Figure 5.4: Relative POD modal values of the cylinder response. a) ε_i, where $i = [1, 2, ..., 8]$. b) $\varepsilon_1 + \varepsilon_2$

These trajectories indicate a strong periodic component alongside a random motion. The identification and characterisation of the large-scale motion is addressed later using the Proper Orthogonal Decomposition (POD) technique (Appendix B). The cylinder reached a maximum streamwise position of $2.5D$ and inclination angle of 2.1° at the highest tested flow velocity. Figure 5.3d and 5.3c show the maximum amplitude in the streamwise A_x and crossflow A_y direction, respectively. The maximum amplitude corresponds to the mean value of the highest 10% of the recorded response [38]. The maximum displacement increased with U_r up to $A_\mathrm{y} = 0.74D$ and $A_\mathrm{x} = 0.04D$ at $U_\mathrm{r} = 5.15$. At further increments in the reduced velocity, the maximum displacement decreased to $A_\mathrm{y} = 0.43D$ and $A_\mathrm{x} = 0.03D$ at $U_\mathrm{r} = 7.5$. Comparable amplitudes of $A_\mathrm{y} = 0.72D$ and $A_\mathrm{x} = 0.08D$ were observed on a bottom-fixed cylinder subjected to VIV [76]. The comparable $m^*\zeta = 0.126$ [76] with the experimental $m^*\zeta = 0.105$ partially explains the similarity in terms of maximum amplitude. The ratio $A_\mathrm{y}/A_\mathrm{x}$ ranged from eight at $U_\mathrm{r} = 3.18$ up to 19 at $U_\mathrm{r} = 6.04$. Thus, the cylinder had a dominant crossflow response across U_r.

The response data were separated into vectors of equal length (i.e. snapshot) and arranged in matrix form as described in Appendix B. The vector length selection is a trade-off between the number of snapshots used for POD and the cylinder trajectory within each snapshot. Snapshots of 700 data points (53 oscillations on average) were selected to ensure the convergence of the first (average) and second (variance) order statistics. Figure 5.4a shows the relative modal value ε_i ($i = [1, ..., 8]$) across U_r. The first two POD modes captured an important part of the total variance at higher responses ($U_\mathrm{r} > 5$) as opposed to lower displacements ($U_\mathrm{r} < 5$), from which the energy of higher-order POD modes was also significant. Figure 5.4b shows the energetic contribution of the first two POD modes at different flow velocities. $\varepsilon_1 + \varepsilon_2$ increased alongside U_r, reaching a maximum value of 71% at $U_\mathrm{r} = 6.04$.

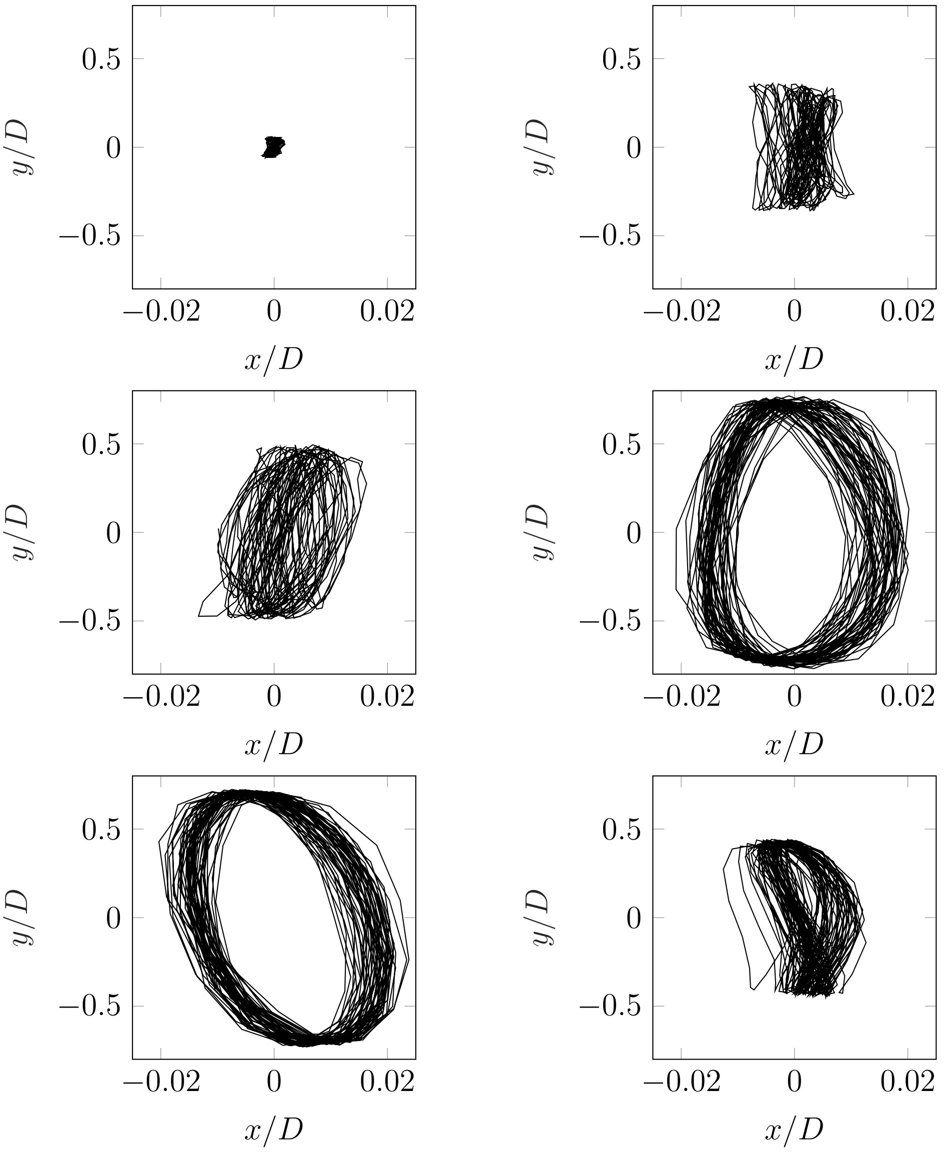

Figure 5.5: Reconstructed cylinder response from $\mathbf{\Phi}_1 + \mathbf{\Phi}_2$. From top left to bottom right: $U_\mathrm{r} = [3.38, 4.03, 4.5, 5.15, 6.04, 7.5]$.

Then, it decreased to 63% at the highest tested U_r. It is important to notice that $\varepsilon_1 + \varepsilon_2 \approx 45\%$ at the maximum cylinder amplitude. The higher $\varepsilon_1 + \varepsilon_2$ at greater reduced velocities is associated with an important contribution of the first two POD modes on the cylinder response. Since these modes are highly coherent at $U_\mathrm{r} > 5$ (shown later), the cylinder response has an important coherent component. This increment in response coherence after reaching the maximum cylinder amplitude could be associated with a transition to the lower branch, characterised by a higher periodic motion compared to the upper branch [49].

Figure 5.5 shows the reconstructed displacement signal obtained by adding the two most energetic spatial POD modes, $\mathbf{\Phi}_1 + \mathbf{\Phi}_2$. Higher-order POD modes only increased the irregularity of the trajectory for all U_r. Irregular POD mode shapes

Axis	Mode	U_r					
		3.38	4.03	4.5	5.15	6.04	7.5
X	1	0.76	0.86	0.90	1.01	1.02	1.04
	2	0.76	1.68	0.90	1.01	1.02	1.03
Y	1	0.76	0.84	0.89	1.01	1.02	1.03
	2	0.76	0.84	0.89	1.01	1.02	1.03
	f_c	0.76	0.85	0.90	1.01	1.02	1.04

Table 5.2: Streamwise and crossflow normalised frequencies of the first two spatial POD modes. Oscillation frequency normalised by f_{nw}

were observed at $U_r < 5$. Conversely, clockwise elliptical-type trajectories were identified for $U_r = 5.15$ and $U_r = 6.04$. Similar elliptical-type trajectories at $U_r \geq 5$ and irregular responses at $U_r < 5$ were identified for a bottom-fixed cylinder subjected to VIV [76]. The researchers indicated that non-regular cylinder oscillations at low reduced velocities might be associated with a high dependence of the added mass on U_r [76]. An eight- and elliptical-type combination was observed at the maximum flow velocity. This particular trajectory can be explained by the relationship between the streamwise vibration at the natural frequency and its first harmonics to the crossflow oscillation (Chapter 2.3.2). A power spectral density (PSD) analysis showed an important contribution of the first frequency harmonic in the streamwise direction. Specifically, the energetic value of the first harmonic was 83% of its main frequency. Thus, the influence of the first harmonic contributes an eight-type trajectory component to the expected elliptical-type. Despite the irregular trajectories, the main oscillation frequency of the first two spatial POD modes was successfully extracted across U_r. These results are summarised in Table 5.2. The dominant streamwise frequency of the second spatial POD mode at $U_r = 4.03$ ($f_x/f_{nw} = 1.68$) was approximately two times higher than its crossflow counterpart. This outlier introduces an eight-type component to the overall cylinder trajectory. Still, its contribution seems to be minor in comparison to the irregularity of the POD modes at $U_r = 4.03$ (Figure 5.5). The main oscillation frequency of the cylinder f_{cy} was defined as the average between the main streamwise (f_x) and crossflow (f_y) oscillation frequencies. Overall, $f_x \approx f_y$ throughout U_r, which is consistent with an elliptical-type trajectory [52, 76]. f_{cy} increased from 0.76 to 1.03 at higher U_r. The maximum cylinder response was achieved when $f_{cy} \approx f_{nw}$ at $U_r = 5.15$.

5.3.2 Wake dynamics

The wake dynamics across U_r were characterised using one vertical and four horizontal PIV planes at $(x, y, z) = (x, y, [20, 34, 52, 60]D)$. The time-averaged streamwise $\overline{U}$ and crossflow $\overline{V}$ velocity fields, as well as the root-mean-square (rms) of the fluctu-

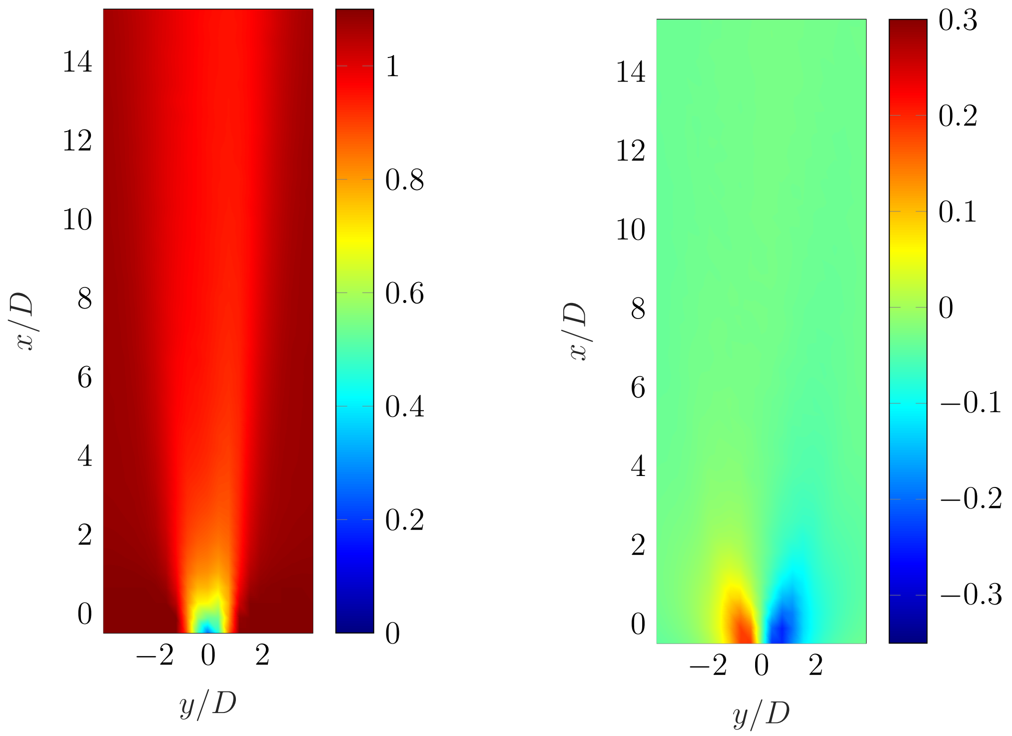

(a) $\overline{U}/U_{\mathrm{in}}$ (b) $\overline{V}/U_{\mathrm{in}}$

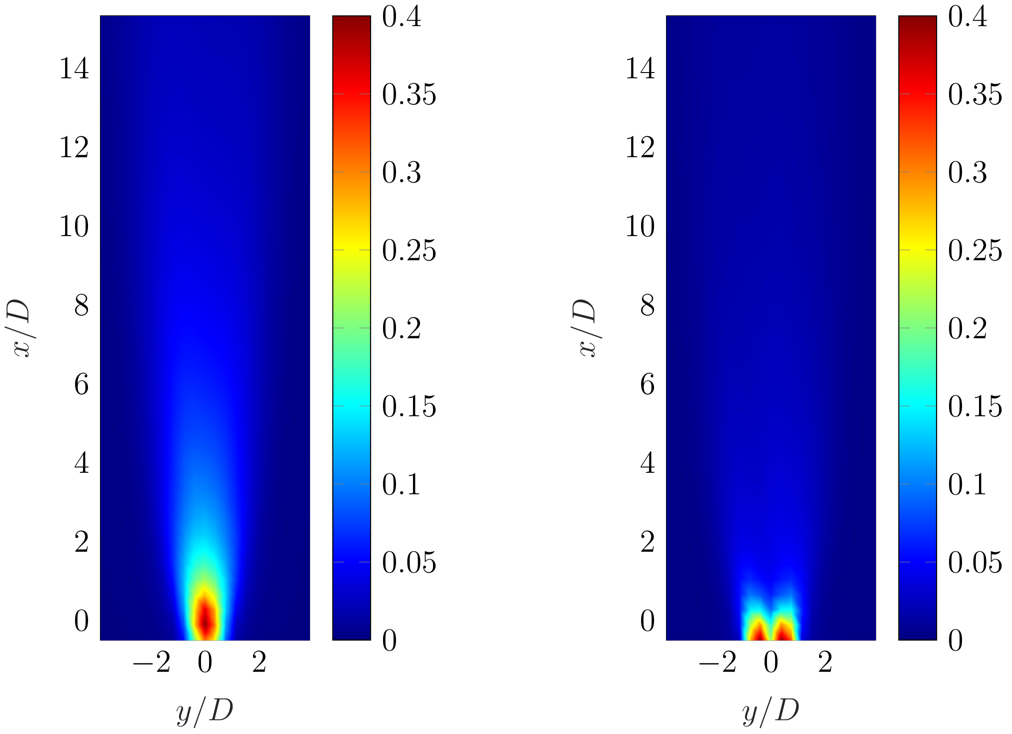

(c) $\mathrm{rms}(u')/U_{\mathrm{in}}$ (d) $\mathrm{rms}(v')/U_{\mathrm{in}}$

Figure 5.6: Velocity field at $z = 60D$ and $U_{\mathrm{r}} = 7.5$. Time-averaged streamwise (a) and crossflow (b) velocity. Root-mean-square streamwise (c) and crossflow (d) velocity

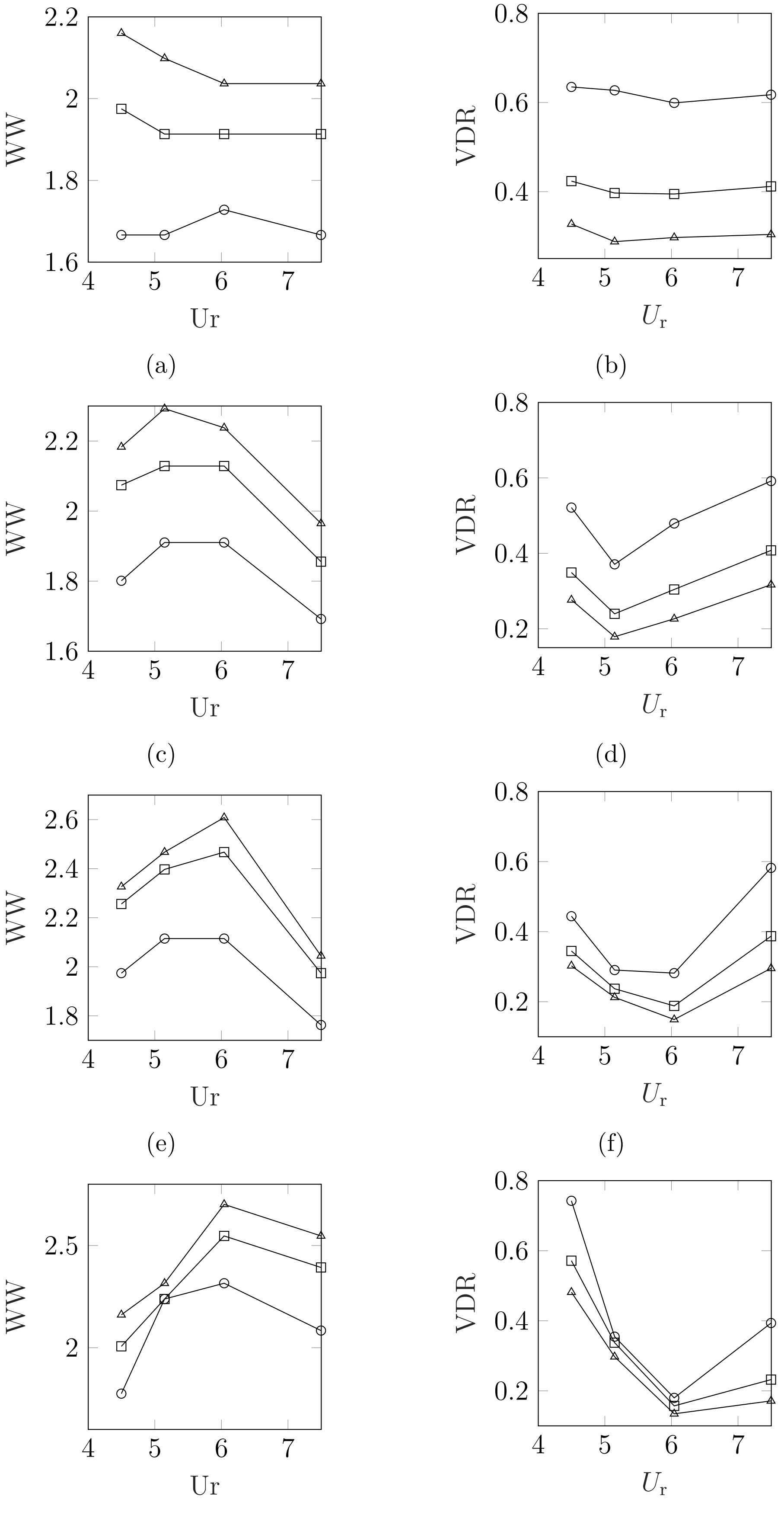

(a) (b)

(c) (d)

(e) (f)

(g) (h)

Figure 5.7: Velocity deficit recovery (VDR) and wake width (WW) measured at ○: $x = 5D$. □: $x = 8D$. △: $x = 11D$. a) VDR, $z = 20D$. b) WW, $z = 20D$. c) VDR, $z = 34D$. d) WW, $z = 34D$. c) VDR, $z = 52D$. d) WW, $z = 52D$. c) VDR, $z = 60D$. d) WW, $z = 60D$

ating streamwise rms(u') and crossflow rms(v') velocities, were used to characterise the wake behind the cylinder. As an example, the flow fields of these statistics are shown in Figure 5.6 for $U_{\mathrm{r}} = 7.5$ and $z = 60D$. The flow fields for the rest reduced velocities and water depths are shown in Appendix C.1. Several parameters were calculated to quantify the wake dynamics behind a bottom-fixed cylinder: recirculation region (ReRe), velocity deficit recovery (VDR), wake width (WW), and vortex strength. The recirculation region corresponds to the area of negative streamwise velocity ($\overline{U}(x, 0, z) < 0$) and is identified as the zero-cross point of $\overline{U}(x, 0, z)$ along the wake centreline. The velocity deficit recovery corresponds to the percentage between $\overline{U}(x, 0, z)$ along the wake centreline and the free-stream velocity. The wake width is defined as the transverse distance of the wake where $\overline{U}$ reaches 90% of the free-stream velocity. VDR and WW were calculated at $x = [5, 8, 11]D$. Lastly, an indication of the vortex strength is given by the position (L_{f}) and magnitude (VS) of the maximum rms(u') along the wake centreline [3]. All these statistics were normalised by their associated bulk velocity U_{in}. The results for $U_{\mathrm{r}} = 3.38$ and $U_{\mathrm{r}} = 4.03$ are not presented here since they were similar to $U_{\mathrm{r}} = 4.5$.

The recirculation region across U_{r} fluctuated between $1.9D$ and $2.5D$ at $z = 20D$. A smaller ReRe between $0.8D$ and $1.9D$ was found at $z = 34D$. At a higher water depth of $z = 52D$, ReRe increased up to $\approx 2.8D$ for $U_{\mathrm{r}} \leq 4.03$, and then it could not be measured for higher flow velocities since $\overline{U} \geq 0$ along the wake centreline. Likewise at $z = 60D$, no recirculation region could be measured across U_{r}. The local linear-elastic motion along the cylinder span varies along the following trend, $A_{\mathrm{x,y}}(z = 60D) \geq ... \geq A_{\mathrm{x,y}}(z = 20D)$. Thus, these results suggest that the recirculation region is affected and even disappears as the cylinder amplitude increases above a certain threshold. The velocity deficit recovery and wake width at different streamwise positions and water depths are shown in Figure 5.7. Figures 5.7a and 5.7b show a relatively constant WW and VDR despite the different cylinder responses across U_{r}. The maximum amplitude in this region reached $A_{\mathrm{y}} \approx 0.05D$, which seems to be low enough to not induce significant changes in the wake. At higher z, VDR and WW departure from Figure 5.7a and 5.7b, showing a clear influence of the cylinder response over the wake behaviour. VDR decreased at higher body motions and at $x = 5D$ compared to $x = 11D$. This reduction is explained by an increment in the level of mixing (momentum transference) in the vortex region enhanced by the higher cylinder responses. Considering the measurement region $x = 5D$, VDR reached a minimum value at $U_{\mathrm{r}} = 5.15$ ($z = 34D$) or $U_{\mathrm{r}} = 6.04$ ($z = [52, 60]D$). This minimum occurred when the cylinder response reached the two highest maximum crossflow amplitudes. On the other hand, the wake width is maximal at $U_{\mathrm{r}} = 5.15$ ($z = 34D$) or $U_{\mathrm{r}} = 6.04$ ($z = [52, 60]D$), reaching a value of $2.7D$ at $z = 60D$. It is interesting to notice that, at the highest water depth, VDR and WW reached their critical values after the cylinder achieved its maximum response ($U_\mathrm{r} = 6.04$). This particular case is related to changes in the vortex shedding pattern and it will be explained in the next section.

5.3.3 Spanwise synchronisation region

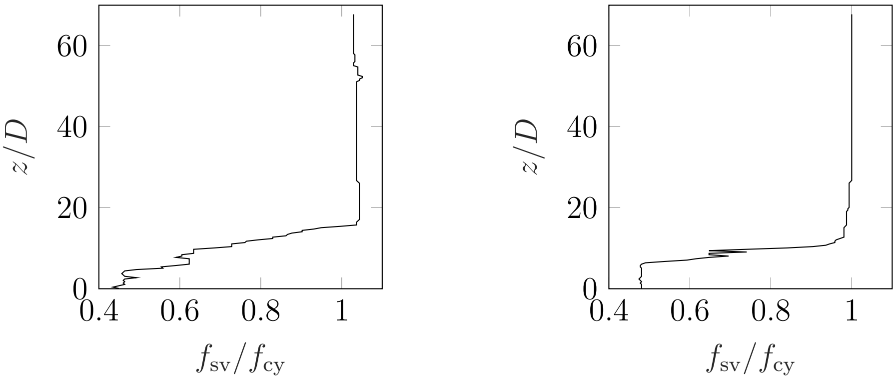

(a) $U_\mathrm{r} = 4.5$ (b) $U_\mathrm{r} = 5.15$

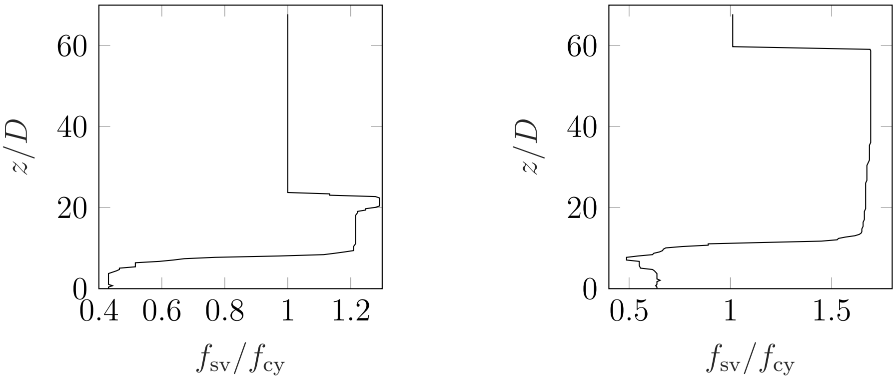

(c) $U_\mathrm{r} = 6.04$ (d) $U_\mathrm{r} = 7.5$

Figure 5.8: Normalised vortex shedding frequency at $x = 4.8D$

The spanwise vortex dynamics were analysed using the PIV vertical measurements. The streamwise velocity was decomposed as $u(x, y, z, t) = u'(x, y, z, t) + \overline{U}(x, y, z)$ (see Section 2.2) and a Power Spectra Density (PSD) analysis was performed. The frequency of the highest PSD magnitude was extracted and filtered through a moving median filter of size 10 data points. The results are summarised in Figure 5.8, showing the vortex shedding frequency f_sv at $u'(4.8D, 0, z, t)$. A particular region was observed, starting from the bed surface and extending between $9D$ and $16D$, where $f_\mathrm{sv} < f_\mathrm{cy}$. This region encloses the interaction between the bed surface, the vertical velocity profile (Section 5.2.2), and the cylinder with a low local maximum amplitude ($A_\mathrm{y} \approx 0.05D$). Measurements of the streamwise velocity in that region showed that $\overline{U}(4.8D, 0, z) \approx U_\mathrm{in}/2$, which explains the observed reduction in vortex shedding frequency. Figure 5.8a and 5.8b show that $f_\mathrm{sv} \approx f_\mathrm{cy}$ at $z > 16D$. This result and Table 5.2 show that the maximum cylinder amplitude

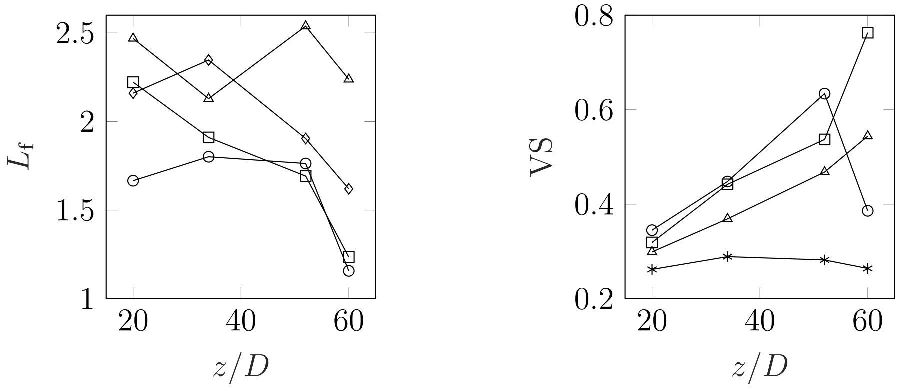

(a) U_r. ○: 4.5. □: 5.15.
◇: 6.04, △: 7.5.

(b) U_r. ○: 4.5. □: 5.15.
◇: 6.04, △: 7.5.

Figure 5.9: L_f and vortex strength (VS) at different water depths

is achieved when $f_\mathrm{vs} \approx f_\mathrm{cy} \approx f_\mathrm{nw}$ and when this equivalence is preserved along the cylinder span, i.e. when the spanwise synchronisation region is maximal. At higher U_r, f_sv increased between 1.2 and 1.3 at $9D \leqslant z \leqslant 25D$. Likewise, f_sv increased between 1.65 and 1.70 at $13D \leqslant z \leqslant 59D$ for the maximum tested flow velocity. As the desynchronised region extended towards the free-surface, A_y decreased 5.4% and 39.7% for $U_\mathrm{r} = 6.04$ and $U_\mathrm{r} = 7.5$, respectively.

Figure 5.9 shows the vortex formation length L_f and vortex strength (VS) along the wake centreline. L_f reached its lowest value across z at $U_\mathrm{r} = 4.5$ and $U_\mathrm{r} = 5.15$. Except for $U_\mathrm{r} = 7.5$, L_f decreased at higher water depths. In contrast, VS mostly reached its highest value at $U_\mathrm{r} = 4.5$ and $U_\mathrm{r} = 5.15$, where the spanwise synchronisation was maximal. These results are in line with previous experimental studies [3], indicating that higher body amplitudes lead to a stronger and smaller vortex formation near the cylinder with a subsequent stronger vortex shedding. At $U_\mathrm{r} = 6.04$, L_f slightly increases from $z = 20D$ (desynchronised region) to $z = 34D$ (synchronised region). Then, L_f restores its previous inverse relationship with z. At the maximum flow rate condition, where only $z \geq 59D$ is synchronised, L_f fluctuates between $2.2D$ and $2.5D$ with no clear trend. In contrast at $U_\mathrm{r} = 7.5$, VS slowly increased from 0.26 to 0.28 throughout the desynchronised region and then jumps to 0.36 at $z = 60D$. A significant reduction in L_f and VS was observed at $z = 60D$ for $U_\mathrm{r} = 4.5$. The rms(u') along the wake centreline showed a double peak in its vortex formation region, suggesting the confluence of two vortex shedding patterns. Additional research is needed to analyse this particular case.

The observed desynchronisation process can be broadly explained from previous experimental studies. One and two degree-of-freedom cylinder has been shown to agree qualitatively well in terms of maximum amplitudes and vortex patterns when the streamwise motion is low [21, 41]. Moreover, the synchronisation range, depen-

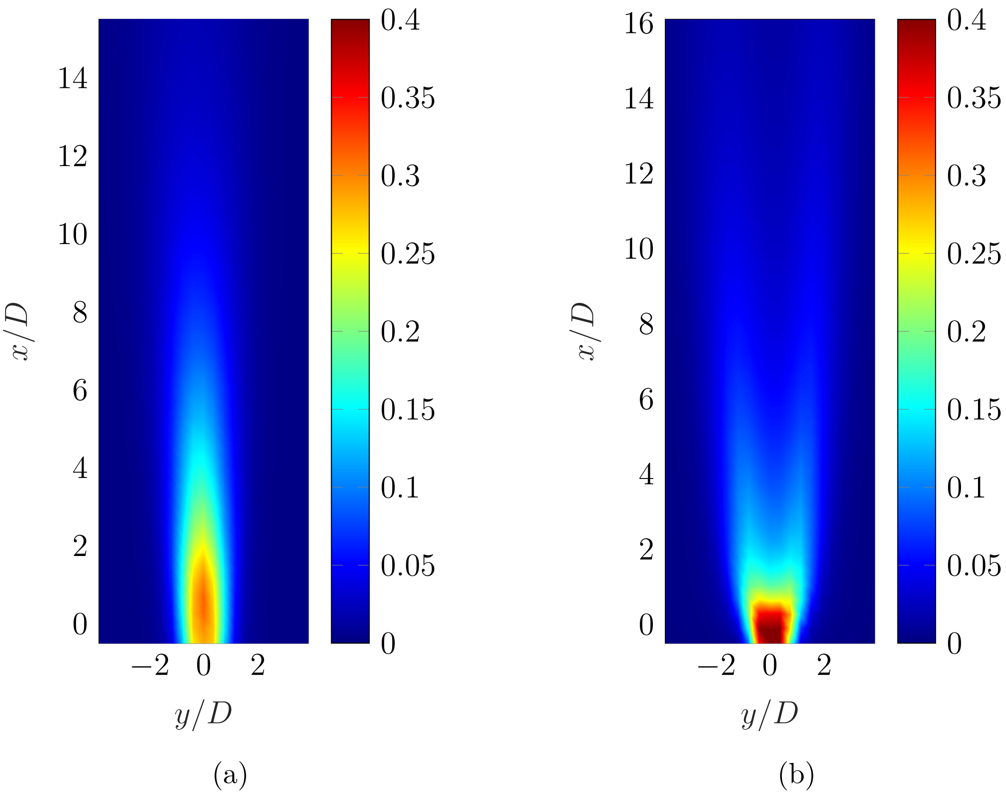

Figure 5.10: $\mathrm{rms}(u')/U_{\mathrm{in}}$ field at $z = 60D$. a) $U_{\mathrm{r}} = 5.15$. b) $U_{\mathrm{r}} = 6.04$

dent on the cylinder-fluid acceleration timing, increases with the cylinder amplitude [112]. The bottom-fixed cylinder had a dominant crossflow response throughout U_{r}, which makes it largely responsible for the range of U_{r} in which synchronisation occurs. As U_{r} increases and the cylinder motion is significant, the synchronisation region along the span of the cylinder is maximal, and the vortex shedding frequency is locked-in to the cylinder oscillation frequency. This relationship is preserved up to $f_{\mathrm{cy}} = f_{\mathrm{nw}}$, where the maximum cylinder amplitude is achieved. At further increments of U_{r}, the cylinder displacement near its fixed end cannot reach the needed increment in acceleration to sustain a synchronised condition, and desynchronisation occurs. As a consequence, the vortex region strength along the cylinder span decreases with a subsequent reduction in body motion. This desynchronisation process, reduction in vortex strength and body motion, is systematically enhanced as the desynchronised region develops towards the water surface.

Figure 5.10 shows the $\mathrm{rms}(u')$ fields at $z = 60D$. Following the contour distribution in [29], Figure 5.10a and 5.10b correspond to a 2S and 2P vortex mode, respectively. This change in vortex mode seems to be responsible for the maximum values of VDR and WW observed at $U_{\mathrm{r}} = 6.04$ and $z = 60D$. A dual 2S-2P vortex-mode configuration is observed at $U_{\mathrm{r}} = 5.15$ and $U_{\mathrm{r}} = 6.04$, changing the contour distribution from a 2S mode at $z = [20, 34, 52]D$ (2S) to a 2P pattern at $z = 60D$ (see Appendix C.1). In-depth analysis using statistical techniques (e.g. POD) could uncover large-scale coherent patterns from these velocity fields [84].

5.4 Conclusions

This chapter analyses the spanwise vortex dynamics and structural response of a bottom-fixed cylinder subjected to a range of open-channel flows. A PIV system and three synchronised cameras were used to capture the wake region and the cylinder free end response. Important experiences and knowledge in the LaVision PIV system were acquired. Firstly, the image resolution and acquisition frequency of one MX 4M camera was high enough to capture the wake by increasing the camera-object distance instead of adding an additional camera. Secondly, the Lucas-kanade technique with the Forward-backward tracking failure algorithm successfully estimated the cylinder position at all tested flow velocities. Thirdly, the data analysis allowed to study the interaction between the spanwise wake dynamics and the structural response. These techniques were used in Chapter 6 for the pivoted cylinder experiment.

The results of the bottom-fixed cylinder showed a highly modulated cylinder response across tested flow velocities. Coherent trajectory patterns from these responses were successfully extracted using the Proper Orthogonal Decomposition technique. Irregular trajectory patterns were observed for $U_{\mathrm{r}} < 5$, whereas a clockwise elliptical-type trajectory was identified for $U_{\mathrm{r}} \geq 5$. A combination between an eight-type and an elliptical-type trajectory was observed at the maximum flow velocity. This characteristic pattern was explained by the energetic relationship between the main streamwise frequency of its second spatial POD mode and its first harmonic. The spanwise wake dynamics showed that the maximum response was achieved when the cylinder motion and vortex shedding frequencies coincide (i.e. lock-in or synchronisation) to the natural frequency measured in still water, and when this equivalence is maintained along the cylinder span. As the flow velocity increased, the local response of the bottom-fixed cylinder near its fixed-end could not sustain the required increment in acceleration to maintain synchronisation. Thus, the vortex strength decreased along the cylinder span with a subsequent reduction in the maximum amplitude. This process was enhanced as the desynchronisation region extended towards the water surface. Changes in the wake dynamics showed a transition from a 2S-2P dual-mode configuration at the highest cylinder response to a predominant 2S mode at the highest tested flow velocity.

Chapter 6

VIV on pivoted cylinder

6.1 Introduction

The case of a pivoted cylinder undergoing VIV is an interesting problem on its own. The pivoted configuration can have the same structural parameters in the streamwise and crossflow direction. Moreover, its structural components can be easily adjusted to increase or reduce its dynamic properties, such as natural frequency and damping ratio. One particular characteristic of the pivoted configuration is its linear variable amplitude along its span, which promotes structural responses dependant on the three-dimensional body-wake interaction. This chapter analyses the wake dynamics and structural response of a pivoted cylinder subjected to a range of open-channel flows. The wake was analysed by measuring one vertical (xz-axis) plane across the cylinder centreline and two horizontal (xy-axis) planes at different water depths. Several statistics were calculated to characterise the spanwise wake dynamics as the cylinder reaches its maximum amplitude. The experimental conditions were used as input for the two-dimensional RANS model developed in Chapter 7.

Some of the techniques applied in this Chapter has been published in international conferences [64].

6.2 Experimental setup

6.2.1 Instrumentation and measurements

The experimental setup in Figure 6.1 consists of a recirculating water channel, a pivoted cylinder made of acrylic, and the laser-based LaVision PIV system. The details of each equipment were described in Chapter 3. The flume maintained a fixed longitudinal slope of 0.001 m/m and a water depth $H_{\mathrm{w}} = 255$ mm throughout the experiments. The pivoted configuration of diameter $D = 20$ mm and length $L = 310$ mm was placed 10.5 m downstream from the flume's entrance. Additional informa-

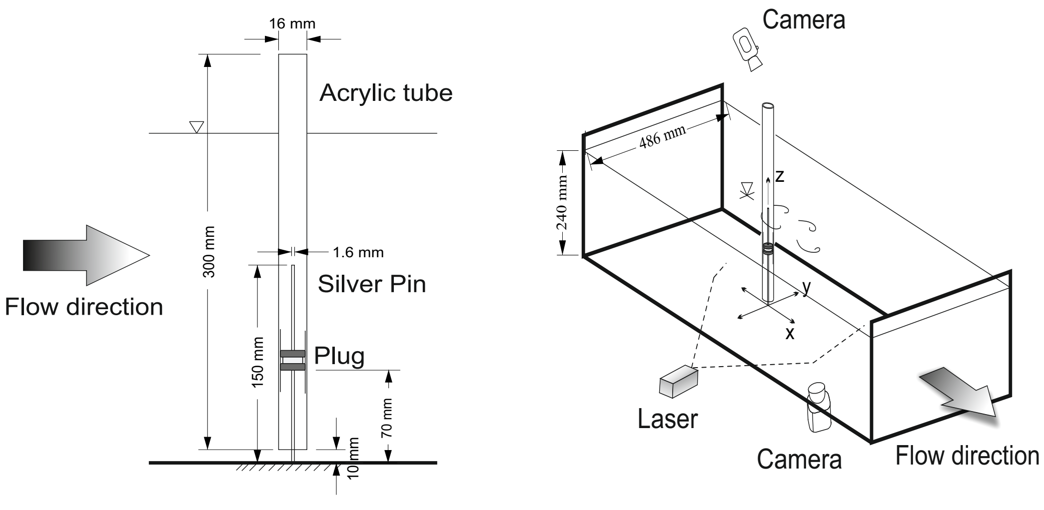

(a) (b)

Figure 6.1: Experimental setup. Coordinate system: streamwise (x-axis) and cross-flow (y-axis) directions. The spanwise (z-axis) direction lies along the span of the cylinder at rest. a) Side view. b) Three-dimensional view with a horizontal PIV measurement

Bulk velocity (cm/s)	R_e	U_r	water slope (m/m)
9.68	1937	2.95	-0.00019
12.34	2469	3.76	-0.00096
14.93	2986	4.55	-0.00188
17.11	3421	5.21	-0.00279
19.69	3938	6.00	-0.00404
21.94	4390	6.69	-0.00526
24.44	4890	7.42	-0.00678
27.19	5439	8.29	-0.00863

Table 6.1: Relevant hydraulic parameters of the experimental conditions. Water depth $H_w = 347$ mm fixed at the measurement zone (10.5 m from the inlet). Flume's slope fixed at 0.001 m/m

tion on the cylinder mounting process and behaviour can be found in Chapters 3.2.2 and 3.4.3. Overall, the two degree-of-freedom pivoted cylinder had an aspect ratio (length-to-diameter) equal to 15.5, mass ratio $m^* = 1.5$, inertia ratio $I^* = 1.82$, and a blockage ratio of 24.3 (blockage ratio effects were discussed in Chapter 3.5).

The PIV system used a single MX 4M camera to record the wake behind the vibrating cylinder. Simultaneously and synchronised, another MX 4M camera recorded the cylinder free end response. Each recording was taken at 80 Hz for 90 seconds. The measurements were taken under increasing velocity conditions (Chapter 3.3.1), from $U_r = 2.95$ up to $U_r = 8.29$. Other relevant hydraulic parameters are summarised in Table 6.1. The flume and water slope differed at different flow velocities as expected from gradually varied open-channel flows (Chapter 3.5). A negative water slope indicates a systematic decrement of the water depth as the flow moves downstream. Still, the experiments were performed at the same location (10.5 metres downstream of the inlet) and the water depth was fixed at the measurement zone. Thus, the cylinder is subjected to the same inflow condition on average as long as the flow rate remains constant. The wake was characterised by measuring one vertical plane across the cylinder centreline and two horizontal planes at $(x, y, z) = (x, y, [10, 60]D)$. The velocity field was obtained using a multi-pass cross-correlation approach. An initial interrogation window of 64x64 pixels with two passes, followed by a 32x32 pixels window with four passes was used. The Universal Outlier detection [108] algorithm was used to remove vectors with small correlation value and replace them using a 5x5 pixel smoothing window. The overlap was set to 87.5% between interrogation windows, leaving a maximum spatial resolution of 0.54 mm for the horizontal PIV planes and 0.56 mm for the vertical PIV plane. The cylinder response images were calibrated and its motion estimated following the procedure described in Chapters 3.3.2 and 3.3.4. Details of the image-based tracking technique can be found in Appendix A.

A free decay test (Chapter 3.4.1) was performed using a video camera with eight MegaPixel image resolution and 30 Hz acquisition frequency. This new camera did not required cables and was easier to mount compared to the one used in Chapter 5. A frequency analysis showed that $f_{\mathrm{na}} = 1.88$ Hz and $f_{\mathrm{nw}} = 1.64$ Hz on the first structural mode. A decaying exponential curve fit on the cylinder response showed that ζ was approximately 0.39% in air and 0.64% in water. These dynamic parameters were not affected by the direction of the unidimensional displacement. The free decay test was repeated after all the experiments were completed without degradation of the cylinder dynamic properties. Thus, a linear-elastic response was assumed.

6.2.2 Inflow characterisation

A broad characterisation of open-channel flows in the context of this research project was provided in Chapter 3.5. Figure 5.2 shows the time-averaged velocity profile of the free stream flow. Dashed lines indicate the bulk velocity U_{in} (flow rate divided by the flow cross-sectional area). The velocity profile resembles a parabolic distribution as expected from open-channel flows. Approximately 90% of the average incoming reduced velocity was achieved at $z = 2.2D$ for the minimum reduced velocity and decreased to $z = 1.8D$ at the maximum tested velocity. Considering the $z = 2.2D$ case, the flume's frictional resistance reduced the mean velocity profile over the lowest 16.7% water depth region. This interaction has a direct impact on the wake dynamics of that region, as shown in Section 6.3.3. Still, a small influence on the

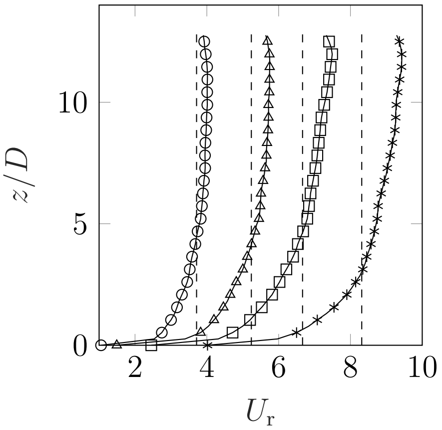

Figure 6.2: Time-averaged velocity profile measured at the flume's centreline. ○: $U_{\mathrm{r}} = 3.76$. △: $U_{\mathrm{r}} = 5.21$. □: $U_{\mathrm{r}} = 6.69$. $*$: $U_{\mathrm{r}} = 8.29$. Dashed lines: bulk velocity

cylinder response is expected due to the low forcing moment of that region on the cylinder fixed end. The maximum difference between the bulk velocity and the mean velocity at the measurement zone was 3.8%. Since the mean velocity of the vertical velocity profile varied as a function of z, the bulk velocity was used as a normalisation parameter.

6.3 Results

6.3.1 Cylinder response

Figure 6.3 summarises the cylinder response across tested U_{r}. Adding the mean streamwise displacement (Figure 6.3a) with its associated amplitude (Figure 6.3b), the cylinder achieves a maximum streamwise position of $2.1D$ and an associated inclination angle of 7.8°. The maximum streamwise amplitude initially decreased at higher U_{r}. Then, A_{x} rapidly grew to $0.4D$ at $U_{\mathrm{r}} = 5.21$. This rapid increment slowed down throughout $5.21 \leq U_{\mathrm{r}} \leq 7.42$, where A_{x} reached a maximum value of $0.44D$ at $U_{\mathrm{r}} = 7.42$. At the maximum tested flow velocity, A_{x} significantly decreased from its maximum value to $0.27D$. Figure 6.3c shows an increment of the maximum crossflow amplitude alongside the reduced velocity, changing its slope at $U_{\mathrm{r}} = 3.76$ and $U_{\mathrm{r}} = 5.21$, and reaching a maximum value of $2.1D$ at $U_{\mathrm{r}} = 7.42$. At the maximum tested flow velocity, A_{y} slightly decreased from its maximum value to $2D$. The critical mass ratio for pivoted cylinder undergoing VIV is 0.5 [30]. Since this value is lower than the experimental m^*, further reductions in oscillation amplitudes are expected beyond the maximum tested U_{r}. The cylinder showed a dominant crossflow response throughout U_{r}. The ratio $A_{\mathrm{y}}/A_{\mathrm{x}}$ ranged between 3.7 and 4.7 within $5.21 \leq U_{\mathrm{r}} \leq 7.42$, which later will be identified as the upper branch. Figures 6.3d and 6.3e shows the oscillation frequency associated with the

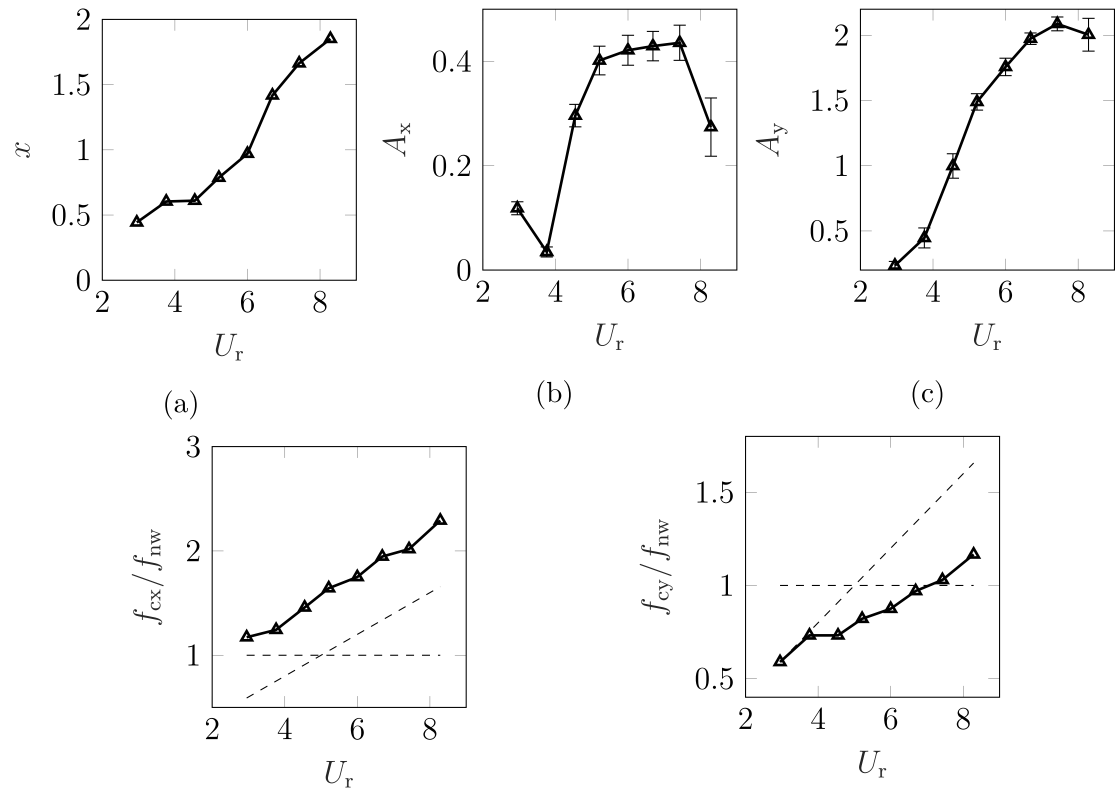

(a) (b) (c)

(d) (e)

Figure 6.3: Cylinder response at $2.5 \times 10^3 \leq R_e \leq 5.8 \times 10^3$. a) Mean streamwise position. Maximum streamwise (b) and crossflow (c) amplitude. Error bars represent one standard deviation around the maximum displacement. Streamwise (d) and crossflow (e) normalised oscillation frequency. Diagonal dashed line represents the vortex shedding frequency of a fixed cylinder ($S_t = 0.2$)

crossflow and streamwise motion, respectively. $f_{cx} \approx 2f_{cy}$, except at $U_r = 3.76$, where $f_{cx} \approx 1.7f_{cy}$. The crossflow oscillation frequency deviated from the vortex shedding frequency of a fixed cylinder at $U_r \geq 4.55$, indicating the beginning of the vortex-cylinder synchronisation. f_{cy} steadily increased from $0.73f_{nw}$ ($U_r = 4.55$), crossing f_{nw} between $U_r = 6.69$ and $U_r = 7.42$, and reaching a maximum value of $1.17f_{nw}$ at the highest reduced velocity. The maximum cylinder amplitude was achieved when $f_{cy} = 1.03f_{nw}$, which is consistent with previous low mass-damping two degree-of-freedom cylinders [41].

Four response branches were identified in Figure 6.4 by changing the x-axis of the maximum streamwise amplitude from U_r to $U_r^* = U_r(f_{nw}/f_{cy})$ [41]. Firstly, a response branch at $U_r^* = 5$, characterised by an eight-type trajectory and a significant streamwise amplitude equal to half its crossflow counterpart (Figure 6.5a). Secondly, an initial branch between $5.14 \leq U_r^* \leq 6.35$, where the cylinder amplitude rapidly increased per U_r. Thirdly, an upper branch between $5.14 < U_r^* \leq 7.21$, with a slow growth of the cylinder amplitude per U_r^* and an overall maximum response

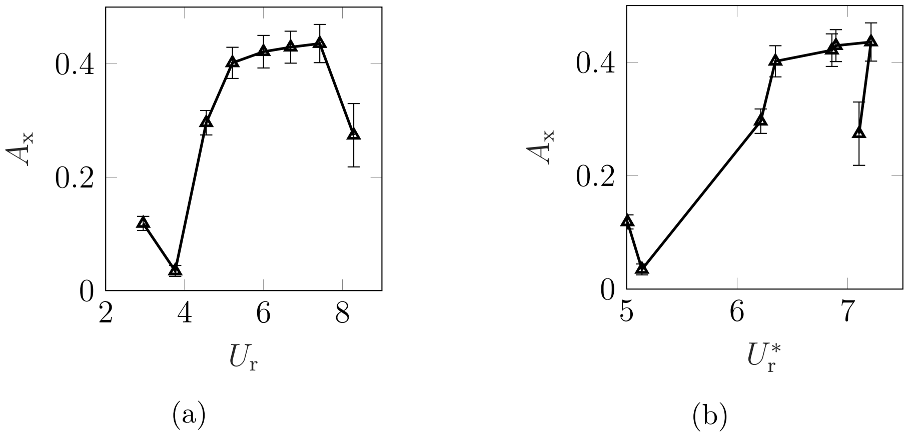

Figure 6.4: Response branch identification by changing the normalisation parameter from U_{r} (a) to $U_{\mathrm{r}}^* = U_{\mathrm{r}}(f_{\mathrm{nw}}/f_{\mathrm{cy}})$ (b)

at $U_{\mathrm{r}}^* = 7.21$. Finally, a branch transition seems to take place at $U_{\mathrm{r}}^* = 7.1$. This transition was marked by a significant change in the streamwise response, from a roughly regular to a beating-like motion with a significantly lower amplitude (see magnitude and error bars in Figure 6.3b). On the other hand, the crossflow response maintained most of its sinusoidal nature and amplitude throughout this transition.

Figure 6.5 shows the cylinder trajectory at each tested reduced velocity. A motion history that included at least 40 cycles of motion in the crossflow direction (double in the streamwise direction) was plotted against its best first-order sinusoidal fit as

$$x = A_{\mathrm{x}} sin(2\pi f_{\mathrm{cx}} + \phi_{xy}) \tag{6.1}$$

$$y = A_{\mathrm{y}} sin(2\pi f_{\mathrm{cy}}) \tag{6.2}$$

where ϕ_{xy} is the phase angle between the streamwise and crossflow motion. The shape of the trajectory depends on ϕ_{xy} and the frequency ratio $f_{\mathrm{cx}}/f_{\mathrm{cy}}$, which indicates the level of structural coupling between the streamwise and crossflow motion [51, 52]. If $f_{\mathrm{cx}}/f_{\mathrm{cy}} = 2$, such as the tested pivoted cylinder, the trajectory shape vary from an eight-type at $\phi_{xy} = 0$ to a crescent-type at $\phi_{xy} = 0.5\pi$. If $f_{\mathrm{cx}}/f_{\mathrm{cy}} = 1$, such as the bottom-fixed cylinder in Chapter 5, the trajectory shape will be elliptical with different inclinations. As a first approximation, Figure 6.5 shows that Eq. 6.1 and 6.2 captured the main features of the cylinder motion except at $U_{\mathrm{r}} = 3.76$, where the oscillations became irregular, and $U_{\mathrm{r}} = 8.29$, where the streamwise motion became highly modulated. The phase angle of the cylinder motion started with a value close to zero ($\phi_{xy} = -0.075\pi$) at $U_{\mathrm{r}} = 2.95$, decreased up to -0.4π within the initial branch, and maintained a value of -0.45π throughout the upper branch. Finally, the best sinusoidal fit for the modulated response at $U_{\mathrm{r}} = 8.29$ indicates an

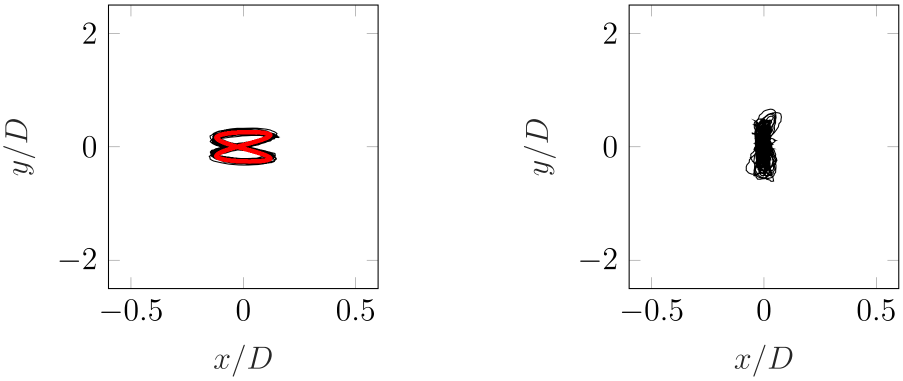

(a) $U_\mathrm{r} = 2.95$. $\phi_{xy} = -0.075\pi$

(b) $U_\mathrm{r} = 3.76$. $\phi_{xy} = -$

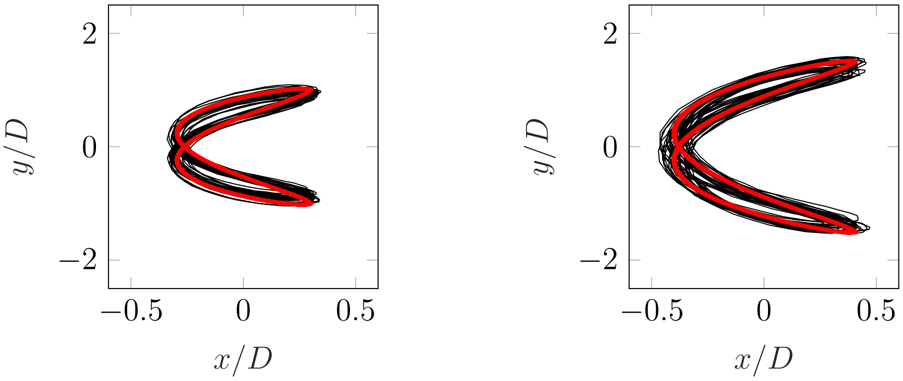

(c) $U_\mathrm{r} = 4.55$. $\phi_{xy} = -0.35\pi$

(d) $U_\mathrm{r} = 5.21$. $\phi_{xy} = -0.4\pi$

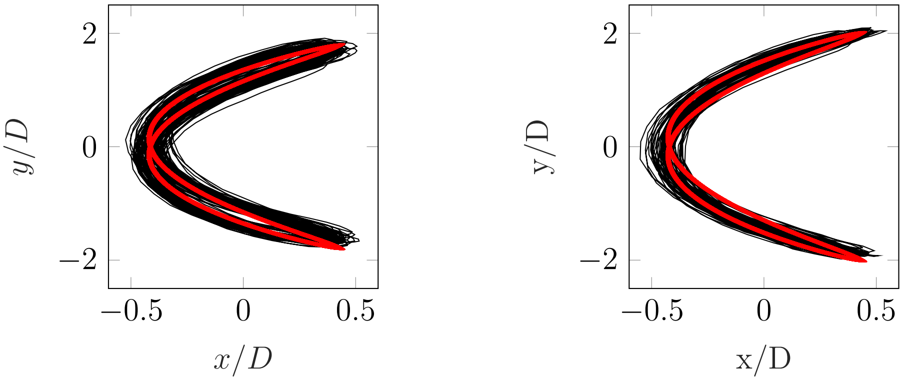

(e) $U_\mathrm{r} = 6$. $\phi_{xy} = -0.45\pi$

(f) $U_\mathrm{r} = 6.69$. $\phi_{xy} = -0.45\pi$

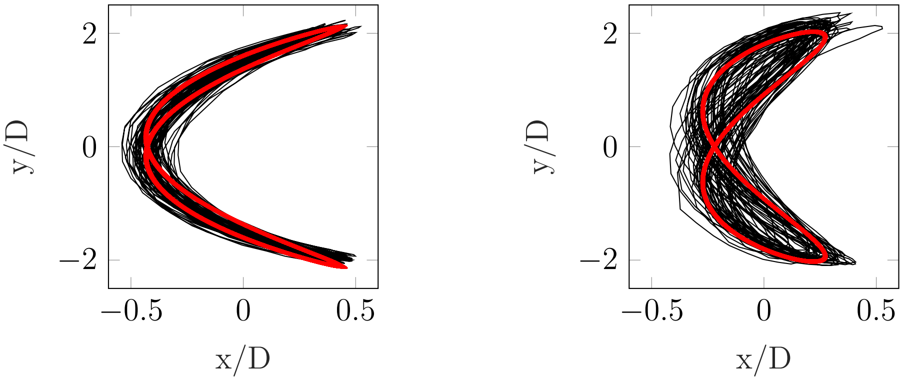

(g) $U_\mathrm{r} = 7.42$. $\phi_{xy} = -0.45\pi$

(h) $U_\mathrm{r} = 8.29$. $\phi_{xy} = -0.3\pi$

Figure 6.5: Pivoted cylinder trajectories across U_r. Red line correspond to the best first-order sinusoidal fit in a root-mean-square sense

Experiment	Mounting	DOF	L/D	$I^*\xi$	$U_{\mathrm{r}}(\theta_{\mathrm{m}})$	θ_{m}	A_{y}
Balasubramanian et al. [2]	top/pinned	1	10.5	0.415	5.3	0.035	0.37
Dong et al. [17]	bottom/fixed	1	50.4	0.054	5.4	0.019	0.95
Flemming and Williamson [21]	top/fixed	2	31	0.031	8.2	0.049	1.53
			2.68	0.080	6.5	0.032	1
			7.69	0.231	7.8	0.029	0.9
Voorhees et al. [103]	bottom/fixed	1	55.5	0.050	5.4	0.017	0.95
Leong and Wei* [57]	bottom/fixed	2	43	0.030	6.3	0.047	2
Kheirkhah et al [51]	bottom/pined	2	64.6	0.501	5.9	0.018	1.15
Johnstone and Stappenbelt [42]	top/pinned	1	18.6	0.004	7.8	0.042	1.55
Marble et al. [62]	bottom/pinned	2	64.4	0.739	6.1	0.016	1.03
Present work	bottom/fixed	2	15.5	0.007	7.4	0.135	2.1

Table 6.2: Compilation of previous pivoted cylinder studies. Top/bottom: cylinder orientation with its tip pointing towards the ceiling (bottom) or the flume's bed (top). Fixed/pinned: connection with no rotation and displacement (fixed) or no displacement (pinned). DOF: degree-of-freedom. $U_{\mathrm{r}}(\theta_{\mathrm{m}})$: reduced velocity associated to the maximum deflection angle θ (rad). $^*A_{\mathrm{x}}$ was 28% higher than A_{y}

increment in the phase angle to -0.3π.

Table 6.2 compared the experimental results to previous pivoted cylinder studies. The reported maximum amplitude (A_{y}) and its corresponding inclination angle θ were added to account for different structural dimensions [51]. The inclination angle was calculated as $\theta \approx tan^{-1}(A_{\mathrm{y}}/L)$, valid for small deflection angles. A consequence of this approximation was the exclusion of cylinders with large inclination angles (e.g., [27]). The Reynolds numbers from most studies was within $\mathcal{O}(10^3)$ with a maximum $R_{\mathrm{e}} = 2 \times 10^4$ [42]. There is a general inverse relationship between $I^*\zeta$ and θ (see also [21]). This relationship is more apparent when one and two degree-of-freedom cases are grouped separately. Another important distinction is the reduced velocity associated with the maximum deflection angle, which occurs mostly between $5 \leq U_{\mathrm{r}} \leq 6$ for one degree-of-freedom cylinders (except [42]) and $5.9 \leq U_{\mathrm{r}} \leq 8.2$ for two degree-of-freedom cylinders. The tested pivoted cylinder achieved a maximum displacement comparable to [57], although the associated θ is significantly higher than previous pivoted cylinders. This difference can be explained by the lower experimental $I^*\zeta$ (specifically lower ζ) and cylinder length, where this last parameter has a direct impact on the maximum deflection angle. The maximum response occurs at $U_{\mathrm{r}} = 7.4$, which is within the previously described range for two degree-of-freedom pivoted cylinders. It is important to mention that differences in cylinder configuration, partially or fully submerge conditions, Reynolds number, aspect ratio, damping ratios that varied as a function of θ (e.g., [42, 62]), among others parameters, explains the diverse range of responses compiled in Table 6.2.

Overall, the experimental results show an interesting range of high-amplitude responses, comparable to the case of a two degree-of-freedom pivoted cylinder with high crossflow amplitudes of $2D$ [57]. Unlike the bottom-fixed cylinder of Chapter 5, the observed high streamwise amplitudes are expected to have a critical role in the fluid-structure interaction.

6.3.2 Wake dynamics

Wake dynamics at $(x, y, z = [6, 10]D)$ were analysed in terms of time-averaged and root-mean-square (rms) statistics, as in Chapter 5. The flow fields of these statistics are shown in Figure 6.6 at at $z = 6D$ and $U_{\mathrm{r}} = 7.4$. The flow fields for the rest reduced velocities and water depths are shown in Appendix C.2. The wake was characterised using four statistics (definition in Chapter 5.3.2): recirculation region (ReRe), velocity deficit recovery (VDR), wake width (WW), and vortex length and strength (VS). All values were normalised by their bulk velocity U_{in}. VDR and WW were calculated at $x = [3, 6, 8]D$ downstream the cylinder pivot point.

The recirculation region ranged between $0.3D$ and $0.5D$ at $z = 6D$. This range increased from $1D$ to $2D$ for the higher horizontal measurement plane ($z = 10D$). These results were measured for $U_{\mathrm{r}} \leq 5.21$. On the other hand, ReRe could not be measured at higher flow velocities since $\overline{U} > 0$ along the wake centreline. The significant reduction and even disappearance of the recirculation region reflects a drastic change in the vortex shedding process as the cylinder reaches a certain amplitude threshold. This threshold was reached when the cylinder entered the upper branch. Previous studies have also observed the disappearance of ReRe at certain vibrating amplitudes [39] and in the upper branch [84]. Figure 6.7 summarises the velocity deficit recovery and wake width at different streamwise positions and water depths. VDR decreased closer to the cylinder rest position and towards the water surface. Considering the measurement distance $x = 5D$, the minimum VDR was reached at the beginning of the upper branch, with values of 32.6% and 6.7% at $z = 6D$ and $z = 10D$, respectively. Then, VDR increased within the upper branch to 43.3% ($z = 6D$) and 34.4% ($z = 10.1D$) at $U_{\mathrm{r}} = 7.89$. Due to the pivoted configuration of the vibrating structure, $A_{\mathrm{x,y}}(z = 6D) \geq ... \geq A_{\mathrm{x,y}}(z = 10D)$. Thus, increments in the cylinder response could be associated with higher momentum transference (flow mixing) in the wake region. The wake width increased downstream the cylinder rest position as the wake loses strength and diffuses. WW increased up to a maximum value of $3.6D$ ($z = 6D$) and $5.9D$ ($z = 10D$) when the cylinder reached its maximum amplitude ($U_{\mathrm{r}} = 7.4$). Under the same inflow conditions and cylinder responses, the ratio $\mathrm{WW}(z = 10D)/\mathrm{WW}(z = 6D)$ relates the wake width increment in the spanwise direction with the linear response variation of the pivoted cylinder. As expected, this ratio collapsed well at different downstream measurements.

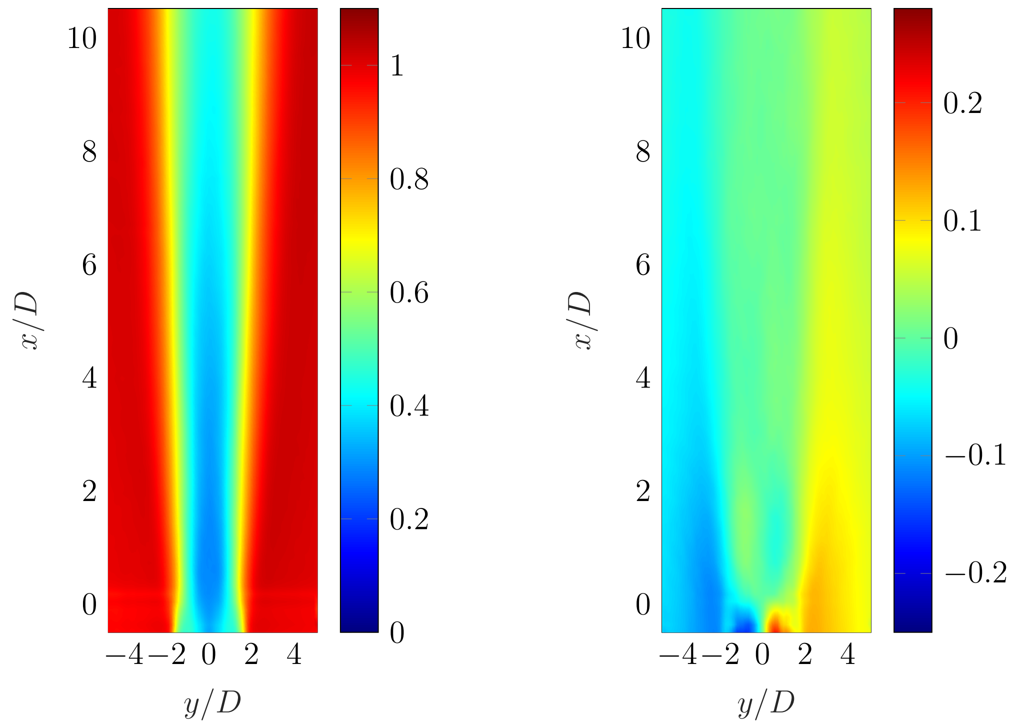

(a) $\overline{U}/U_{\mathrm{in}}$ (b) $\overline{V}/U_{\mathrm{in}}$

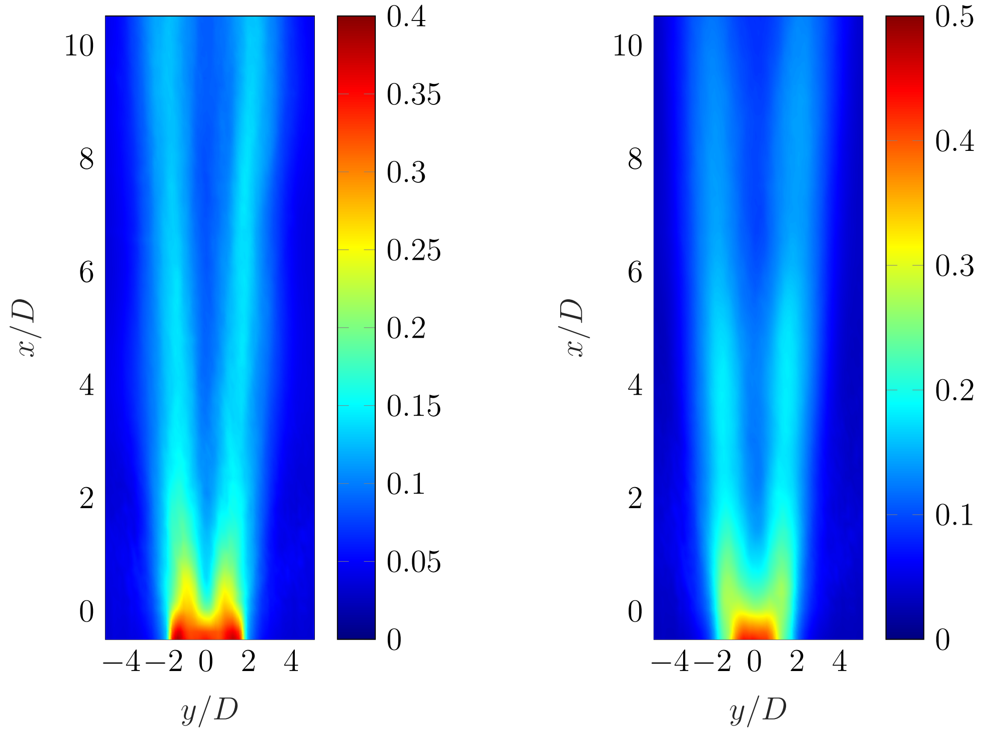

(c) $\mathrm{rms}(u')/U_{\mathrm{in}}$ (d) $\mathrm{rms}(v')/U_{\mathrm{in}}$

Figure 6.6: Velocity field at $z = 6D$ and $U_{\mathrm{r}} = 7.4$. Time-averaged streamwise (a) and crossflow (b) velocity. Root-mean-square streamwise (c) and crossflow (d) velocity

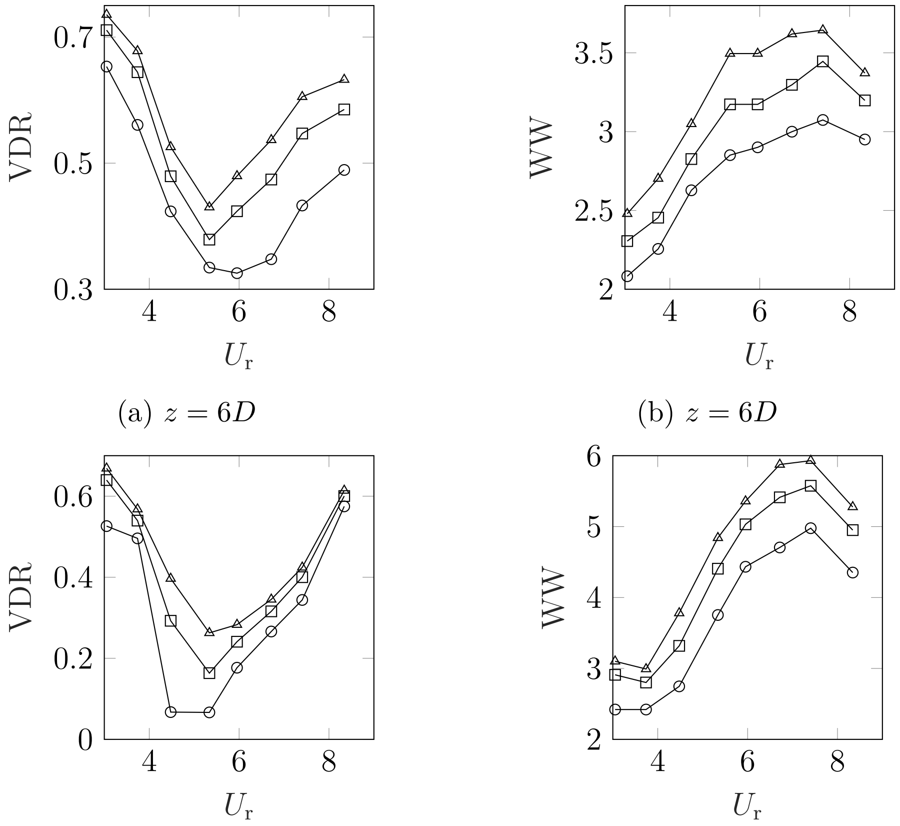

(a) $z = 6D$ (b) $z = 6D$

(c) $z = 10D$ (d) $z = 10D$

Figure 6.7: Velocity deficit recovery (VDR) and wake width (WW) measured at $x = [5, 8, 11]D$. ○: $x = 5D$. □: $x = 8D$. △: $x = 11D$

WW($z = 10D$)/WW($z = 6D$) ranged between 1.05 and 1.16 for $U_\mathrm{r} \leq 4.55$ and significantly increased to an average value of 1.55 within the upper branch. Thus, changes in the cylinder amplitude are not proportional to the observed spanwise variability of the wake width.

6.3.3 Spanwise synchronisation region

Figure 6.8 shows L_f and VS at different water depths and U_r. The behaviour of the vortex formation length was similar for both measurement planes. L_f started at a maximum value of $1.5D$ ($z = 6D$) and $2D$ ($z = 10D$), systematically decreasing up to the beginning of the upper branch. Then, the vortex formation length stabilised around $0.15D$ ($z = 6D$) and $0.34D$ ($z = 10D$) at higher U_r. On the other hand, the vortex strength maintained a relatively stable value of 0.45 at $U_\mathrm{r} \leq 5.21$ and increased within the upper branch with a higher magnitude at $z = 10D$ compared to $z = 6D$. As explained in Chapter 5, higher cylinder motions lead to a stronger and smaller vortex formation with a subsequent stronger vortex shedding [3]. At the maximum U_r, VS decreased at $z = 10D$ while it increased at $z = 6D$. As it will be shown later, this result indicates a significant change in the wake dynamics near

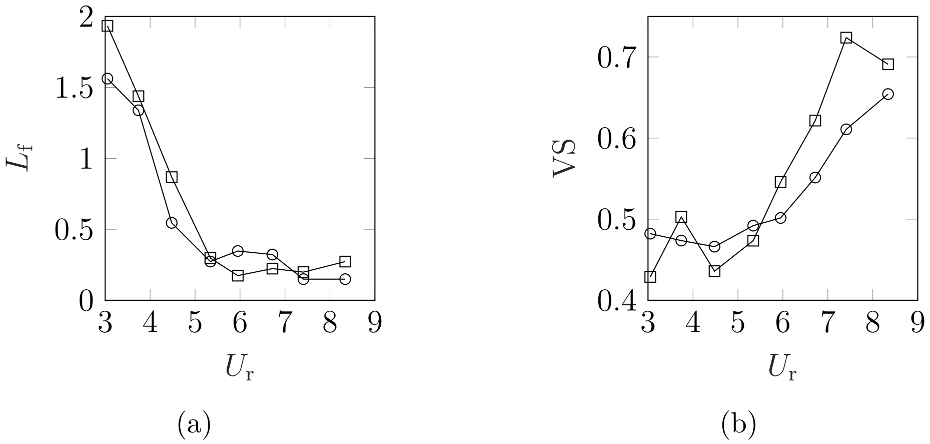

(a) (b)

Figure 6.8: L_f and vortex strength (VS) at $z = [6, 10]D$. ○: $z = 6D$. □: $z = 10D$

the $z = 10D$ region as the cylinder goes through its branch transition.

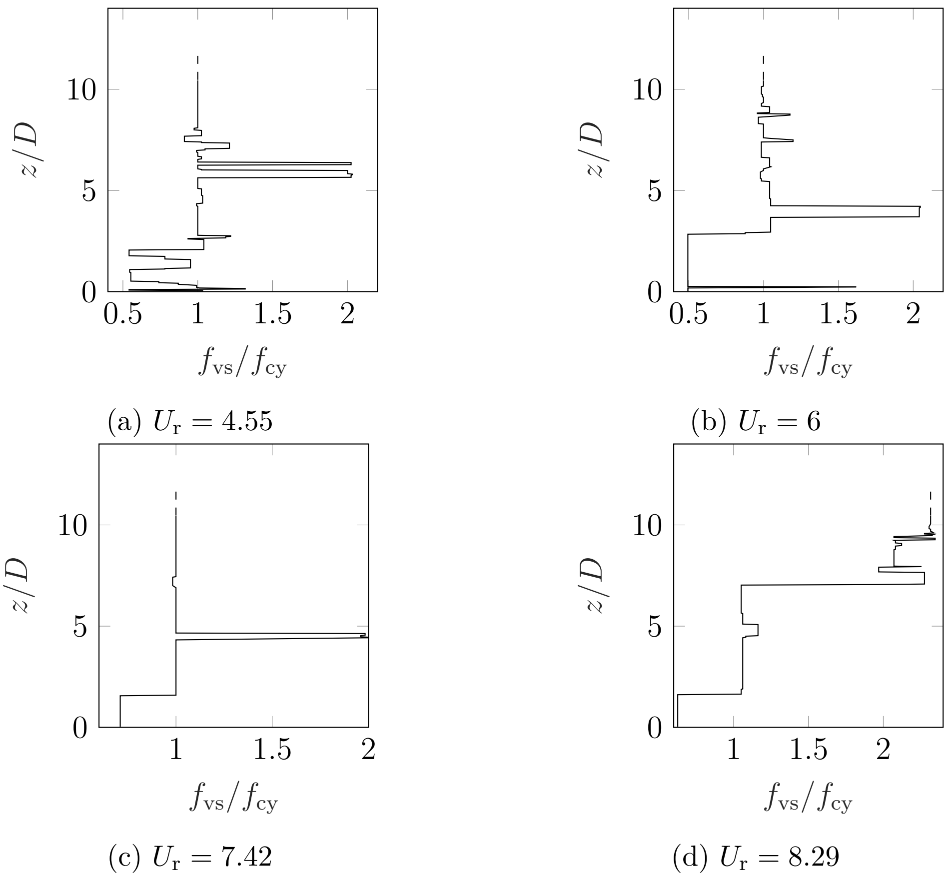

(a) $U_r = 4.55$

(b) $U_r = 6$

(c) $U_r = 7.42$

(d) $U_r = 8.29$

Figure 6.9: Normalised vortex shedding frequency measured at $x = 3.5D$. Dashed lines of $1.5D$ length extends the last measured point to the free-surface

Changes in the vortex shedding frequency along the cylinder span were analysed using vertical PIV measurements along the cylinder centreline. Inflow velocities within the initial branch ($U_r = 4.55$), upper branch ($U_r = 6$ and $U_r = 7.42$), and branch transition ($U_r = 8.29$) were considered. A PSD analysis was applied to the fluctuating streamwise velocity at different downstream distances from the pivot point, $u'(x = [3, 3.5, 4, 5]D, 0, z, t)$. The frequency of the highest PSD magnitude was extracted and filtered through a moving median filter of size 10 data points. Figure 6.9 shows the vortex shedding frequency at $x = 3.5D$, which resulted in the most stable peak frequency results. Significant differences with the bottom-fixed cylinder (Chapter 5) were observed across inflow velocities. One similarity is the region near the bed surface where $f_{\mathrm{vs}} < f_{\mathrm{cy}}$. This region varied from $2.9D$ at the beginning of the upper branch to $1.9D$ at the highest cylinder response and it shows the complex interaction between the bed surface, the incoming flow velocity, and the cylinder (see Chapter 5.3.3). At $U_{\mathrm{r}} = 4.55$, the vortex shedding frequency varied around the cylinder crossflow frequency throughout most of the cylinder span. Two frequency jumps, where $f_{\mathrm{vs}} = 2f_{\mathrm{cy}} = f_{\mathrm{cx}}$, were observed at $z \approx [5.8D, 6.4D]$. A similar trend was observed at $U_{\mathrm{r}} = 6$, with a single $f_{\mathrm{vs}} = f_{\mathrm{cx}}$ region of $0.7D$ length. When the cylinder reached its highest amplitude ($U_{\mathrm{r}} = 7.42$), f_{vs} was locked-in to f_{cy} throughout most of the cylinder length. Still, there was one $f_{\mathrm{vs}} = f_{\mathrm{cx}}$ region of $0.57D$ length that persisted at the maximum cylinder response. At the highest tested inflow velocity, f_{vs} deviated from its previous relationships, ranging between $1.96f_{\mathrm{cy}}$ and $2.37f_{\mathrm{cy}}$ at $z \geq 6.4D$. The variability of f_{sv} around f_{cy} was systematically reduced as the cylinder reached its maximum amplitude. It is not clear if the confluence between f_{cx} and f_{cy} over f_{vs} explains the observed frequency variability along the cylinder span.

As described before, f_{cx} seems to lead f_{vs} in specific spanwise regions. This influence persist even at the highest amplitudes, where $f_{\mathrm{sv}} = f_{\mathrm{cy}}$ is maximal along the cylinder span. These dominant streamwise frequency regions indicate a higher energetic contribution of the streamwise response over its crossflow counterpart. Different parameters, such as non-linear variation of the spanwise wake dynamics, non-uniform velocity profiles and spanwise flow motions [103], enhance flow three-dimensionality and can reduce (increase) the energetic contribution of the crossflow (streamwise) response, triggering the observed dominant streamwise frequency regions. Although it is not possible to determine the individual contribution of f_{cx} on the vortex shedding process, these results and the observed high streamwise amplitude described in Section 6.3.1 shows the importance of the streamwise response on the fluid-structure interaction process. Similar to the bottom-fixed cylinder in Chapter 5, the pivoted cylinder achieved its maximum amplitude when $f_{\mathrm{vs}} \approx f_{\mathrm{cy}} \approx f_{\mathrm{nw}}$, and when this equivalence was preserved along its span, i.e. when the spanwise synchronisation region was maximal. Nevertheless, the desynchronisation process seems to start at the water surface and progresses towards the bed surface, as opposed to the bottom-up desynchronisation of the bottom-fixed cylinder. After the pivoted cylinder achieved its maximum amplitude, the streamwise response transitioned from roughly regular to a beating-like motion with a lower amplitude. On

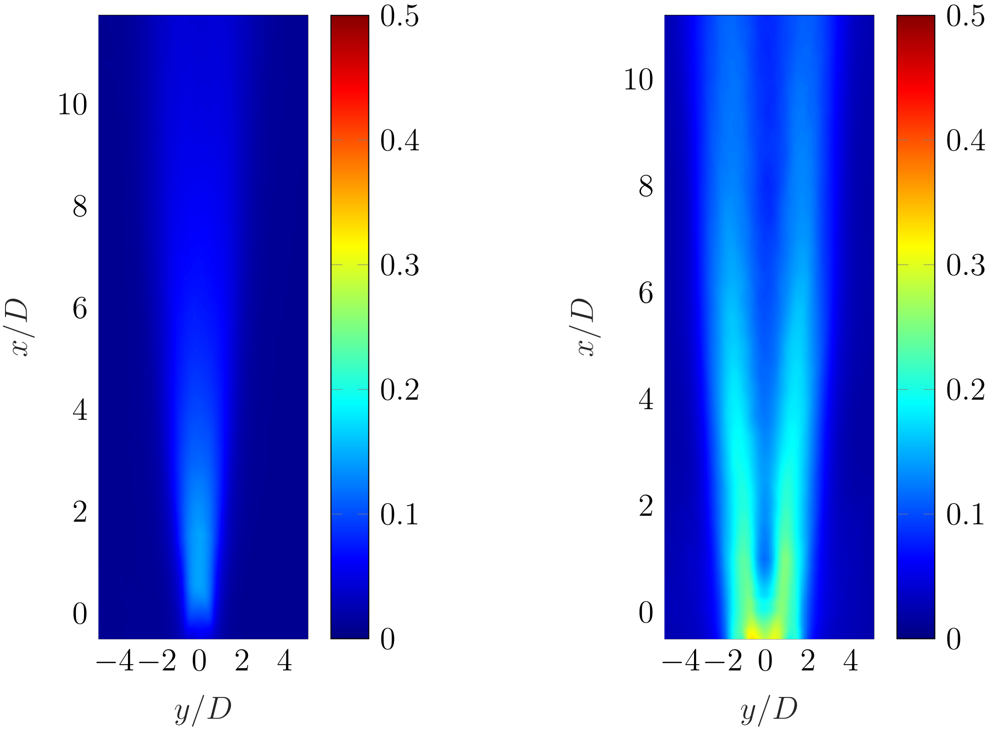

(a) (b)

Figure 6.10: $\mathrm{rms}(u')/U_{\mathrm{in}}$ field at $z = 10D$. a) $U_{\mathrm{r}} = 2.95$. b) $U_{\mathrm{r}} = 6$

the other hand, the crossflow response maintained most of its sinusoidal nature and amplitude. Thus, the cylinder-wake synchronisation process seems to be affected by an increment in streamwise response modulation. Due to the linear amplitude variation of the pivoted cylinder, regions near the water surface (higher structural responses) are more affected by this increment in streamwise modulation, potentially triggering a desynchronised region. However, the cylinder-wake interaction seems strong enough to overcome the irregular streamwise motion at lower water depths (lower cylinder response), and synchronisation is maintained. Additional information at higher flow velocities is required to analyse this particular behaviour.

Vortex pattern identification from flow field statistics, as in Section 5.3.3, was not possible due to the observed high streamwise amplitude and its influence in complex vortex modes, such as 2T [41] or 2C [21]. Still, regions with complex vortex patterns can be differentiated from the commonly observed 2S mode by comparing the contour distribution of previous experimental studies [29]. Figure 6.10a shows a typical $\mathrm{rms}(u')$ flow field of the 2S mode found at $U_{\mathrm{r}} = 2.95$, while Figure 6.10b shows a complex distribution at $U_{\mathrm{r}} = 6$. The 2S mode was observed for $U_{\mathrm{r}} \leq 4.55$ ($z = 6D$) and $U_{\mathrm{r}} \leq 3.76$ ($z = 10D$), showing a longer pattern presence as the local cylinder amplitude decreases. Moreover, these results implies the presence of a spanwise hybrid mode at $U_{\mathrm{r}} = 4.5$ (see Appendix C.2). Complex vortex patterns are expected at higher U_{r}, from which different statistical techniques (e.g. POD) can be used to uncover large-scale features from their respective velocity fields.

6.4 Conclusions

This chapter analyses the spanwise wake dynamics and structural response of a pivoted cylinder subjected to a range of open-channel flows. Planar PIV measurements and two synchronised cameras were used to capture the wake region and the cylinder free end response. The maximum cylinder amplitude at different flow velocities showed three characteristic regions: a high streamwise, initial, and upper branch. Only a transition to, what seems to be, the lower branch could be captured due to limitations on the maximum flow velocity. The cylinder achieved a maximum response within the upper branch of $0.44D$ and $2.1D$ in the streamwise and crossflow direction, respectively. A first-order sinusoidal function with a phase angle between directions can approximate the main features of the cylinder motion. The trajectory shape varied from an eight-type at the minimum tested flow velocity to a crescent-type at higher U_r. The wake dynamics at $z = 10D$ had a bigger recirculation region, higher momentum transference, broader wake width, and higher vortex strength in the upper branch compared to $z = 6D$. Moreover, the $\mathrm{rms}(u')$ flow fields showed changes in vortex patterns along cylinder span and throughout different flow velocities. These differences in the spanwise wake dynamics can not be fully explained by the linear variability of the cylinder response along its span. Other influential factors, such as spanwise vortex correlation, free-surface effects, among others, could play a significant role in the wake dynamics between $z = 6D$ and $z = 10D$. An analysis of the vortex shedding frequency along the cylinder span showed a complex behaviour with significant differences from the bottom-fixed cylinder in Chapter 5. The streamwise oscillation frequency dominated the vortex shedding frequency in specific spanwise regions throughout the upper branch. Moreover, the desynchronisation process started at the water surface and seemed to progress towards the flume's bed. Nevertheless, similar to the bottom-fixed cylinder case, the maximum response was achieved when the cylinder motion and vortex shedding frequencies are equal (i.e. lock-in or synchronisation) to the natural frequency measured in still water, and when this equivalence is maintained along the cylinder span.

The maximal spanwise synchronisation at the highest cylinder response supports the use of two-dimensional RANS models, from which a complete spanwise synchronisation is assumed. Nevertheless, there are important variations in the spanwise wake dynamics that are not uniquely explained by the difference in local motion of the pivoted configuration. These differences can not be directly reproduced by a two-dimensional model, complicating its predicting capabilities at high-amplitude responses. Moreover, it is not clear if the two-dimensional model can capture the cylinder's motion variability beyond a first-order sinusoidal fit. These hypothesis are tested in Chapter 7, where a two-dimensional RANS model is built using the structural characteristics of the pivoted configuration.

Chapter 7

Numerical model: Pivoted cylinder

7.1 Introduction

Vortex-induced vibration is a complex phenomenon that imposes significant challenges to its numerical simulation. An attractive alternative commonly used in research and industry are two-dimensional numerical representations of the inherently three-dimensional VIV. Recent numerical studies based on two-dimensional RANS models have successfully extracted the main features of cylinders undergoing VIV with high-amplitude responses and above the laminar vortex shedding regime. These results encourage using these numerical models on complex configurations, such as pivoted cylinders, characterised by its linear amplitude variation along its span. This chapter analyses the capabilities and accuracy of two-dimensional RANS models to simulate the response of a pivoted cylinder subjected to VIV. The inflow and structural characteristics of the experimental pivoted cylinder in Chapter 6 were used as input for the numerical model. The SST $k-\omega$ turbulence model with the Runge-Kutta fourth-order algorithm were implemented in Ansys Fluent, alongside a User Defined Function to account for the fluid-structure coupling mechanism. The numerical model was first validated by simulating a low mass-damping two degree-of-freedom cylinder [41]. Then, the influence of the inflow conditions that trigger the experimental upper branch was analysed. These inflow conditions were critical to ensuring a high-response state in the simulations. Finally, the numerical model of the pivoted cylinder was compared to its experimental counterpart in terms of displacements and oscillation frequencies.

7.2 Numerical model

7.2.1 Numerical set-up

The RANS equations were solved with the SST $k - \omega$ turbulence model. The numerical model used the following spatial and time discretisation schemes: Second-order implicit for temporal discretisation, Semi-Implicit Method for Pressure Linked Equations (SIMPLE) for pressure and velocity coupling, Body Force Weighted for pressure, Quadratic Upwind Interpolation for Convection (QUICK) for momentum, first upwind scheme for the dissipation rate, and second upwind scheme for kinetic energy. Convergence was achieved when the residuals of all flow parameters reached 1×10^{-5}. These parameters were selected based on previous studies [35, 45, 105].

A staggered approach with dynamic mesh deformation was used for the coupling mechanism (Section 4.4). The RANS equations with the SST $k - \omega$ turbulence model were iteratively solved until converge was achieved. Then, the total pressure and viscous forces on the cylinder were extracted using a User Defined Function. The equation of motion of an elastically mounted or pivoted cylinder was solved using the Runge-Kutta fourth-order method. As the cylinder updates its position, the nearby mesh adapts accordingly, following a diffusion-based smoothing scheme.

7.2.2 Computational domain and mesh

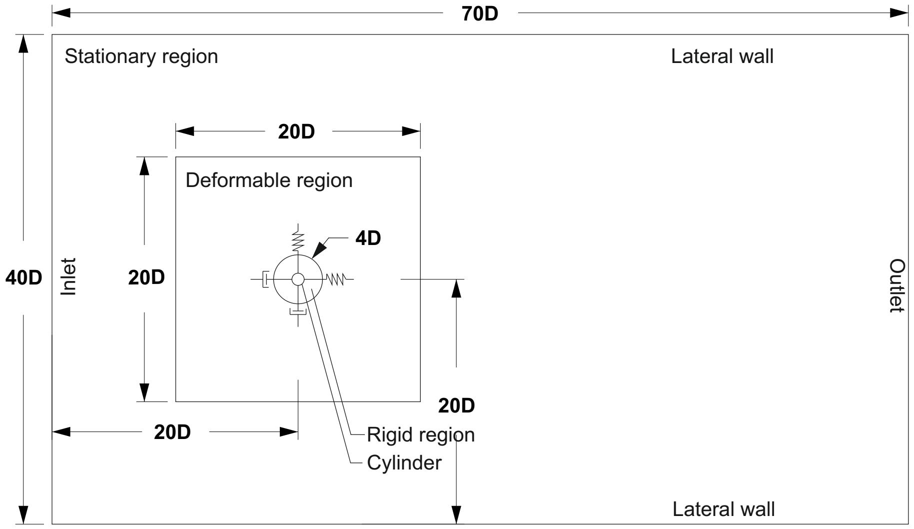

Figure 7.1: Computational domain of the numerical model. Flow velocity from left to right

Figure 7.1 show the mesh domain of $40D$ width and $70D$ length. The chosen width had negligible effects on the cylinder response [116]. The origin of the coordinate system was located at the cylinder centreline. The flow enters from the inlet

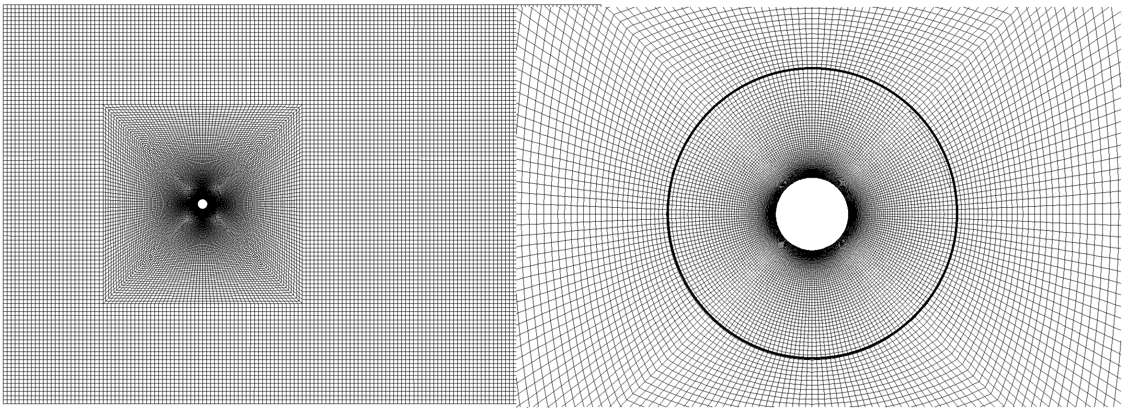

(a) (b)

Figure 7.2: Mesh configuration scheme. a) Mesh domain. b) Mesh around the cylinder

at $20D$ upstream the cylinder and exits from the outlet located at $70D$ downstream the origin. The mesh domain was divided into three regions, as shown in Figure 7.2. Firstly, a dense O-grid around the cylinder extending $4D$ from the origin. This region moves with the cylinder preserving its shape. Secondly, a square-shaped grid of quadrilateral elements. This region absorbs the cylinder motion by deforming its mesh elements. Thirdly, a stationary region. The upper and lower walls were set to free-slip boundaries, while the no-slip condition was used at the cylinder surface. The inflow had a time-dependent streamwise velocity. The outflow boundary had a reference pressure equal to zero.

7.3 Preparation and validation

This section analyses the simulation of a low mass-damping two degree-of-freedom cylinder using the numerical parameters described previously and the equations of motion described in Section 4.3.1. Several reasons are given for the modelling of Jauvtis and Williamson's cylinder [41]. Firstly, the experimental study shares several similarities with the tested pivoted cylinder of Chapter 6, such as low mass-damping ratio, two degree-of-freedom, streamwise amplitudes of $0.3D$, and maximum cross-flow amplitude of $1.5D$. Secondly, the performance and accuracy of the numerical model can be compared against previous state-of-the-art studies. Thirdly, as described in Section 2.4, high-responses in low mass-damping cylinders are triggered under specific inflow conditions. Thus, it is critical to determine these conditions to ensure that the numerical model reaches high-amplitude responses.

7.3.1 Experimental parameters

A two degree-of-freedom elastically mounted cylinder was subjected to a range of Reynolds number between $1.4\times10^3 \leq R_\mathrm{e} \leq 1\times10^4$. The main structural parameters are: $D = 38.1$ mm, $f_\mathrm{nw} = 0.4$ Hz, $m^* = 2.6$, and $\xi = 0.00361$ [41].

7.3.2 Mesh independence

Case	N_e	N_c	N_L	g_r	$H_{\mathrm{y}+}$	$\overline{C_\mathrm{D}}$	rms(C_D)	rms(C_L)	A_x	A_y	$f_\mathrm{c}/f_\mathrm{nw}$
M1	16704	120	56	1.11	0.00067D	2.57	1.10	1.85	0.18	1.02	0.90
M2	25953	160	62	1.1	0.00053D	2.42	1.16	1.80	0.19	1.01	0.92
M3	39100	200	70	1.1	0.00053D	2.27	1.10	1.77	0.18	1.00	0.92
M4	57324	240	92	1.07	0.00039D	2.34	1.09	1.72	0.18	1.01.	0.92
Num. (1)	226800	160	-	-	-	1.91	1.52	1.2	0.17	1.07	0.87
Num. (2)	42761	200	-	-	0.003D	2.42	1.14	1.71	0.15	1.14	0.93
Exp.	-	-	-	-	-	2.53	1.07	2.18	0.21	1.07	0.9

Table 7.1: Mesh independence analysis. Num. (1): [35], Num. (2): [105]. Exp: [41]

A mesh independence analysis was performed at $U_\mathrm{r} = 6$, which is a stable region within the experimental upper branch [45]. The mesh resolution was controlled by the total number of mesh elements N_e, the number of elements around the cylinder N_c, the number of layers N_L and growth rate g_r in the radial direction within the O-grid zone, and the height of the first element around the cylinder $H_{\mathrm{y}+}$. The time step was $\Delta_\mathrm{t} = 0.0015$ s, ensuring a CFL number of less than one. The inflow velocity started at $U_\mathrm{r} = 2$ and was slowly increased for 50 seconds until $U_\mathrm{r} = 6$ was reached. The simulation continued until at least 20 cycles of stable oscillations were obtained. The following statistics were used for comparison: mean drag coefficient $\overline{C_\mathrm{D}}$, root-mean-square of the drag rms(C_D) and lift rms(C_L) coefficient, maximum amplitude in the streamwise A_x and crossflow A_y direction, and oscillation frequency in the crossflow direction. The results are summarised in Table 7.1. Previous numerical results are also added for comparison [35, 105]. The highest variability between tested cases was observed in the force coefficient statistics with a difference of 13.2%, 6.4%, and 7.6% for $\overline{C_\mathrm{D}}$, rms(C_D), and rms(C_L), respectively. Despite these differences, the cylinder amplitude and oscillation frequency had an excellent agreement across simulations. The streamwise amplitude was 10.5% lower than the experimental results despite having an excellent agreement in terms of their associated force statistics. Likewise, the crossflow amplitude was 7% lower than the experimental A_y. The numerical model had a similar or superior accuracy compared to previous studies [35, 105] in all calculated statistics except for A_y.

The M3 mesh was used in subsequent sections since a higher mesh density did not significantly improve the model's accuracy. This mesh was also tested under different integration algorithms for the mass-spring-damping model and spatial discretisation schemes for the momentum flow equations (Appendix D.1). These results showed no significant differences with the parameters selected in Section 7.2.1.

7.3.3 Response across U_r

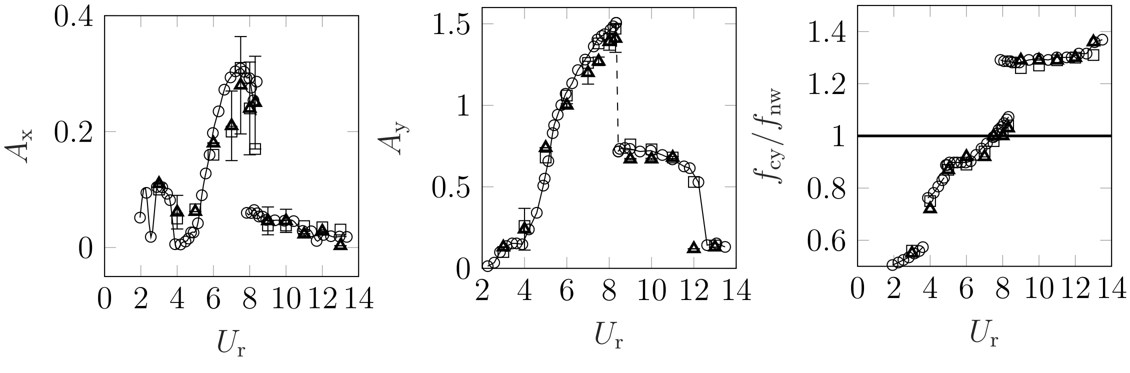

(a) (b) (c)

Figure 7.3: Maximum response and oscillation frequency of a low mass-damping two degree-of-freedom cylinder. Error bars represent one standard deviation around the maximum displacement. △: Numerical model. ○: Experimental result [41]. □: Numerical study [35]

Figure 7.3 shows the results of the numerical model in terms of maximum amplitudes and oscillation frequencies. The transitions between branches were properly captured as jumps in the crossflow oscillation frequency (Figure 7.3c). The initial branch ranged between $4 \leq U_\mathrm{r} < 5$, marked by an steady increment in the maximum amplitude and oscillation frequency. The cylinder transitioned to the upper branch at $U_\mathrm{r} \approx 5$. The amplitude response increased within the upper branch up to a maximum value of $A_\mathrm{x} = 0.28D$ and $A_\mathrm{y} = 1.41D$, which were 9.5% and 6% lower than the experimental results, respectively. f_cy increased with U_r within the upper branch, crossing f_nw and reaching a maximum value of $1.03 f_\mathrm{nw}$ at $U_\mathrm{r} = 8.3$. At higher flow velocities, the transition to the lower branch was characterised by a jump in the maximum amplitude and oscillation frequency. These values remained fairly constant within the lower branch until the cylinder entered its desynchronised phase at $U_\mathrm{r} \approx 11$. This desychronisation occurred at an earlier U_r than the experimental result, which has been attributed to the SST $k - \omega$ turbulence model [45].

Figure 7.4 shows the cylinder trajectory and associated instantaneous vorticity contours at $U_\mathrm{r} = [3, 8.3, 9]$. A classic 2S vortex mode was observed at $U_\mathrm{r} = 3$. The characteristic 2T pattern was captured within the upper branch ($U_\mathrm{r} = 8.3$).

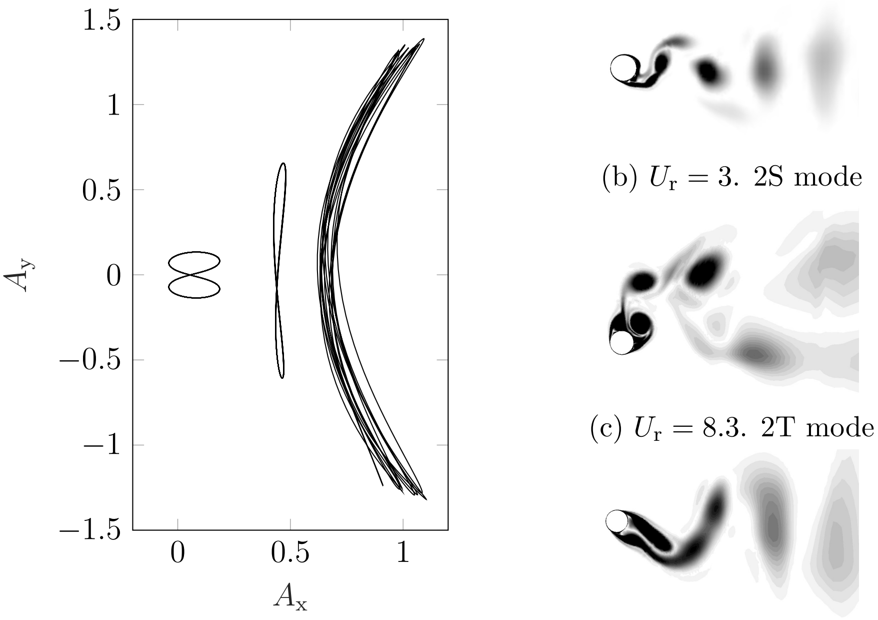

(b) $U_r = 3$. 2S mode

(c) $U_r = 8.3$. 2T mode

(a) Left to right: $U_r = [3, 8.3, 9]$

(d) $U_r = 9$. 2P mode

Figure 7.4: Cylinder trajectories (a) and instantaneous vorticity contours (b-d) at $U_r = [3, 8.3, 9]$

Lastly, the 2P vortex mode was observed at $U_r = 9$. These results are consistent with the experiment being modelled [41] and previous numerical simulations (see, for example, [35, 105]).

7.3.4 Inflow velocity conditions

It is well documented that the inflow conditions influence the response of cylinders subjected to VIV. Depending on the time history of the inflow velocity, which encloses increasing or decreasing conditions with their respective acceleration magnitude, the cylinder could exhibit a high- or low-amplitude response. The inflow conditions that trigger these responses are often not reported in VIV experiments [89] and vary widely between the few numerical studies that implicitly describe them. One reason for this lack of information is that measurements in physical experiments are usually taken between small flow velocity increments, fulfilling the inflow acceleration requirements to trigger high-amplitude responses. On the other hand, different numerical studies have shown difficulties to simulate the experimental high-amplitude responses due to inadequate considerations of the inflow conditions (see recent examples, [25, 32]). The only numerical study that this researcher could find indicated that by slowly increasing the inflow velocity below a certain acceleration, the simulation reached the experimental maximum amplitude [45]. Recent numerical studies have achieved similar results using significantly higher inflow accelerations ([35, 105]). This discrepancy is analysed here by testing different initial conditions under systematic increments of the inflow acceleration until the cylinder reached the experimental high-response state.

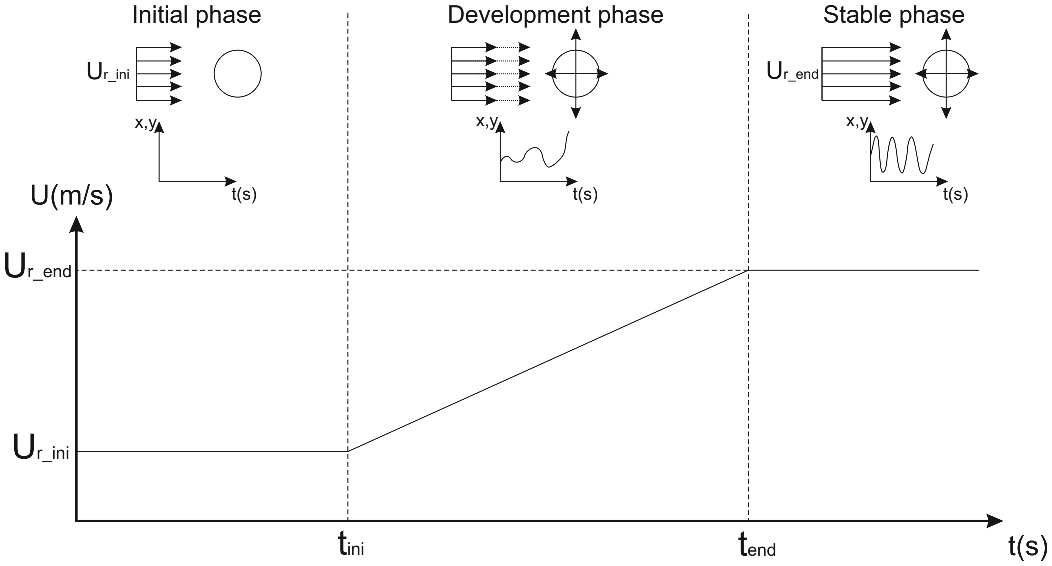

Figure 7.5: Time-history of the inflow under increasing velocity condition

The time history of the inflow velocity was divided into three phases (Figure 7.5), as in [115]. Firstly, the initial phase, where the cylinder is fixed and subjected to $U_{\mathrm{r\_ini}}$ for an initial time t_{ini}. Secondly, the development phase, where the cylinder is free to move while the inflow velocity slowly increases under a constant normalised acceleration a_{c} for an acceleration time t_{a}. Thirdly, the stable phase, where the inflow velocity reaches $U_{\mathrm{r\_end}}$ and is maintained until at least 20 stable oscillations. $t_{\mathrm{ini}} = 0$ s implies that the cylinder is free to move since the beginning of the simulation. Likewise, $t_{\mathrm{a}} = 0$ s indicates a constant inflow velocity condition throughout the simulation. The normalised acceleration is defined as

$$a_{\mathrm{c}} = \frac{U_{\mathrm{r\_end}} - U_{\mathrm{r\_ini}}}{t_{\mathrm{a}} f_{\mathrm{nw}}} \tag{7.1}$$

where $t_{\mathrm{a}} = t_{\mathrm{end}} - t_{\mathrm{ini}}$.

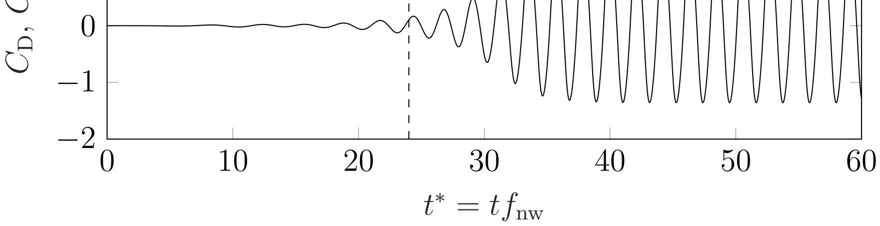

Figure 7.6: a) Total drag and lift coefficient around a fixed cylinder at $R_{\mathrm{e}} = 1.2\times10^3$

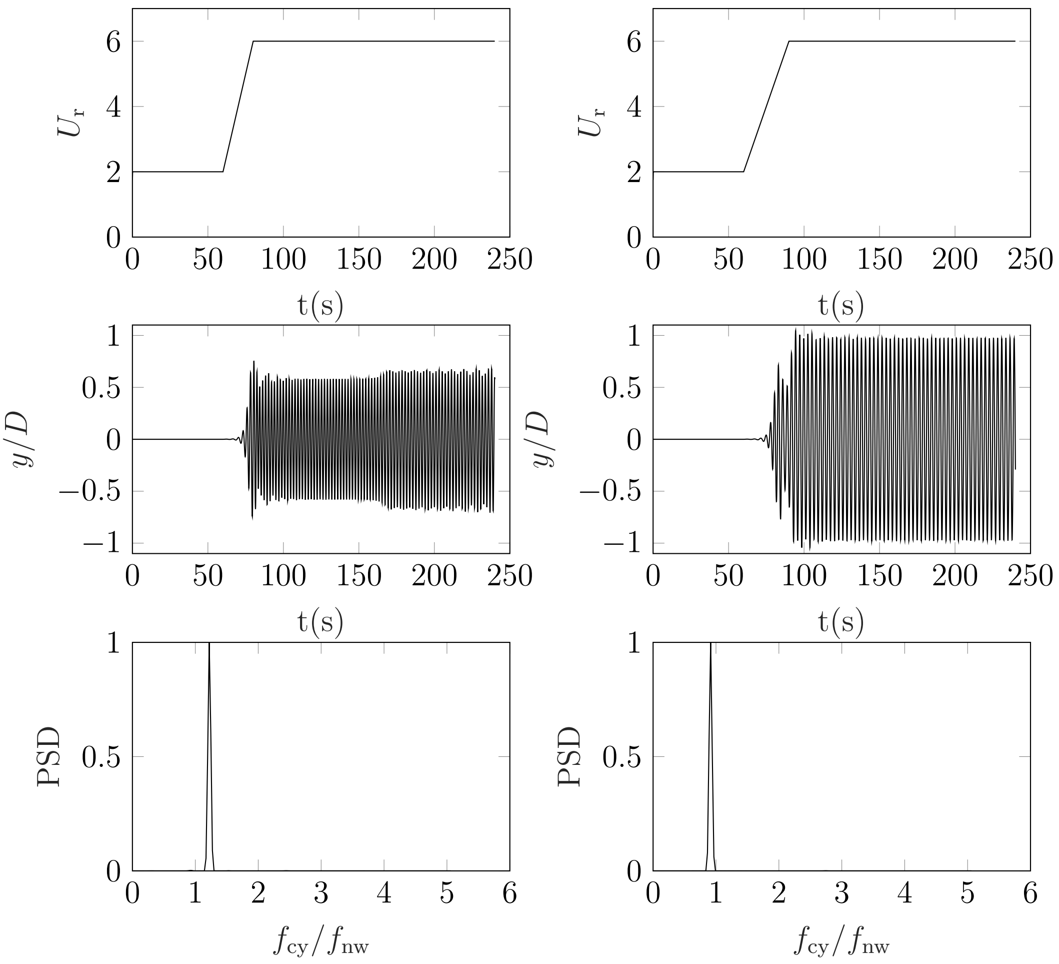

(a) (b)

Figure 7.7: Increasing velocity condition (up), cylinder crossflow motion (middle) and PSD (down) at (a) $t_a = 20$ s and (b) $t_a = 30$ s for the $t_{ini} = 60$ s case

Figure 7.6 shows the time history of C_D and C_L within the initial phase (stationary cylinder condition, $R_e = 1.2 \times 10^3$). Both force coefficients reached a steady oscillatory state after 110 seconds. Thus, different responses are expected as a function of the simulation time spent on the initial phase. This hypothesis was tested by simulating three initial time conditions, $t_{ini} = 0$ s (cylinder is free to move from the start of the simulation), $t_{ini} = 60$ s (cylinder is released while the lift and drag forces are developing), and $t_{ini} = 150$ s (cylinder is releaser after the fluid forces around the body reached an oscillatory steady state). Each case started at $U_{r\_ini} = 2$ and was systematically increased to $U_{r\_ini} = 6$ under different acceleration times. As an example, Figure 7.7 shows the results of two simulations at different acceleration times. When the acceleration time increased from 20 to 30 seconds, A_y and f_{cy}/f_{nw} reached values comparable to the experimental results.

The maximum amplitudes and main peak frequencies of each tested initial time ($t_{ini} = [0, 60, 150]$ s) and at different acceleration times are summarised in Figure 7.8.

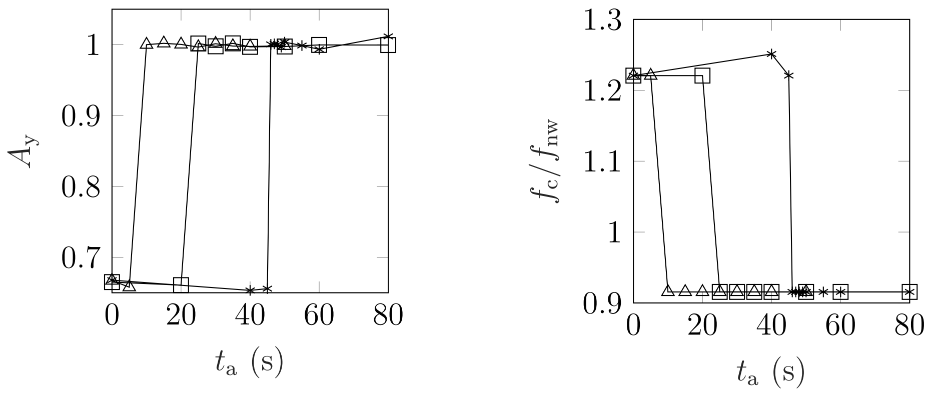

(a)

(b)

Figure 7.8: t_{ini} influence on the maximum cylinder response (a) and oscillation frequency (b). □: $t_{ini} = 0$ s, ○: $t_{ini} = 60$ s, △: $t_{ini} = 150$ s

A bistable response is identified. A low-amplitude response at low t_a, where $A_y = 0.56D$ and $f_{cy}/f_{nw} = 1.3$, and a high-response state at high t_a, where $A_y = 0.97D$ and $f_{cy}/f_{nw} = 0.92$. The cylinder response and oscillation frequency within states were not affected by t_a or t_{ini}. The minimum acceleration time required to trigger a high-response state decreased up to four times when the initial time increased to $t_{ini} = 150$ s. These acceleration times are significantly lower than the ones reported in previous numerical studies [45, 115]. Moreover, the transition between response states occurred suddenly as opposed to the smooth increments reported in [45] (see Figure 2.9).

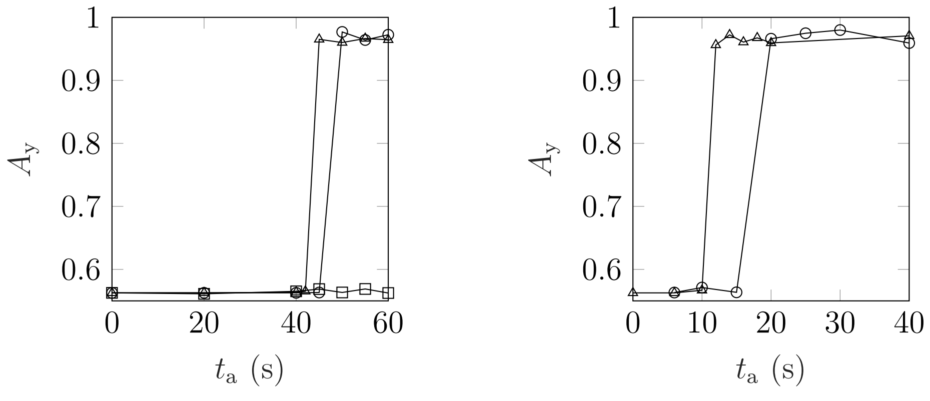

(a)

(b)

Figure 7.9: U_{r_ini} influence on the maximum cylinder response at (a) $t_{ini} = 0$ s and (b) $t_{ini} = 150$ s. □: $U_{r\_ini} = 0$, ○: $U_{r\_ini} = 1$, △: $U_{r\_ini} = 2$

The results in Figure 7.8 were obtained considering $U_{r\_ini} = 2$, as in [115]. Next, the effects of the initial inflow velocity on the cylinder response were analysed. Figure 7.9 shows the maximum crossflow amplitude at three initial reduced velocities $U_{r\_ini} = [0, 1, 2]$, each at $t_{ini} = 0$ s (Figure 7.9a) and $t_{ini} = 150$ s (Figure 7.9b). The

$U_{\mathrm{r\_ini}} = 0$ case at $t_{\mathrm{ini}} = 150$ s was not considered for obvious reasons. The $U_{\mathrm{r\_ini}} = 0$ case did not trigger a high-response state at all tested t_{a}. Higher acceleration times could not be analysed due to the prohibitive computational time required to reach the stable phase. Simulations that do not impose an initial flow velocity ($U_{\mathrm{r\_ini}} = 0$) require extremely high acceleration times to build up the fluid forces required to trigger a high-response state. This condition partially explains the significantly higher t_{a} reported in previous numerical studies [45]. There is an inverse non-linear relationship between the minimum acceleration time required to trigger a high-response state and $U_{\mathrm{r\_ini}}$. This relationship is secondary compared to t_{ini} (Figure 7.8).

Figures 7.8 and 7.9 show the importance of the inflow conditions on the cylinder response and oscillation frequency. A high-response state can be achieved at significantly lower acceleration times when the initial phase considered a small initial flow velocity and when the lift and drag forces in the initial phase were allowed to develop and reach an oscillatory steady state.

7.4 Results

The pivoted cylinder model considered the mesh resolution, time step, and inflow conditions from previous sections. The M3 mesh case was used (Table 7.1), maintaining proportionality as a function of the cylinder's diameter. A time step value that ensures a CFL number lower than one was enforced, reaching a minimum value of $\Delta_{\mathrm{t}} = 0.0002$ seconds at the highest tested U_{r}. An initial phase of 90 seconds with $U_{\mathrm{r\_ini}} = 1$ was used to speed up the total simulation time required to reach its stable phase. Moreover, the acceleration time was systematically increased up to 30 seconds to ensure a high-response state.

7.4.1 Preliminary considerations

As described in Chapter 4.3.2, the equations of motion for the two-dimensional representation of a pivoted cylinder are

$$\ddot{x} + 4\pi f_{\mathrm{nw}} \zeta \dot{x} + 4\pi^2 f_{\mathrm{nw}}^2 x = \frac{M_x L}{1 + C_{\mathrm{a}} I^*} \tag{7.2}$$

$$\ddot{y} + 4\pi f_{\mathrm{nw}} \zeta \dot{y} + 4\pi^2 f_{\mathrm{nw}}^2 y = \frac{M_y L}{1 + C_{\mathrm{a}} I^*} \tag{7.3}$$

The total forcing moment in Equations 7.2 and 7.3 correspond to the sum of

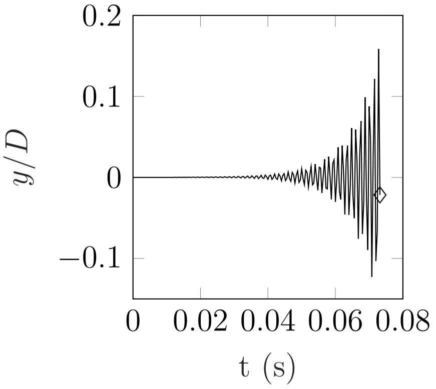

Figure 7.10: Unstable response example. Exponential increment of the cylinder displacement between time steps until the mesh was not able to accommodate the new cylinder position

hydrodynamic forces in a given direction multiplied by its corresponding lever arm. Several considerations are given for the forcing moment. The independence principle states that VIV is driven by the flow component normal to the cylinder surface and that the perpendicular (axial) component is negligible [9]. This principle is valid for inclination angles of less than 20° [9, 96, 114], which is a higher threshold than the one given by the maximum response of the tested pivoted cylinder. Moreover, the axial component of the hydrodynamic force corresponds to 1% of its magnitude at the maximum inclination angle. Thus, this axial component is considered negligible in the numerical simulation. Since the spatio temporal position of the lever arm is unknown in two-dimensional models, a fixed position is commonly assumed. As an example, previous studies have used the projected span length for curved cylinders [96] or considered a linear variation of the total force for pivoted cylinders [51]. Both approaches were applied to Equations 7.2 and 7.3 with the structural parameters of the pivoted cylinder. The resultant numerical model led to non-convergent sinusoidal responses with increasing amplitudes (Figure 7.10). The cylinder response exponentially increased its displacement between time steps, eventually triggering numerical errors due to the mesh inability to deform with the cylinder new position. This unstable response is one of the five possible responses observed in second-order linear systems and can be explained by the combined effect of the damping ratio and the self-excited hydrodynamic forces. The wake-cylinder energy transfer mechanism is commonly portrayed as a negative-damping-type instability [55]. The self-excited hydrodynamic forces introduce an aerodynamic damping component that opposes the structural damping ratio. Under certain conditions, the energy transfer to the cylinder is transformed into gradual increments in structural oscillations until the total damping ratio is zero and the wake-cylinder interaction reaches (on average) equilibrium under self-limited VIV conditions [107]. When the aerodynamic-to-structural damping ratio is significantly high, unrealistic cylinder responses (and associated velocities and accelerations) are needed to reach a zero damping system. This criterion is easier to meet in low damping systems, such as the tested pivoted cylinder, where the energy required to reach self-limiting VIV is low [54]. Later it will be shown that the mass-spring-damping model with the structural parameters of the pivoted cylinder led to self-limiting VIV amplitudes when the hydrodynamic forces were directly applied. Thus, depending on the selected lever arm, the system could become unstable (Figure 7.10) or even over damped.

Based on the previously described relationship between the lever arm and the hydrodynamic force, the forcing moment was considered equal to the total hydrodynamic force multiplied by a constant three-dimensional force correction factor C_{F}. A similar approach was used to simulate VIV experiments with incomplete spanwise synchronisation [18]. The researchers scaled the lift force at different constant values to account for three-dimensional flow effects. This parameter was tested over the complete range of stable responses to determine which case led to the highest accuracy compared to the experimental results and estimate the threshold of unstable responses. Equations 7.2 and 7.3 are rewritten in terms of C_{F} as

$$\ddot{x} + 4\pi f_{\mathrm{nw}} \zeta \dot{x} + 4\pi^2 f_{\mathrm{nw}}^2 x = \frac{C_{\mathrm{F}} F_{\mathrm{x}} L}{1 + C_{\mathrm{a}} I^*} \tag{7.4}$$

$$\ddot{x} + 4\pi f_{\mathrm{nw}} \zeta \dot{x} + 4\pi^2 f_{\mathrm{nw}}^2 x = \frac{C_{\mathrm{F}} F_{\mathrm{y}} L}{1 + C_{\mathrm{a}} I^*} \tag{7.5}$$

It is important to consider that the case $C_{\mathrm{F}} = 1$ equals to the direct application of the hydrodynamic forces on the cylinder model.

7.4.2 Cylinder response across U_r

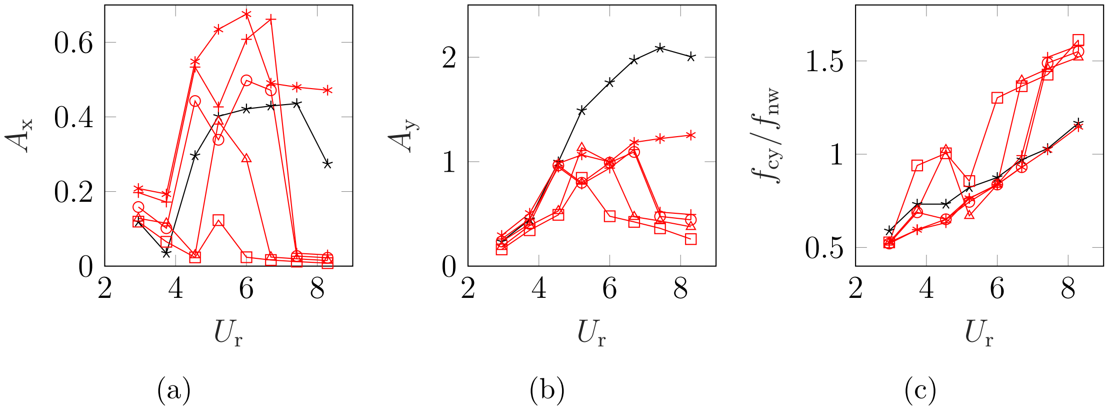

(a) (b) (c)

Figure 7.11: Maximum amplitude and oscillation frequency at $2.5 \times 10^3 \leq R_e \leq 5.8 \times 10^3$. a) Maximum streamwise response. b) Maximum crossflow response. c) Crossflow oscillation frequency. Black line: experimental data. □: $C_F = 0.6$. △: $C_F = 0.8$. ○: $C_F = 1$. ◇: $C_F = 1.2$. +: $C_F = 1.4$

Figure 7.11 summarises the numerical model results in terms of maximum amplitudes and crossflow oscillation frequencies. The streamwise oscillation frequency was not included since $f_{cx} \approx 2f_{cy}$ throughout U_r. Only the simulations associated to $C_F = [0.6, 0.8, 1, 1.2, 1.4]$ were considered since they showed the most interesting results. Higher values of C_F led to unstable responses (Figure 7.10). Within the initial branch ($U_r \leq 4.55$), the numerical model achieved good agreement in terms of A_y. On the other hand, A_x showed a high dependency on C_F with values that ranged between its experimental counterpart ($C_F = 0.6$) to twice its value ($C_F = 1.4$). At $U_r = 4.55$, the amplitudes associated to $C_F < 1$ were significantly lower than the experimental results, whereas the amplitudes for $C_F \geq 1$ reached a similar (crossflow) and double (streamwise) values compared to their experimental counterparts. As the cylinder entered the upper branch ($U_r = 5.21$), the numerical model was not able to keep the experimental upward trend in the crossflow direction, reaching maximum amplitudes between $A_y \approx 0.8D$ and $A_y \approx 1.1D$ for all tested C_F. The streamwise amplitude agreed with its experimental counterpart except at $C_F = 0.6$ and $C_F = 1.4$, were $A_x \approx 0.1D$ (under-prediction) and $A_x \approx 0.6D$ (over-prediction), respectively. Within the upper branch, the response amplitude associated to $C_F < 1$ significantly decreased and stabilised around a low amplitude value. The results associated to $C_F \geq 1$ showed a similar upward trend in the crossflow direction at a significantly lower amplitude compared to the experimental results. When the cylinder achieved its maximum response ($U_r = 7.42$), the $C_F = 1$ and $C_F = 1.2$ cases drastically decreased their simulation responses, stabilising around values comparable to $C_F \leq 1$. Only the $C_F = 1.4$ case kept a maximum amplitude of $A_x = 0.48D$ and $A_y = 1.22D$, this last value being 41.5% lower compared to the experimental amplitude in the crossflow direction. At the maximum tested flow velocity, the $C_{\mathrm{F}} = 1.4$ case maintained its previous maximum amplitude even though the pivoted cylinder entered its transition phase, characterised by an important decrement in the streamwise motion.

Figure 7.11c shows the main oscillation frequency in the crossflow direction. In general, important deviations in terms of maximum amplitudes are accompanied with significantly higher oscillation frequencies compared to their experimental counterpart. This relationship is illustrated for the $C_{\mathrm{F}} < 1$ cases. The main oscillation frequency associated to $C_{\mathrm{F}} \geq 1$ showed good agreement with the experimental results in the initial and part of the upper branch. At $U_{\mathrm{r}} \geq 7.42$, only the $C_{\mathrm{F}} = 1.4$ case maintained good accuracy while the main frequency of the $C_{\mathrm{F}} = [1, 1.2]$ cases jumped to match the $C_{\mathrm{F}} < 1$ results. Considering the best performing case ($C_{\mathrm{F}} = 1.4$), the difference between the numerical and experimental main oscillation frequency reached a maximum of 17.5% ($U_{\mathrm{r}} = 3.76$), with an average of 2.2% across U_{r}. This maximum difference at $U_{\mathrm{r}} = 3.76$ can be explained by its experimental $f_{\mathrm{cx}}/f_{\mathrm{cy}} \approx 1.7$ ratio, which introduces a coupling component between the streamwise and crossflow motion not included in the numerical model.

Unexpected transitions between a high- to a low-response state were observed within the upper branch. Figure 7.12 exemplifies this phenomenon by comparing the motion history of the $C_{\mathrm{F}} = [1.2, 1.4]$ cases at $U_{\mathrm{r}} = 6.69$. The results associated to $C_{\mathrm{F}} = 1.4$ maintained its high-response state throughout the simulation (Figure 7.12a). This stable response was characterised by an equal main frequency peak in its crossflow motion (Figure 7.12b) and lift force (Figure 7.12c), which ensures a stable synchronised state. On the other hand, Figure 7.12d shows a two-state response for the $C_{\mathrm{F}} = 1.2$ case. The high-response state was characterised by a multi-frequency lift force around the main oscillation frequency and between its first and second harmonics. These additional frequencies, besides the one equal to f_{cy}, seems to interfere with the cylinder-flow synchronisation and trigger its eventual transition to a low-response state. Then, the crossflow oscillation (Figure 7.12e) and lift force (Figure 7.12f) spectra were characterised by an equal main frequency peak, as in the $C_{\mathrm{F}} = 1.4$ case. The transition time between states was partially dependant on the initial flow conditions, specially the acceleration time. Still, the cylinder eventually transitioned to a low-response state in all tested acceleration times and no clear trend between inflow conditions and transition time could be observed. The experimental pivoted cylinder showed a stable response within the upper branch. Thus, the numerical model is susceptible to unexpected transitions to a low-response in cases of multi-frequency lift forces.

Figures 7.13 to 7.16 show the response trajectories of the numerical model across U_{r}. Only the responses associated to $C_{\mathrm{F}} = [1, 1.2, 1.4]$ were considered since they

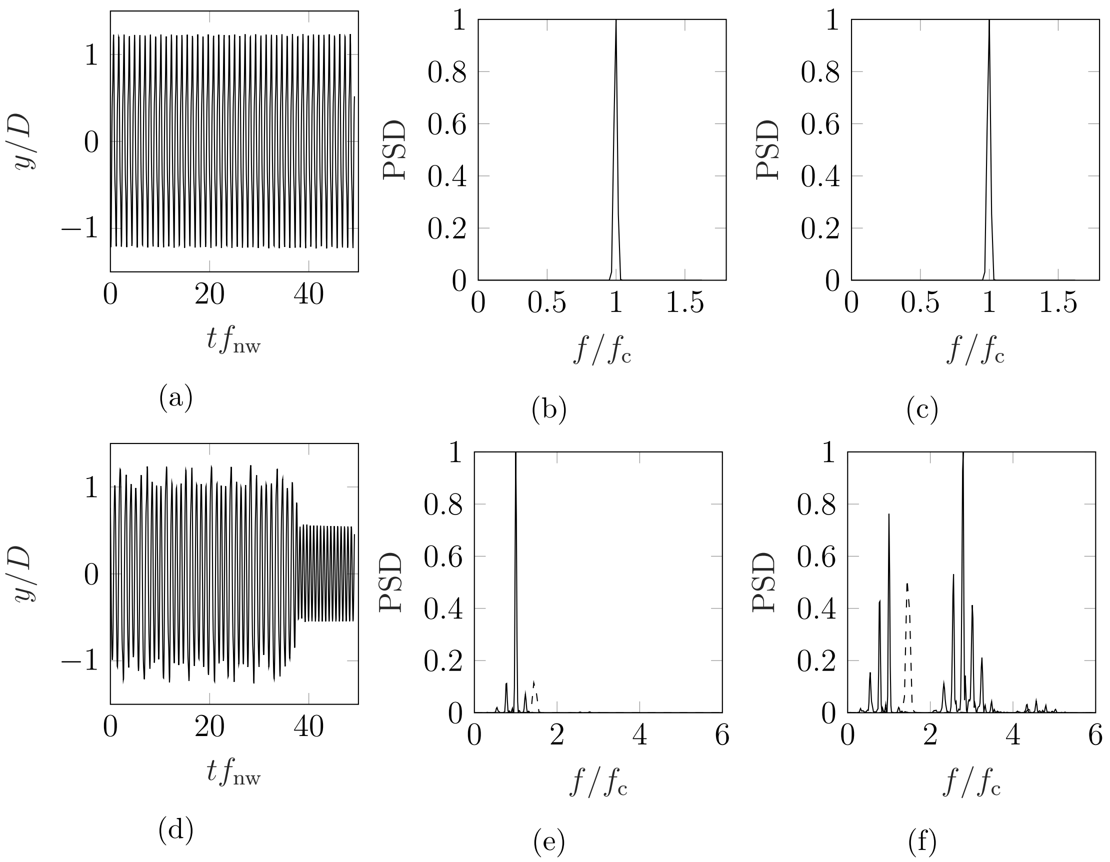

Figure 7.12: Example of an unexpected high- to low-response transition. $C_{\mathrm{F}} = 1.4$ (a,b,c) and $C_{\mathrm{F}} = 1.2$ (d,e,f) at $U_{\mathrm{r}} = 6.69$. Crosflow motion history (a,d). Crossflow frequency spectra (b,e). Lift force spectra (c,f). Dashed lines in e) and f) correspond to the low-response state

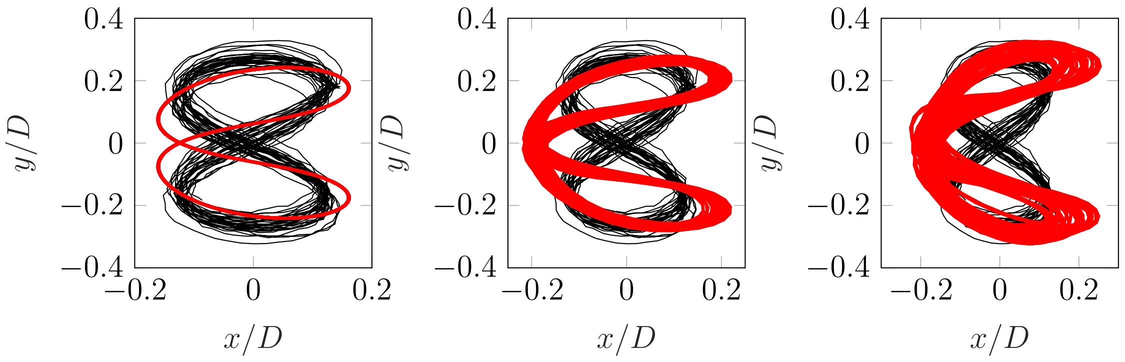

(a) $C_{\mathrm{F}} = 1$ (b) $C_{\mathrm{F}} = 1.2$ (c) $C_{\mathrm{F}} = 1.4$

Figure 7.13: Numerical (red) and experimental (black) trajectories at $U_{\mathrm{r}} = 2.95$

showed best performance in terms of amplitudes and oscillation frequencies. The rest of the cylinder trajectories alongside relevant statistics can be found in Appendix D.1.3. Figure 7.13 shows that, at the lowest inflow velocity, the $C_{\mathrm{F}} = 1$ case had the highest accuracy in terms of trajectory shape compared to higher C_{F} cases. A similar frequency content was observed across C_{F}. Thus, differences in

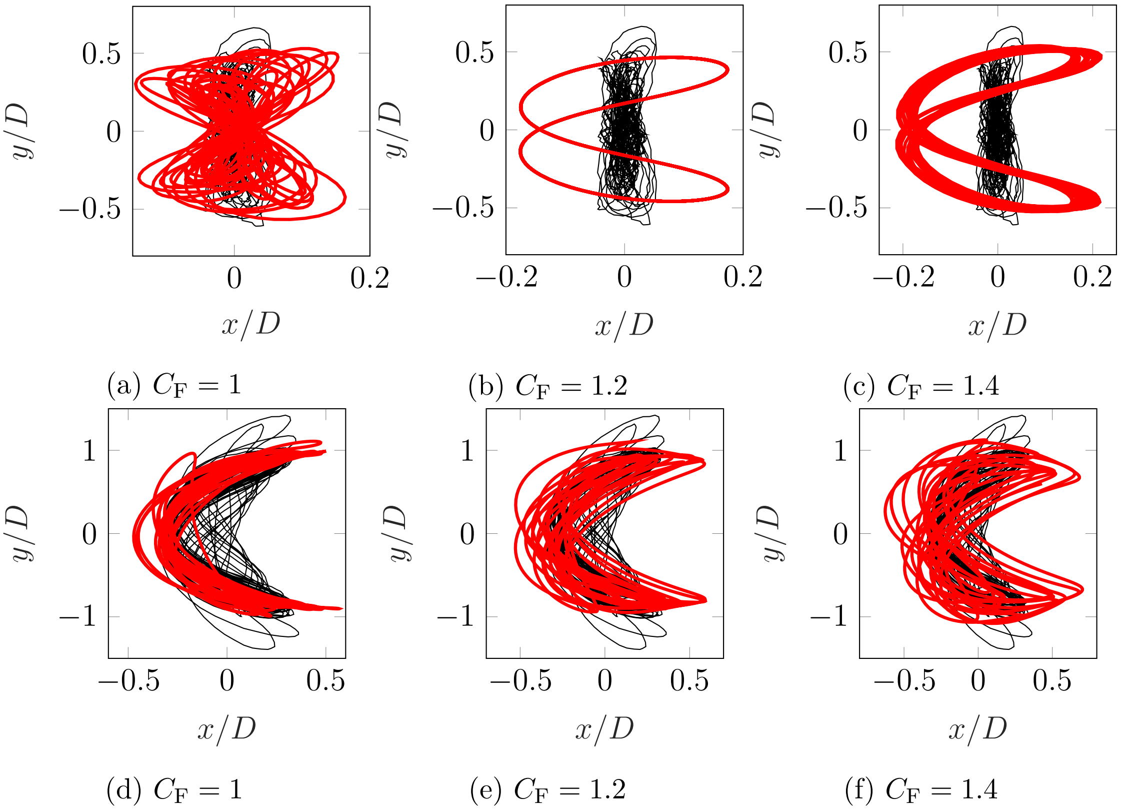

(a) $C_{\mathrm{F}} = 1$ (b) $C_{\mathrm{F}} = 1.2$ (c) $C_{\mathrm{F}} = 1.4$

(d) $C_{\mathrm{F}} = 1$ (e) $C_{\mathrm{F}} = 1.2$ (f) $C_{\mathrm{F}} = 1.4$

Figure 7.14: Initial branch. Numerical (red) and experimental (black) trajectories. $U_{\mathrm{r}} = 3.76$ (a,b,c). $U_{\mathrm{r}} = 4.55$ (d,e,f)

the trajectory shape are attributed to changes in the response amplitude (specially in the streamwise direction) as C_{F} increased. The highly modulated experimental response at $U_{\mathrm{r}} = 3.76$ was partially captured by the $C_{\mathrm{F}} = 1$ case. At higher C_{F}, the cylinder trajectory became highly regular with a streamwise amplitude more than two times its experimental counterpart. At the end of the initial branch ($U_{\mathrm{r}} = 4.55$), the modulation of the streamwise motion increased alongside C_{F}. Still, good agreement in terms of main trajectory motion was achieved, specially for the $C_{\mathrm{F}} = 1$ and $C_{\mathrm{F}} = 1.2$ cases. Within the upper branch at $U_{\mathrm{r}} = 5.21$ and $U_{\mathrm{r}} = 6$, the cylinder trajectory followed the experimental response with a higher streamwise modulation as C_{F} increased. This streamwise variability is associated with the presence of a low-frequency response ($\approx 0.17 f_{\mathrm{nw}}$) across the simulation time. At the maximum experimental cylinder response ($U_{\mathrm{r}} = 7.42$), there are significant differences in terms of the trajectory shape for all C_{F}. The high-response trajectory of the $C_{\mathrm{F}} = 1.4$ case deviates from the first-order sinusoidal function (Section 6.3.1) used to fit the experimental data. At the maximum tested flow velocity, the $C_{\mathrm{F}} = 1.4$ case maintained its trajectory shape even though the pivoted cylinder entered its transition phase, characterised by an important decrement in the streamwise motion.

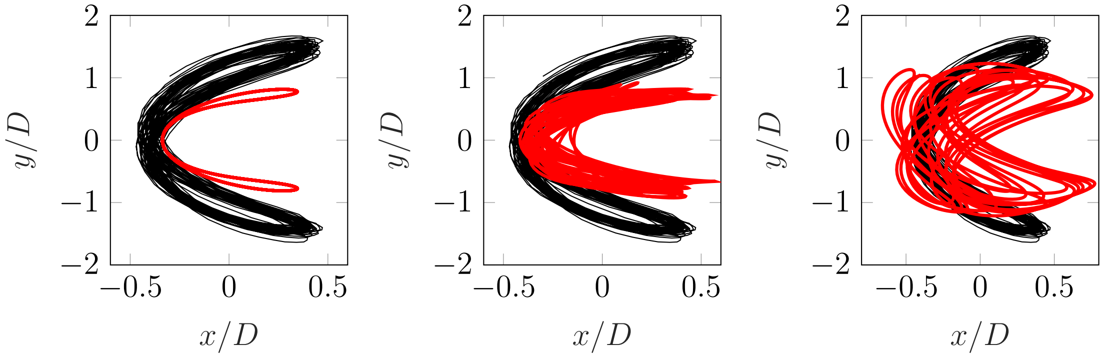

(a) $C_{\mathrm{F}} = 1$ (b) $C_{\mathrm{F}} = 1.2$ (c) $C_{\mathrm{F}} = 1.4$

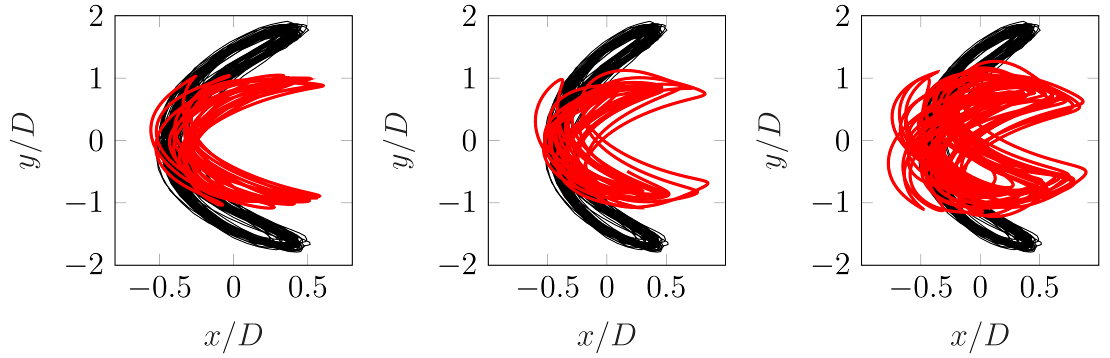

(d) $C_{\mathrm{F}} = 1$ (e) $C_{\mathrm{F}} = 1.2$ (f) $C_{\mathrm{F}} = 1.4$

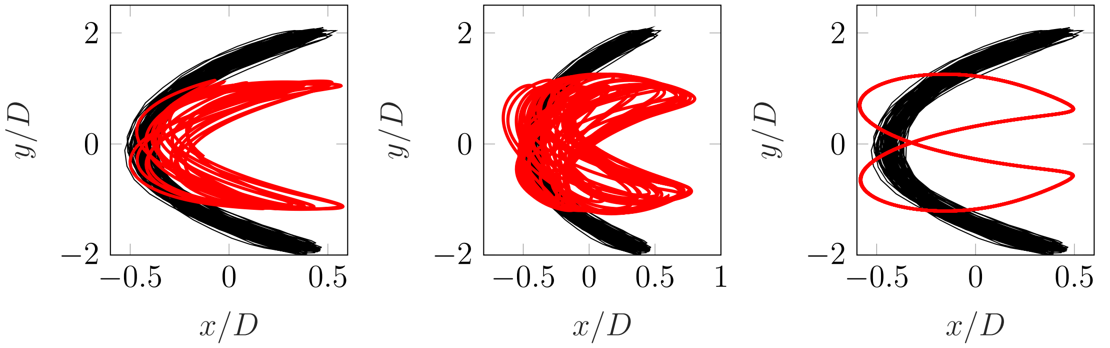

(g) $C_{\mathrm{F}} = 1$ (h) $C_{\mathrm{F}} = 1.2$ (i) $C_{\mathrm{F}} = 1.4$

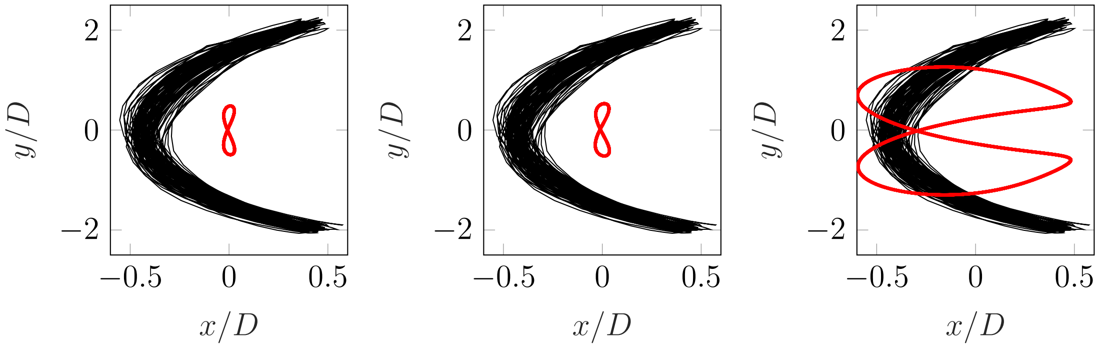

(j) $C_{\mathrm{F}} = 1$ (k) $C_{\mathrm{F}} = 1.2$ (l) $C_{\mathrm{F}} = 1.4$

Figure 7.15: Upper branch. Numerical (red) and experimental (black) trajectories. $U_{\mathrm{r}} = 5.21$ (a,b,c). $U_{\mathrm{r}} = 6$ (d,e,f). $U_{\mathrm{r}} = 6.69$ (g,h,i). $U_{\mathrm{r}} = 7.42$ (j,k,l)

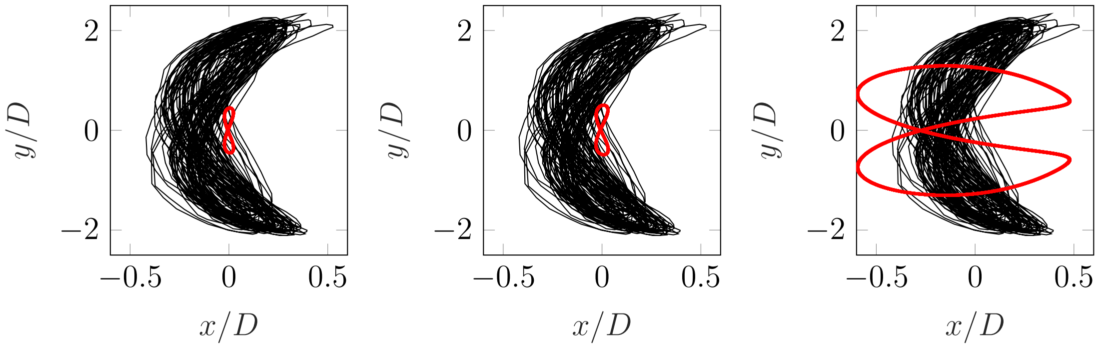

(a) $C_{\mathrm{F}} = 1$ (b) $C_{\mathrm{F}} = 1.2$ (c) $C_{\mathrm{F}} = 1.4$

Figure 7.16: Transition. Numerical (red) and experimental (black) trajectories at $U_{\mathrm{r}} = 8.29$

7.5 Conclusions

This chapter analyses the capabilities and accuracy of two-dimensional RANS models to simulate the response of a pivoted cylinder subjected to VIV. The experimental conditions of the pivoted cylinder in Chapter 6 were used as input for the numerical model. The SST $k - \omega$ turbulence model with the Runge-Kutta fourth order was implemented in Ansys Fluent, alongside a User Defined Function to account for the fluid-structure coupling mechanism. The numerical model's prediction capabilities were first assessed by simulating a low mass-damping two degree-of-freedom cylinder [41], achieving good accuracy across tested flow velocities. Then, the numerical model was used to study the influence of the inflow conditions on the cylinder motion. The cylinder response varied between a low- and high-response state depending on the initial inflow conditions. The transition between states depended on the acceleration time, while the conditions of the initial phase (velocity and time) significantly influenced the minimum acceleration time needed to trigger a high-response state. Specifically, the acceleration time was reduced up to four times when the initial phase allowed the forces around the cylinder to reach an oscillatory steady state.

After considering the initial inflow conditions, time step, and mesh resolution, the numerical model simulated the pivoted cylinder's experimental conditions described in Chapter 6. The most significant results were obtained by considering $C_{\mathrm{F}} \geq 1$. Before the pivoted cylinder reached its maximum response, the numerical model properly captured the main oscillation frequency while it overestimated the maximum streamwise amplitude. The model showed good agreement in terms of maximum crossflow amplitude within the initial branch. At higher reduced velocities, the numerical model could not sustain the upward trend of the experimental crossflow amplitude, reaching maximum values that were on average 40% lower than its experimental counterpart. After the pivoted cylinder achieved its maximum response, only the $C_{\mathrm{F}} = 1.4$ case maintained its high-amplitude response with a significantly different trajectory shape compared to the experimental crescent-shape motion. This different trajectory was maintained at the maximum tested flow velocity even though the pivoted cylinder entered its transition phase, characterised by an important decrement in the streamwise motion. The main oscillation frequency for the $C_{\mathrm{F}} = 1.4$ case was the only parameter that was properly captured throughout the tested flow velocities. These results showed that, despite its good agreement with low mass-damping cylinders [41], the numerical model with the three-dimensional factor was insufficient to account for the characteristic spanwise variability of the pivoted cylinder. Moreover, the numerical model was susceptible to unexpected transitions from a high- to a low-response state in cases of multi-frequency lift forces. These transitions were not observed in the experimental results, indicating an inherent instability of the numerical model. Additional research is needed to understand the spanwise cylinder-wake dynamics of the pivoted cylinder, especially related to its synchronisation-desynchronisation process, to improve the prediction capabilities of two-dimensional models. As an alternative, three-dimensional models directly account for the spanwise dynamics and may reduce the stability issues if a multi-frequency lift force diminishes its dominance along the cylinder span. Still, there are important limitations in terms of the computational power required to simulate the full three-dimensional fluid-structure interactions in engineering applications.

Chapter 8

Conclusions and Recommendations

8.1 Conclusions

This thesis analyses the experimental case of a pivoted cylinder subjected to VIV and its numerical representation using two-dimensional RANS models. The wake and cylinder motion were measured using Particle Image Velocimetry (PIV) and image-based tracking techniques. The wake dynamics, emphasising its variability along the structural span, and the cylinder response were analysed across a range of open-channel flow velocities. A two-dimensional model was developed based on the experimental conditions and the pivoted configuration. The numerical model's limitations, capabilities, and accuracy were evaluated by comparing its cylinder responses and oscillation frequencies with the experimental results. An initial experiment related to a bottom-fixed cylinder subjected to VIV was conducted. Its main goal was to acquire experience with the experimental equipment, calibration system, and data analysis. Moreover, the variable amplitude along the bottom-fixed cylinder span provided important insights in preparation for the pivoted cylinder case. The nature of this research project led to significant results that, although not directly related to the main objective of this thesis, are included due to their novelty and importance to VIV. The main conclusions are presented in the same order as the body of this thesis.

The experimental case of a bottom-fixed cylinder subjected to a range of flow velocities shed light on the motion and spanwise dynamics of a complex VIV configuration, characterised by a multi-degree-of-freedom and variable-amplitude response. The results showed a highly modulated motion, from which the Proper Orthogonal Decomposition successfully uncovered dominant elliptical-type trajectories at the maximum cylinder response. This trajectory shape maintained its dominance at higher flow velocities except at its maximum recorded value, where a combination between an eight-type and an elliptical-type was observed. This characteristic pattern was explained by the energetic relationship between the main streamwise frequency of its second spatial mode and its first harmonic. The wake analysis along the span of the cylinder showed that the maximum response is achieved when the cylinder motion and vortex shedding frequencies are equal (i.e. synchronised) to the natural frequency of the structure measured in still water, and when this equivalence is preserved along the span of the cylinder. As the flow velocity increases, the cylinder displacement near its fixed end cannot reach the needed increment in acceleration to sustain a synchronised condition, and desynchronisation occurs. This process is followed by a reduction in the spanwise vortex strength and a decrement in the maximum cylinder amplitude. As the desynchronised region develops, the spanwise vortex strength further decreases alongside the maximum amplitude. Changes in the wake dynamics showed a transition from a 2S-2P dual-mode configuration at the highest cylinder response to a predominant 2S mode at the highest tested flow velocity.

The experimental case of a pivoted cylinder subjected to a range of flow velocities had a characteristic high streamwise amplitude, observed in previous low mass-damping two-degree-of-freedom cylinders [21, 41]. The maximum crossflow amplitude showed three response regions across tested flow velocities: a streamwise dominant, initial, and upper branch. Only the transition to an apparent lower branch could be captured due to limitations on the maximum tested flow velocity. The cylinder trajectory varied from an eight-type at the lowest inflow velocity to a crescent-type at the initial and upper branch. Wake measurements closer to the water surface had a bigger recirculation region, higher momentum transference, broader wake width, and higher vortex strength in the upper branch compared to regions at lower water depths. These differences can not be fully explained by the linear variability of the cylinder response along its span. Other influential factors, such as spanwise vortex correlation and free-surface effects, could play a significant role in the spanwise wake dynamics. An analysis of the vortex shedding frequency along the cylinder span showed a complex behaviour with significant differences from the bottom-fixed cylinder case. The streamwise motion was strong enough to dominate the vortex shedding frequency in specific spanwise regions throughout the upper branch. Moreover, the desynchronisation process started at the water surface and seemed to progress towards the flume bed. Still, similar to the bottom-fixed cylinder case, the maximum response is achieved when the cylinder motion and vortex shedding frequencies are equal (i.e. synchronised) to the natural frequency of the structure measured in still water, and when this equivalence is preserved along the span of the cylinder.

The two-dimensional RANS model was developed based on the experimental conditions of the pivoted cylinder. Before analysing its accuracy and applicability, the model was first validated by simulating an experimental low mass-damping two-degree-of-freedom cylinder [41]. A novel result from this process was the systematic study of the inflow velocity conditions on the cylinder response and oscillation frequency. The cylinder response varied between a low- and high-response state, closer to the experimental results. The transition between states depended on the acceleration time, while the conditions of the initial phase (inflow velocity and time) significantly influenced the minimum acceleration time needed to trigger a high-response state. These results were used for the pivoted cylinder model to ensure high responses and significantly reduce the total numerical time per simulation. The pivoted configuration was modelled using the experimental characteristics of Chapter 6 and by using a three-dimensional factor ($0.6 \leq C_{\mathrm{F}} \leq 1.4$) that accounts for the three-dimensional effects of the fluid force on the pivoted cylinder. The highest accuracy of the numerical model was achieved by considering $C_{\mathrm{F}} \geq 1$. Nevertheless, the simulations could not fully predict the upper and lower branch associated with the highest experimental responses. Moreover, the numerical model was susceptible to unexpected transitions from a high- to a low-response state not observed in the experiments. Despite its good agreement with low mass-damping two degree-of-freedom cylinders [41], the numerical model with the three-dimensional force correction factor was insufficient to account for the characteristic spanwise variability of the pivoted cylinder. Additional research is needed to understand the spanwise cylinder-wake dynamics of the pivoted cylinder, especially related to its synchronisation-desynchronisation process, to improve the prediction capabilities of two-dimensional numerical models.

8.2 Recommendations for future work

The author identified several gaps and recommendations for future work.

- The author measured the wake region at different two-dimensional planes using Particle Image Velocimetry. Three-dimensional measurements seem to be a logical step towards the complete capture of the spanwise cylinder-wake dynamics. This information can be used to gain insight into the physical understanding of VIV, which, in turn, can be used to compare or calibrate future numerical models.

- The experiments were performed at low Reynolds numbers ($4.5 \times 10^2 \leqslant \mathrm{R_e} \leqslant 1 \times 10^3$ for the bottom-fixed and $2.5 \times 10^3 \leq R_{\mathrm{e}} \leq 5.8 \times 10^3$ for the pivoted cylinder, respectively). Experiments or numerical simulations at high

Reynolds numbers could provide practical information to a diverse range of engineering problems.

- Parameters extracted from time-averaged and root-mean-square statistics were used to characterise the wake behind a cylinder subjected to VIV. Other characterisations based on coherent vortex patterns extracted through the Proper Orthogonal Decomposition could provide important insights into reduced-order modelling.

- The current two-dimensional representation of the pivoted cylinder case can be further improved as more knowledge is gained. Improvements in the equations of motion (e.g. three-dimensional force correction dependent on the reduced velocity) can be developed as the cylinder's spanwise wake dynamics are better understood. Still, there is the possibility that these two-dimensional representations could never reach an acceptable level of prediction. As an alternative, three-dimensional models can simulate the spanwise wake dynamics (to an unknown degree of accuracy) with the potential to capture the main features of VIV. Further research needs to be conducted to determine the accuracy of three-dimensional models. The current limitations are due to the computational power needed to simulate complex VIV cases in engineering applications.

Appendix A

Image-based measurements

The remote and non-contact nature of image-based measurement techniques offer an attractive alternative to traditional methods, such as accelerometers, strain gauges, and Laser Doppler vibrometers. Their main advantage is evidenced in structures with difficult access or when simultaneous multi-point or full-field measurements are required. In the context of engineering, image-based techniques have been used to measure structural vibrations, damage detection, crack growth monitoring, fluid-structure interactions, among others [66]. This thesis employs different image-based tracking techniques to extract velocity fields and structural motions from images. Two tracking techniques are presented in this section, digital image correlation (DIC) via Fourier transform and a solution of the optical flow equations by means of the Lucas-Kanade method. Both techniques are compared against a high-precision motion tracking system under changes in image resolution, target motion and sampling frequency. The results showed that the Lucas-Kanade technique achieved a higher accuracy when it is able to track the target. Nevertheless, it has an important dependency on the relative pixel value (intensity gradients) of the initial target point, which difficult the achievement of its higher accuracy. This dependency was minimised through the implementation of the Forward-Backward tracking failure technique [43] without depending on additional external measurements.

A.1 Digital Image Correlation

Digital Image Correlation (DIC) uses correlation functions to measure the similarity between a region around a target (called interrogation window or template) and an image. A correlation map is built by calculating the correlation function as the template shifts around the image. The position that corresponds to the maximum value of the correlation map is used to locate the template on the image. Consider two consecutive images with intensity values $\boldsymbol{I}(\boldsymbol{x})$ and $\boldsymbol{J}(\boldsymbol{x})$, respectively. Given an initial target position $\boldsymbol{u}$ and a template size $\boldsymbol{w} = [w_x, w_y]^T$ around $\boldsymbol{u}$, the discrete correlation function is given by

$$r(\boldsymbol{d}) = \sum_{\boldsymbol{x}=\boldsymbol{u}-\boldsymbol{w}/2}^{\boldsymbol{x}=\boldsymbol{u}+\boldsymbol{w}/2} (\boldsymbol{I}(\boldsymbol{x})\boldsymbol{J}(\boldsymbol{x}+\boldsymbol{d})) \tag{A.1}$$

where $\boldsymbol{d} = [d_x, d_y]^T$ is a vector of pixel displacement between frames. Eq. A.1 is applied at every $\boldsymbol{d}$ within a region W, resulting in a correlation map $\boldsymbol{R}(\boldsymbol{d})$. An efficient approach to calculate the correlation function is through the Fast Fourier transform, where the Fourier transform of $\boldsymbol{I}$ and $\boldsymbol{J}$ are defined as $\mathcal{F}(\boldsymbol{I})$ and $\mathcal{F}(\boldsymbol{J})$, respectively. Under this approach, the correlation map is expressed as

$$\boldsymbol{R}(\boldsymbol{d}) = \mathcal{F}^{-1}(\mathcal{F}(\boldsymbol{I}(\boldsymbol{x}))\mathcal{F}^{*}(\boldsymbol{J}(\boldsymbol{x}+\boldsymbol{d}))) \tag{A.2}$$

where $\mathcal{F}^{*}$ is the complex conjugate of its Fourier transform, and $\mathcal{F}^{-1}$ is the inverse Fourier transform. The integer pixel position of the maximum correlation map corresponds to the most probable displacement of the template. The accuracy of this result can be improved through subpixel registration, where the information around the maximum correlation value is used to find its true maxima. The Gaussian subpixel method has been shown to obtain satisfactory results in PIV [58] and structural tracking motion [66]. This technique fits the spatial distribution of correlations around the peak using a Gaussian function. The target position corresponds to the subpixel location of the Gaussian function maximum value.

Davis 8.3 uses DIC with the Gaussian subpixel method to estimate the flow velocity field from raw flow images (Chapter 3.2.3). Consider two consecutive flow images with high-density tracers. Each image is subdivided into templates. The templates of the first image are correlated with their corresponding templates of the second image. A correlation map per template is built. The position of the correlation map maximum value corresponds to the most probable displacement of the tracers between images. This position is improved using the Gaussian subpixel method. The velocity field is then calculated as the ratio between the local flow displacement and the acquisition time between images.

A.2 Lucas-Kanade technique

The Lucas-Kanade technique [60] estimates the position of a target using the intensity differences between two consecutive images. An in-depth description can be found in [8]. Consider two consecutive images with intensity values $\boldsymbol{I}(\boldsymbol{x})$ and $\boldsymbol{J}(\boldsymbol{x})$, respectively. Considering an initial target located at $\boldsymbol{u} = [x_0, y_0]^T$, the goal is to estimate its location in the second image $[\boldsymbol{u}+\boldsymbol{d}]^T$, such as its intensity values around $\boldsymbol{u} = [x_0, y_0]^T$ reaches a minimum difference. This procedure assumes small displacements and minor variations of the target intensity values between frames. Moreover, the implementation of the Lucas-Kanade technique accounts for the following affine transformation of the target intensity values

$$\boldsymbol{A} = \begin{pmatrix} 1 + d_{xx} & d_{xy} \\ d_{yx} & 1 + d_{yy} \end{pmatrix} \tag{A.3}$$

where d_{xx}, d_{xy}, d_{yx} and d_{yy} characterise the affine deformation of the interrogation window $\boldsymbol{W}$ of size $\boldsymbol{w} = [2w_x + 1, 2w_y + 1]$ around $\boldsymbol{u}$. Approximating the target displacement by a first order Taylor series and assuming small variations of the target intensity values between frames, the displacement $\boldsymbol{d}$ and matrix $\boldsymbol{A}$ are obtained by minimising the following function

$$\epsilon(\boldsymbol{d}, \boldsymbol{A}) = \sum_{\boldsymbol{u}-\boldsymbol{w}/2}^{\boldsymbol{u}+\boldsymbol{w}/2} (\boldsymbol{I}(\boldsymbol{x}) - \boldsymbol{J}(\boldsymbol{A}\boldsymbol{x} + \boldsymbol{d}))^2 \tag{A.4}$$

Equation A.4 is minimised following a Newton-Rapson iteration approach. The pixel target position is improved using a bilinear subpixel interpolation. Moreover, a pyramidal scheme is implemented to overcome large displacements between frames. The original image is reduced 2^N times, where N is the pyramid level previously selected (a value of four is recommended [8]). The Lucas-Kanade technique is applied at the lowest pyramid level (lowest image resolution) and the results are used as an initial guess to estimate the target position at a superior pyramid level.

A.3 DIC vs Lucas-Kanade

This section compares the accuracy and capabilities of the DIC-based and Lucas-Kanade technique against a high-precision motion tracking system. The comparison was performed under changes in image resolution, target motion and sampling frequency.

A.3.1 Experimental setup

A shaker model APS 400 Electro-Seis was setup to produce a one-dimensional oscillatory motion of constant amplitude. Two systems were used to capture the shaker motion: a high-resolution CODA CX1 system, used as a benchmark, and a PS3 Eye camera. The CODA system had two self-calibrated infra-red LED scanners capable of tracking a marker at 800 Hz and at a three-metre distance with 0.05 mm accuracy. On the other hand, the PS3 Eye camera recorded 8-bit uncompressed images with a resolution of 640x480 pixels and an acquisition frequency of 75 Hz. Figure A.1 shows the experimental setup. The CODA system was located two meters from

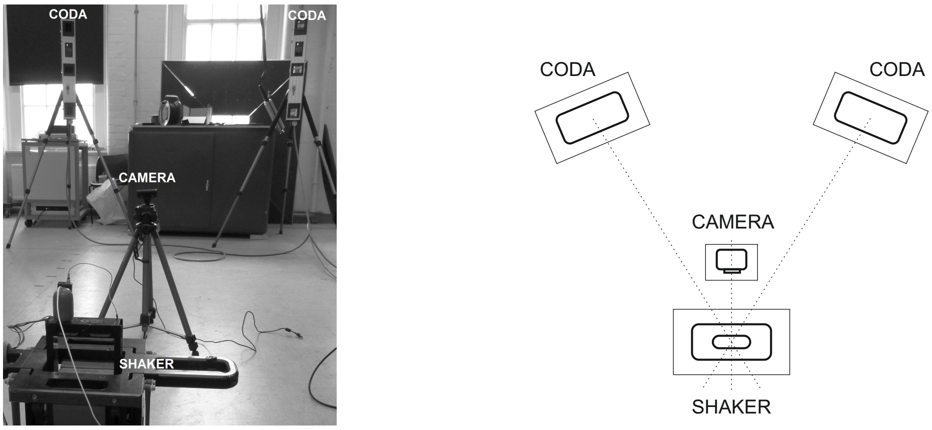

(a) (b)

Figure A.1: Experimental setup of a shaker recorded at three oscillatory frequencies

the shaker, whereas the PS3 Eye camera was placed at 0.5 meters. A 1% distortion was expected from the PS3 Eye camera, considering a field-of-view of 75 and a focal length of 2.1.

The shaker movement was recorded at three different frequencies: 1 Hz, 3 Hz and 4 Hz. The amplitude associated with these frequencies were 120.2 mm, 45.6 mm and 25.4 mm, respectively. The CODA system tracked the shaker motion at 200 Hz. Simultaneously but unsynchronised, recordings using the PS3 Eye camera were taken at 75 Hz for 40 seconds. A calibration process was applied to the PS3 Eye camera measurements to establish a correspondence between Pixel and real-world coordinates. Details of this process can be found in Chapter 3.3.2. Differences between recording systems were addressed by normalising the signals of the CODA system. Firstly, a spline cubic interpolation was used to sub-sample the CODA signal and match the sampling frequency of the PS3 Eye camera. Secondly, the minimum root-mean-square (RMS) between the CODA signal and both tracking systems was used to align their corresponding initial recording time. Finally, all signals are normalised by their corresponding mean amplitude, followed by the subtraction of their mean position. The RMS of the normalised signals between a tracking technique and CODA system was used as an error measurement throughout this experiment.

A.3.2 Sensitivity Analysis

DIC: Template size and subpixel method

The effects of the interrogation window size on the tracking technique accuracy were analysed using different square-shape templates with width of 30 to 100 pixels and 10-pixel increment. The influence of the centroid, parabolic and Gaussian subpixel techniques at each tested template size were also investigated. As described in Sec-

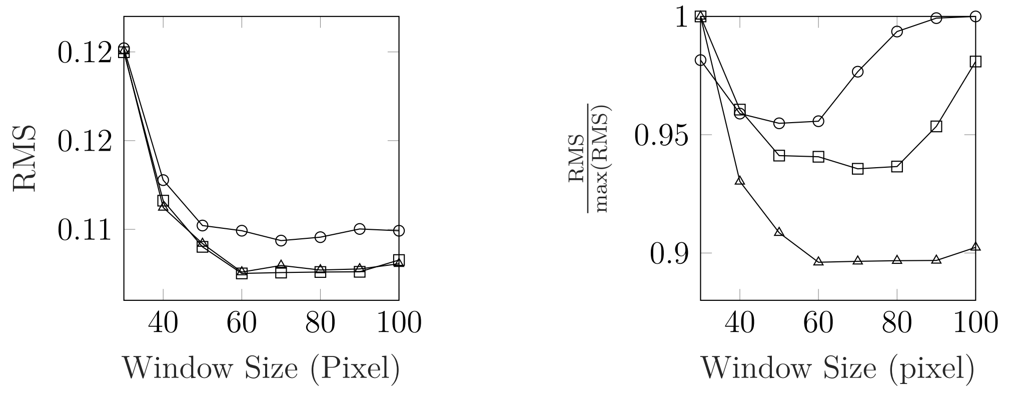

(a) ○: centroid. □: Gaussian. △: Parabolic

(b) ○: 1 Hz. □: 3 Hz. △: 4 Hz

Figure A.2: DIC-based technique sensitivity analysis. a) Subpixel method. b) Interrogation window size

tion A.1, subpixel accuracy is reached when the information around the maximum correlation value is used to find its true maxima. These methods commonly use the correlation values of nearby pixels to calculate the centroid (centroid method), fit a parabolic function (parabolic method) or fit a Gaussian function (Gaussian method). Figure A.2a shows the RMS for the 4 Hz shaker frequency as a function of the interrogation window size. The centroid method has the highest RMS across interrogation window sizes. On the other hand, there are no significant differences between the parabolic and Gaussian methods. Figure A.2b shows the RMS as a percentage of its maximum value at different shaker frequencies. A maximum 10% RMS difference was observed across tested cases, showing the stability of the DIC technique under changes in shaker frequency (i.e., target velocity). Still, there is a clear region of interrogation window sizes that maximise the technique accuracy.

Lucas-Kanade: Template size and initial point selection

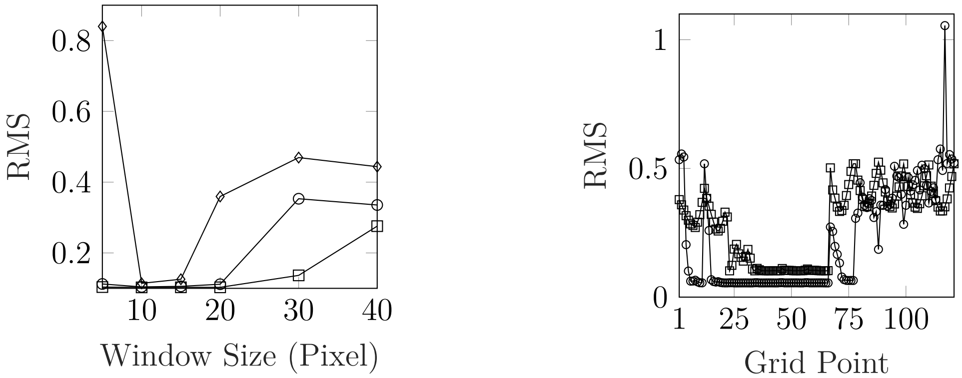

(a) Percentiles. ○: 30th. □: 60th. △: 90th

(b) ○: 1 Hz. □: 4 Hz

Figure A.3: Lucas-Kanade technique sensitivity analysis. a) Interrogation window size. b) Initial point selection

A square grid of 121 initial target points with one-pixel separation was placed on the shaker. The Lucas-Kanade technique was applied to each grid point using square templates with width from five to 40 pixels. Figure A.3a shows their corresponding RMS values grouped in their 30th, 60th, and 90th percentiles. At least 30% of initial target points reached the smallest RMS value of all grid points when a 20-pixel interrogation window size was used. The RMS values related to the 90th percentile shows that the tracking technique accuracy is maximised with an interrogation window size of 10 pixels. Smaller interrogation window sizes rely on a small amount of information to accurately track the movement of the shaker, which makes the tracking technique more sensitive. On the other hand, larger interrogation windows sizes produce excessive smoothing in the motion estimation, and the error increases [8]. Figure A.3b shows all RMS values from the 121 initial grid points at two shaker frequencies. A suboptimal template of 30 pixels was used to better illustrate the differences. A low RMS region was observed between grid points 25 to 65, characterised for its high intensity gradient values. Except for a few grid points, the RMS decreases with the shaker frequency, explained by the relationship between the camera exposure time and the target displacement between frames. Considering a constant exposure time, higher target displacements reduce the image intensity gradients and, as a consequence, lower the tracking technique accuracy. Overall, Figure A.3b shows that the Lucas-Kanade technique is highly dependent on the initial target point selection.

A.3.3 Changes in acquisition frequency

Changes in the camera acquisition frequency were simulated by resampling the original image dataset. The new acquisition frequencies f'_{camera} of these sets were equal to the PS3 Eye camera acquisition frequency (75 Hz) divided by integer factor. After a series of tests above the Nyquist criteria, a lower f'_{camera} limit for the shaker motion at 1 Hz, 3 Hz and 4 Hz were 12.5 Hz, 15 Hz, and 18.75 Hz, respectively. The CODA signal was also resampled to match f'_{camera}.

Figures A.4a, A.4b and A.4c shows the RMS value of the DIC-based and Lucas-Kanade technique at different sampling frequencies. A general increment in RMS at lower sampling frequencies can be explained by a reduction of the image intensity gradients as the target displacement increases between consecutive images. The maximum increment in RMS across f'_{camera} was 7.9% and 12.3% for the Lucas-Kanade and DIC-based technique, respectively. The Lucas-Kanade technique showed a higher accuracy of 5.6% over the DIC-based algorithm at the highest shaker frequency. Figure A.4 shows the difference in RMS between two Lucas-Kanade grid point signals sampled at 75 Hz and 18.75 Hz. This comparison was repeated for

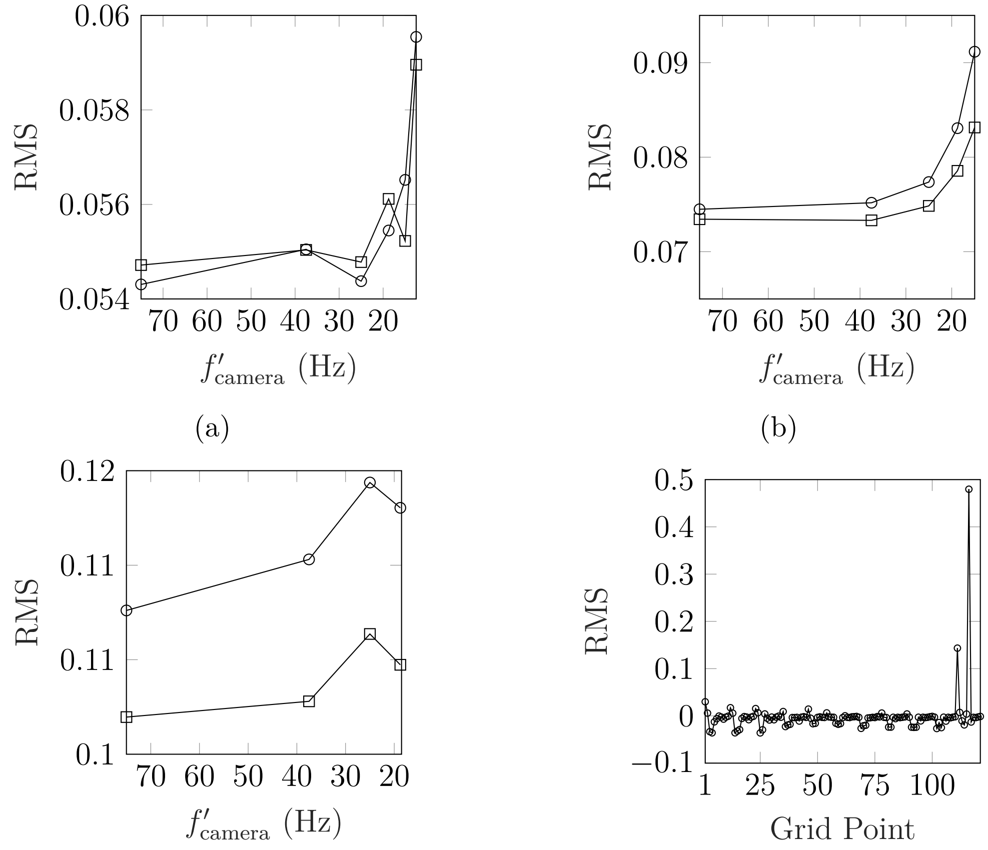

(a) (b)

(c) (d)

Figure A.4: Camera acquisition frequency vs tracking accuracy. ○: DIC-based. □: Lucas-Kanade. a) 1 Hz. b) 3 Hz. c) 4 Hz. d) Difference in RMS between two Lucas-Kanade grid point signals sampled at 75 Hz and 18.75 Hz

121 points arranged in a square grid as in Section A.3.2. Except for two outliers, decrements in f'_{camera} do not increase the Lucas-Kanade dependency on the initial target point selection.

A.3.4 Changes in image resolution

The original dimensions of the shaker images (640x480 pixels) were reduced up to 10 times using four different interpolation techniques: nearest (the nearest pixel from the original image is used directly), bilinear (2x2 pixel window), bicubic (4x4 pixel window) and Lanczos (downsampling filter, `https://pillow.readthedocs.io`). Then, these low-resolution images were scaled back up to the original image dimensions using the nearest interpolation technique, which preserves their image intensity gradients. Figure A.5a shows the RMS of both tracking techniques at different image resolutions. Overall, the interpolation technique does not have a significant impact on RMS. A decrement in image resolution affects the tracking techniques differently. The DIC-based technique shows an almost linear relationship

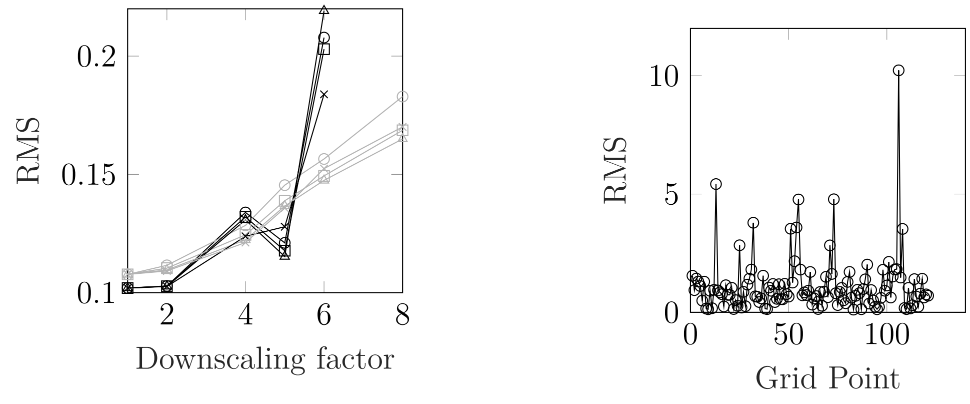

(a) ○: Bilinear. □: Bicubic. △: Lanczos. ×: Nearest

(b)

Figure A.5: Image resolution effect. 4 Hz shaker frequency. a) Downscaling factor at different interpolation techniques. Black: Lucas-Kanade. Gray: DIC-based. b) Difference in RMS between two Lucas-Kanade grid point signals obtained from the original dataset and from images downscaled five times in resolution

across the analysed range of image resolutions. In contrast, the LK technique does not show a clear pattern up to a downscaling of five. Then, there is a sudden increment in RMS for a downscaling factor of six. It seems that there are higher restrictions in terms of image intensity gradients, from which the Lucas-Kanade technique relies on, compared to the target intensity pattern used in the DIC-based technique. Analogous to Section A.3.4, Figure A.5b shows the difference in RMS between two Lucas-Kanade grid point signals obtained from the original dataset and from images downscaled five times in resolution. As expected, changes in image resolution have a significant influence on the location of the best initial target point selection.

A.3.5 Improvement to the Lucas-Kanade technique

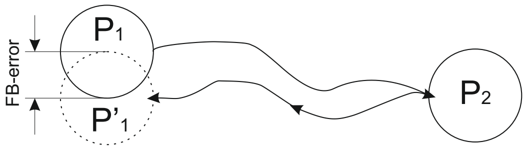

Figure A.6: Forward-Backward tracking technique sketch

As shown in previous sections, the Lucas-Kanade technique achieves an overall higher accuracy with a strong dependency on the initial target point. This last limitation was minimised through the implementation of the Forward-Backward tracking failure technique [43] without depending on additional external measurements. The Forward-Backward method is based on the fact that the tracking of an object from the spatial position P_1 to P_2 in time is equivalent to its tracking between P_2 and P_1. In an experimental setting, P_1 and the final location tracked from P_2, defined as P_1', will be different. The Euclidean difference is defined as FB-error and is used to quantify the tracking accuracy. If a cloud of points around a target is considered, it is possible to select the signals whose FB-error are in the lowest 5th percentile. The mean displacement of the selected signals is subtracted to make them coordinate independent. At each time step, the cylinder location is calculated as the median value of the selected signals.

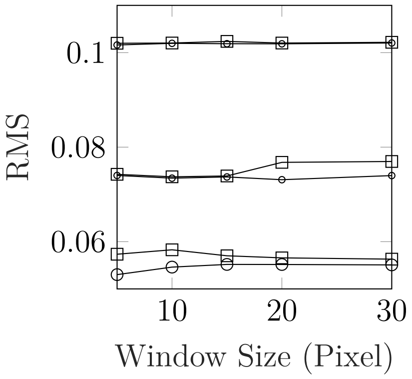

Figure A.7: Testing the Forward-Backward algorithm. Up: 1 Hz. Middle: 3 Hz. Down: 4 Hz. ○: min(RMS). □: Lucas-Kanade with Forward-Backward method

Figure A.7 compares the RMS values between the Lucas-Kanade technique using the Forward-Backward tracking algorithm and the most accurate case from Section A.3.2. The highest RMS difference across all shaker frequencies is 7.5%, showing that the Forward-Backward algorithm effectively finds the initial target points that maximise the Lucas-Kanade technique's accuracy.

The structural motion tracking performed in Chapters 5 and 6 was estimated using the Lucas-Kanade and Forward-Backward techniques. A detailed application to the experimental case of a bottom-fixed cylinder subjected to VIV can be found in Chapter 3.3.4.

Appendix B

Proper Orthogonal Decomposition

The POD is a statistical technique based on the decomposition of spatio-temporal data into a linear combination of orthonormal basis functions or POD modes ($\boldsymbol{\Phi}$) and their corresponding orthogonal temporal coefficients (α). The POD was applied to the bottom-fixed cylinder motion to uncover large-scale coherent trajectories from the modulated response (Chapter 5.3.1). A review of this technique can be found in [6, 13]. Here, a brief description of the snapshot POD method ([93]) is given in the context of cylinder displacement data [65].

The spatiotemporal cylinder position can be expressed as $\boldsymbol{x}_{\mathrm{c}}(t_{\mathrm{d}}) = (x(t_{\mathrm{d}}), y(t_{\mathrm{d}}))$, where $(t_{\mathrm{d}}) = [1, 2, ..., N]$ and N is the number of data points. The fluctuating part of the cylinder displacement $\boldsymbol{x}_{\mathrm{c}}^{'}$ is separated in k vectors of equal size $L (KL = N)$ and arranged in matrix form as

$$\boldsymbol{X} = \begin{bmatrix} x_1' & x_2' & ... & x_N' \\ y_1' & y_2' & ... & y_N' \end{bmatrix} \tag{B.1}$$

Each column in Eq. B.1 is considered a snapshot and represents the trajectory traced by the cylinder over K data points. The dimensions of the assembled matrix are $2LM\text{x}N$.

As explained before, POD decomposes the fluctuating part of the cylinder displacement into an orthonormal subspace of spatial POD modes $\boldsymbol{\Phi}_n$ and their time-dependent coefficients α_n

$$\boldsymbol{x}_{\mathrm{c}}^{'}(t_{\mathrm{d}}) = \sum_{n=1}^{N} \alpha_n(t) \boldsymbol{\Phi}_n \tag{B.2}$$

where N is the number of snapshots. POD is based on a two-point correlation tensor that finds the pairs of $\boldsymbol{\Phi}_n$ and α_n that best fit $\boldsymbol{X}$ in a least-square sense

$$\overline{\left\| \boldsymbol{X} - \sum_{n=1}^{N} \alpha_n \boldsymbol{\Phi}_n \right\|} \tag{B.3}$$

where $\|\cdot\|$ is the L$_2$-norm. Eq. B.3 is solved through the solution of the following eigenvalue problem

$$\boldsymbol{C}\boldsymbol{\Phi}_n = \lambda_n \boldsymbol{\Phi}_n \tag{B.4}$$

where $\boldsymbol{C} = \overline{\boldsymbol{X}^T\boldsymbol{X}}$ is the autocovariance matrix, and λ_n are the eigenvalues. Then, the temporal coefficients can be obtained as

$$\alpha_n = \boldsymbol{\Phi}_n^T X_n \tag{B.5}$$

The eigenvalues of the POD modes represent the contribution of mode n to the total variance of $\boldsymbol{X}$. The POD modes are arranged in descending order based on their corresponding λ_n to identify dominant patterns in the data. The relative of the i-th POD modal value is defined as

$$\varepsilon_i = \frac{\lambda_i}{\sum_{n=1}^{N} \lambda_n} \tag{B.6}$$

Considering Eq. B.2, $\boldsymbol{X}$ can be approximated to a desired degree of accuracy by using POD modes with the highest relative energy ϵ_i, where $i < N$. This low-order representation is commonly used to discover large-scale coherent patterns from a particular dataset (e.g., [11]).

Appendix C

Time-averaged flow velocity fields

The wake dynamics behind a vibrating cylinder were characterised using one vertical PIV plane across the cylinder centre and different horizontal PIV planes measured along the structural span. The time-averaged streamwise $\overline{U}$ and crossflow $\overline{V}$ velocity fields, as well as the root-mean-square (rms) of the fluctuating streamwise rms(u') and crossflow rms(v') velocities, were used to calculate several statistics, such as wake width, recirculation region, and vortex strength. Details of the experimental conditions and results can be found in Chapters 5 and 6 for the bottom-fixed and pivoted cylinders, respectively.

C.1 Bottom-fixed cylinder

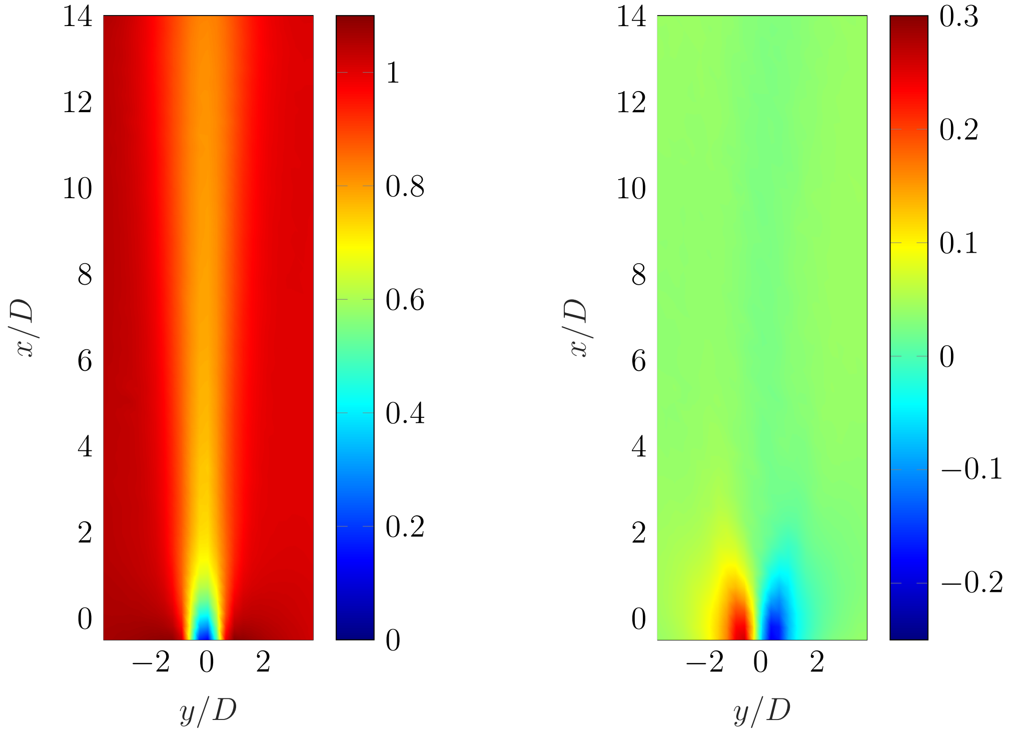

(a) $\overline{U}/U_{\mathrm{in}}$ (b) $\overline{V}/U_{\mathrm{in}}$

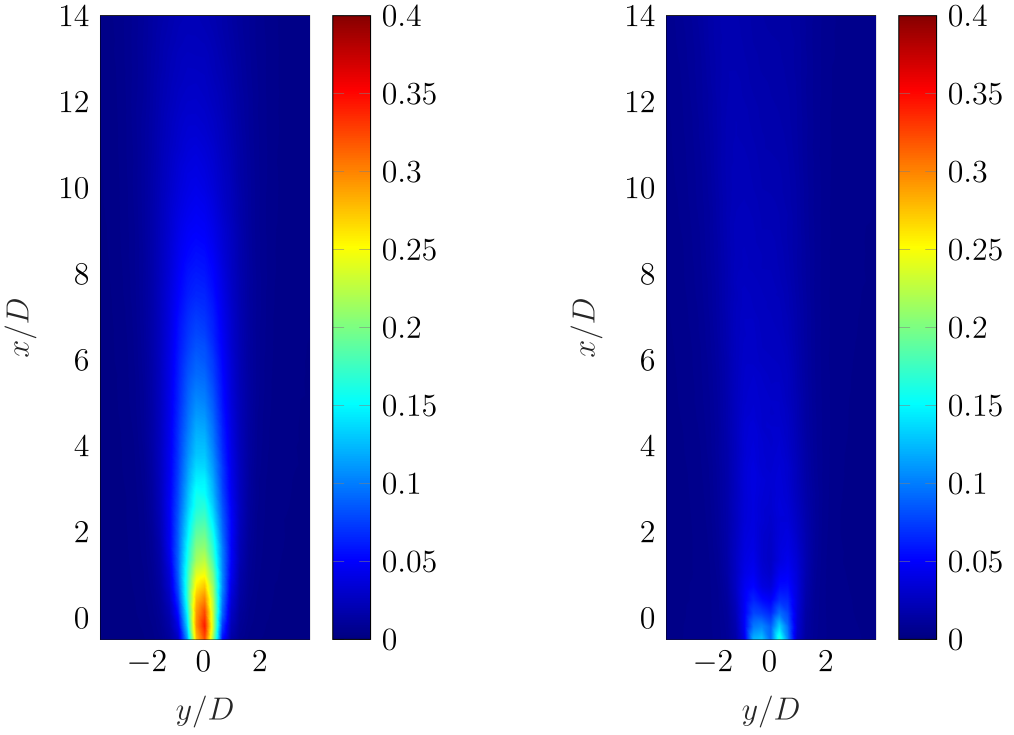

(c) $\mathrm{rms}(u')/U_{\mathrm{in}}$ (d) $\mathrm{rms}(v')/U_{\mathrm{in}}$

Figure C.1: Velocity field at $z = 20D$ and $U_{\mathrm{r}} = 4.5$. Time-averaged streamwise (a) and crossflow (b) velocity. Root-mean-square streamwise (c) and crossflow (d) velocity

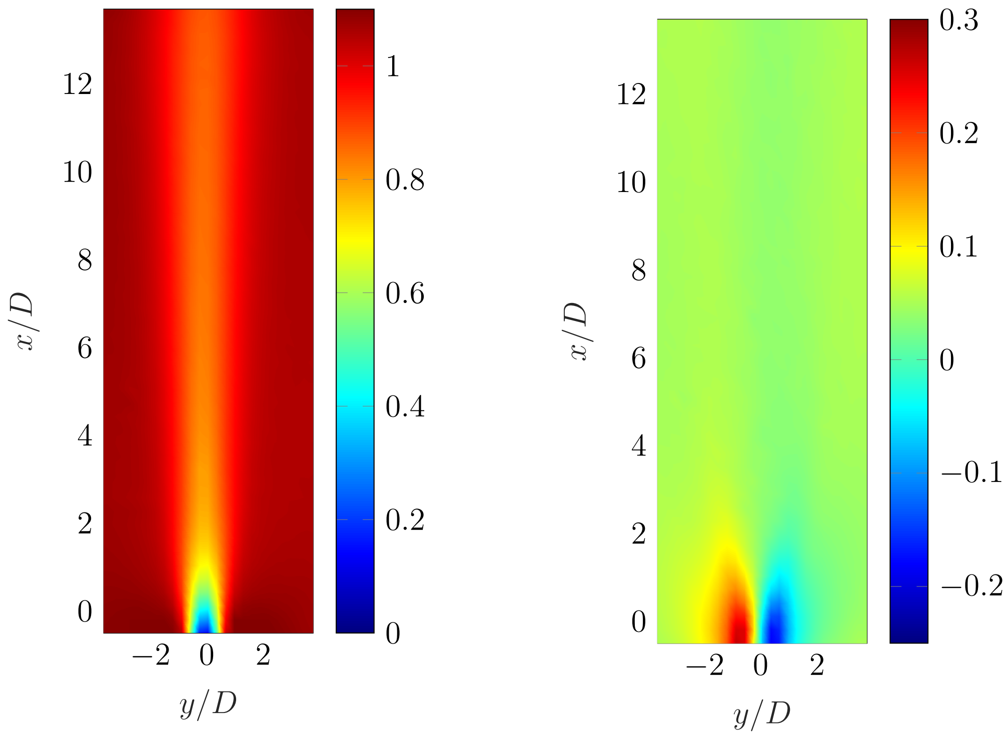

(a) $\overline{U}/U_{\text{in}}$ (b) $\overline{V}/U_{\text{in}}$

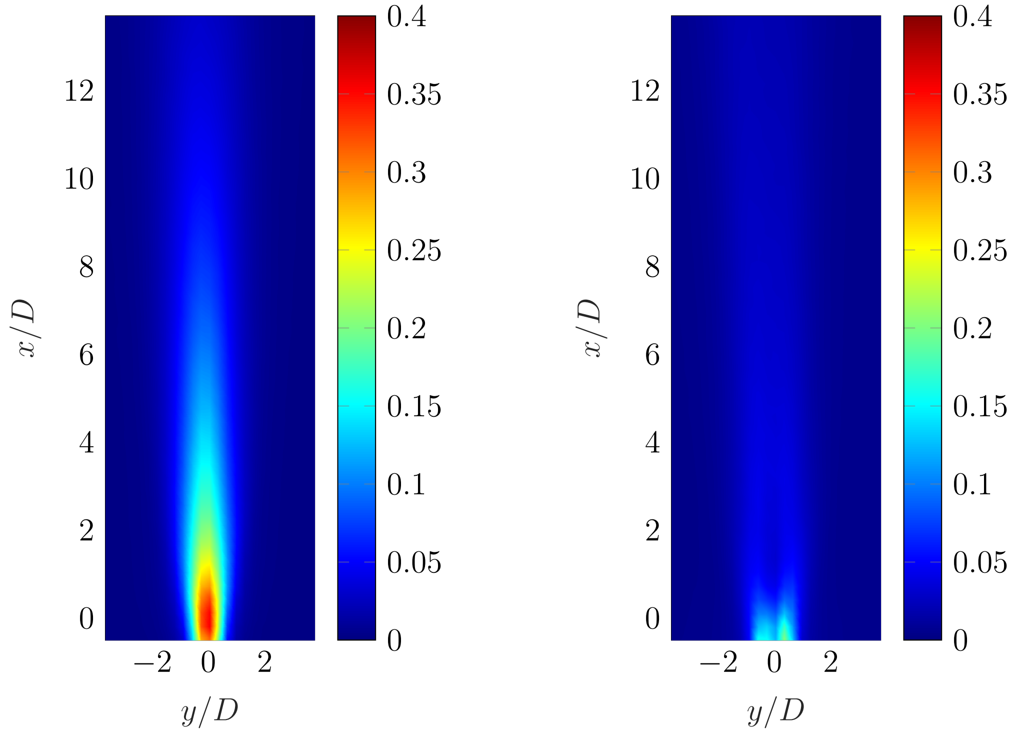

(c) $\text{rms}(u')/U_{\text{in}}$ (d) $\text{rms}(v')/U_{\text{in}}$

Figure C.2: Velocity field at $z = 20D$ and $U_{\text{r}} = 5.15$. a) Time-averaged streamwise (a) and crossflow (b) velocity. Root-mean-square streamwise (c) and crossflow (d) velocity

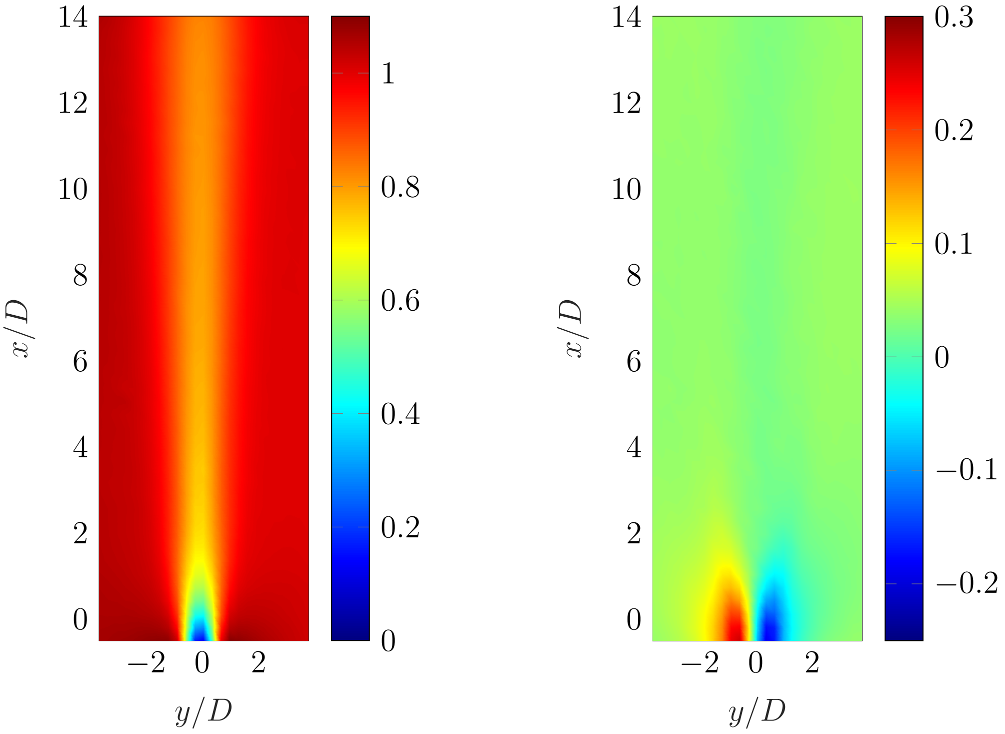

(a) $\overline{U}/U_{\text{in}}$ (b) $\overline{V}/U_{\text{in}}$

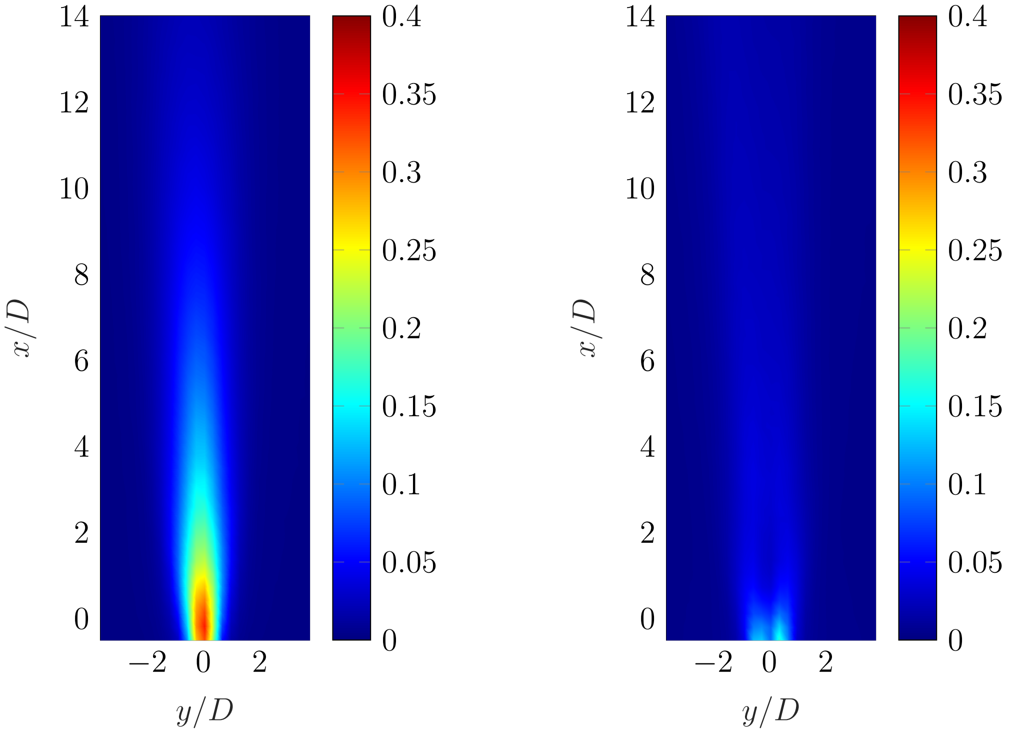

(c) $\text{rms}(u')/U_{\text{in}}$ (d) $\text{rms}(v')/U_{\text{in}}$

Figure C.3: Velocity field at $z = 20D$ and $U_{\text{r}} = 6.04$. a) Time-averaged streamwise (a) and crossflow (b) velocity. Root-mean-square streamwise (c) and crossflow (d) velocity

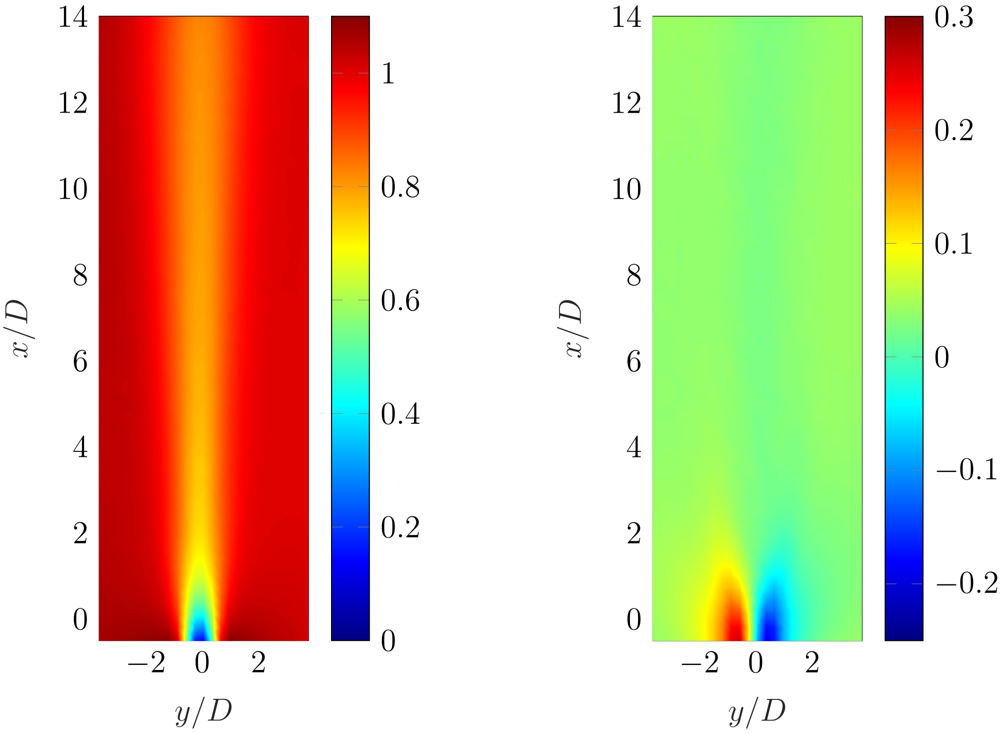

(a) $\overline{U}/U_{\mathrm{in}}$ (b) $\overline{V}/U_{\mathrm{in}}$

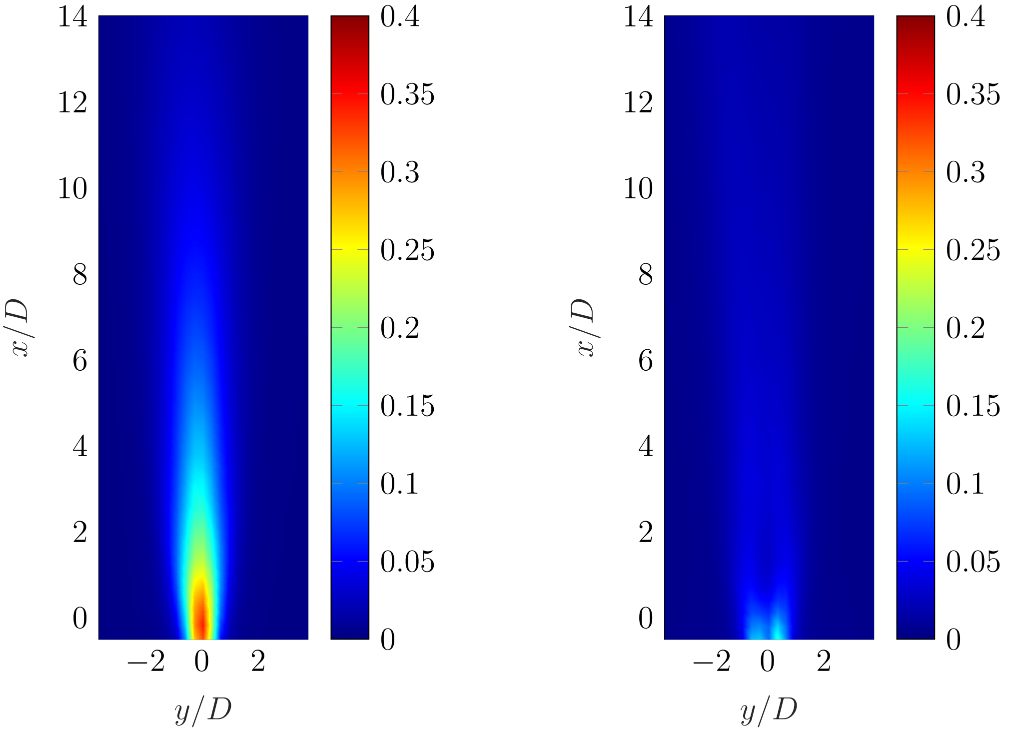

(c) $\mathrm{rms}(u')/U_{\mathrm{in}}$ (d) $\mathrm{rms}(v')/U_{\mathrm{in}}$

Figure C.4: Velocity field at $z = 20D$ and $U_{\mathrm{r}} = 7.5$. a) Time-averaged streamwise (a) and crossflow (b) velocity. Root-mean-square streamwise (c) and crossflow (d) velocity

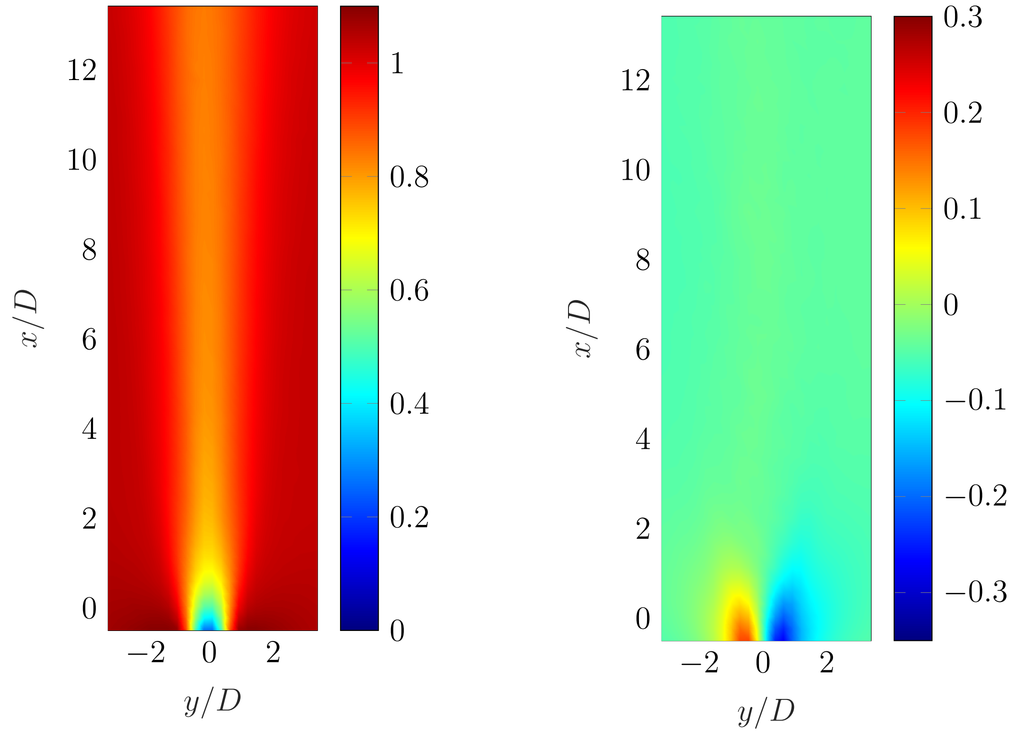

(a) $\overline{U}/U_{\mathrm{in}}$

(b) $\overline{V}/U_{\mathrm{in}}$

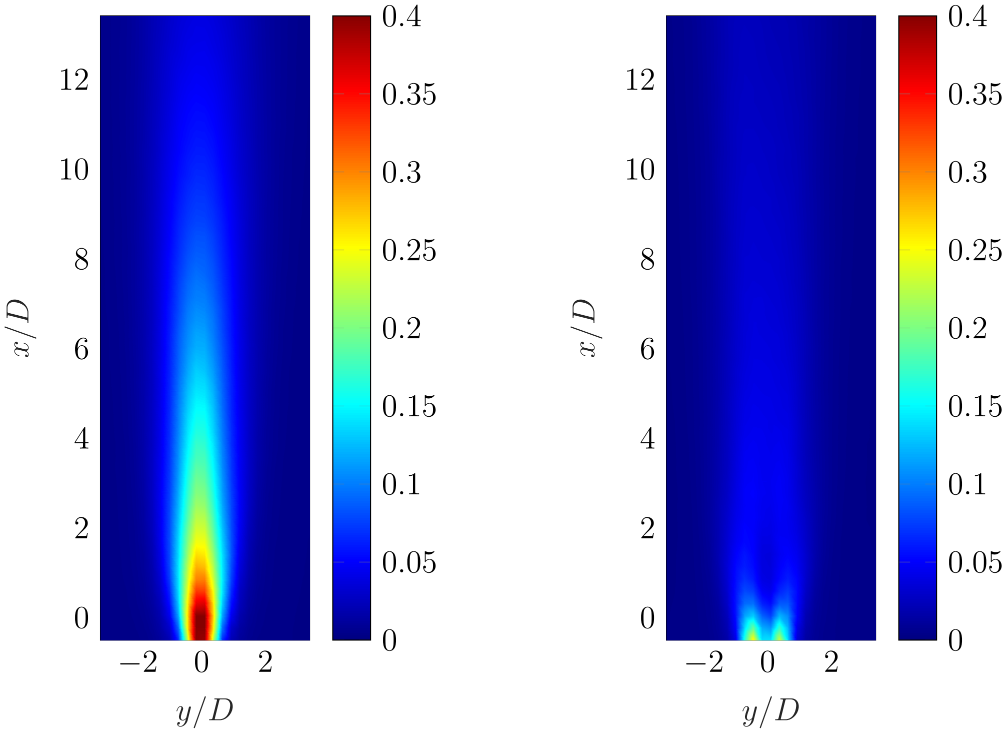

(c) $\mathrm{rms}(u')/U_{\mathrm{in}}$

(d) $\mathrm{rms}(v')/U_{\mathrm{in}}$

Figure C.5: Velocity field at $z = 34D$ and $U_{\mathrm{r}} = 4.5$. a) Time-averaged streamwise (a) and crossflow (b) velocity. Root-mean-square streamwise (c) and crossflow (d) velocity

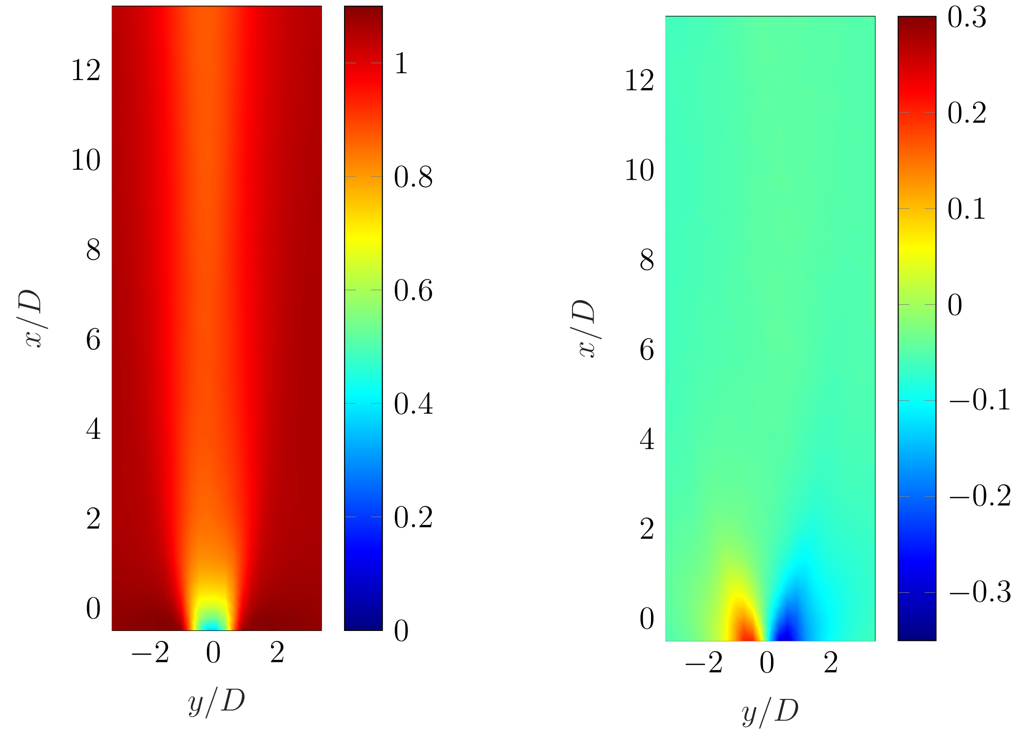

(a) $\overline{U}/U_{\mathrm{in}}$

(b) $\overline{V}/U_{\mathrm{in}}$

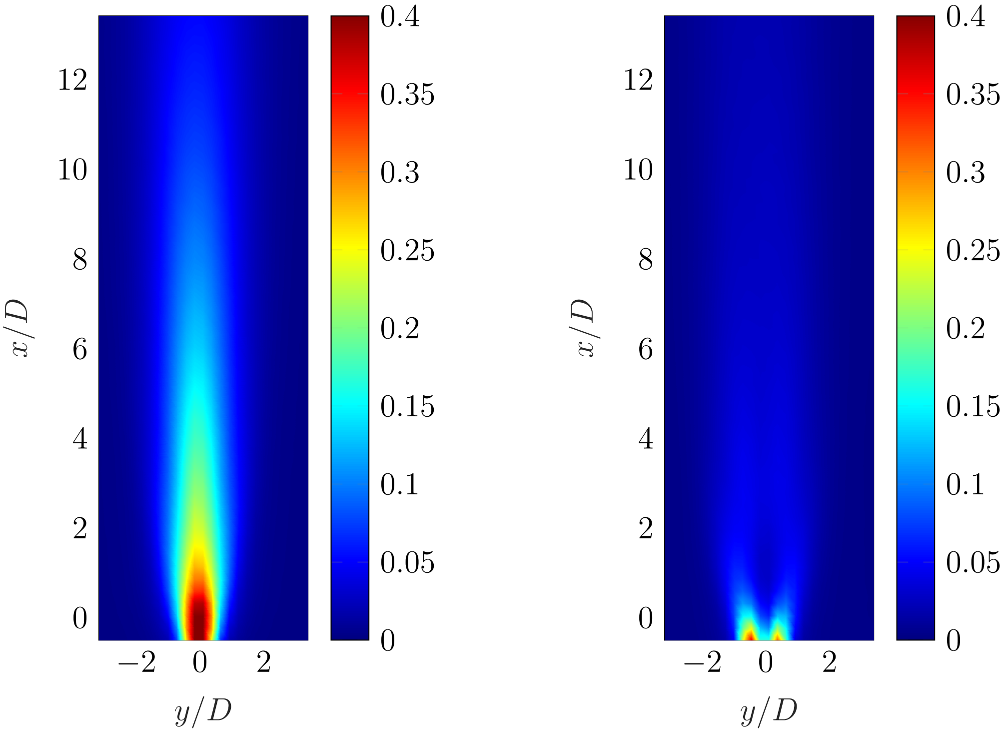

(c) $\mathrm{rms}(u')/U_{\mathrm{in}}$

(d) $\mathrm{rms}(v')/U_{\mathrm{in}}$

Figure C.6: Velocity field at $z = 34D$ and $U_{\mathrm{r}} = 5.15$. a) Time-averaged streamwise (a) and crossflow (b) velocity. Root-mean-square streamwise (c) and crossflow (d) velocity

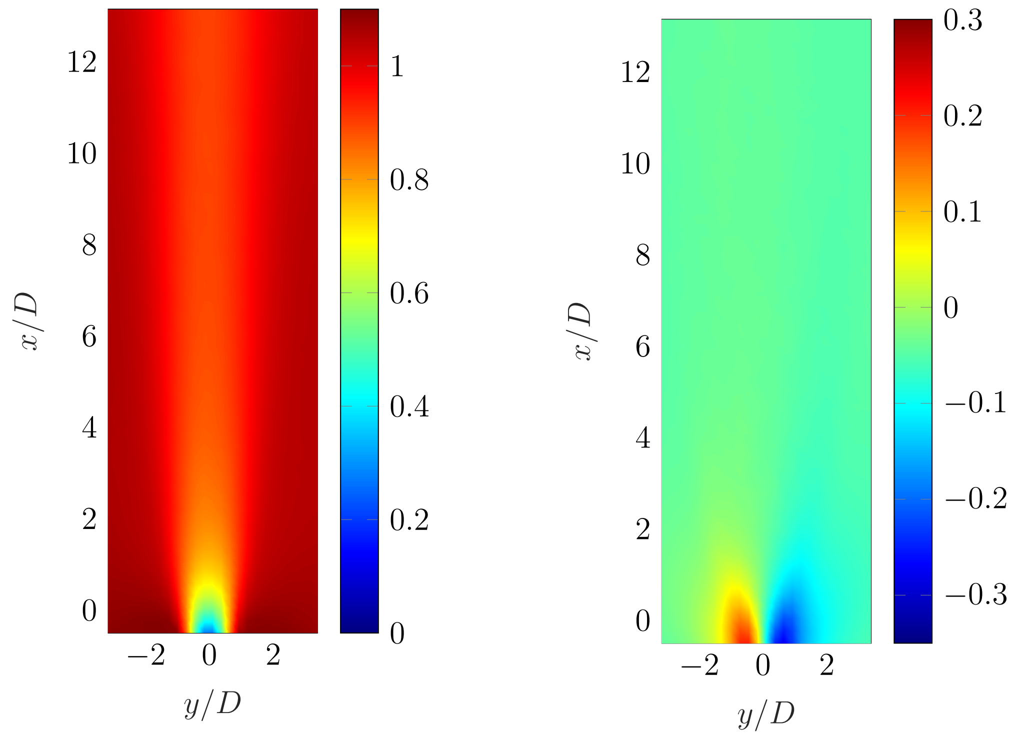

(a) $\overline{U}/U_{\mathrm{in}}$

(b) $\overline{V}/U_{\mathrm{in}}$

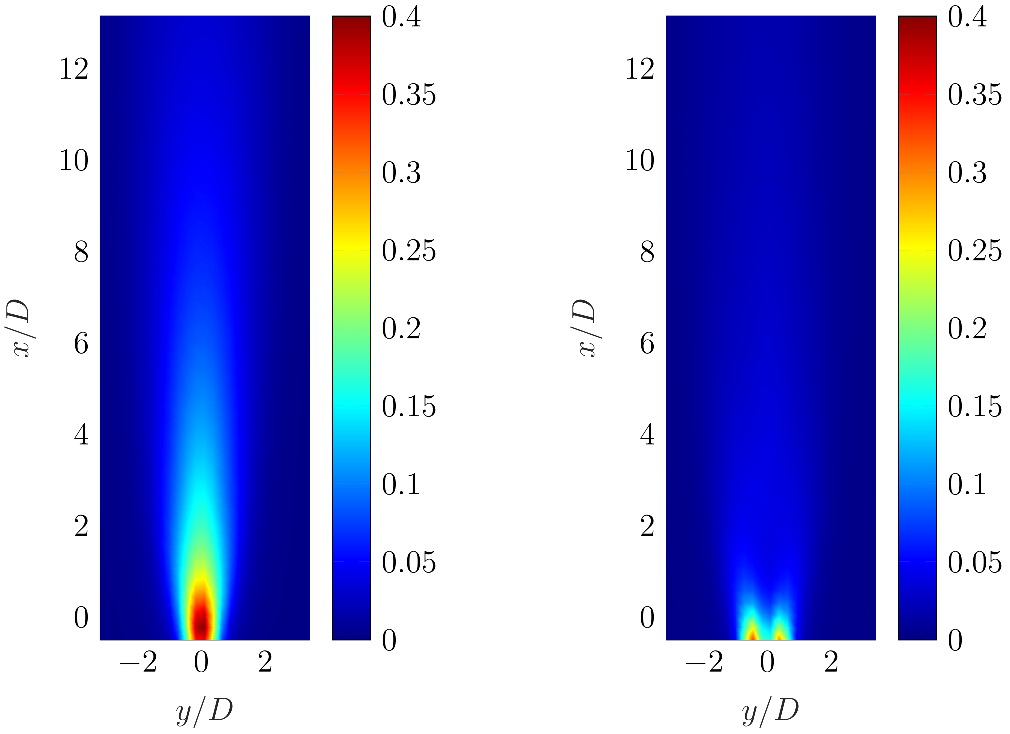

(c) $\mathrm{rms}(u')/U_{\mathrm{in}}$

(d) $\mathrm{rms}(v')/U_{\mathrm{in}}$

Figure C.7: Velocity field at $z = 34D$ and $U_{\mathrm{r}} = 6.04$. a) Time-averaged streamwise (a) and crossflow (b) velocity. Root-mean-square streamwise (c) and crossflow (d) velocity

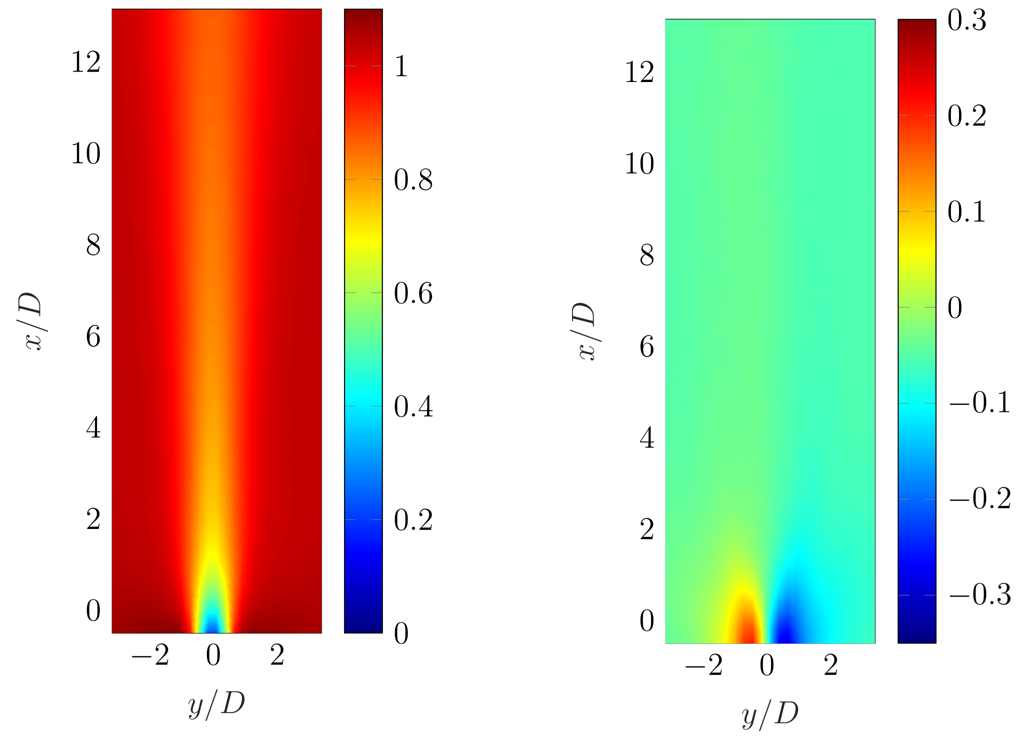

(a) $\overline{U}/U_{\mathrm{in}}$

(b) $\overline{V}/U_{\mathrm{in}}$

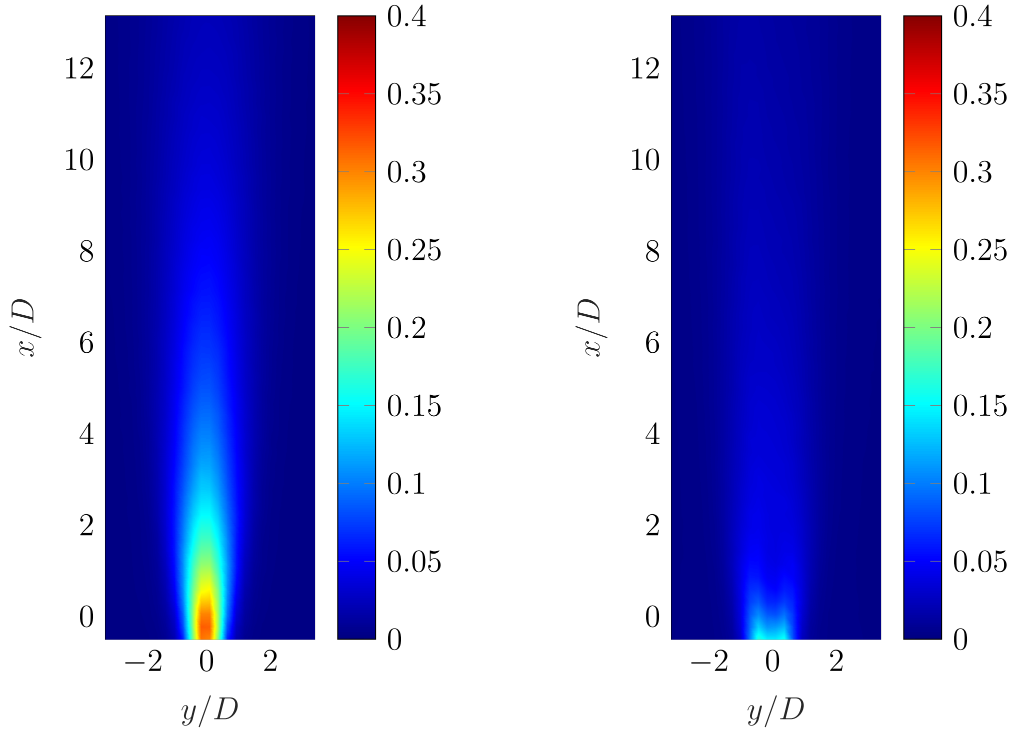

(c) $\mathrm{rms}(u')/U_{\mathrm{in}}$

(d) $\mathrm{rms}(v')/U_{\mathrm{in}}$

Figure C.8: Velocity field at $z = 34D$ and $U_{\mathrm{r}} = 7.5$. a) Time-averaged streamwise (a) and crossflow (b) velocity. Root-mean-square streamwise (c) and crossflow (d) velocity

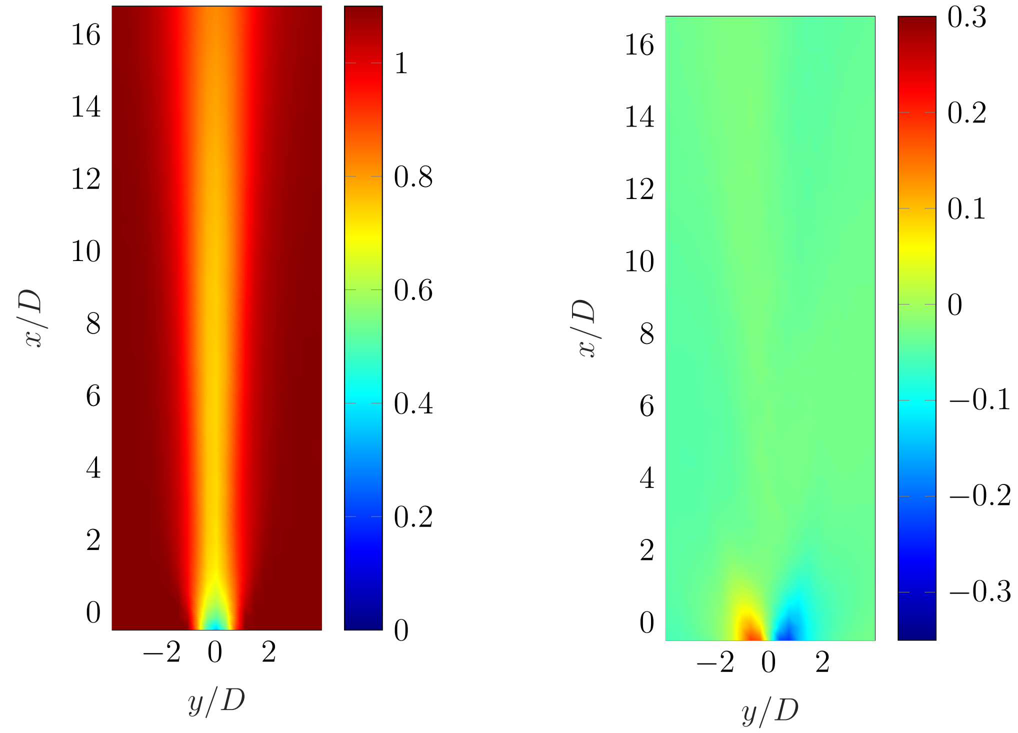

(a) $\overline{U}/U_{\mathrm{in}}$ (b) $\overline{V}/U_{\mathrm{in}}$

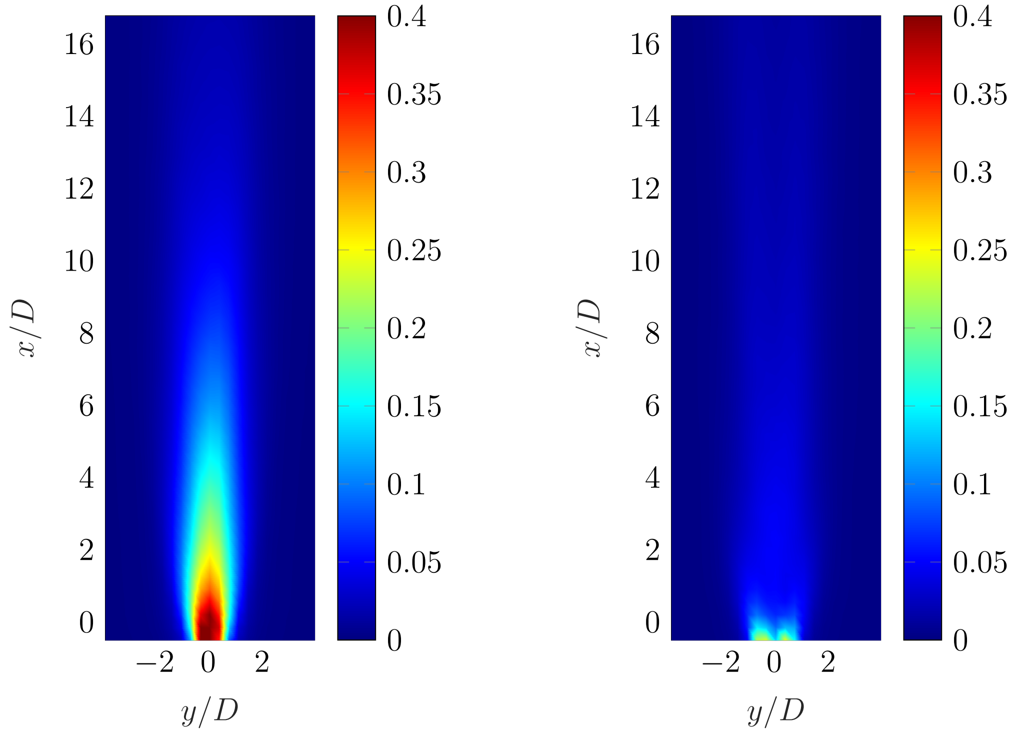

(c) $\mathrm{rms}(u')/U_{\mathrm{in}}$ (d) $\mathrm{rms}(v')/U_{\mathrm{in}}$

Figure C.9: Velocity field at $z = 52D$ and $U_{\mathrm{r}} = 4.5$. a) Time-averaged streamwise (a) and crossflow (b) velocity. Root-mean-square streamwise (c) and crossflow (d) velocity

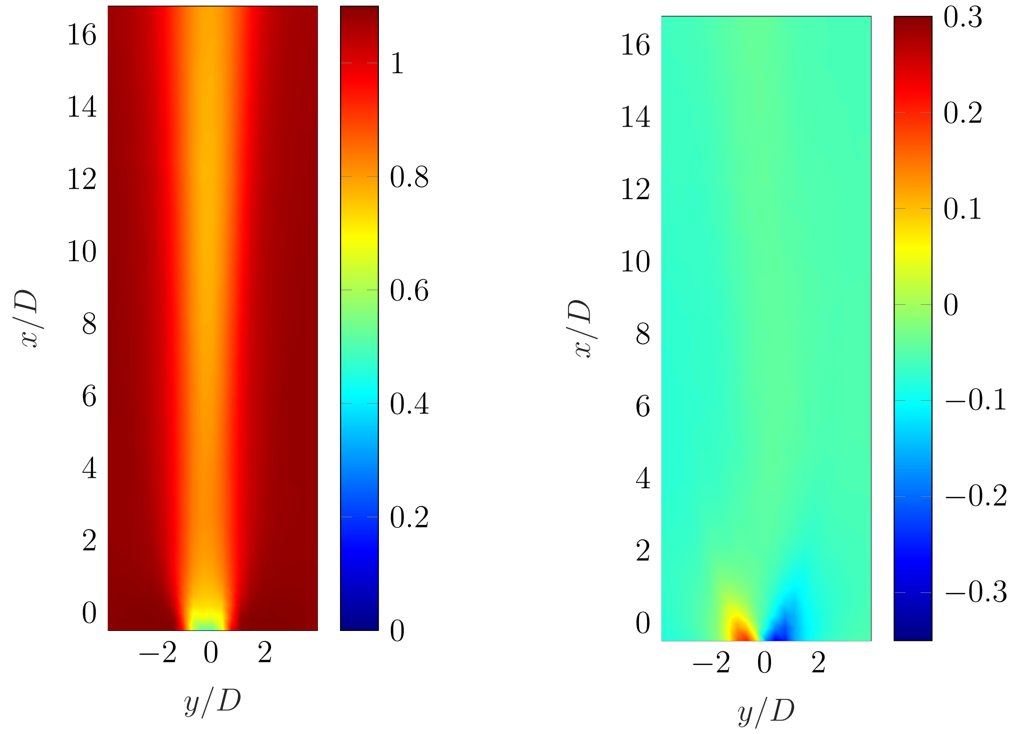

(a) $\overline{U}/U_{\text{in}}$ (b) $\overline{V}/U_{\text{in}}$

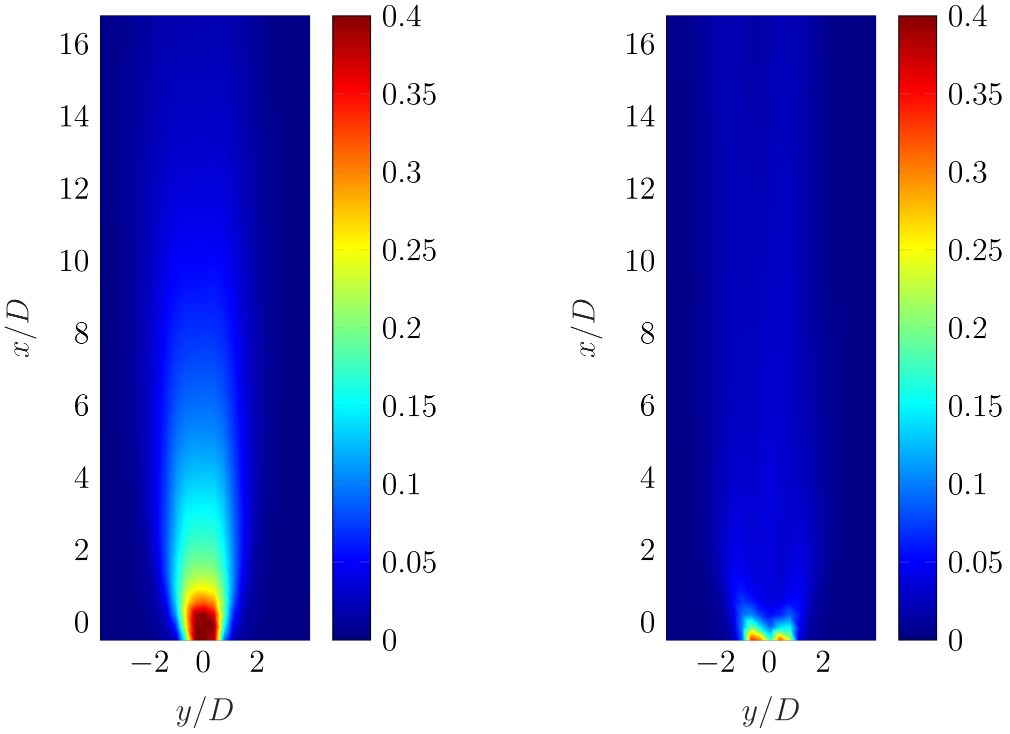

(c) $\text{rms}(u')/U_{\text{in}}$ (d) $\text{rms}(v')/U_{\text{in}}$

Figure C.10: Velocity field at $z = 52D$ and $U_{\text{r}} = 5.15$. a) Time-averaged streamwise (a) and crossflow (b) velocity. Root-mean-square streamwise (c) and crossflow (d) velocity

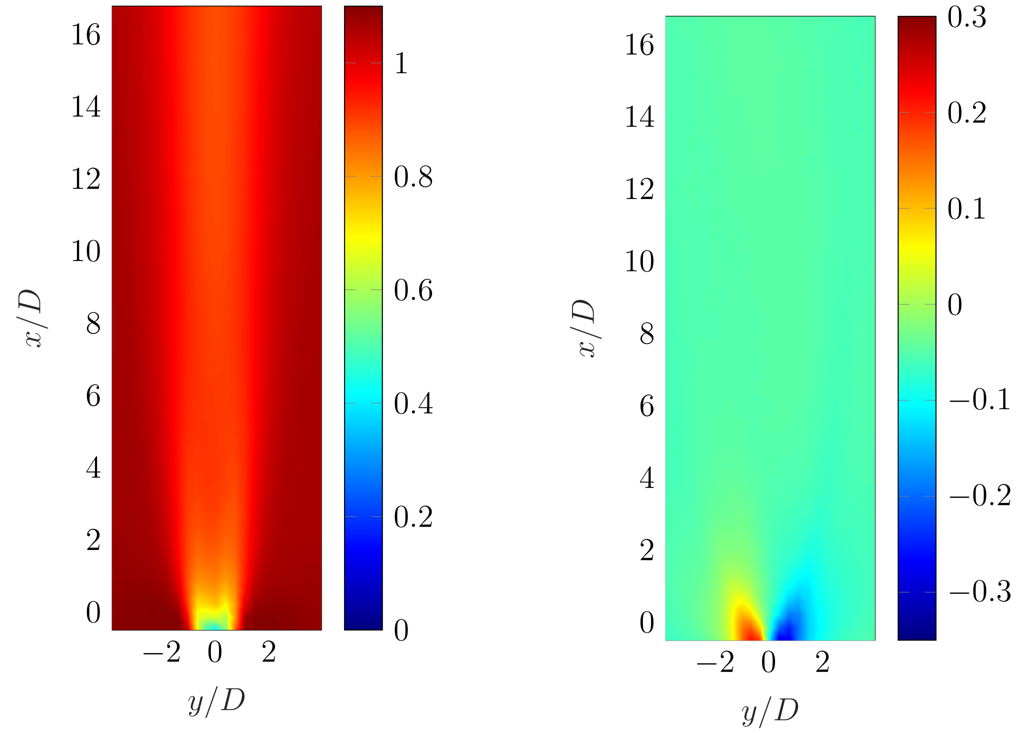

(a) $\overline{U}/U_{\mathrm{in}}$ (b) $\overline{V}/U_{\mathrm{in}}$

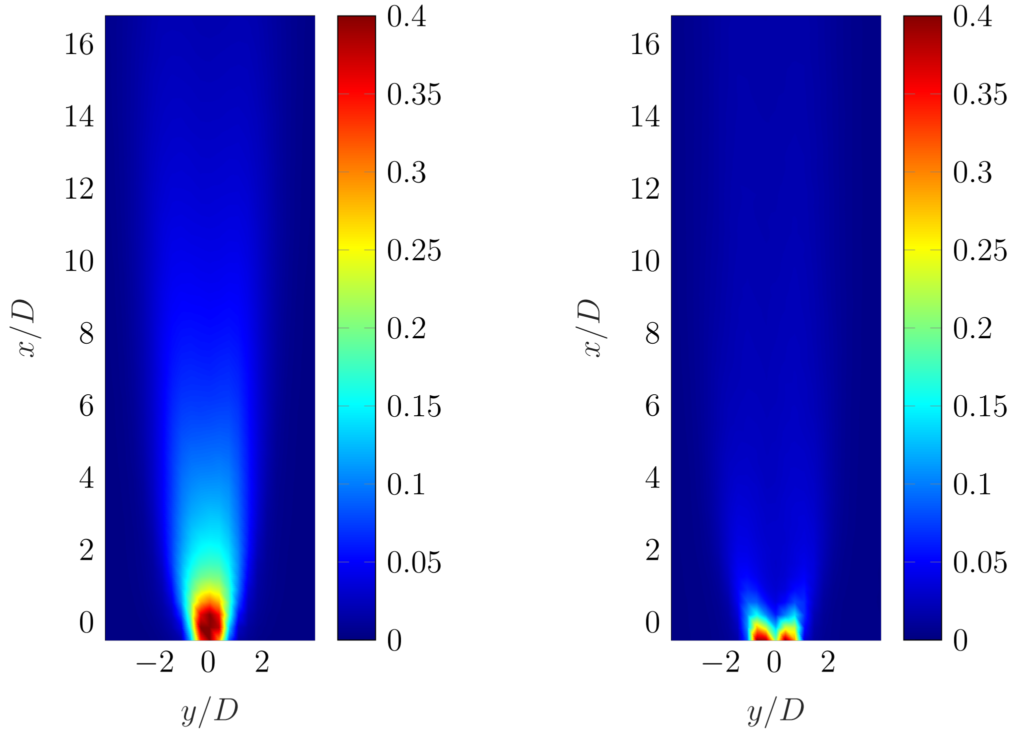

(c) $\mathrm{rms}(u')/U_{\mathrm{in}}$ (d) $\mathrm{rms}(v')/U_{\mathrm{in}}$

Figure C.11: Velocity field at $z = 52D$ and $U_{\mathrm{r}} = 6.04$. a) Time-averaged streamwise (a) and crossflow (b) velocity. Root-mean-square streamwise (c) and crossflow (d) velocity

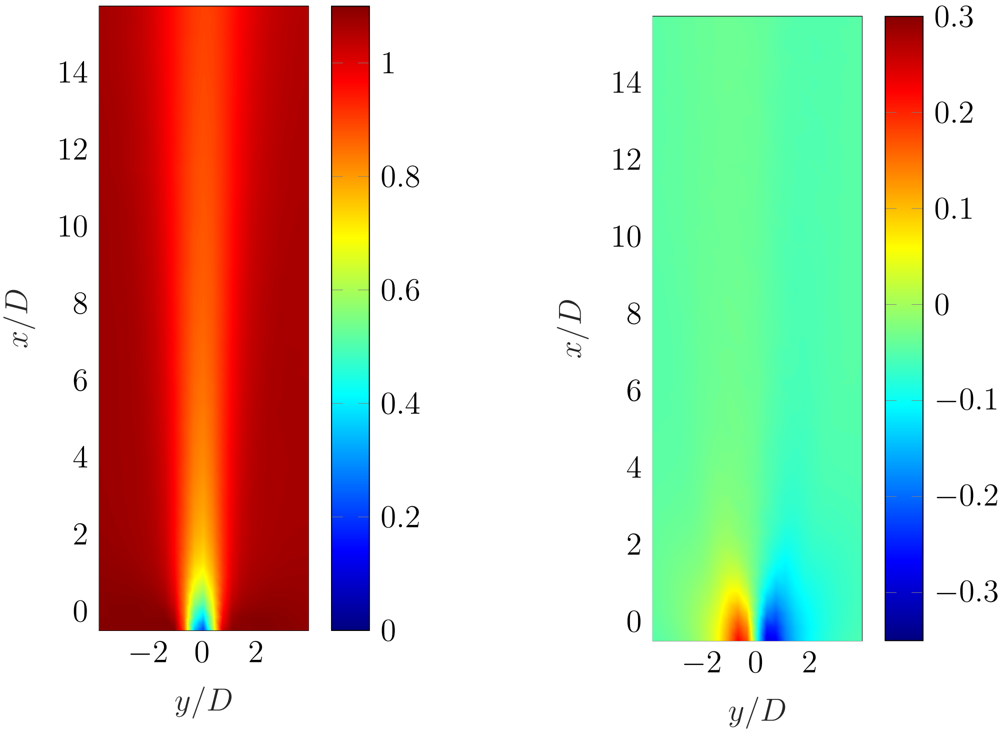

(a) $\overline{U}/U_{\mathrm{in}}$

(b) $\overline{V}/U_{\mathrm{in}}$

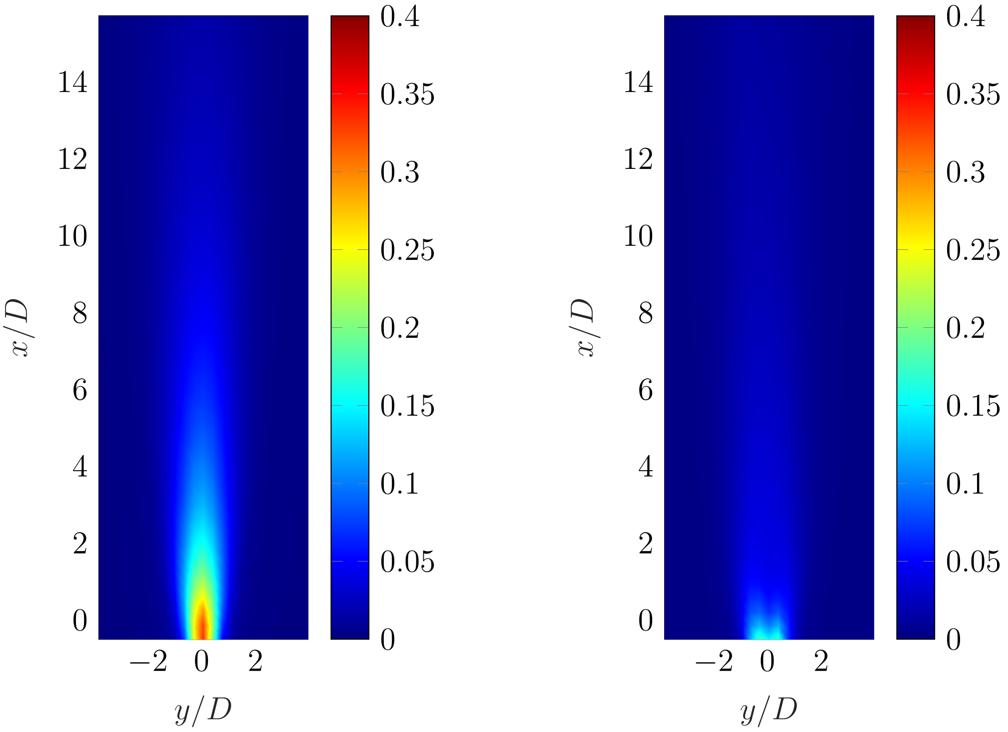

(c) $\mathrm{rms}(u')/U_{\mathrm{in}}$

(d) $\mathrm{rms}(v')/U_{\mathrm{in}}$

Figure C.12: Velocity field at $z = 52D$ and $U_{\mathrm{r}} = 7.5$. a) Time-averaged streamwise (a) and crossflow (b) velocity. Root-mean-square streamwise (c) and crossflow (d) velocity

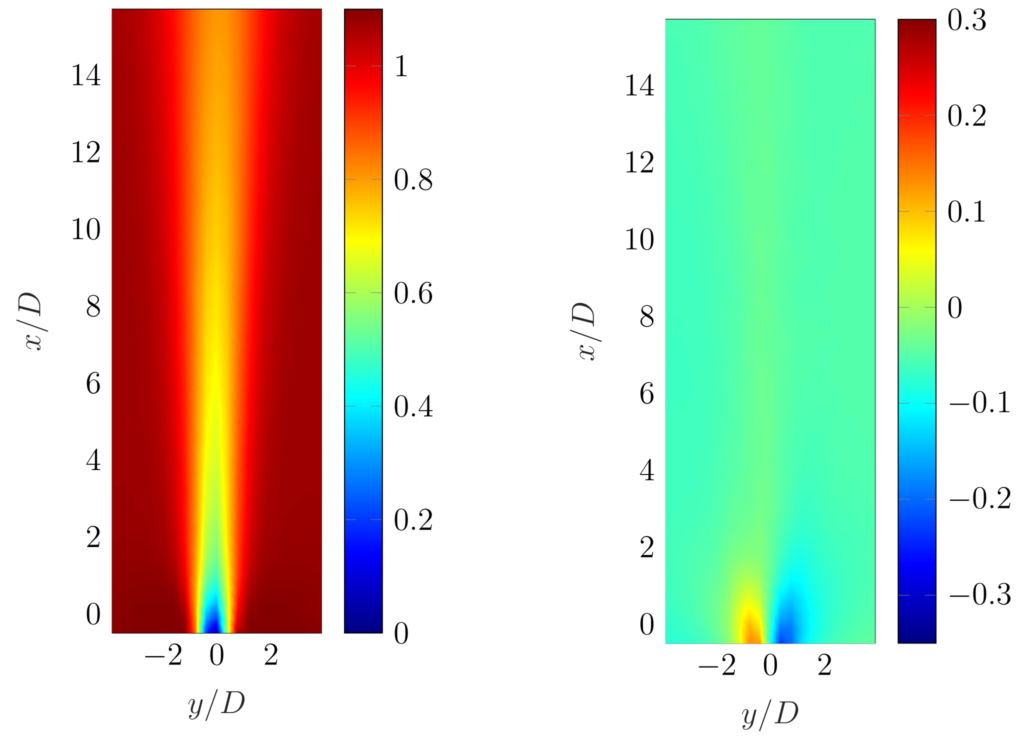

(a) $\overline{U}/U_{\text{in}}$ (b) $\overline{V}/U_{\text{in}}$

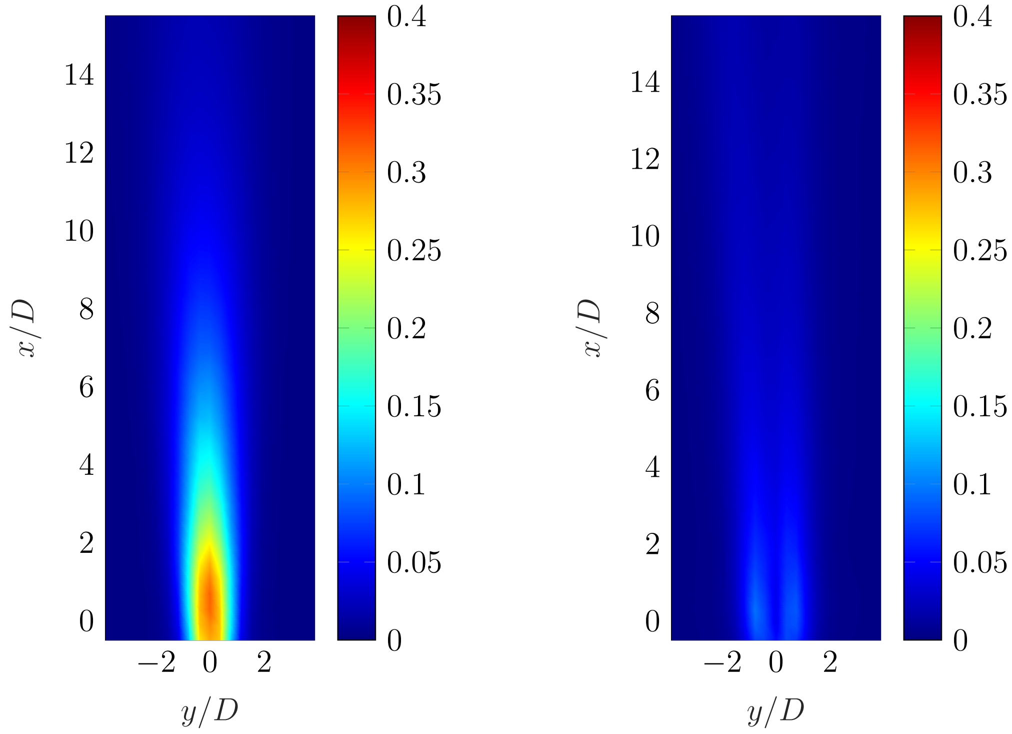

(c) $\text{rms}(u')/U_{\text{in}}$ (d) $\text{rms}(v')/U_{\text{in}}$

Figure C.13: Velocity field at $z = 60D$ and $U_{\text{r}} = 4.5$. a) Time-averaged streamwise (a) and crossflow (b) velocity. Root-mean-square streamwise (c) and crossflow (d) velocity

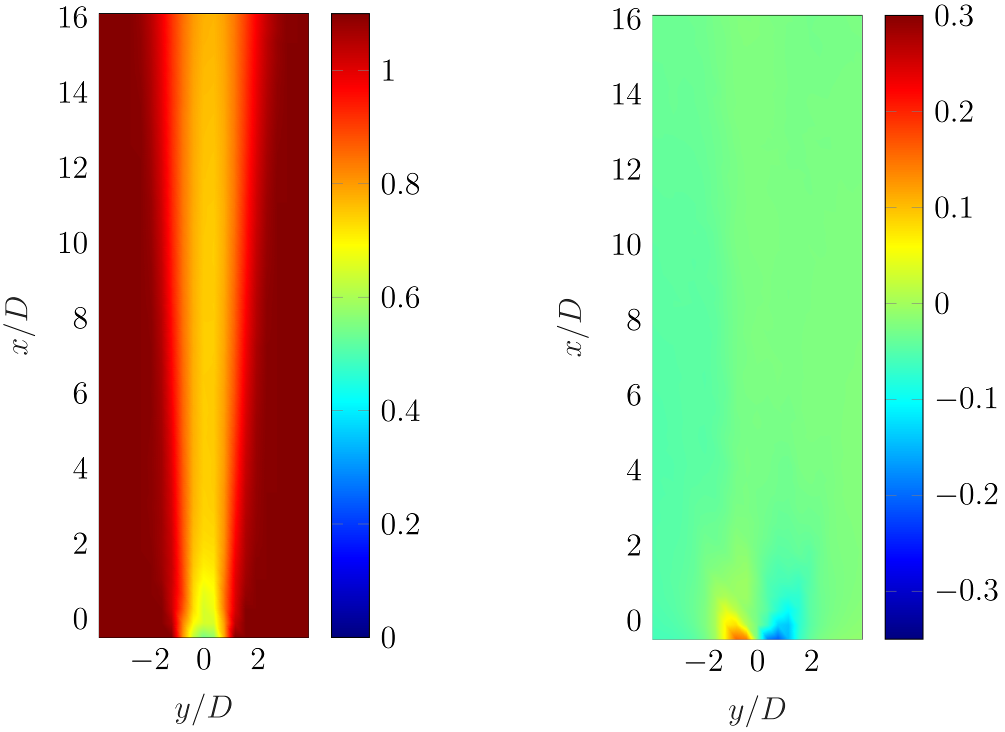

(a) $\overline{U}/U_{\mathrm{in}}$ (b) $\overline{V}/U_{\mathrm{in}}$

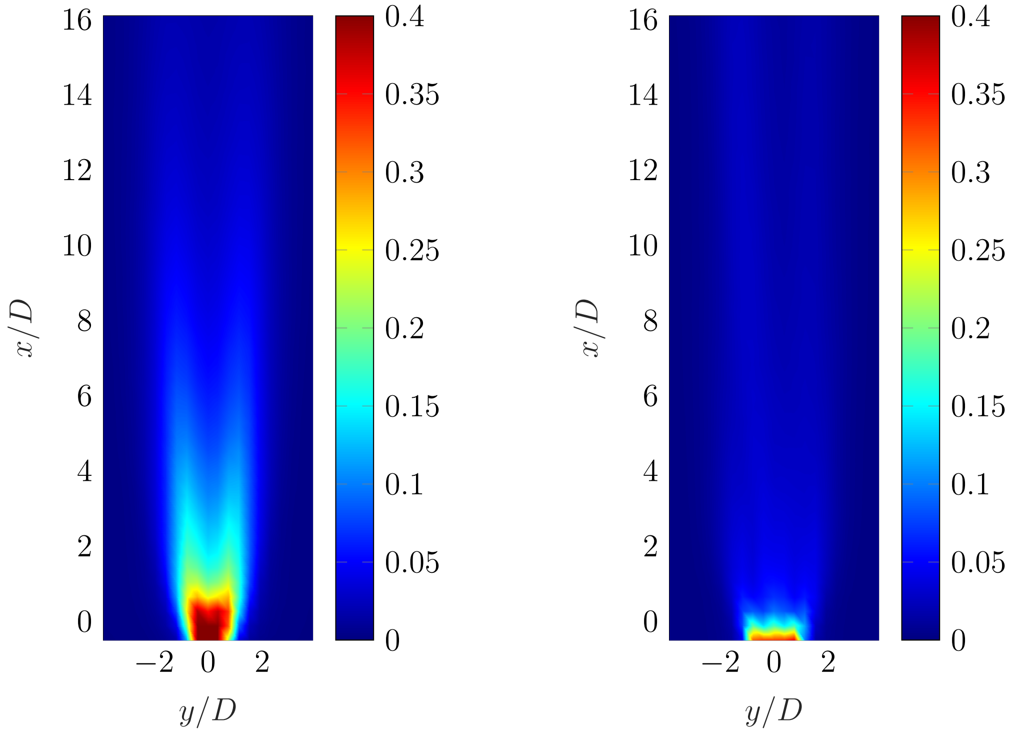

(c) $\mathrm{rms}(u')/U_{\mathrm{in}}$ (d) $\mathrm{rms}(v')/U_{\mathrm{in}}$

Figure C.14: Velocity field at $z = 60D$ and $U_{\mathrm{r}} = 5.15$. a) Time-averaged streamwise (a) and crossflow (b) velocity. Root-mean-square streamwise (c) and crossflow (d) velocity

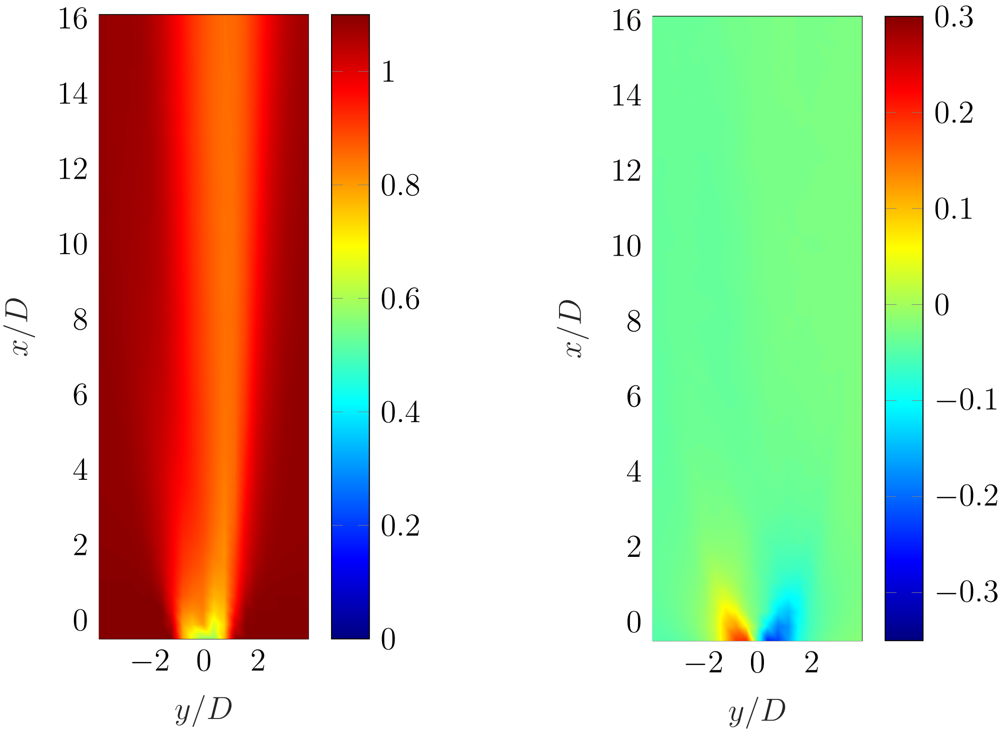

(a) $\overline{U}/U_{\mathrm{in}}$ (b) $\overline{V}/U_{\mathrm{in}}$

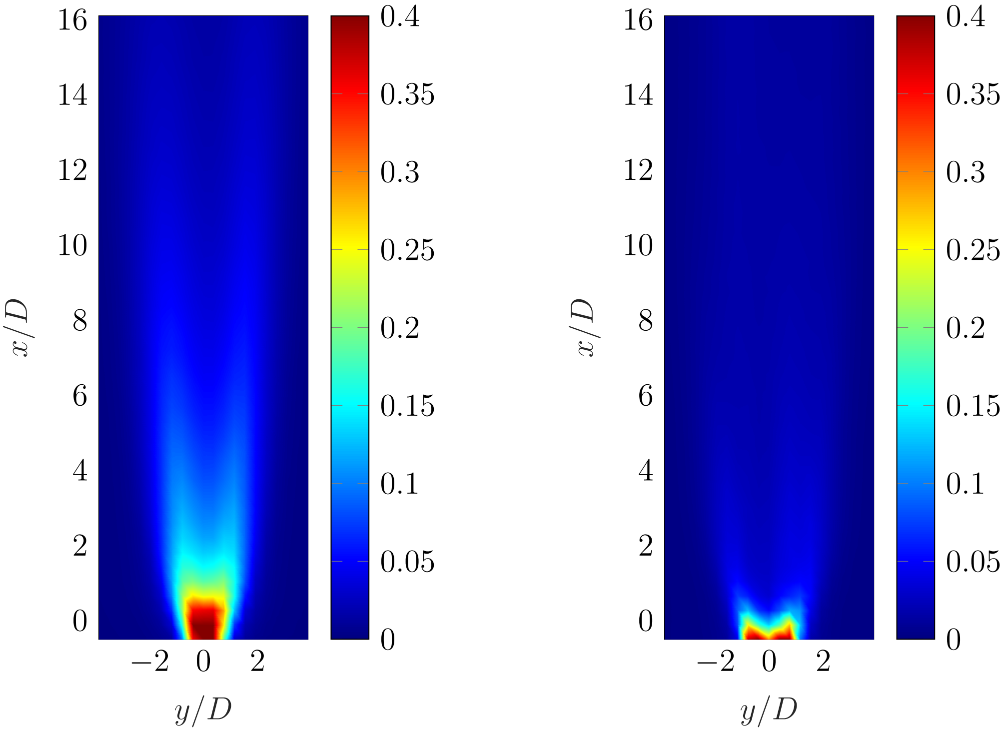

(c) $\mathrm{rms}(u')/U_{\mathrm{in}}$ (d) $\mathrm{rms}(v')/U_{\mathrm{in}}$

Figure C.15: Velocity field at $z = 60D$ and $U_{\mathrm{r}} = 6.04$. a) Time-averaged streamwise (a) and crossflow (b) velocity. Root-mean-square streamwise (c) and crossflow (d) velocity

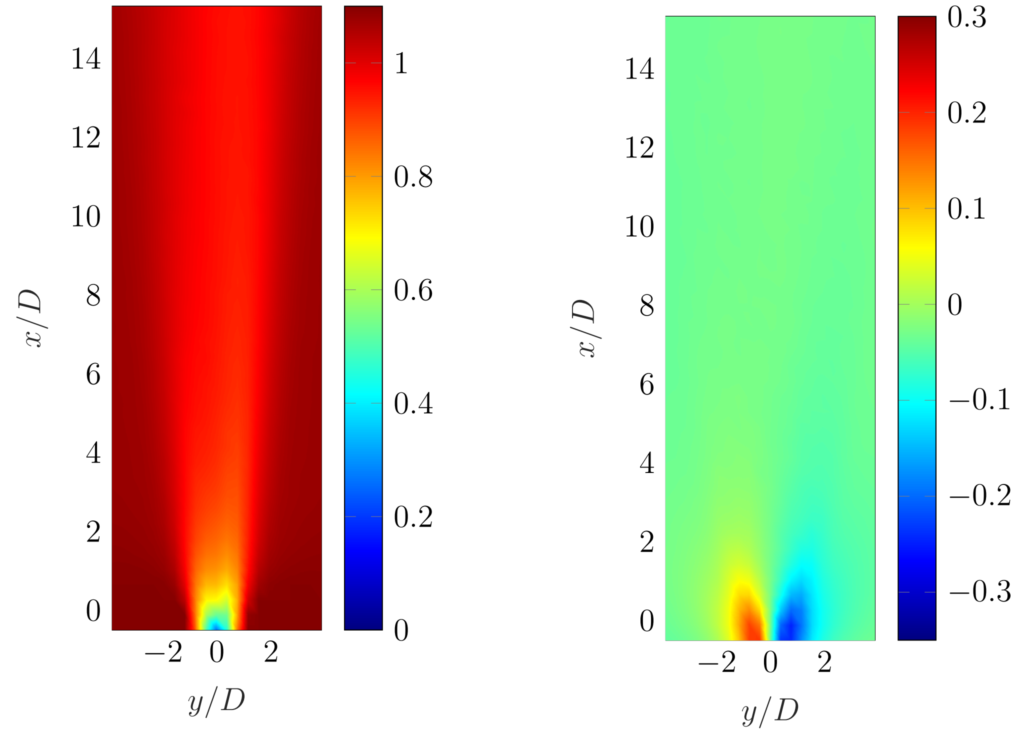

(a) $\overline{U}/U_{\mathrm{in}}$

(b) $\overline{V}/U_{\mathrm{in}}$

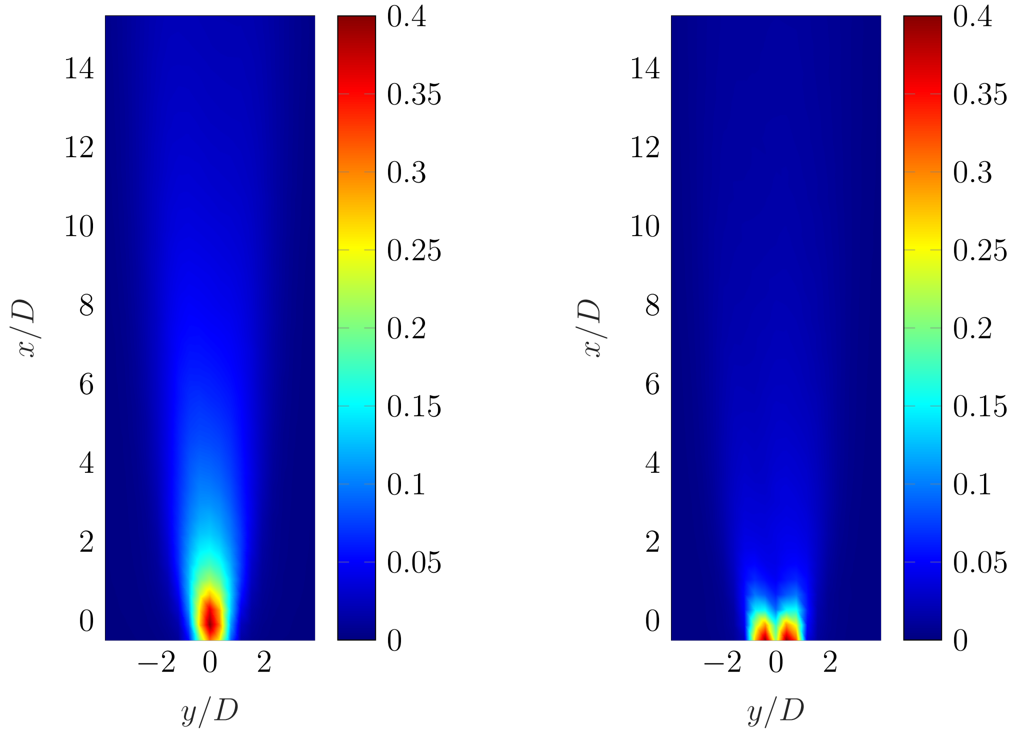

(c) $\mathrm{rms}(u')/U_{\mathrm{in}}$

(d) $\mathrm{rms}(v')/U_{\mathrm{in}}$

Figure C.16: Velocity field at $z = 60D$ and $U_{\mathrm{r}} = 7.5$. a) Time-averaged streamwise (a) and crossflow (b) velocity. Root-mean-square streamwise (c) and crossflow (d) velocity

C.2 Pivoted cylinder

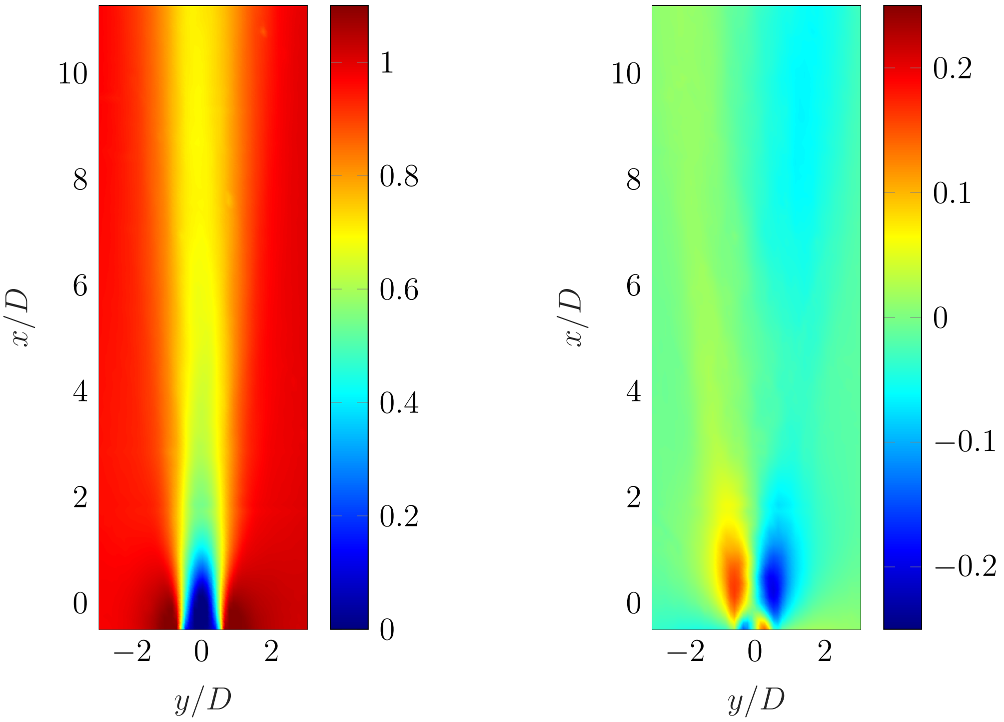

(a) $\overline{U}/U_{\text{in}}$ (b) $\overline{V}/U_{\text{in}}$

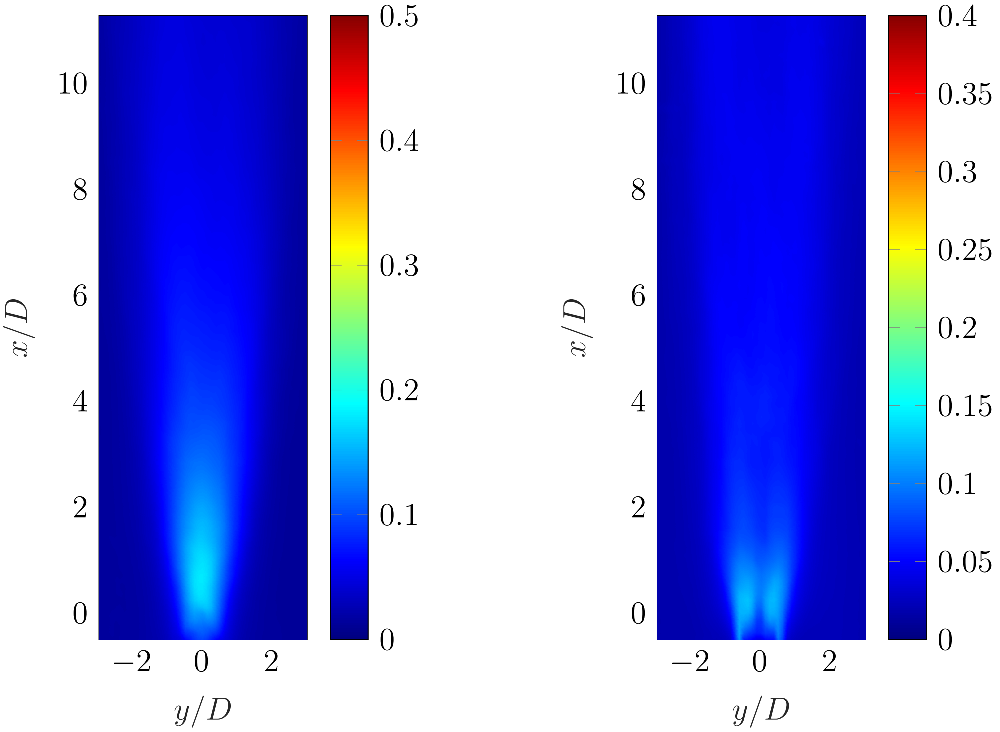

(c) $\text{rms}(u')/U_{\text{in}}$ (d) $\text{rms}(v')/U_{\text{in}}$

Figure C.17: Velocity field at $z = 6D$ and $U_{\text{r}} = 3$. a) Time-averaged streamwise velocity U. a) Time-averaged streamwise velocity U. c) $\text{rms}(u')$. d) $\text{rms}(v')$

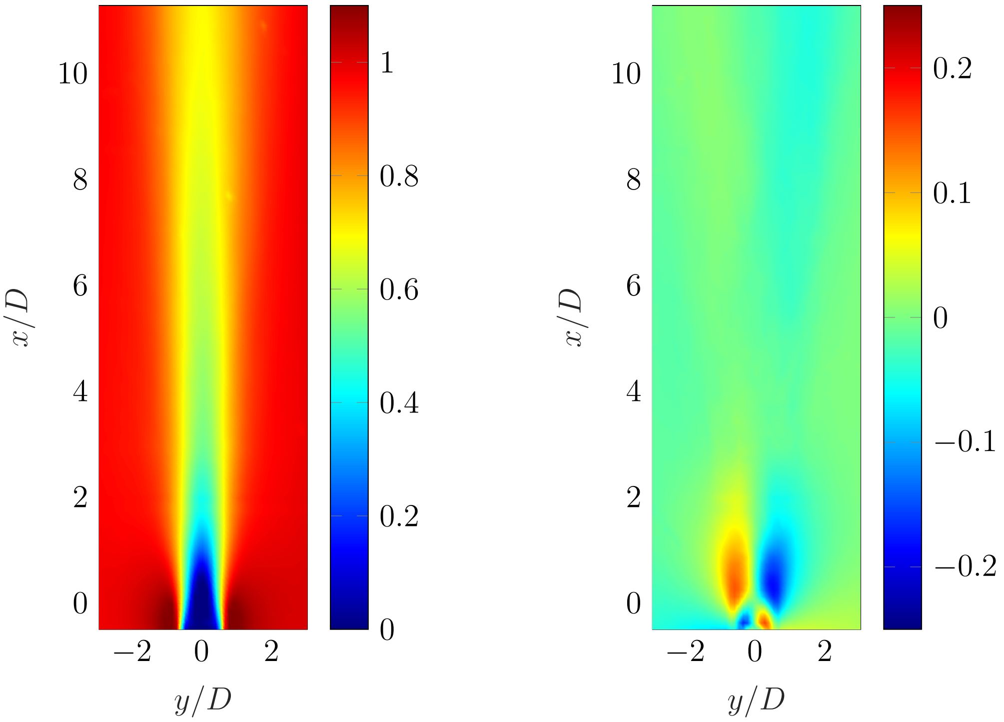

(a) $\overline{U}/U_\mathrm{in}$ (b) $\overline{V}/U_\mathrm{in}$

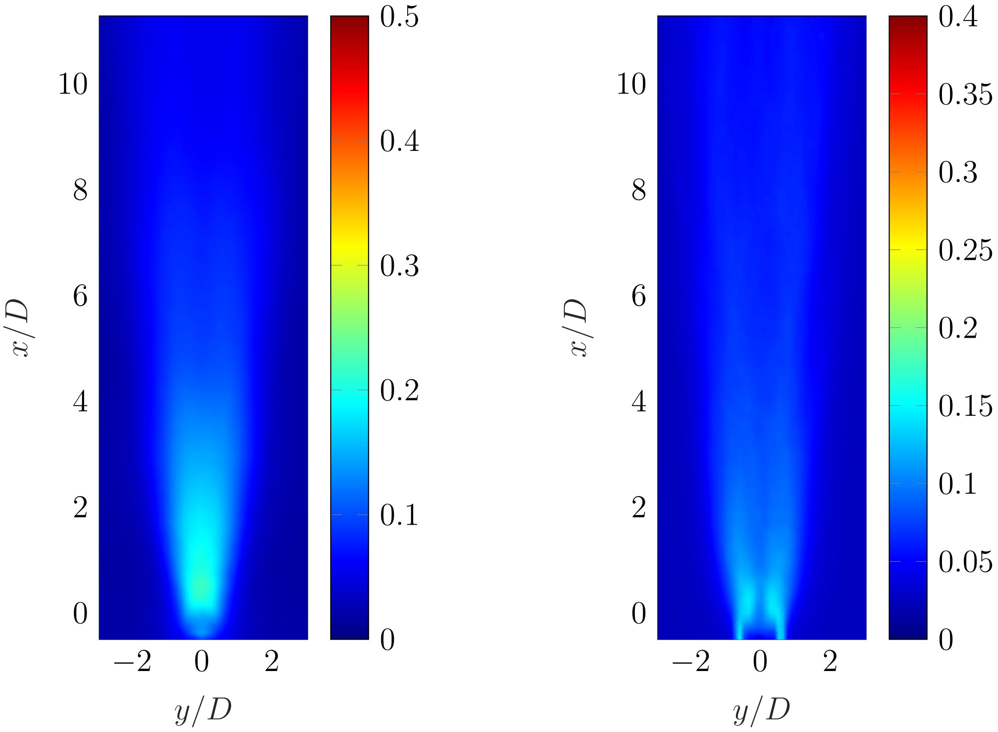

(c) $\mathrm{rms}(u')/U_\mathrm{in}$ (d) $\mathrm{rms}(v')/U_\mathrm{in}$

Figure C.18: Velocity field at $z = 6D$ and $U_\mathrm{r} = 3.8$. a) Time-averaged streamwise velocity U. a) Time-averaged streamwise velocity U. c) rms(u'). d) rms(v')

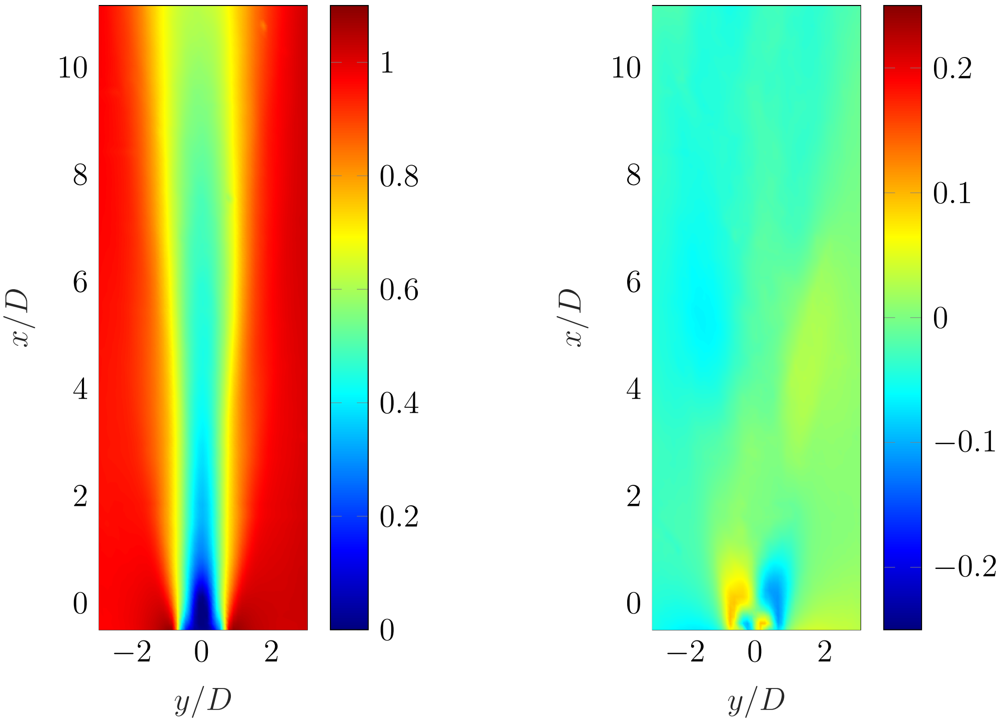

(a) $\overline{U}/U_{\mathrm{in}}$ (b) $\overline{V}/U_{\mathrm{in}}$

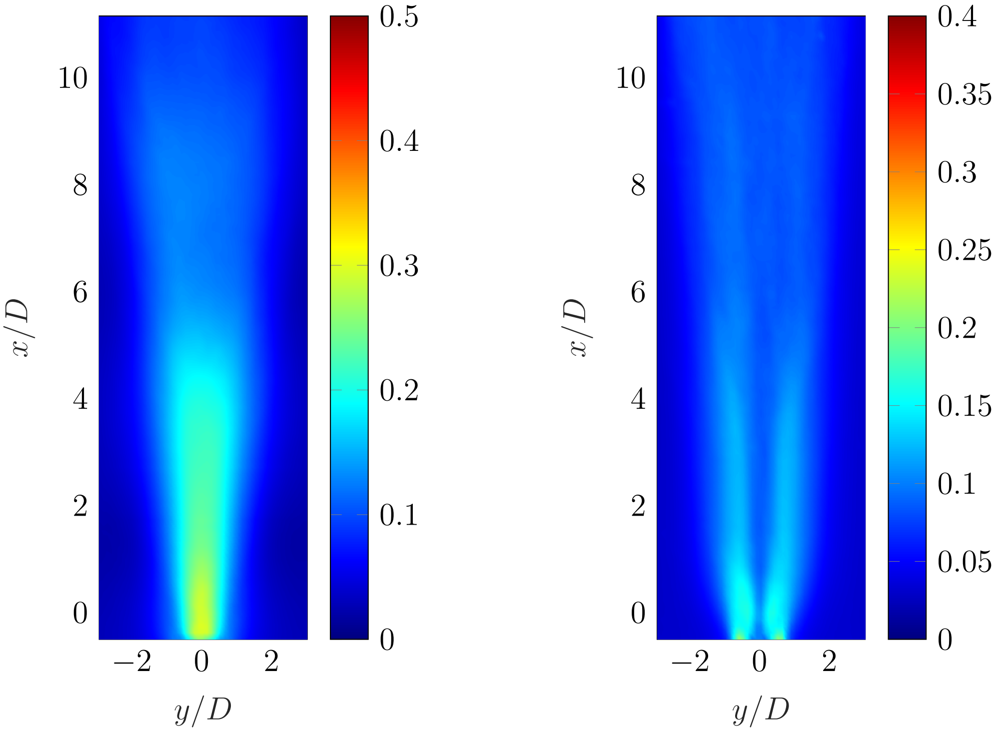

(c) $\mathrm{rms}(u')/U_{\mathrm{in}}$ (d) $\mathrm{rms}(v')/U_{\mathrm{in}}$

Figure C.19: Velocity field at $z = 6D$ and $U_{\mathrm{r}} = 4.5$. a) Time-averaged streamwise velocity U. a) Time-averaged streamwise velocity U. c) $\mathrm{rms}(u')$. d) $\mathrm{rms}(v')$

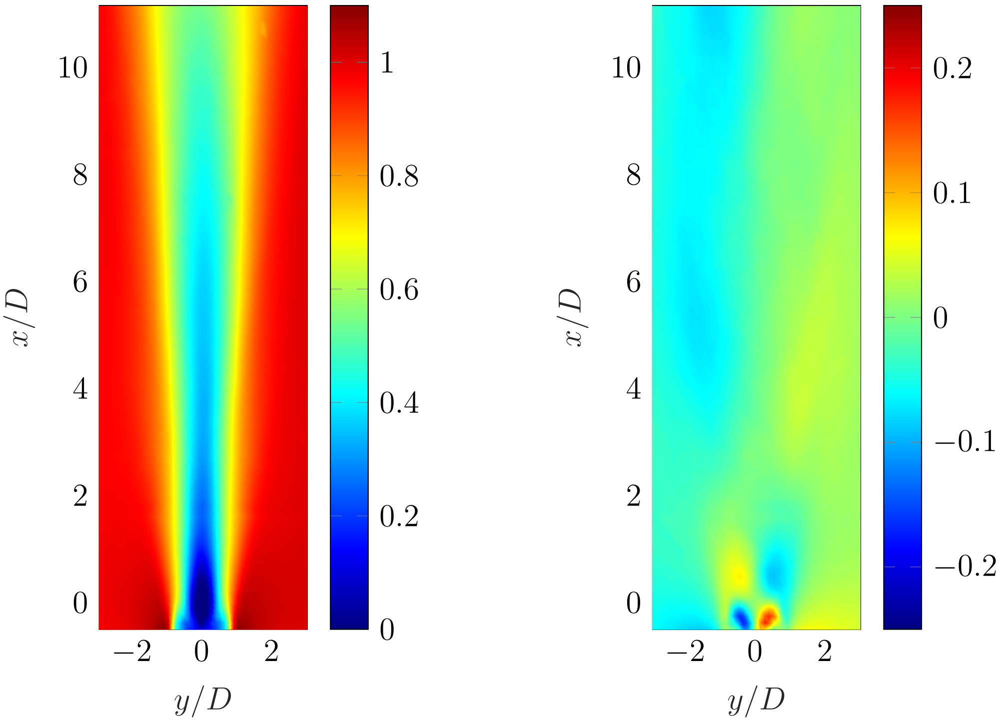

(a) $\overline{U}/U_{\mathrm{in}}$ (b) $\overline{V}/U_{\mathrm{in}}$

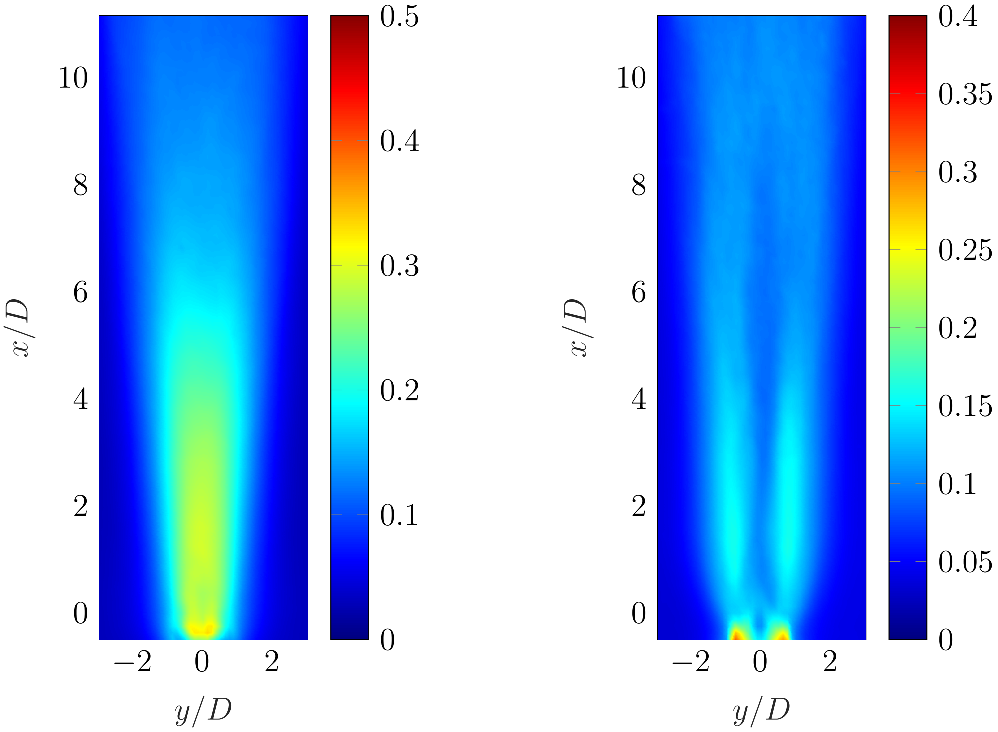

(c) $\mathrm{rms}(u')/U_{\mathrm{in}}$ (d) $\mathrm{rms}(v')/U_{\mathrm{in}}$

Figure C.20: Velocity field at $z = 6D$ and $U_{\mathrm{r}} = 5.2$. a) Time-averaged streamwise velocity U. a) Time-averaged streamwise velocity U. c) rms(u'). d) rms(v')

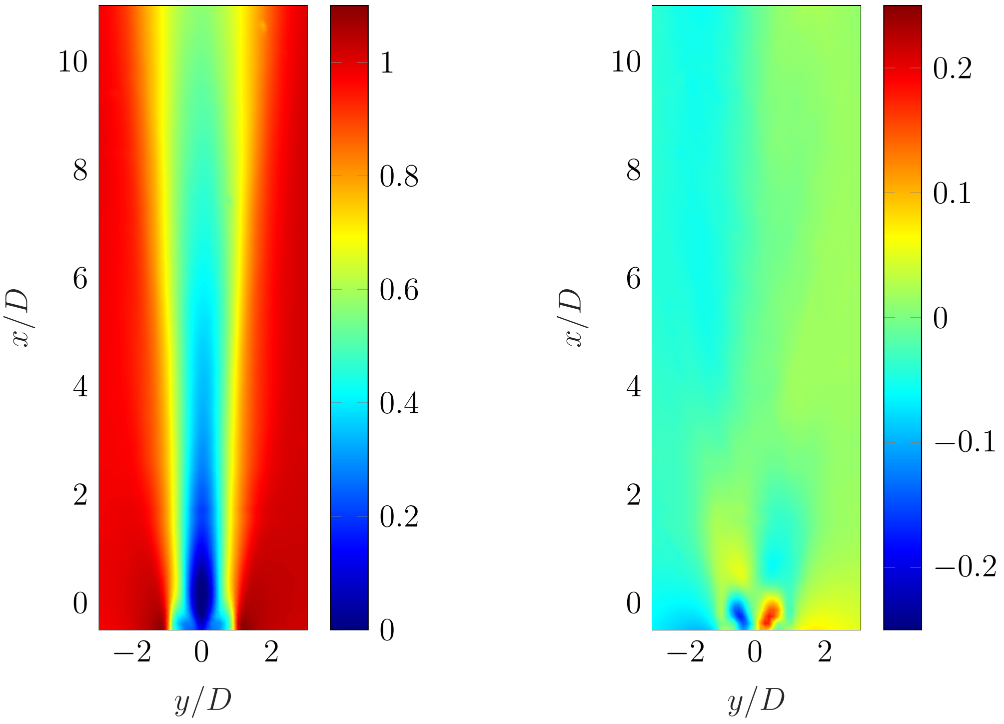

(a) $\overline{U}/U_{\text{in}}$

(b) $\overline{V}/U_{\text{in}}$

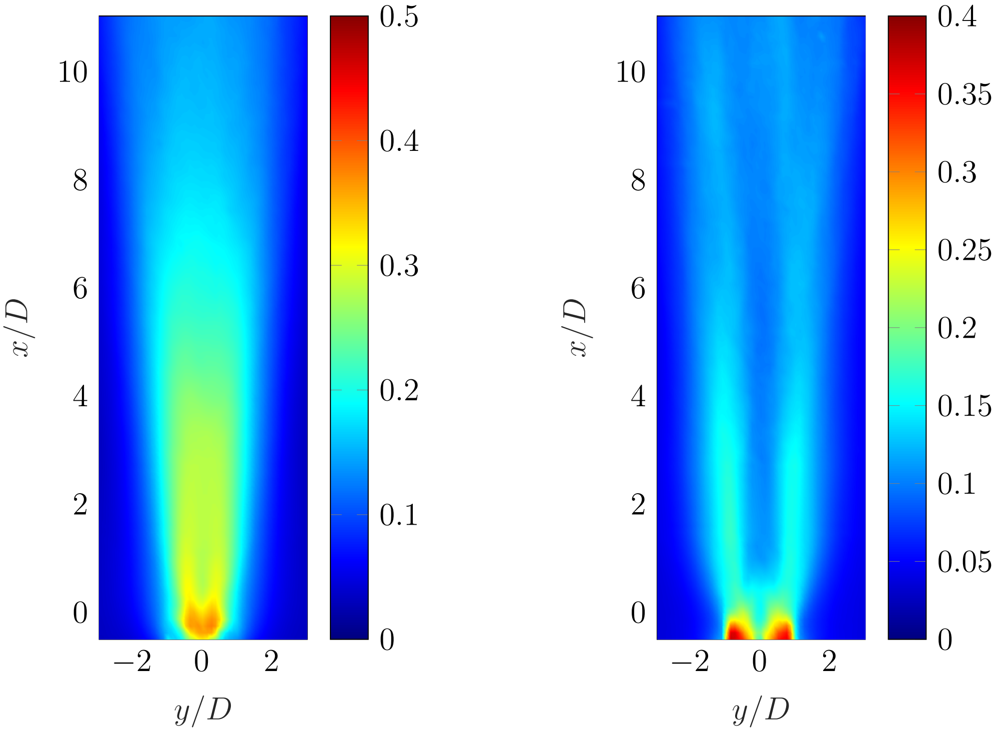

(c) $\text{rms}(u')/U_{\text{in}}$

(d) $\text{rms}(v')/U_{\text{in}}$

Figure C.21: Velocity field at $z = 6D$ and $U_{\text{r}} = 6$. a) Time-averaged streamwise velocity U. a) Time-averaged streamwise velocity U. c) $\text{rms}(u')$. d) $\text{rms}(v')$

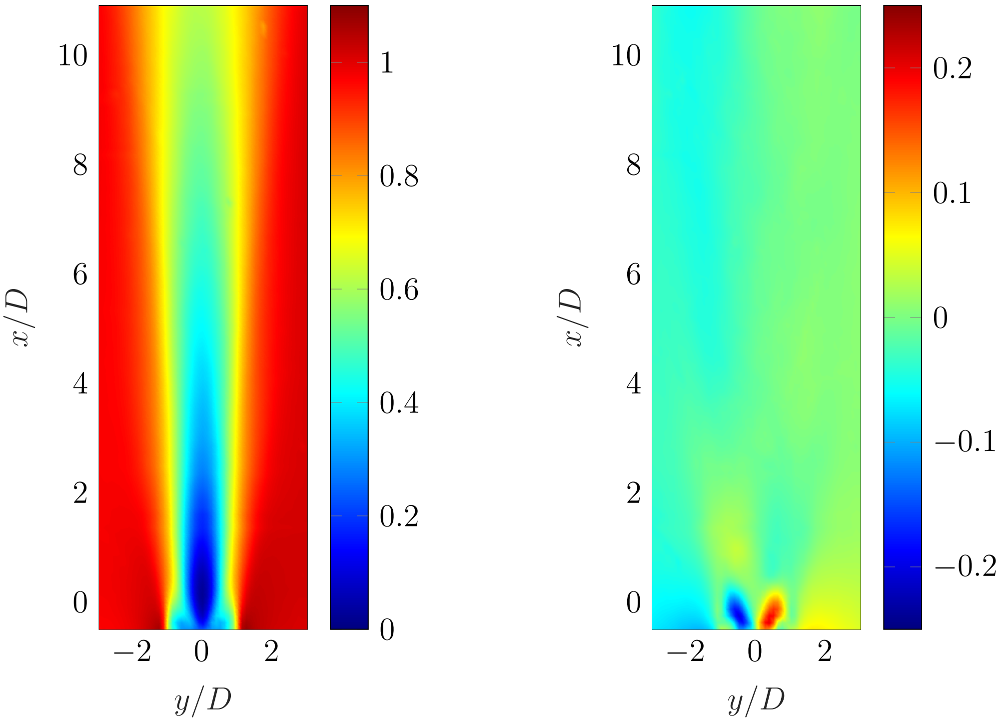

(a) $\overline{U}/U_{\mathrm{in}}$ (b) $\overline{V}/U_{\mathrm{in}}$

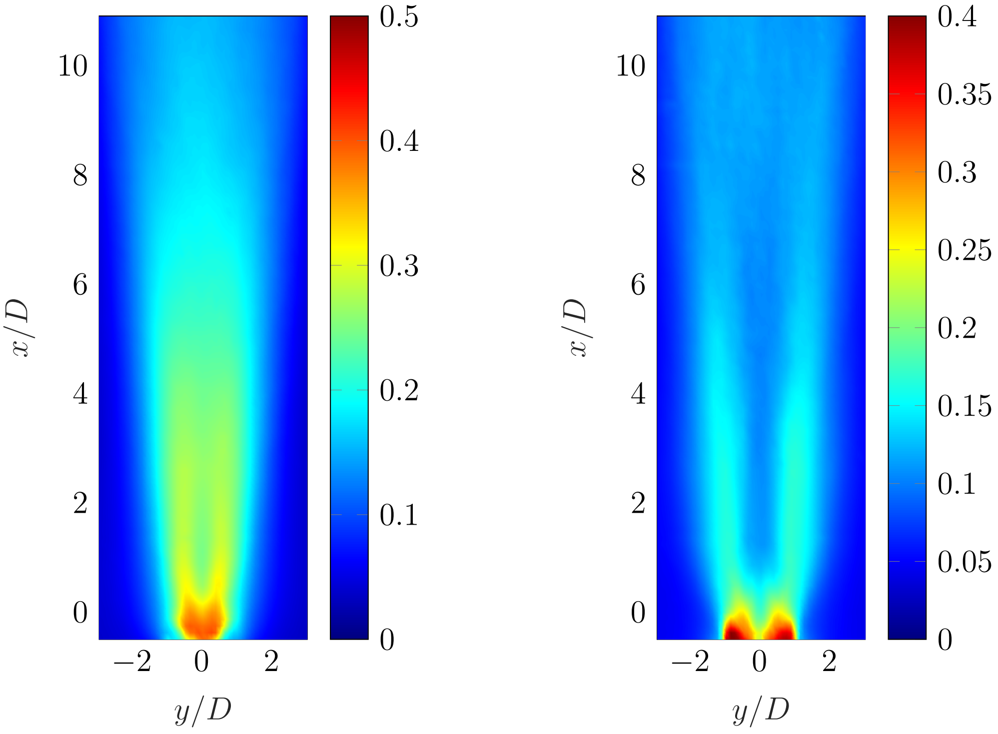

(c) $\mathrm{rms}(u')/U_{\mathrm{in}}$ (d) $\mathrm{rms}(v')/U_{\mathrm{in}}$

Figure C.22: Velocity field at $z = 6D$ and $U_{\mathrm{r}} = 6.7$. a) Time-averaged streamwise velocity U. a) Time-averaged streamwise velocity U. c) $\mathrm{rms}(u')$. d) $\mathrm{rms}(v')$

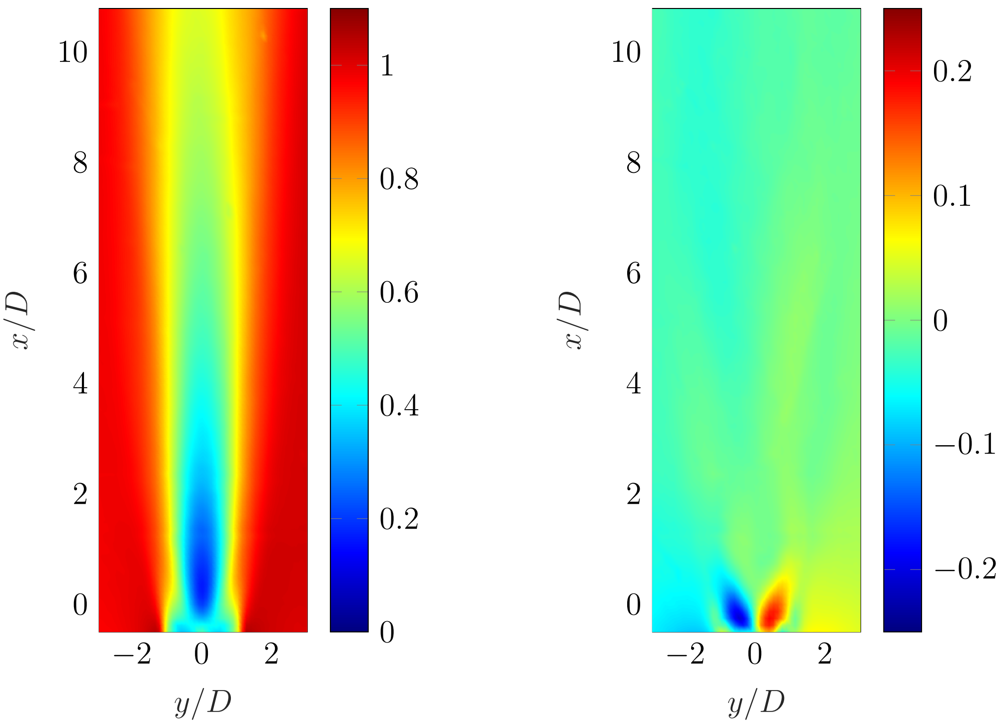

(a) $\overline{U}/U_{\text{in}}$ (b) $\overline{V}/U_{\text{in}}$

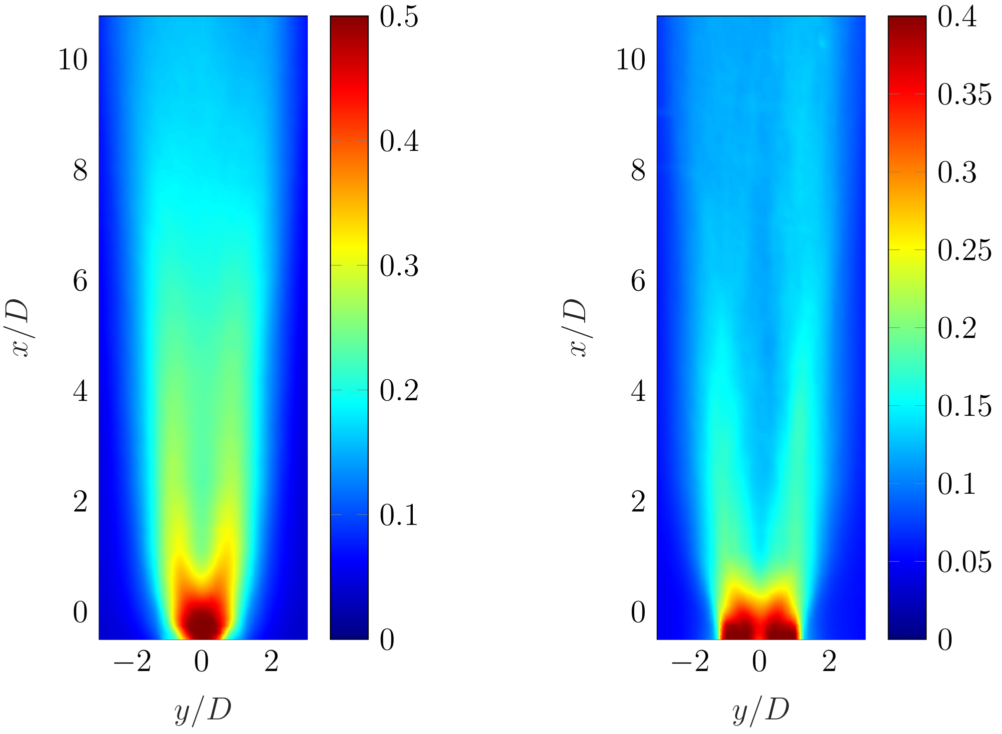

(c) $\text{rms}(u')/U_{\text{in}}$ (d) $\text{rms}(v')/U_{\text{in}}$

Figure C.23: Velocity field at $z = 6D$ and $U_{\text{r}} = 7.4$. a) Time-averaged streamwise velocity U. a) Time-averaged streamwise velocity U. c) $\text{rms}(u')$. d) $\text{rms}(v')$

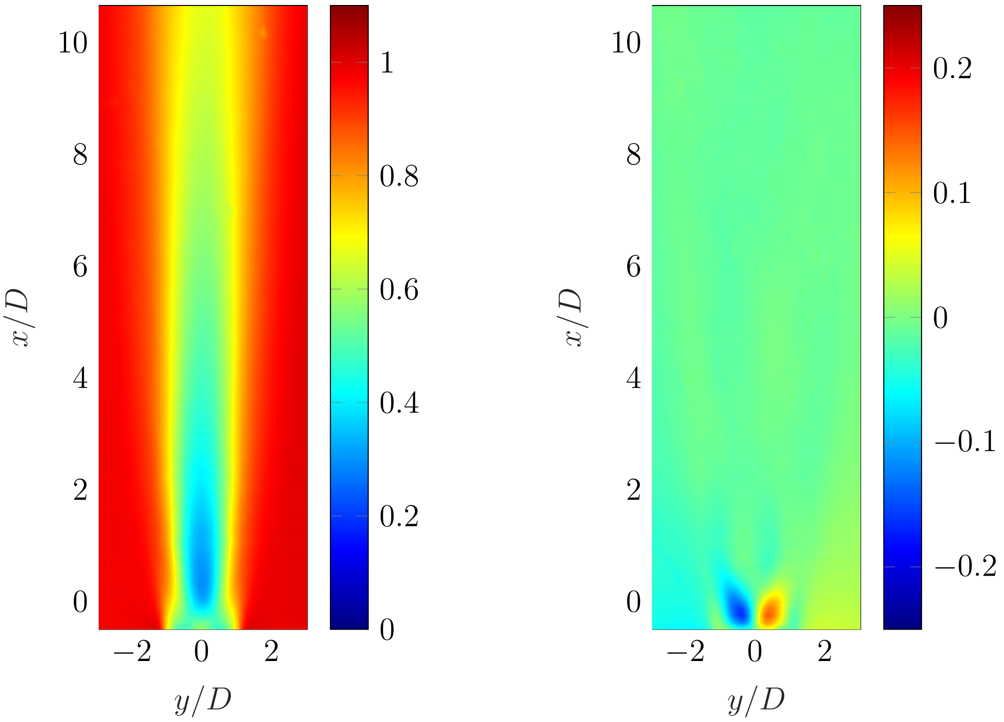

(a) $\overline{U}/U_{\mathrm{in}}$ (b) $\overline{V}/U_{\mathrm{in}}$

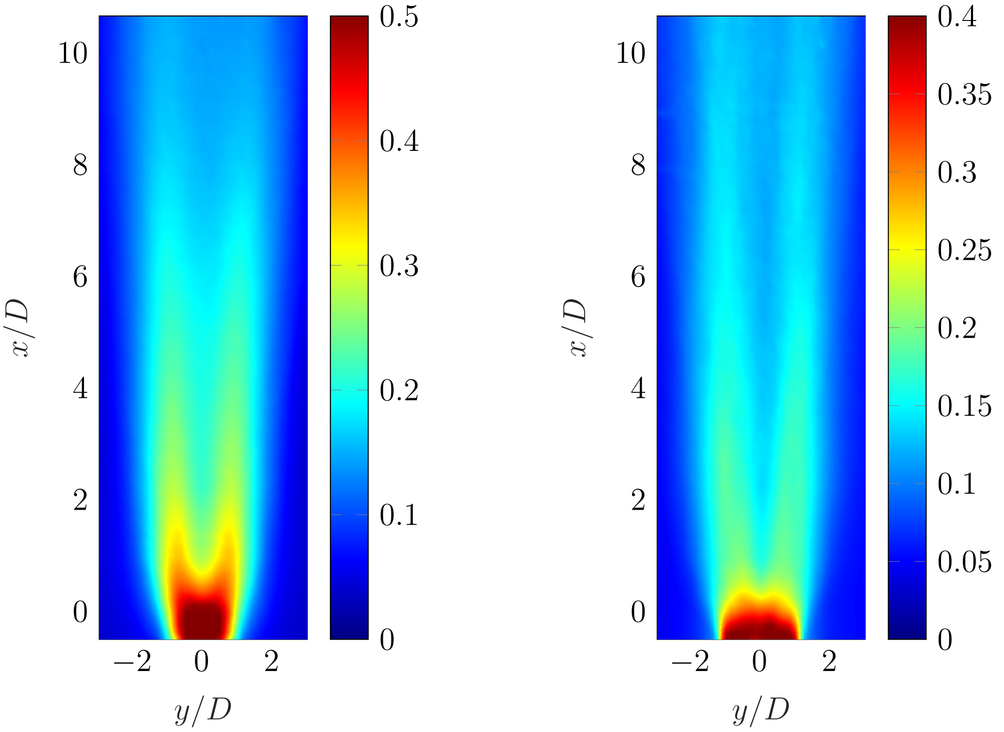

(c) $\mathrm{rms}(u')/U_{\mathrm{in}}$ (d) $\mathrm{rms}(v')/U_{\mathrm{in}}$

Figure C.24: Velocity field at $z = 6D$ and $U_{\mathrm{r}} = 8.3$. a) Time-averaged streamwise velocity U. a) Time-averaged streamwise velocity U. c) $\mathrm{rms}(u')$. d) $\mathrm{rms}(v')$

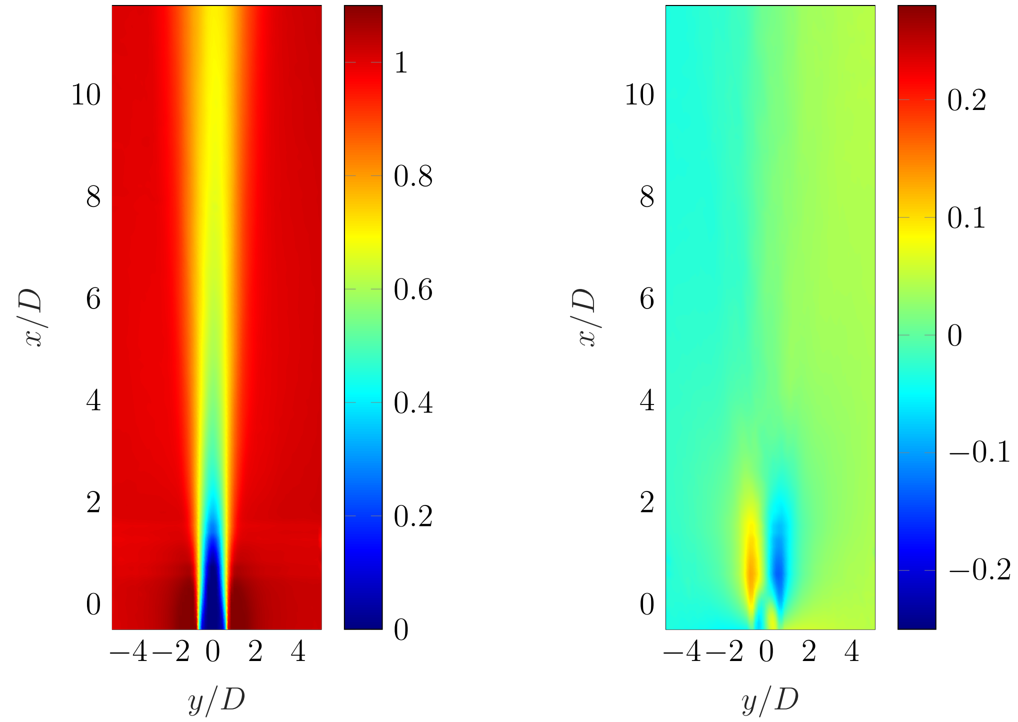

(a) $\overline{U}/U_{\text{in}}$ (b) $\overline{V}/U_{\text{in}}$

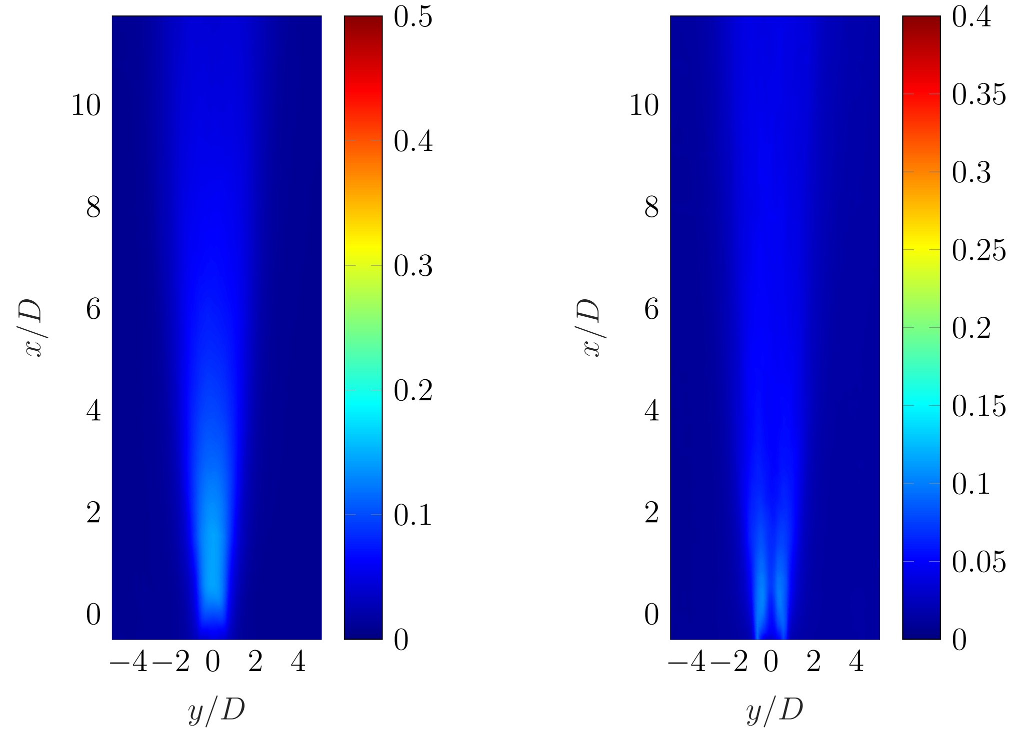

(c) $\text{rms}(u')/U_{\text{in}}$ (d) $\text{rms}(v')/U_{\text{in}}$

Figure C.25: Velocity field at $z = 10D$ and $U_{\text{r}} = 3$. a) Time-averaged streamwise velocity U. a) Time-averaged streamwise velocity U. c) $\text{rms}(u')$. d) $\text{rms}(v')$

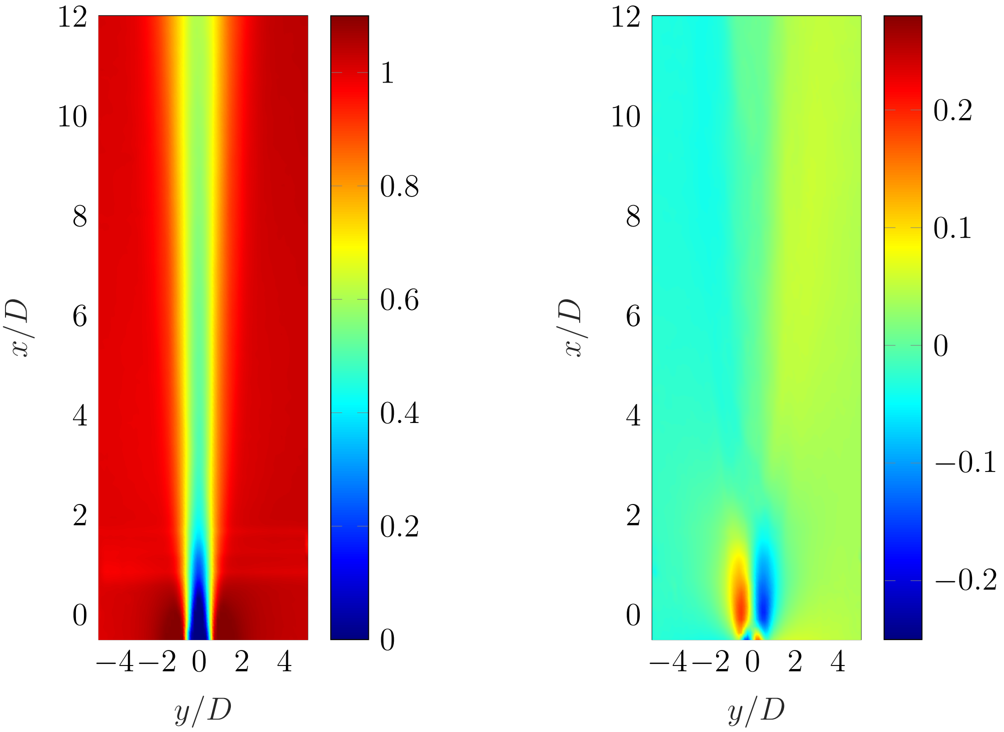

(a) $\overline{U}/U_{\mathrm{in}}$

(b) $\overline{V}/U_{\mathrm{in}}$

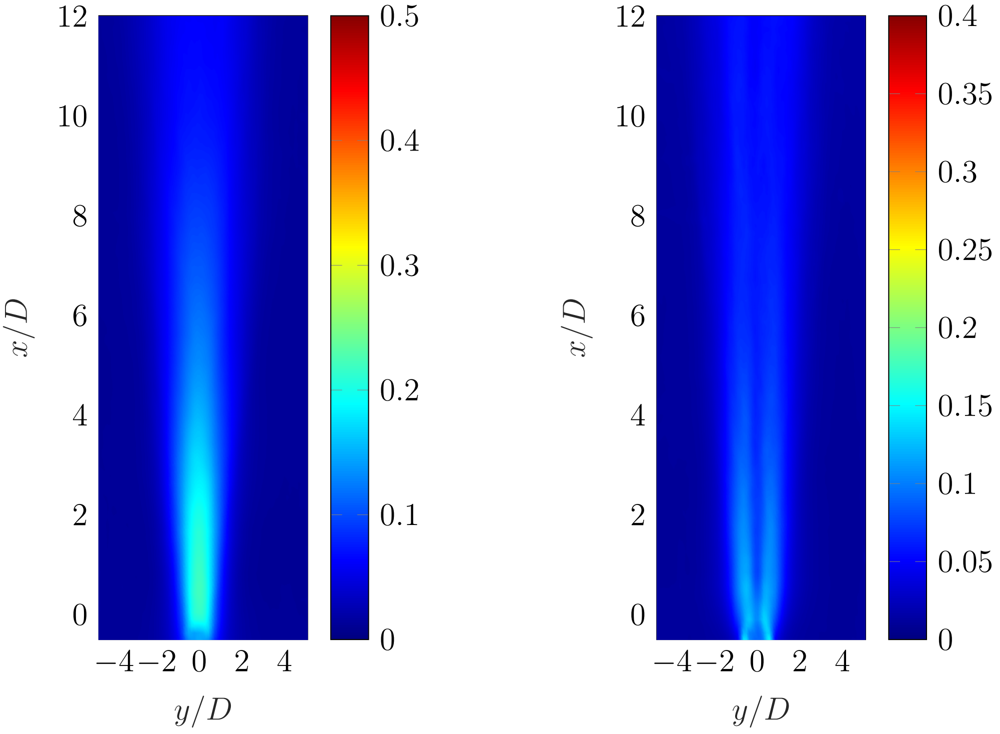

(c) $\mathrm{rms}(u')/U_{\mathrm{in}}$

(d) $\mathrm{rms}(v')/U_{\mathrm{in}}$

Figure C.26: Velocity field at $z = 10D$ and $U_{\mathrm{r}} = 3.8$. a) Time-averaged streamwise velocity U. a) Time-averaged streamwise velocity U. c) $\mathrm{rms}(u')$. d) $\mathrm{rms}(v')$

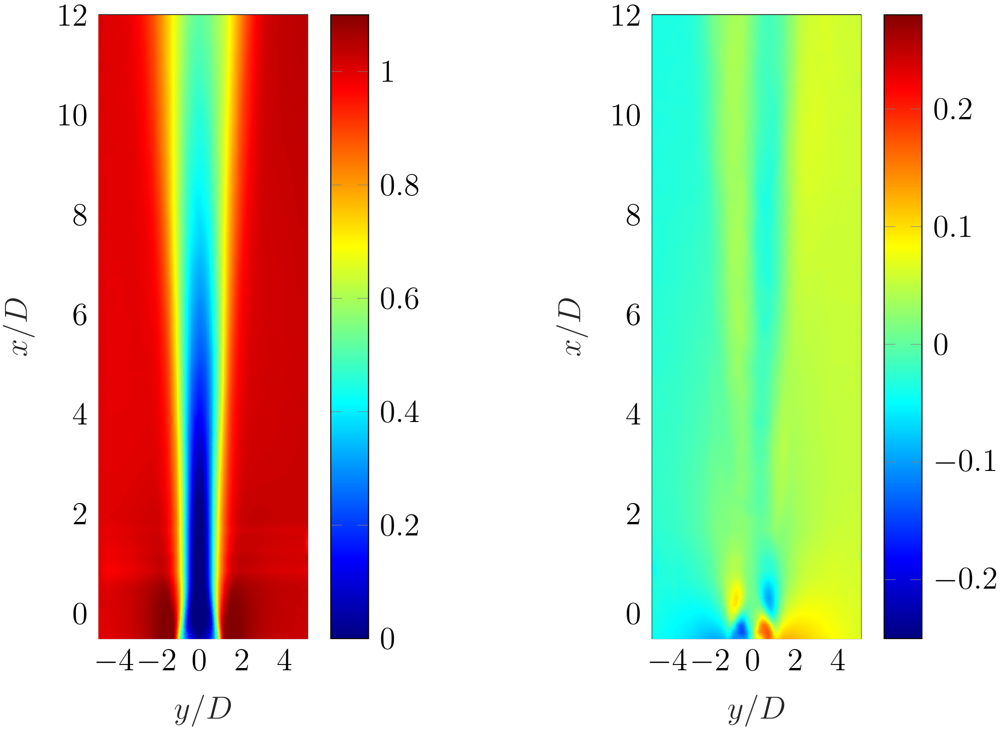

(a) $\overline{U}/U_{\mathrm{in}}$

(b) $\overline{V}/U_{\mathrm{in}}$

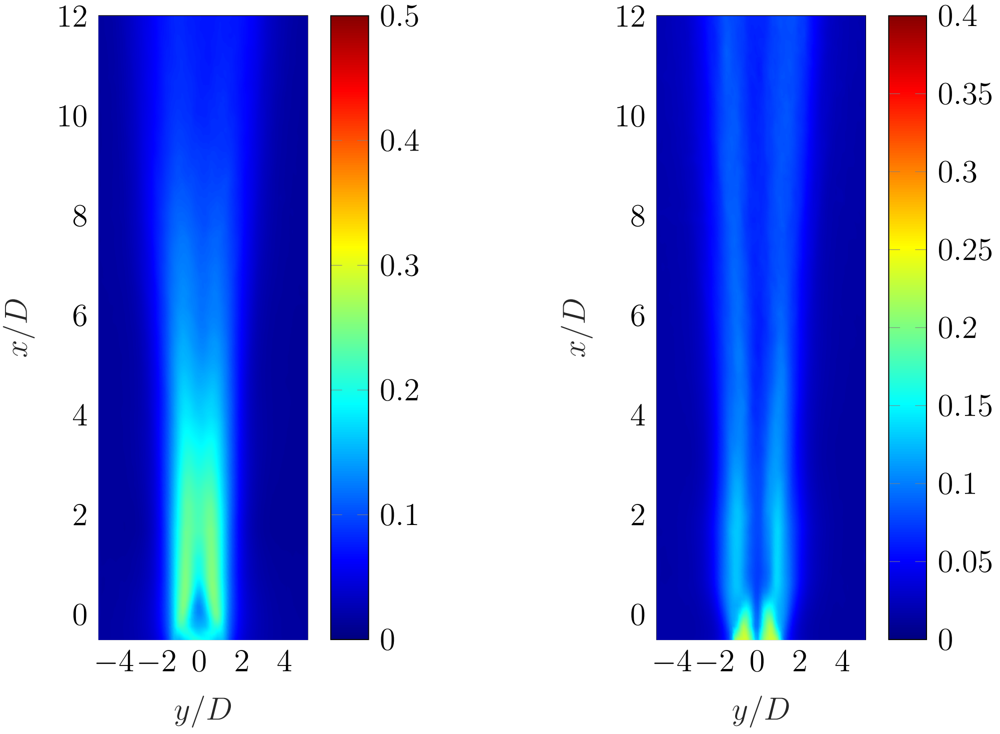

(c) $\mathrm{rms}(u')/U_{\mathrm{in}}$

(d) $\mathrm{rms}(v')/U_{\mathrm{in}}$

Figure C.27: Velocity field at $z = 10D$ and $U_{\mathrm{r}} = 4.5$. a) Time-averaged streamwise velocity U. a) Time-averaged streamwise velocity U. c) $\mathrm{rms}(u')$. d) $\mathrm{rms}(v')$

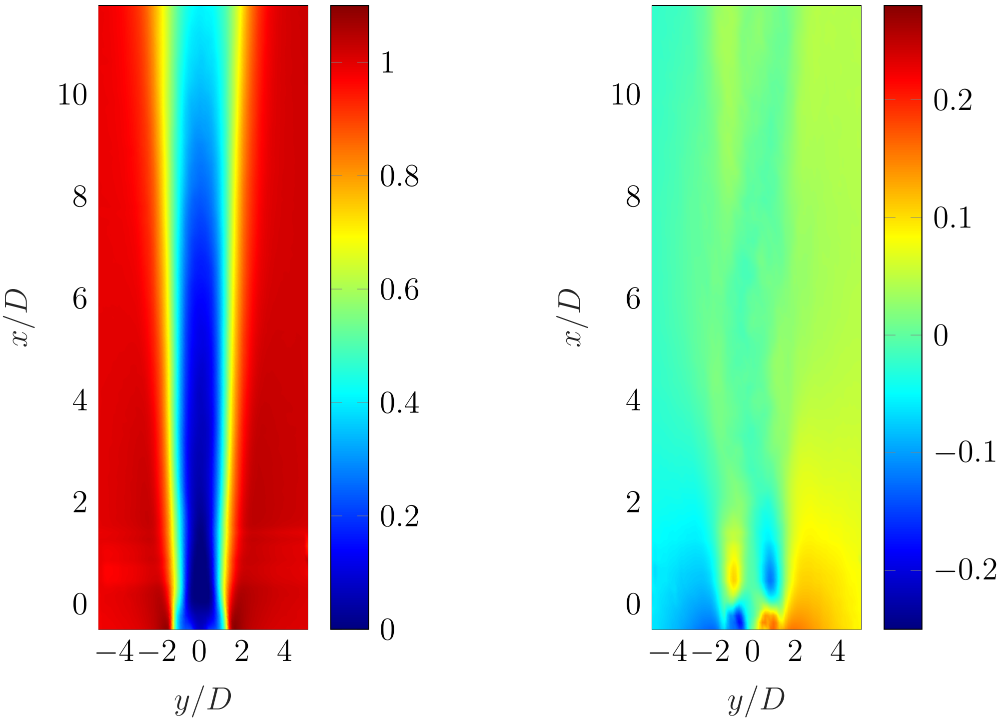

(a) $\overline{U}/U_{\mathrm{in}}$ (b) $\overline{V}/U_{\mathrm{in}}$

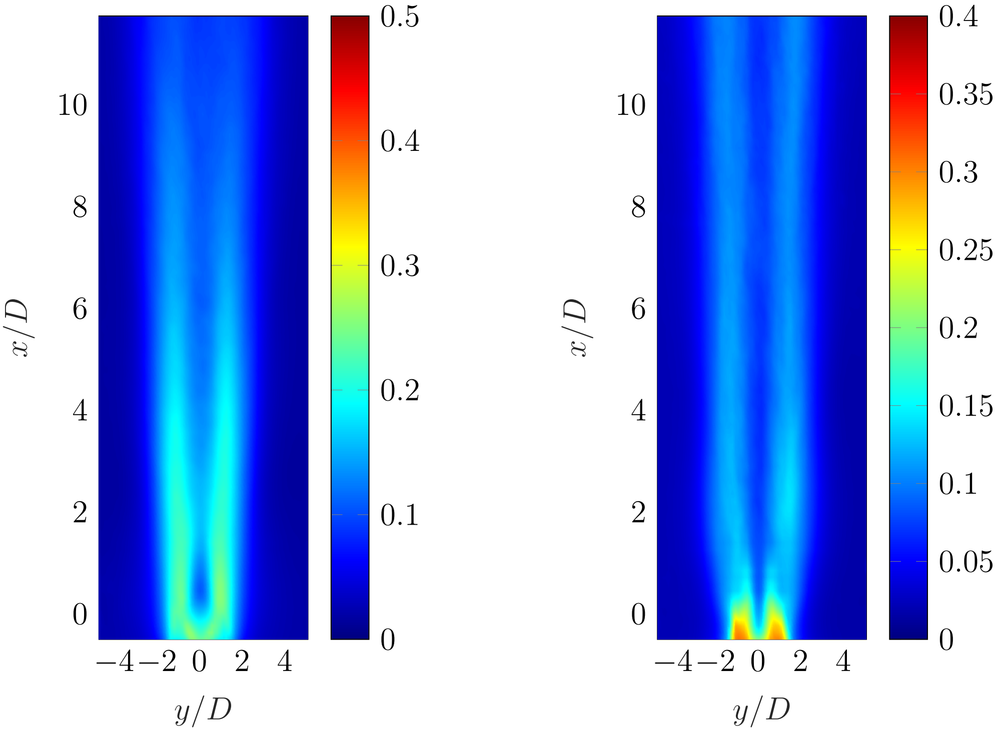

(c) $\mathrm{rms}(u')/U_{\mathrm{in}}$ (d) $\mathrm{rms}(v')/U_{\mathrm{in}}$

Figure C.28: Velocity field at $z = 10D$ and $U_{\mathrm{r}} = 5.2$. a) Time-averaged streamwise velocity U. a) Time-averaged streamwise velocity U. c) $\mathrm{rms}(u')$. d) $\mathrm{rms}(v')$

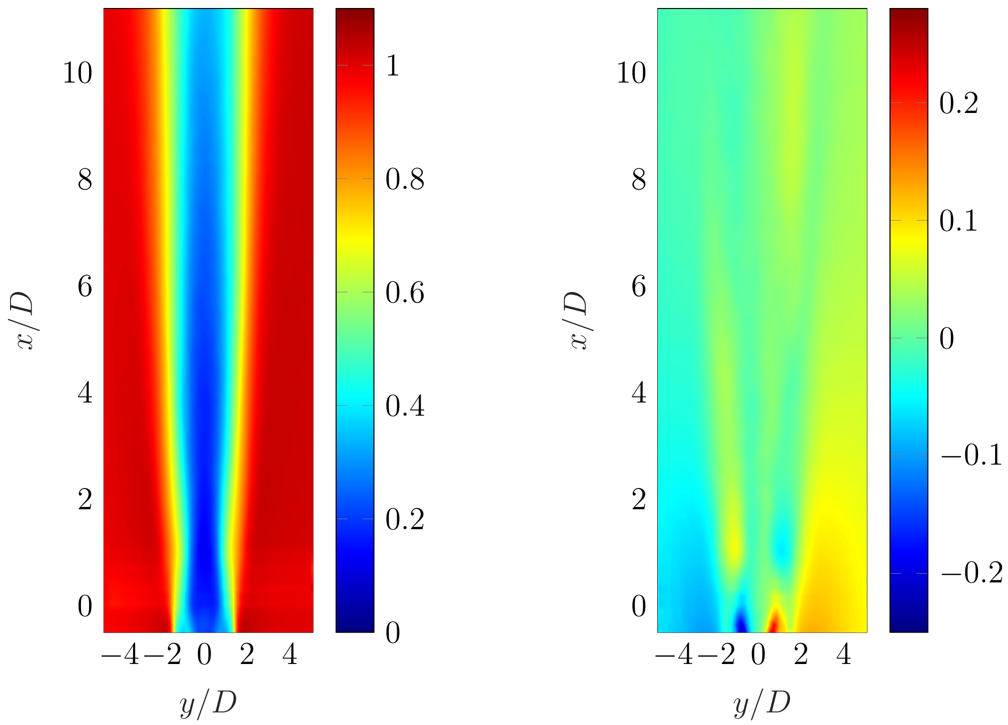

(a) $\overline{U}/U_{\mathrm{in}}$ (b) $\overline{V}/U_{\mathrm{in}}$

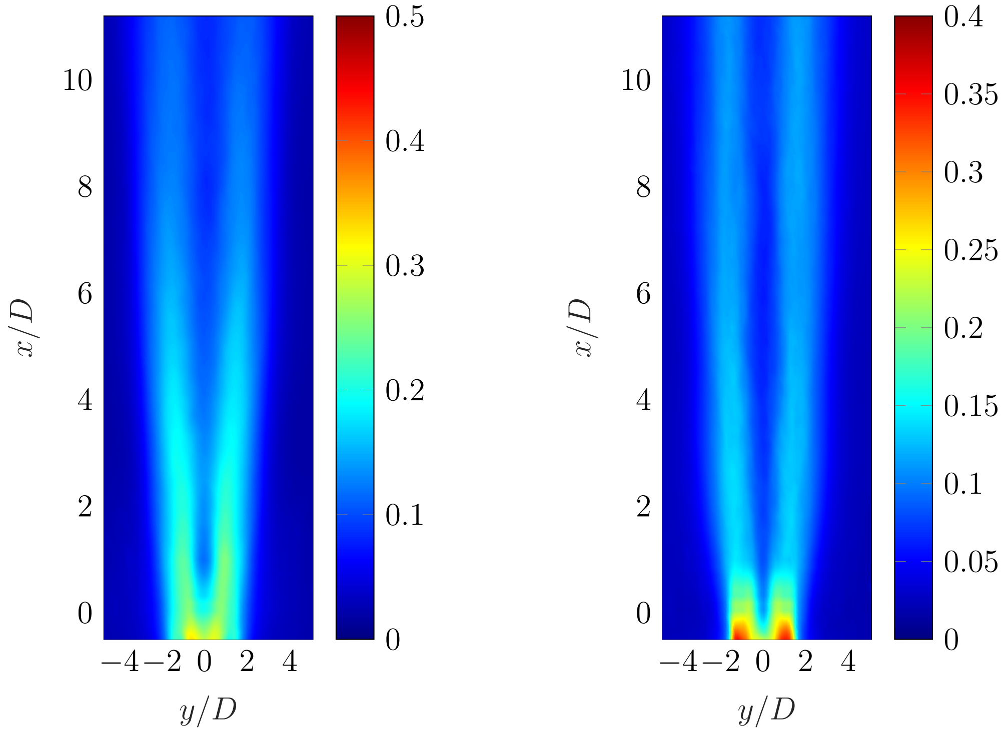

(c) $\mathrm{rms}(u')/U_{\mathrm{in}}$ (d) $\mathrm{rms}(v')/U_{\mathrm{in}}$

Figure C.29: Velocity field at $z = 10D$ and $U_{\mathrm{r}} = 6$. a) Time-averaged streamwise velocity U. a) Time-averaged streamwise velocity U. c) $\mathrm{rms}(u')$. d) $\mathrm{rms}(v')$

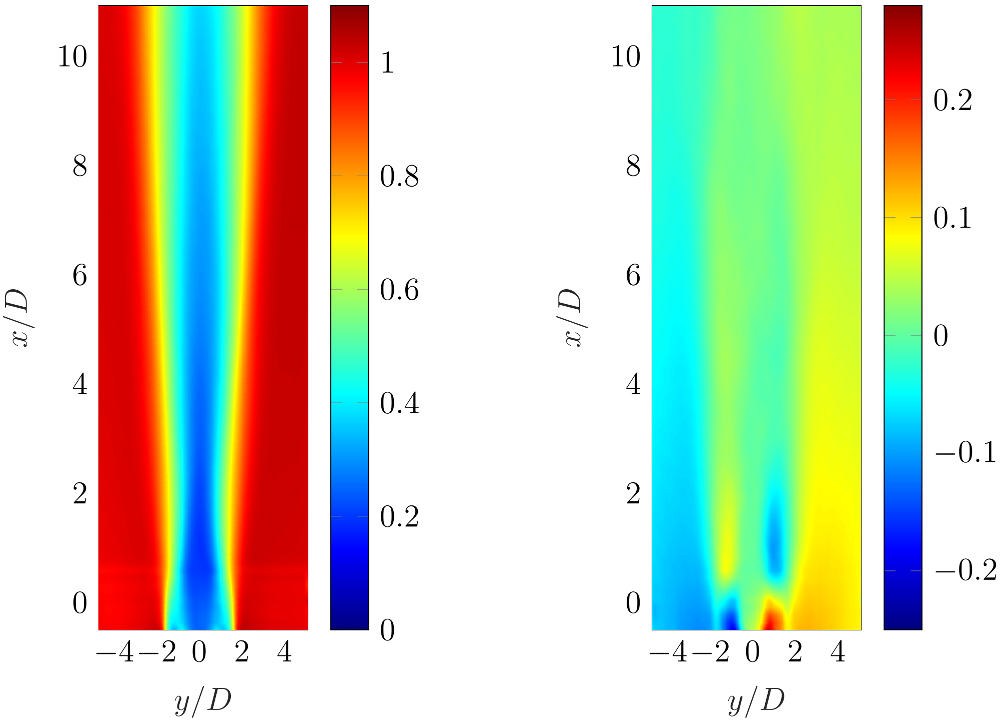

(a) $\overline{U}/U_{\mathrm{in}}$ (b) $\overline{V}/U_{\mathrm{in}}$

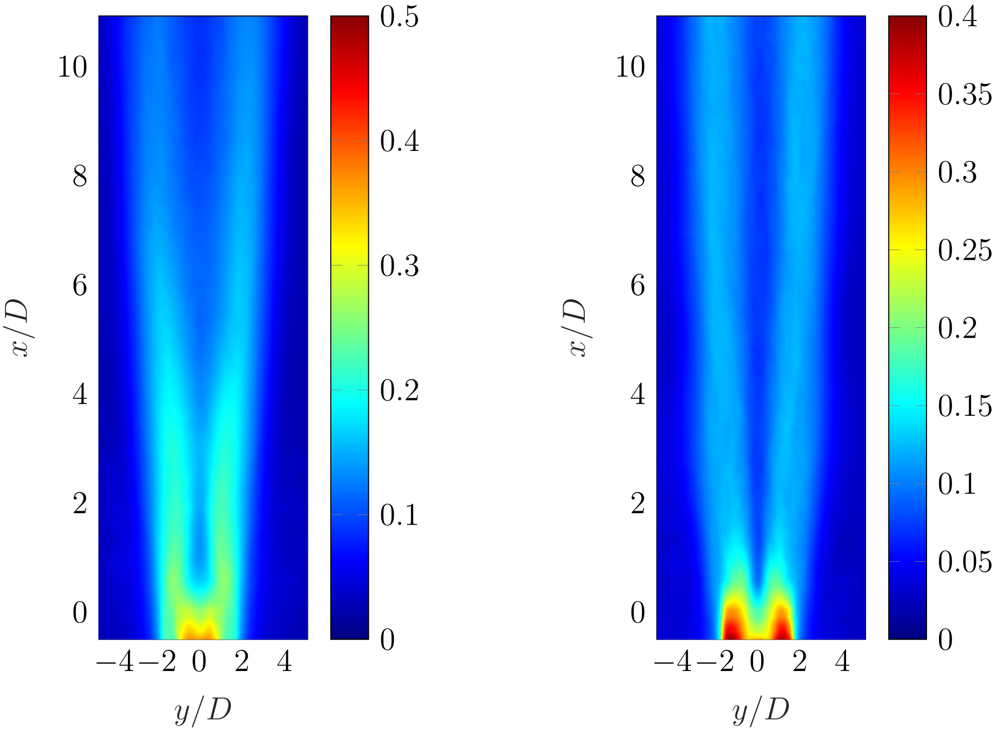

(c) $\mathrm{rms}(u')/U_{\mathrm{in}}$ (d) $\mathrm{rms}(v')/U_{\mathrm{in}}$

Figure C.30: Velocity field at $z = 10D$ and $U_{\mathrm{r}} = 6.7$. a) Time-averaged streamwise velocity U. a) Time-averaged streamwise velocity U. c) $\mathrm{rms}(u')$. d) $\mathrm{rms}(v')$

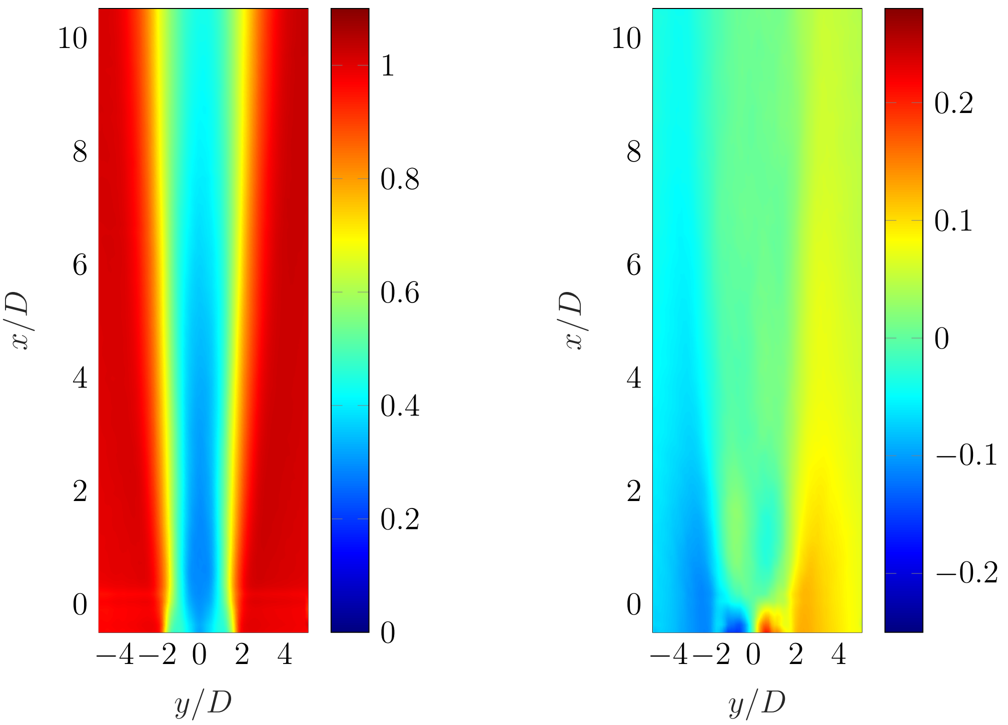

(a) $\overline{U}/U_{\mathrm{in}}$ (b) $\overline{V}/U_{\mathrm{in}}$

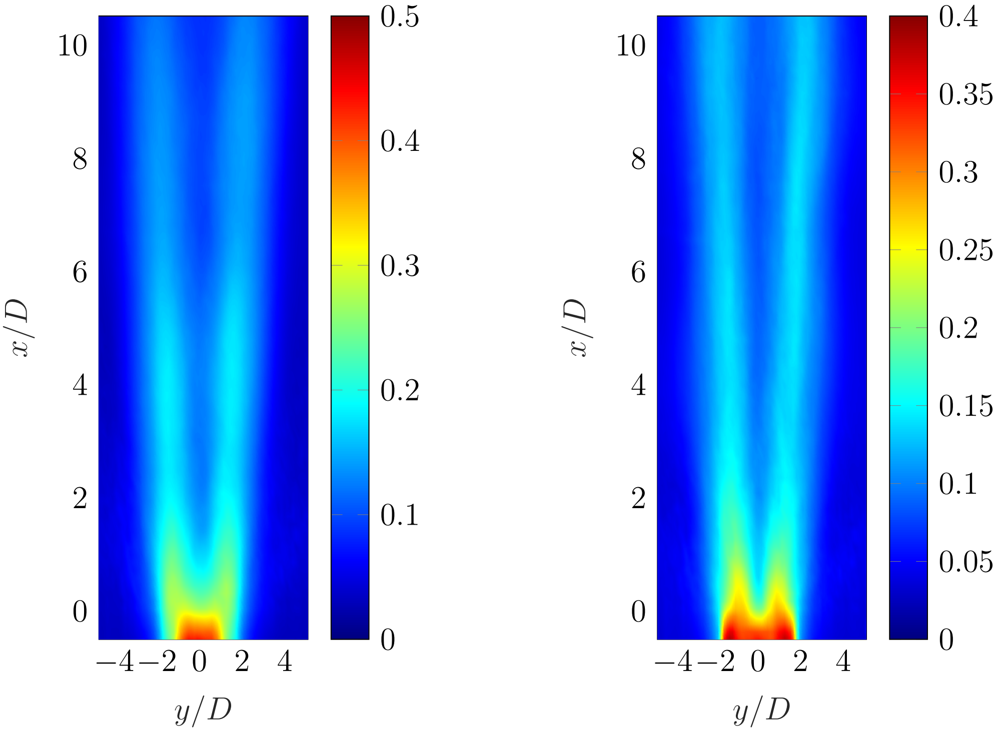

(c) $\mathrm{rms}(u')/U_{\mathrm{in}}$ (d) $\mathrm{rms}(v')/U_{\mathrm{in}}$

Figure C.31: Velocity field at $z = 10D$ and $U_{\mathrm{r}} = 7.4$. a) Time-averaged streamwise velocity U. a) Time-averaged streamwise velocity U. c) $\mathrm{rms}(u')$. d) $\mathrm{rms}(v')$

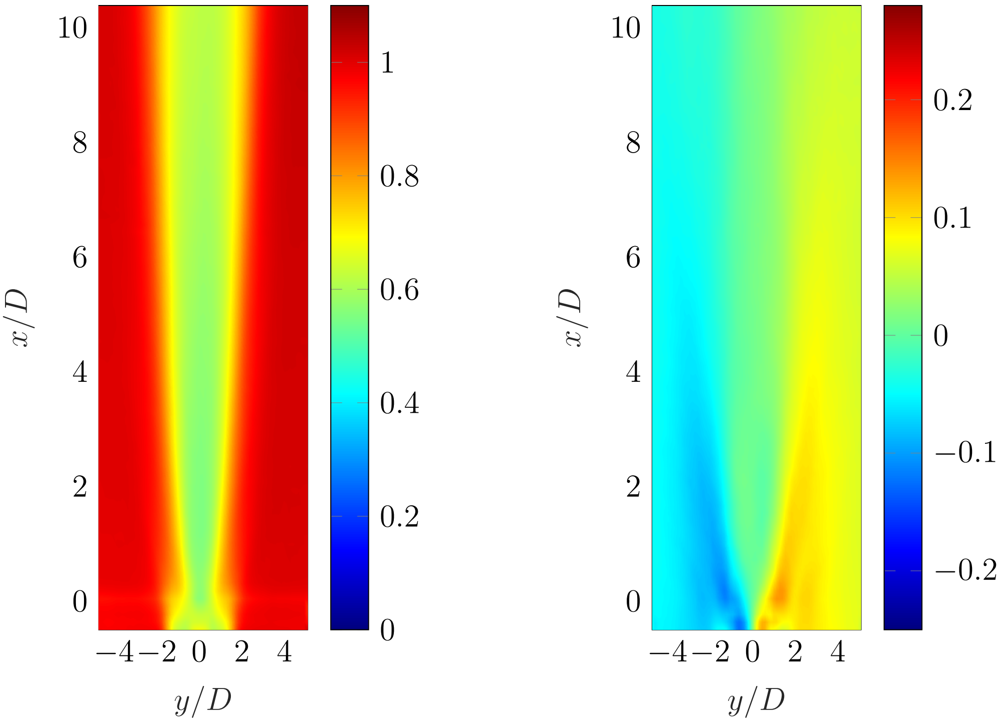

(a) $\overline{U}/U_{\mathrm{in}}$ (b) $\overline{V}/U_{\mathrm{in}}$

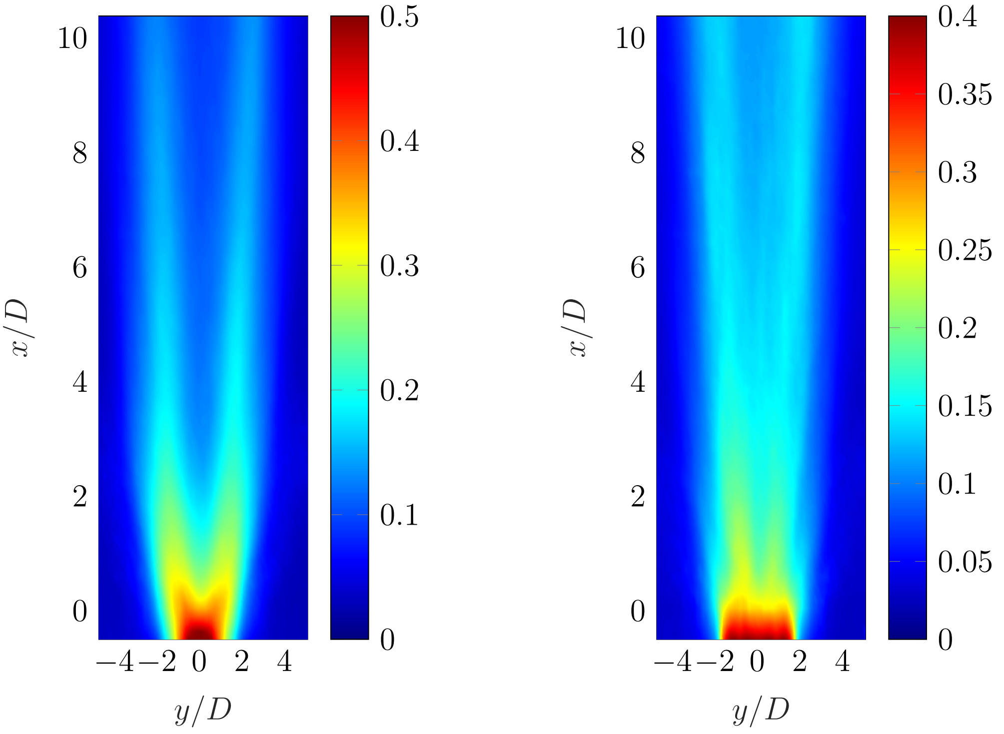

(c) $\mathrm{rms}(u')/U_{\mathrm{in}}$ (d) $\mathrm{rms}(v')/U_{\mathrm{in}}$

Figure C.32: Velocity field at $z = 10D$ and $U_{\mathrm{r}} = 8.3$. a) Time-averaged streamwise velocity U. a) Time-averaged streamwise velocity U. c) $\mathrm{rms}(u')$. d) $\mathrm{rms}(v')$

Appendix D

Numerical model: testing and results

D.1 Sensitivity analysis

The numerical VIV model described in Chapter 7.2.2 was tested under changes in mesh resolution and compared with an experimental low $m^*\zeta$ two degree-of-freedom cylinder [41]. The mass-spring-damping model was solved using the Runge-Kutta fourth-order algorithm, whereas the solution of the flow equations was performed using different spatial discretisation schemes. These parameters were selected based on previous numerical studies [45, 35, 105]. This section analyses the effects of different integration schemes on the cylinder response.

The case study selected for the sensitivity analysis followed the parameters described in Chapter 7.3. As a summary, the numerical model consists on a two degree-of-freedom elastically mounted cylinder with $D = 38.1$ mm, $f_{\mathrm{nw}} = 0.4$ Hz, $m^* = 2.6$, and $\xi = 0.00361$ [41]. The cylinder was tested under increasing velocity conditions (Chapter 3.3.1). The inflow velocity started at $U_{\mathrm{r}} = 2$ and was slowly increased for 50 seconds until $U_{\mathrm{r}} = 6$. The time step was $\Delta_{\mathrm{t}} = 0.0015$ s, ensuring a CFL number of less than one.

D.1.1 Equation of motion

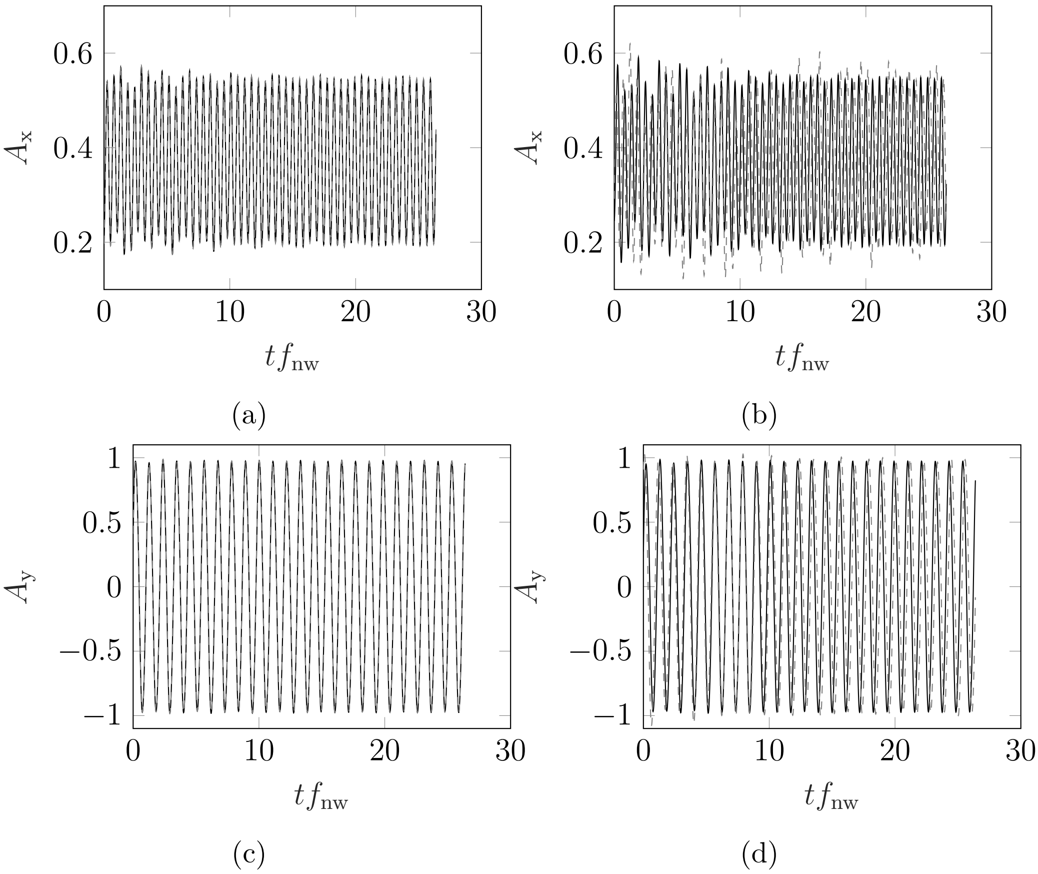

Figure D.1: Effect of the integration scheme on the streamwise (up) and crossflow (down) cylinder response. a,c) NB14 (black) vs NB16 (dashed grey). b,d) RK4 (black) vs RK5 (dashed grey)

The mass-spring-damping model was solved using the Runge-Kutta fourth-order algorithm (Chapter 4.3). Previous studies considered alternative integration schemes to solve the equation of motion and estimate the cylinder displacement, velocity and acceleration at each numerical time step (e.g., [32, 105]). The mass-spring-stiffness model was solved using four integration schemes: Newmark-Beta constant acceleration (NB14) [72], Newmark-Beta linear acceleration (NB16) [72], Runge-Kutta fourth-order (RK4, Chapter 4.3), and Runge-Kutta fifth-order (RK5) [95]. Figure D.1 compares the streamwise and crossflow motion under the previously described integration schemes. The results show an excellent agreement between cylinder responses. The use of RK5 scheme leads to a slightly higher modulation in the streamwise response and a 1.5% lower crossflow oscillation frequency than the other integration schemes. Overall, these results show that the algorithm used to solve the mass-spring-damping model plays a minimal role in the cylinder response as long as the numerical time step is sufficiently low.

D.1.2 Pressure-velocity coupling

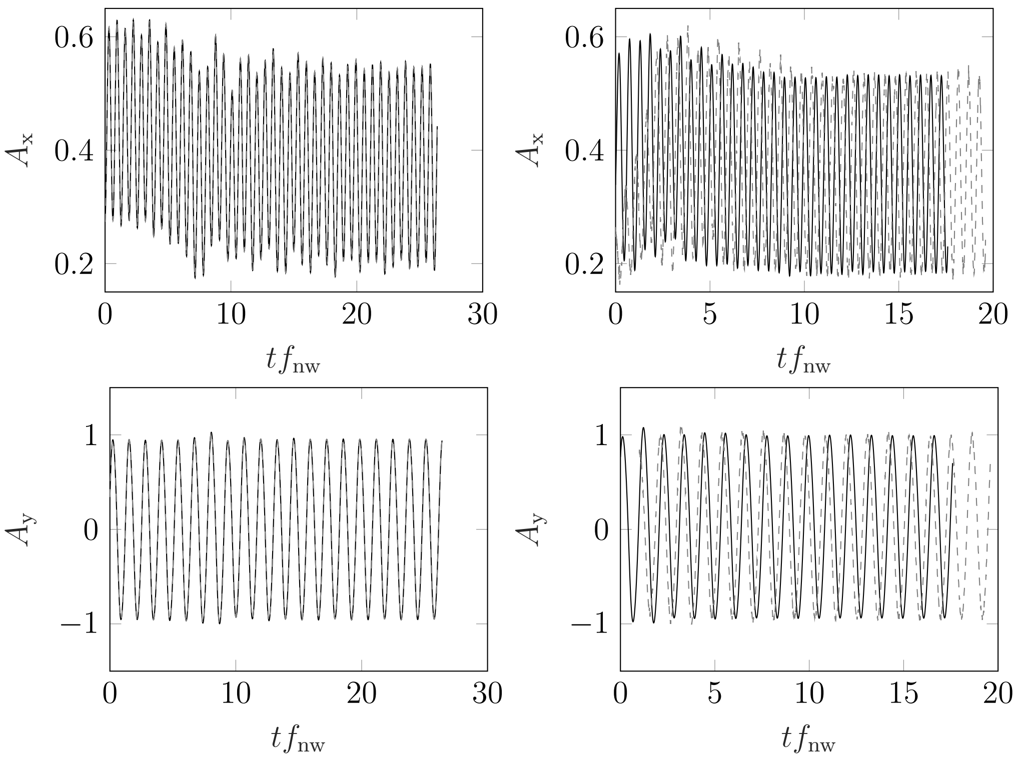

Figure D.2: Effect of the pressure-velocity coupling scheme on the streamwise (up) and crossflow (down) cylinder response. a,c) SIMPLE (black) vs SIMPLEC (dashed grey). b,d) PISO (black) vs Coupled (dashed grey)

The discretisation of the momentum equation requires the interpolation of the pressure and velocity from their cell-centre to their respective face values. Four discretisation schemes available in Fluent [22] were tested: SIMPLE, SIMPLEC, PISO, and Coupled. The Runge-Kutta fourth-order algorithm was used to solve the mass-spring-damping model. Figure D.2. The Coupled scheme led to slight instabilities near the peak of the oscillatory motion, especially in the streamwise direction. Still, the results show an excellent agreement across cylinder responses independent of the pressure-velocity coupling scheme used.

D.1.3 Numerical vs experimental results

The cylinder trajectory and time-history displacement of the numerical model (Chapter 7) are presented in this section. The tested three-dimensional force correction factor was $C_F = [0.6, 0.8, 1, 1.2, 1.4]$. The experimental results are also plotted for comparison purposes.

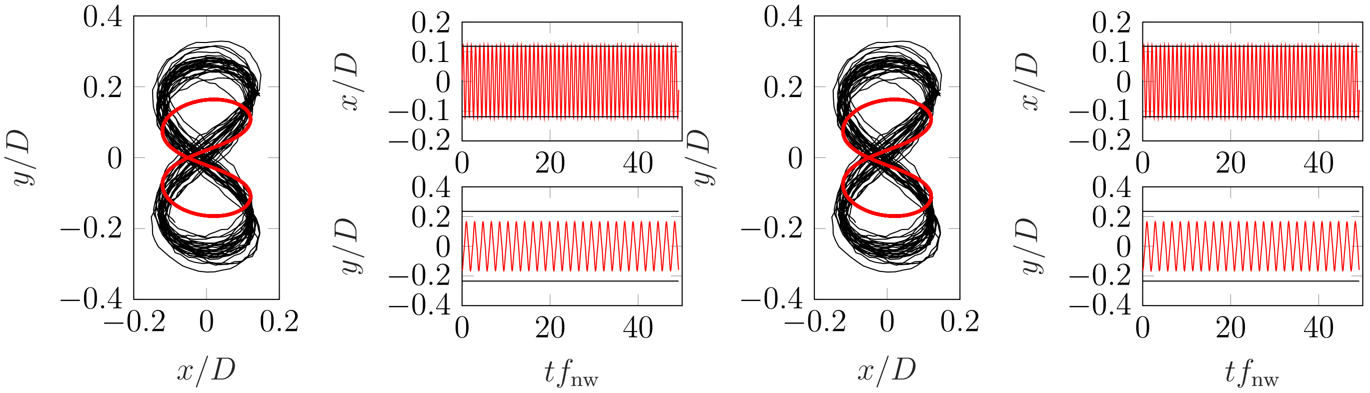

(a) $C_{\mathrm{F}} = 0.6$ (b) $C_{\mathrm{F}} = 0.6$ (c) $C_{\mathrm{F}} = 0.8$ (d) $C_{\mathrm{F}} = 0.8$

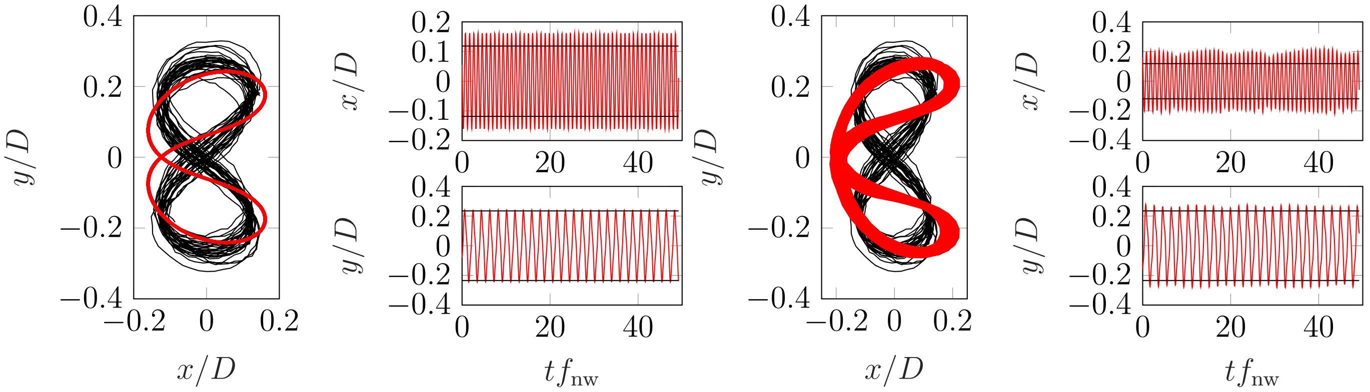

(e) $C_{\mathrm{F}} = 1$ (f) $C_{\mathrm{F}} = 1$ (g) $C_{\mathrm{F}} = 1.2$ (h) $C_{\mathrm{F}} = 1.2$

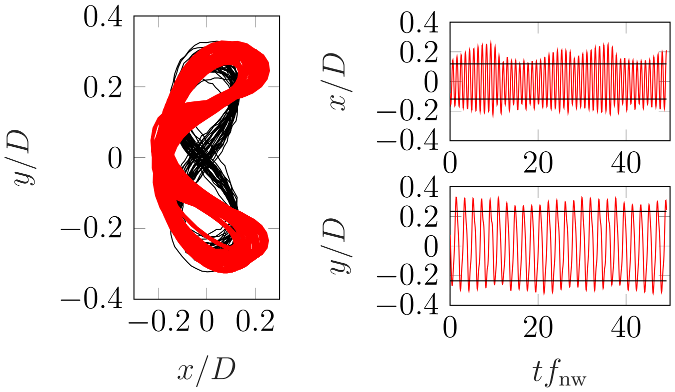

(i) $C_{\mathrm{F}} = 1.4$ (j) $C_{\mathrm{F}} = 1.4$

Figure D.3: Cylinder trajectory (a,c,e,g,i) and time-history (b,d,f,h,j) at $U_{\mathrm{r}} = 2.95$. Red: Numerical results. Horizontal black line: experimental maximum crossflow and streamwise amplitude

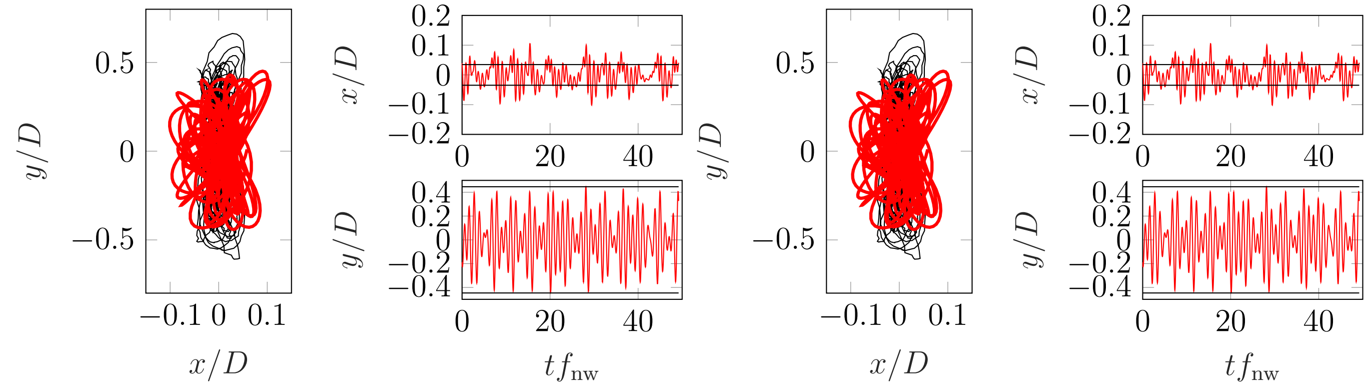

(a) $C_{\mathrm{F}} = 0.6$ (b) $C_{\mathrm{F}} = 0.6$ (c) $C_{\mathrm{F}} = 0.8$ (d) $C_{\mathrm{F}} = 0.8$

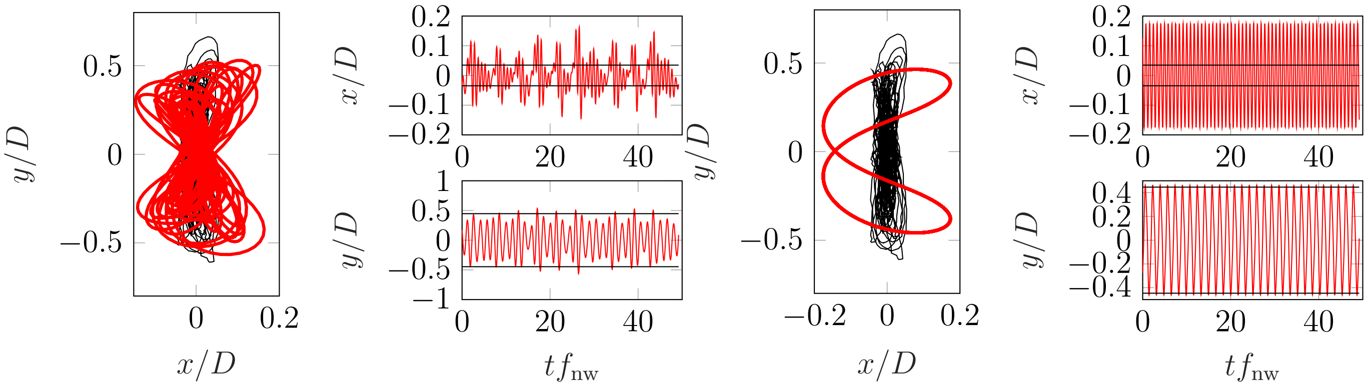

(e) $C_{\mathrm{F}} = 1$ (f) $C_{\mathrm{F}} = 1$ (g) $C_{\mathrm{F}} = 1.2$ (h) $C_{\mathrm{F}} = 1.2$

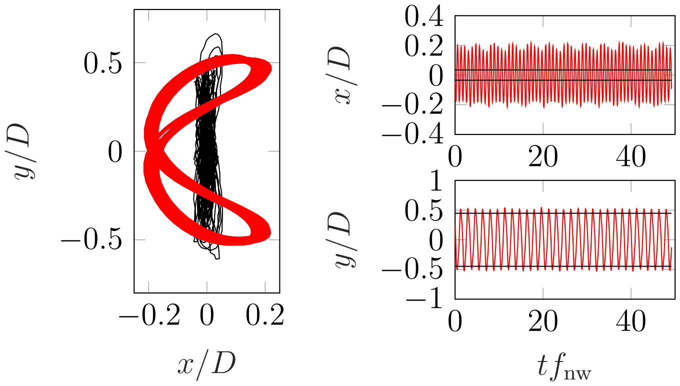

(i) $C_{\mathrm{F}} = 1.4$ (j) $C_{\mathrm{F}} = 1.4$

Figure D.4: Cylinder trajectory (a,c,e,g,i) and time-history (b,d,f,h,j) at $U_{\mathrm{r}} = 3.74$. Red: Numerical results. Horizontal black line: experimental maximum crossflow and streamwise amplitude

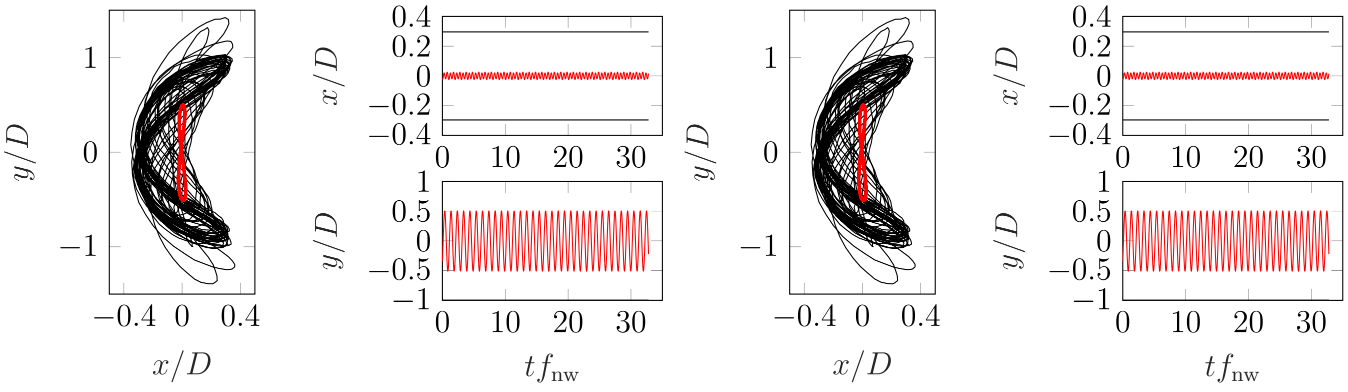

(a) $C_{\mathrm{F}} = 0.6$ (b) $C_{\mathrm{F}} = 0.6$ (c) $C_{\mathrm{F}} = 0.8$ (d) $C_{\mathrm{F}} = 0.8$

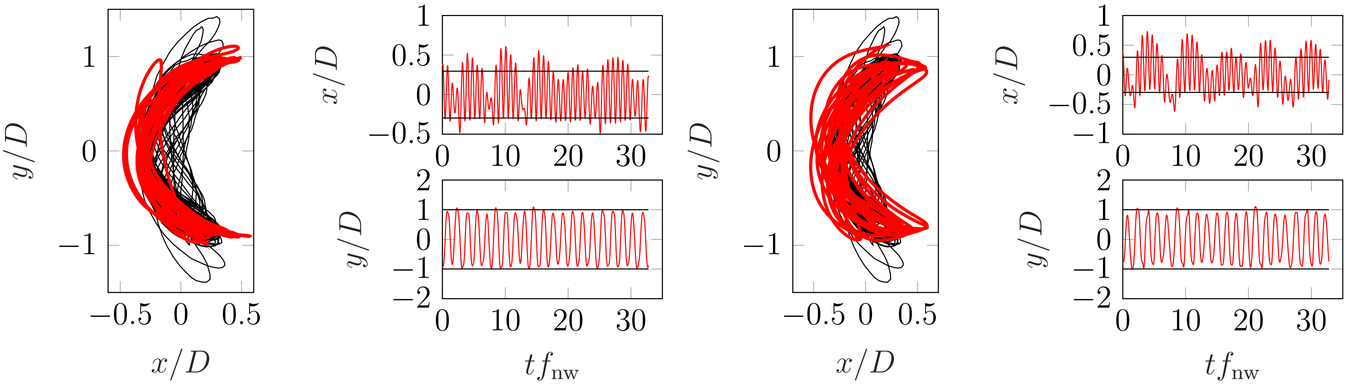

(e) $C_{\mathrm{F}} = 1$ (f) $C_{\mathrm{F}} = 1$ (g) $C_{\mathrm{F}} = 1.2$ (h) $C_{\mathrm{F}} = 1.2$

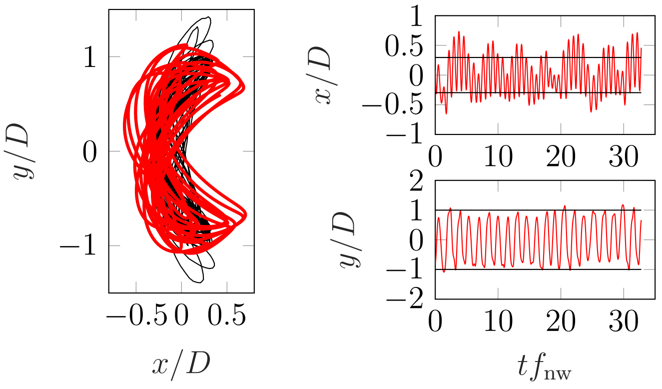

(i) $C_{\mathrm{F}} = 1.4$ (j) $C_{\mathrm{F}} = 1.4$

Figure D.5: Cylinder trajectory (a,c,e,g,i) and time-history (b,d,f,h,j) at $U_{\mathrm{r}} = 4.55$. Red: Numerical results. Horizontal black line: experimental maximum crossflow and streamwise amplitude

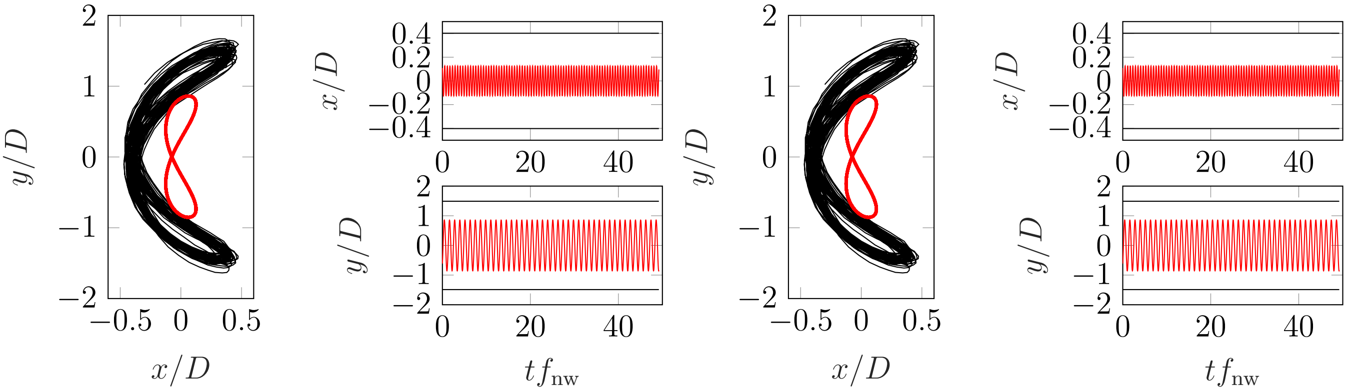

(a) $C_{\mathrm{F}} = 0.6$ (b) $C_{\mathrm{F}} = 0.6$ (c) $C_{\mathrm{F}} = 0.8$ (d) $C_{\mathrm{F}} = 0.8$

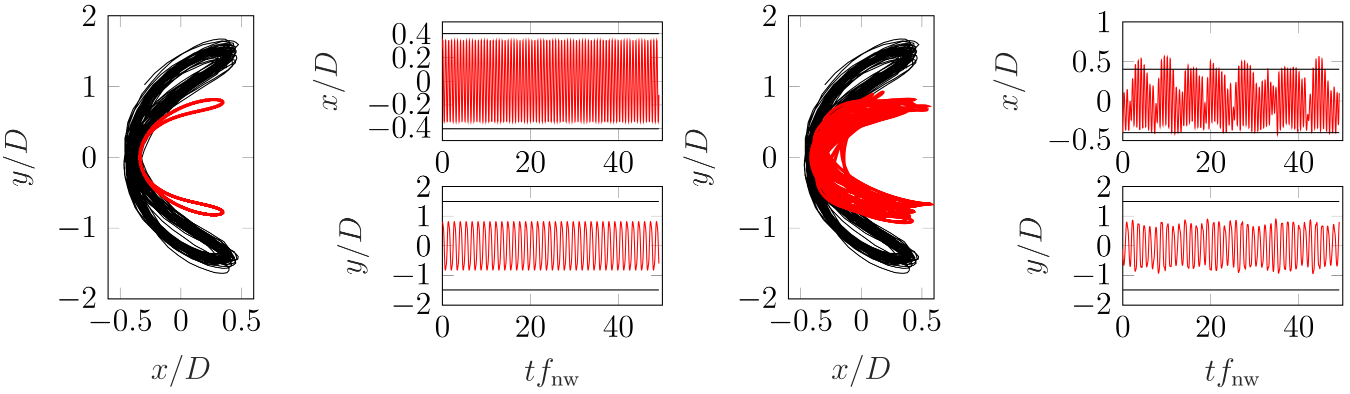

(e) $C_{\mathrm{F}} = 1$ (f) $C_{\mathrm{F}} = 1$ (g) $C_{\mathrm{F}} = 1.2$ (h) $C_{\mathrm{F}} = 1.2$

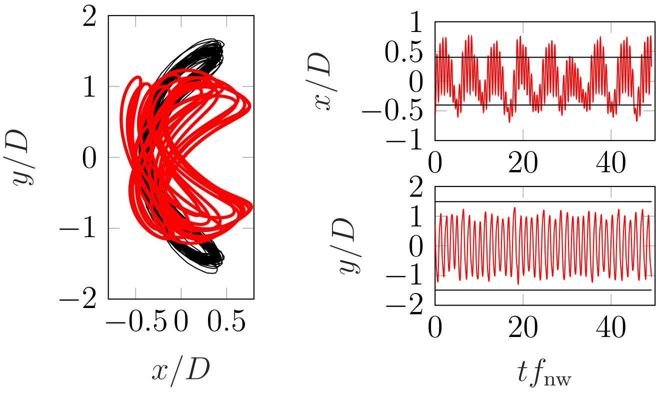

(i) $C_{\mathrm{F}} = 1.4$ (j) $C_{\mathrm{F}} = 1.4$

Figure D.6: Cylinder trajectory (a,c,e,g,i) and time-history (b,d,f,h,j) at $U_{\mathrm{r}} = 5.21$. Red: Numerical results. Horizontal black line: experimental maximum crossflow and streamwise amplitude

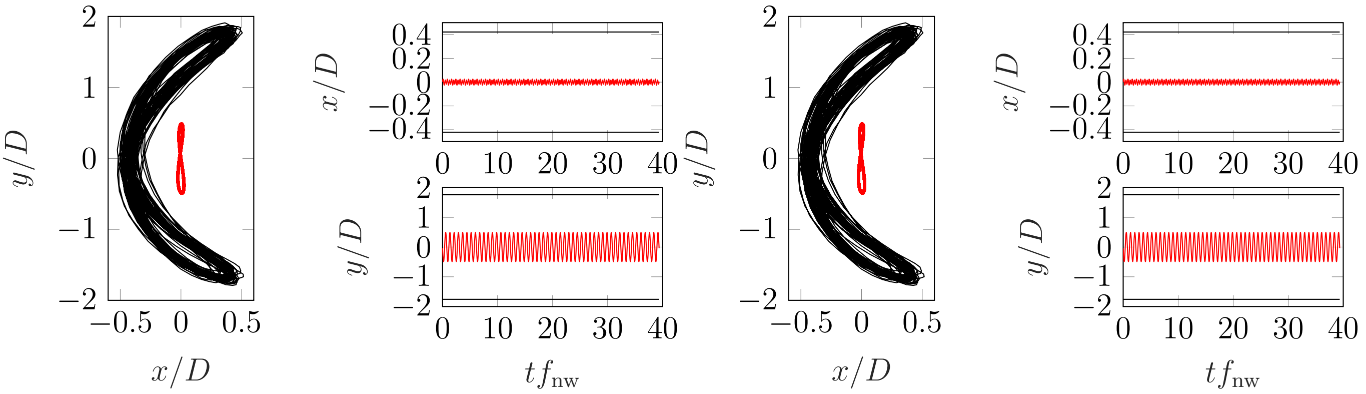

(a) $C_{\mathrm{F}} = 0.6$ (b) $C_{\mathrm{F}} = 0.6$ (c) $C_{\mathrm{F}} = 0.8$ (d) $C_{\mathrm{F}} = 0.8$

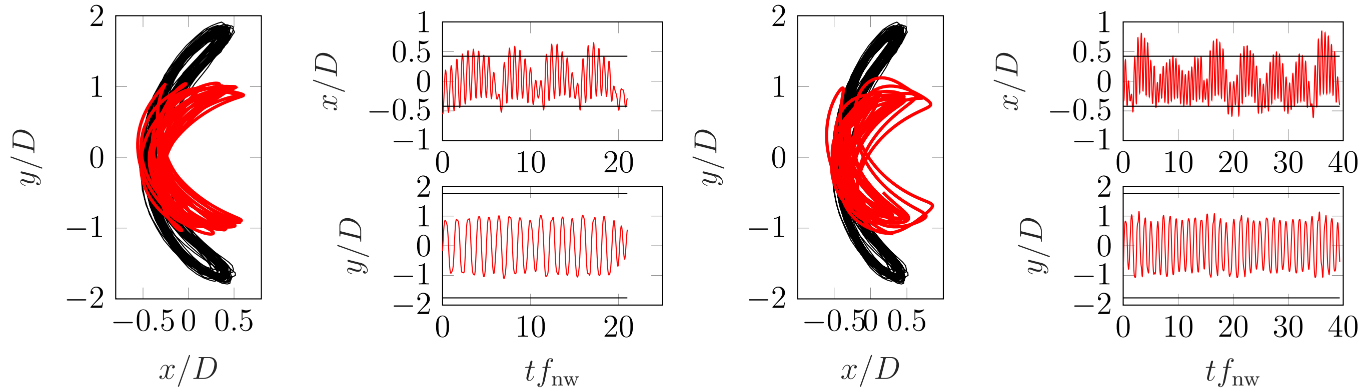

(e) $C_{\mathrm{F}} = 1$ (f) $C_{\mathrm{F}} = 1$ (g) $C_{\mathrm{F}} = 1.2$ (h) $C_{\mathrm{F}} = 1.2$

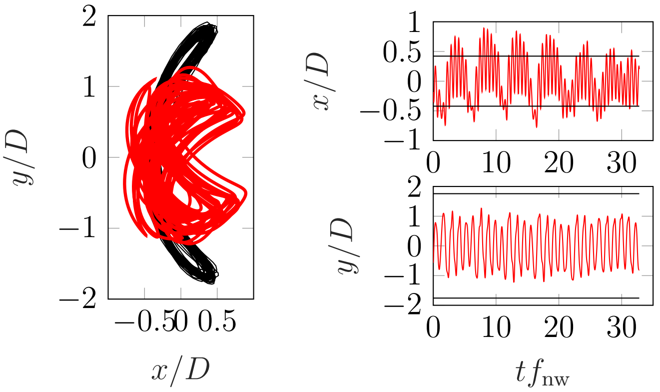

(i) $C_{\mathrm{F}} = 1.4$ (j) $C_{\mathrm{F}} = 1.4$

Figure D.7: Cylinder trajectory (a,c,e,g,i) and time-history (b,d,f,h,j) at $U_{\mathrm{r}} = 6$. Red: Numerical results. Horizontal black line: experimental maximum crossflow and streamwise amplitude

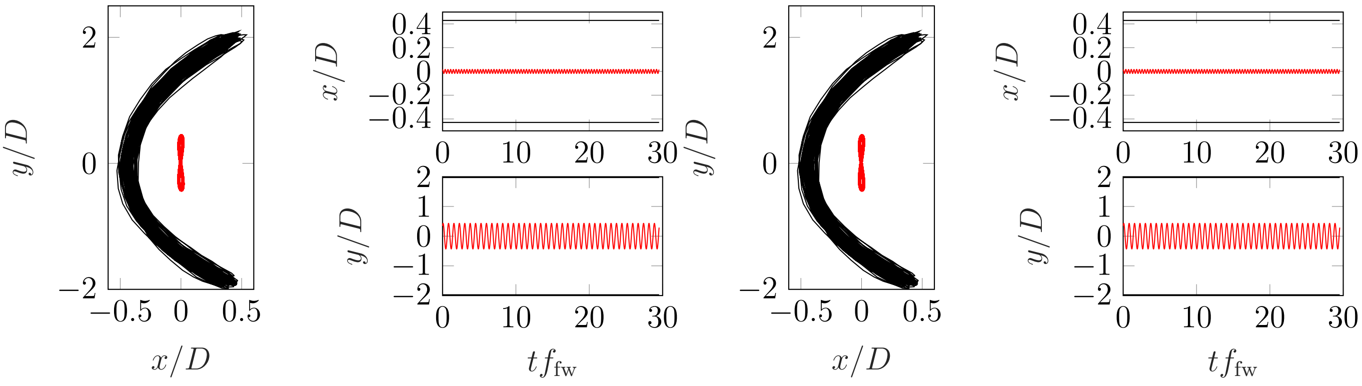

(a) $C_{\mathrm{F}} = 0.6$ (b) $C_{\mathrm{F}} = 0.6$ (c) $C_{\mathrm{F}} = 0.8$ (d) $C_{\mathrm{F}} = 0.8$

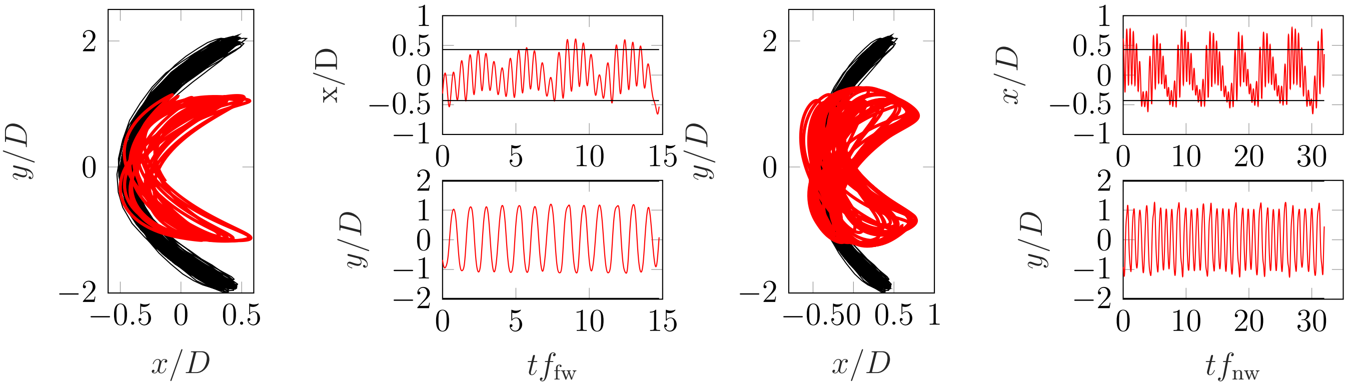

(e) $C_{\mathrm{F}} = 1$ (f) $C_{\mathrm{F}} = 1$ (g) $C_{\mathrm{F}} = 1.2$ (h) $C_{\mathrm{F}} = 1.2$

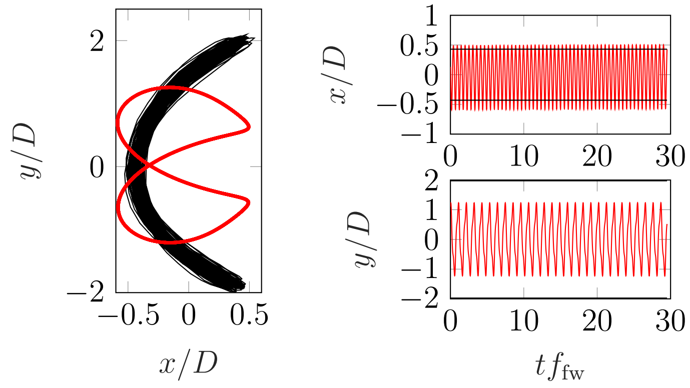

(i) $C_{\mathrm{F}} = 1.4$ (j) $C_{\mathrm{F}} = 1.4$

Figure D.8: Cylinder trajectory (a,c,e,g,i) and time-history (b,d,f,h,j) at $U_{\mathrm{r}} = 6.69$. Red: Numerical results. Horizontal black line: experimental maximum crossflow and streamwise amplitude

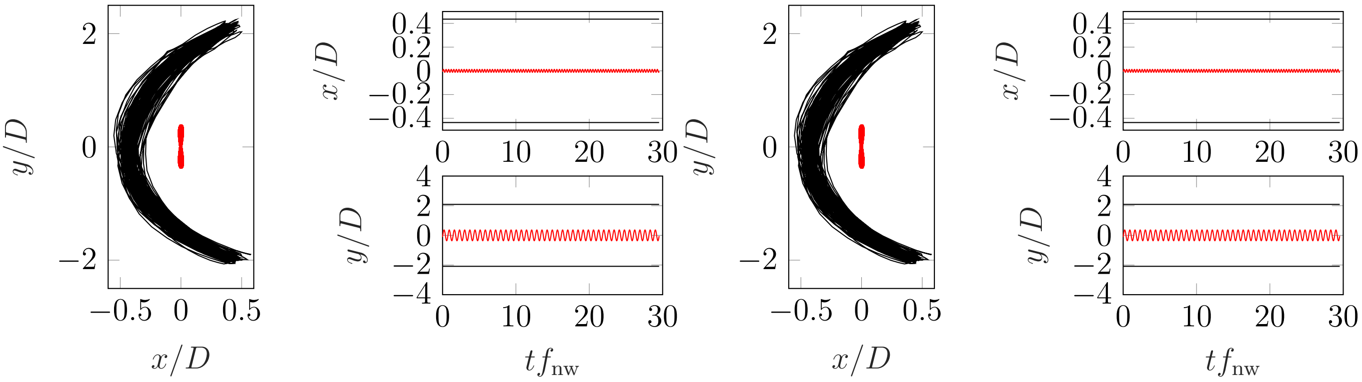

(a) $C_{\mathrm{F}} = 0.6$ (b) $C_{\mathrm{F}} = 0.6$ (c) $C_{\mathrm{F}} = 0.8$ (d) $C_{\mathrm{F}} = 0.8$

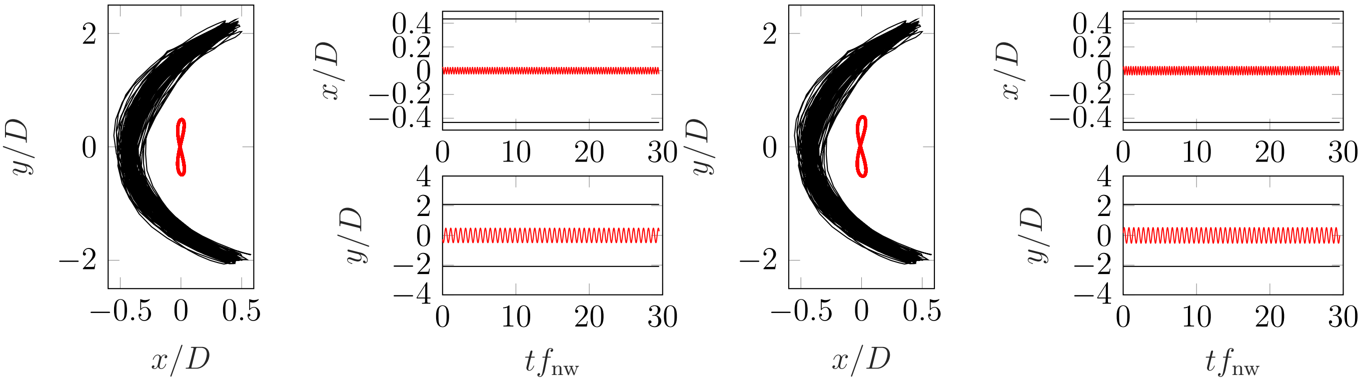

(e) $C_{\mathrm{F}} = 1$ (f) $C_{\mathrm{F}} = 1$ (g) $C_{\mathrm{F}} = 1.2$ (h) $C_{\mathrm{F}} = 1.2$

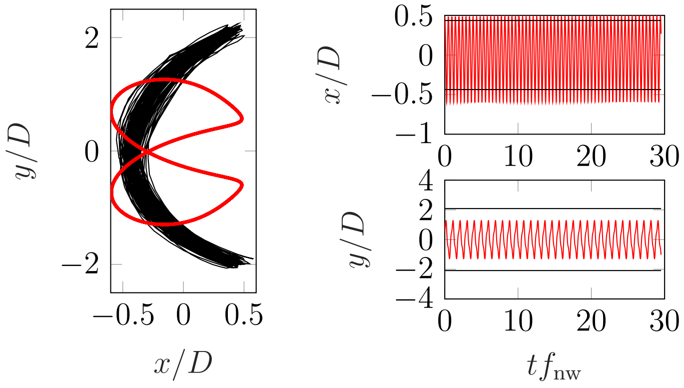

(i) $C_{\mathrm{F}} = 1.4$ (j) $C_{\mathrm{F}} = 1.4$

Figure D.9: Cylinder trajectory (a,c,e,g,i) and time-history (b,d,f,h,j) at $U_{\mathrm{r}} = 7.42$. Red: Numerical results. Horizontal black line: experimental maximum crossflow and streamwise amplitude

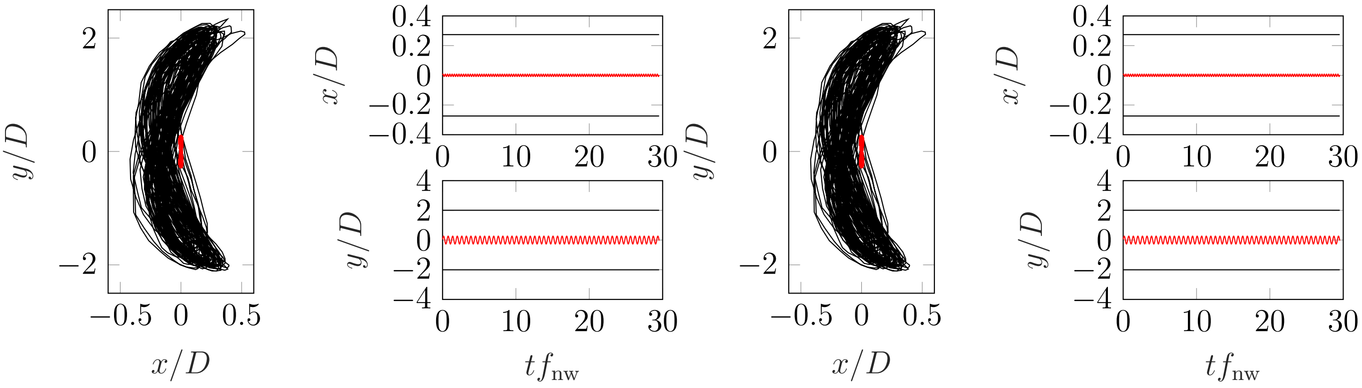

(a) $C_{\mathrm{F}} = 0.6$ (b) $C_{\mathrm{F}} = 0.6$ (c) $C_{\mathrm{F}} = 0.8$ (d) $C_{\mathrm{F}} = 0.8$

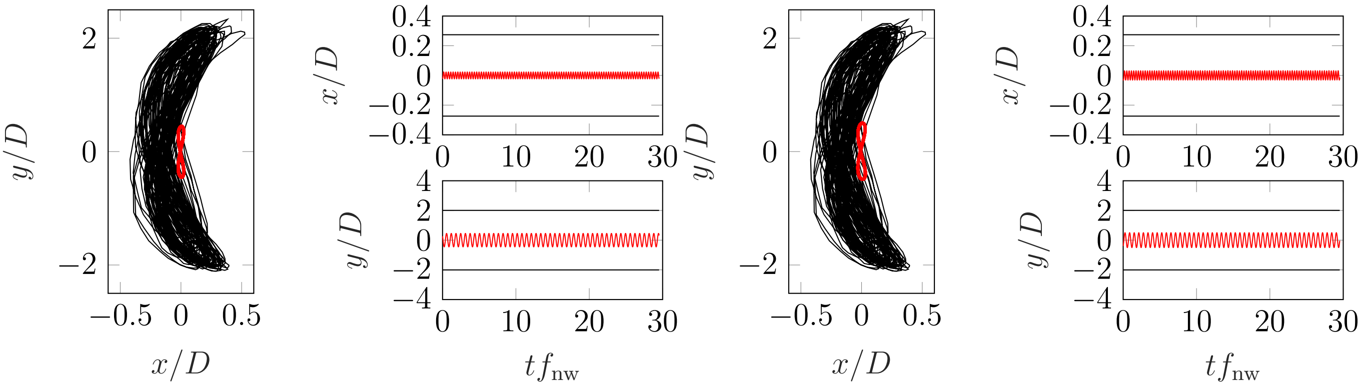

(e) $C_{\mathrm{F}} = 1$ (f) $C_{\mathrm{F}} = 1$ (g) $C_{\mathrm{F}} = 1.2$ (h) $C_{\mathrm{F}} = 1.2$

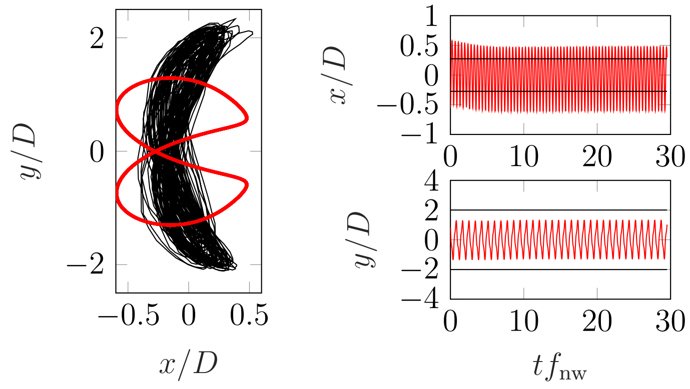

(i) $C_{\mathrm{F}} = 1.4$ (j) $C_{\mathrm{F}} = 1.4$

Figure D.10: Cylinder trajectory (a,c,e,g,i) and time-history (b,d,f,h,j) at $U_{\mathrm{r}} = 8.29$. Red: Numerical results. Horizontal black line: experimental maximum crossflow and streamwise amplitude

D.2 Self-developed codes

D.2.1 Structural motion tracking

The Lucas-Kanade and Forward-Backward techniques for structural motion tracking were implemented in Python 3. The first code of this section is the Lucas-Kanade function and is called by the second code, the Forward-Backward tracking technique.

Lucas-Kanade function

```
import cv2
import numpy as np
import matplotlib.pylab as plt
import scipy.io as sio
from itertools import product

global start_draw
global x0
global y0
x0 = 0
y0 = 0

def parameters(ninit,nend,step,window,intwx,intwy,des,inipoint):

#Input
## Name images
First=True
nameroot='B'
ext='.bmp'

p0=inipoint

## Lucas-Kanade parameters
lk_params = dict( winSize = (intwx,intwy), maxLevel = 4, criteria = (
    cv2.TERM_CRITERIA_EPS | cv2.TERM_CRITERIA_COUNT, 10, 0.03))

pf=[]
error=[]

def getxy(event, x, y, flags, param):

        global start_draw
        global x0
        global y0

        if (event == cv2.EVENT_LBUTTONDOWN):
                start_draw = True
                x0, y0 = x, y
                print(”Centroid␣position␣(x,y):”+str(x0)+”,”+str(y0))
        elif (event==cv2.EVENT_LBUTTONUP):
                start_draw = False
        cv2.circle(ima1, (x0, y0), 1, (0, 255, 0), -1)
        cv2.rectangle(ima1, (x0-window, y0-window), (x0+window, y0+
            window),(0,0,255),1)
        cv2.imshow('image',ima1)
```

```
for i in range(ninit,nend+1-step,step):

    #Load images
    nameima1 = "%s%s%s" % (nameroot, format(i, "d"), ext)
    print(nameima1)
    nameima2 = "%s%s%s" % (nameroot, format(i+step, "d"), ext)
    ima1 = cv2.imread(nameima1)
    ima2 = cv2.imread(nameima2)
    ima1bw = cv2.cvtColor(ima1, cv2.COLOR_BGR2GRAY)
    ima2bw = cv2.cvtColor(ima2, cv2.COLOR_BGR2GRAY)

    size=ima1.shape

    #Open first image and select initial target
    if i==ninit and des==0:
        overlay=ima1.copy()
        cv2.namedWindow('image')
        cv2.setMouseCallback('image', getxy)

        cv2.imshow('image',ima1)
        cv2.waitKey(0)
        cv2.destroyWindow('image')
        xv=np.linspace(x0-window,x0+window,window+1)
        yv=np.linspace(y0-window,y0+window,window+1)
        p0=np.float32(list(product(xv,yv)))

    #Executing the optical flow calculations using opencv
    p1, st, err = cv2.calcOpticalFlowPyrLK(ima1bw, ima2bw, p0, None
      , **lk_params)

    if First:
        pin=p0
        pf.append(pin)
        pf.append(p1)
        error.append(err)
        First=False
    else:
        pf.append(p1)
        error.append(err)
    p0=p1

return pf
```

Forward-Backward implementation

```
import cv2
import numpy as np
```

```
import matplotlib.pylab as plt
import scipy.io as sio
import scipy.ndimage
from itertools import product
import os
import lk_original

#Input
## Folder
flowname=['foldername']
expname=['expname']
inidir=os.getcwd()

#Initial and final frame
ninit=1
nend=1100

##Tracking parameters
step=1 #Skip frames?
window=15 #Interrogation window size
intwx=10 #Interrogation window size
intwy=10 #Interrogation window size
percentile=[5,95] #Lowest FB–error percentile

for flow in range(0,1):
for exp in range(0,1):

        diff=[]
        BF=[]

        #Open folder with files
        Folder=flowname[flow]+expname[exp]
        resultFolder='result_'+Folder
        os.chdir(Folder)

        #Calculate LK forward
        des=0
        forward=lk_original.parameters(ninit,nend,step,window,intwx,
            intwy,des,[])

        #Calculate LK backwards
        p0=forward[−1]
        des=1
        step=–1
        backward=lk_original.parameters(nend,ninit −2,step,window,intwx,
            intwy,des,p0)
```

```python
step=1

#Calculate the difference between the forward and backward calculations
for nframes in range(ninit-1,nend,step):
        diff.append(forward[nframes]-backward[nend-nframes-1])
        BF.append(backward[-nframes])

#Separate the difference in X and Y components.
dim=np.shape(backward)
diffx=np.zeros([dim[0],dim[1]])
diffy=np.zeros([dim[0],dim[1]])
xfd=np.zeros(dim[0])
yfd=np.zeros(dim[0])

for pointpos in range(0,dim[1]):
        for nframes in range(0,dim[0]):
                diffx[nframes,pointpos]=diff[nframes][pointpos][0]
                diffy[nframes,pointpos]=diff[nframes][pointpos][1]

#Calculate FB-error and select the initial points using a percentile criteria
firstdiff=np.sqrt((diffx[0])**2+(diffy[0])**2)
limit=np.percentile(firstdiff,[percentile[0],percentile[1]])
pos=np.where(firstdiff<limit[0])

#Separate the selected signals in their corresponding X and Y components.
fx=np.zeros([dim[0],np.shape(pos[0])[0]])
fy=np.zeros([dim[0],np.shape(pos[0])[0]])

for nframes in range(0,dim[0]):
        for selection in range(0,np.shape(pos[0])[0]):
                fx[nframes,:]=forward[nframes][pos][:,0]
                fy[nframes,:]=forward[nframes][pos][:,1]

#Mean signal removal
fx=fx-np.mean(fx,0)
fy=fy-np.mean(fy,0)

#Estimate the resulting tracking motion as the median of the selected signals.
for nframes in range(0,dim[0]):
        xfd[nframes]=np.median(fx[nframes,:])
        yfd[nframes]=np.median(fy[nframes,:])
```

```
#Save data
sio.savemat(Folder+'_raw'+'.mat',{'x':xfd,'y':yfd})
sio.savemat(Folder+'_data_Lk.mat',{'pos':pos,'forward':forward,
    'backward':backward,'firstdiff':firstdiff})
sio.savemat(Folder+'_data_NCC.mat',{'max_val':max_val,'posNCC':
    posNCC})
```

D.2.2 User Defined Function

A User Defined Function (UDF) is a function that can be dynamically loaded into Ansys Fluent to enhance its capabilities. The code is written in C and must be compiled in Fluent for its use.

Cylinder model

```
#include "udf.h"
#include "mem.h"
#include "para.h"
#include "math.h"

/*Cylinder zone ID*/
#define zoneID_cylinder 16

FILE *outNB,*outRK,*fp;
static float x;
static float xRK;
static float vx;
static float vxRK;
static float ax;

static float y;
static float yRK;
static float vy;
static float vyRK;
static float ay;

static float fx_prev;
static float fy_prev;
static float delta_x;
static float delta_y;
static float delta_xRK;
static float delta_yRK;

static float vxRK_prev;
static float vyRK_prev;
```

```
/*Read data from .cas.gz file*/
DEFINE_RW_FILE(reader_RK4_NB14, fp)
{
#if !RP_NODE
fscanf(fp, ”%f␣%f␣%f␣%f␣%f␣%f␣%f␣%f␣%f␣%f␣%f␣%f␣%f␣%f␣%f␣%f␣%f␣%f”, &x,
    &vx, &ax, &y, &vy, &ay, &xRK, &vxRK, &yRK, &vyRK, &fx_prev, &
    fy_prev, &delta_x, &delta_y, &delta_xRK, &delta_yRK, &vxRK_prev, &
    vyRK_prev);
Message(”READER:␣%.12f␣%.12f␣%.12f␣%.12f␣%.12f␣%.12f␣%.12f␣%.12f␣%.12f␣
    %.12f␣%.12f␣%.12f␣%.12f␣%.12f␣%.12f␣%.12f␣%.12f␣%.12f\n”, x, vx, ax,
     y, vy, ay, xRK, vxRK, yRK, vyRK, fx_prev, fy_prev, delta_x,
    delta_y, delta_xRK, delta_yRK, vxRK_prev, vyRK_prev);
#endif

host_to_node_float_6(x, vx, ax, y, vy, ay);
host_to_node_float_4(xRK, vxRK, yRK, vyRK);
host_to_node_float_2(fx_prev, fy_prev);
host_to_node_float_6(delta_x, delta_y, delta_xRK, delta_yRK, vxRK_prev,
    vyRK_prev);

}

/*Execute function at the end of each timestep*/
DEFINE_EXECUTE_AT_END(grid_update_position_RK4_NB14)
{

/*Cylinder variables*/
real diameter = 0.0381;
real fna = RP_Get_Real(”fna”);
real fnw = RP_Get_Real(”fnw”);
real density = RP_Get_Real(”density”);
real length = 0.381;
real water_depth = 0.381;
real f_corr = water_depth/length;
real mass_ratio = RP_Get_Real(”mass_ratio”);
real damping_ratio = RP_Get_Real(”damping_ratio”);

real fluid_mass = 0.25*M_PI*pow((diameter),2)*density;
real solid_mass = 0.25*M_PI*pow((diameter),2)*density*mass_ratio;
real total_mass = RP_Get_Real(”total_mass”);
real k = 4*pow((M_PI*fna),2)*(total_mass);
real c = 4*damping_ratio*M_PI*fna*(total_mass);

/*Force calculation. Force = F_pressure + F_viscous*/
real fy = 0.0;
real fvy = 0.0;
real fx = 0.0;
```

```
real fvx = 0.0;

#if !RP_HOST
Thread *thread;
Domain *d = Get_Domain(1);
thread = Lookup_Thread(d,zoneID_cylinder);
face_t f;
real NV_VEC(A);

begin_f_loop(f,thread)
{
if (PRINCIPAL_FACE_P(f,thread))
{
        fvy = F_STORAGE_R_N3V(f,thread,SV_WALL_SHEAR)[1]*-1;
        fvx = F_STORAGE_R_N3V(f,thread,SV_WALL_SHEAR)[0]*-1;
        F_AREA(A,f,thread);

        /*Force calculation with a depth of 1m*/
        fx += F_P(f,thread)*A[0] + fvx;
        fy += F_P(f,thread)*A[1] + fvy;
        }
}
end_f_loop(f,thread)

fx = PRF_GRSUM1(fx);
fy = PRF_GRSUM1(fy);
#endif

node_to_host_real_2(fx,fy);

/*Numerical methods*/
/*Numark-beta*/
real beta = 1/4.0f;
real gamma = 0.5;
real term0 = (1/(beta*dtime*dtime))*(total_mass) + (gamma/(beta*dtime))
   *c;
real term1 = (1/(beta*dtime))*(total_mass) + ((gamma/beta)-1)*c;
real term2 = ((1/(2*beta))-1)*(total_mass) + dtime*((gamma/(2*beta))-1)
   *c;

real Keffx = k + term0;
real Reffx = fx*f_corr + term0*x + term1*vx + term2*ax;
real Keffy = k + term0;
real Reffy = fy*f_corr + term0*y + term1*vy + term2*ay;

real dx = Reffx/Keffx - x;
real dy = Reffy/Keffy - y;
```

```
real vprev_x = vx;
real aprev_x = ax;
vx = (gamma/(beta*dtime))*dx + (1-(gamma/beta))*vx + dtime*(1-(gamma
    /(2*beta)))*ax;
ax = (1/(beta*dtime*dtime))*dx - (1/(beta*dtime))*vprev_x - ((1/(2*beta
    ))-1)*ax;
x = x + dtime*vprev_x + dtime*dtime*0.5*((1-2*beta)*aprev_x + 2*beta*ax
    );
delta_x = dtime*vprev_x + dtime*dtime*0.5*((1-2*beta)*aprev_x + 2*beta*
    ax);

real vprev_y = vy;
real aprev_y = ay;
vy = (gamma/(beta*dtime))*dy + (1-(gamma/beta))*vy + dtime*(1-(gamma
    /(2*beta)))*ay;
ay = (1/(beta*dtime*dtime))*dy - (1/(beta*dtime))*vprev_y - ((1/(2*beta
    ))-1)*ay;
y = y + dtime*vprev_y + dtime*dtime*0.5*((1-2*beta)*aprev_y + 2*beta*ay
    );
delta_y = dtime*vprev_y + dtime*dtime*0.5*((1-2*beta)*aprev_y + 2*beta*
    ay);

/*Runge-kutta 4th order*/
vxRK_prev = vxRK;
vyRK_prev = vyRK;
real funcx1 = vxRK;
real funcx2 = (fx_prev*f_corr - c*vxRK - k*xRK) / total_mass;
real Kx0 = funcx1;
real Mx0 = funcx2;
real Kx1 = (funcx1 + dtime*Mx0*0.5);
real Mx1 = (funcx2 - (c/total_mass)*0.5*dtime*Mx0 - (k/total_mass)*0.5*
    dtime*Kx0);
real Kx2 = (funcx1 + dtime*Mx1*0.5);
real Mx2 = (funcx2 - (c/total_mass)*0.5*dtime*Mx1 - (k/total_mass)*0.5*
    dtime*Kx1);
real Kx3 = (funcx1 + dtime*Mx2);
real Mx3 = (funcx2 - (c/total_mass)*dtime*Mx2 - (k/total_mass)*dtime*
    Kx2);

xRK = xRK + dtime*(Kx0 + 2*Kx1 + 2*Kx2 + Kx3)/6.0f;
vxRK = vxRK + dtime*(Mx0 + 2*Mx1 + 2*Mx2 + Mx3)/6.0f;

real funcy1 = vyRK;
real funcy2 = (fy_prev*f_corr - c*vyRK - k*yRK) / total_mass;
real Ky0 = funcy1;
real My0 = funcy2;
```

```
real Ky1 = (funcy1 + dtime*My0*0.5);
real My1 = (funcy2 − (c/total_mass)*0.5*dtime*My0 − (k/total_mass)*0.5*
    dtime*Ky0);
real Ky2 = (funcy1 + dtime*My1*0.5);
real My2 = (funcy2 − (c/total_mass)*0.5*dtime*My1 − (k/total_mass)*0.5*
    dtime*Ky1);
real Ky3 = (funcy1 + dtime*My2);
real My3 = (funcy2 − (c/total_mass)*dtime*My2 − (k/total_mass)*dtime*
    Ky2);

yRK = yRK + dtime*(Ky0 + 2*Ky1 + 2*Ky2 + Ky3)/6.0f;
vyRK = vyRK + dtime*(My0 + 2*My1 + 2*My2 + My3)/6.0f;

delta_xRK = dtime*(Kx0 + 2*Kx1 + 2*Kx2 + Kx3)/6.0f;
delta_yRK = dtime*(Ky0 + 2*Ky1 + 2*Ky2 + Ky3)/6.0f;
fx_prev = fx;
fy_prev = fy;
}

/*Impose cylinder displacement*/
DEFINE_GRID_MOTION(grid_motion_cylinder_RK4_NB14, domain, dt, time,
    dtime2)
{
/*Transfer result to the dynamic mesh*/
real NTsel = RP_Get_Real("rk4_or_nb14"); /*RK4 = 1; NB14 = 2*/
real dof = RP_Get_Real("dof"); /*one dof = 1; two dof = 2*/

#if !RP_HOST
Thread *t;
t = DT_THREAD(dt);
face_t fm;
Node *Ncylinder;
int n;

SET_DEFORMING_THREAD_FLAG(THREAD_T0(t));

begin_f_loop(fm,t)
{
f_node_loop(fm,t,n)
{
Ncylinder = F_NODE(fm,t,n);

if (NODE_POS_NEED_UPDATE(Ncylinder))
{

if (NTsel == 1)
{
```

```
if (dof == 1)
{
NODE_Y(Ncylinder) += delta_yRK;
}
if (dof == 2)
{
NODE_X(Ncylinder) += delta_xRK;
NODE_Y(Ncylinder) += delta_yRK;
}
}

if (NTsel == 2)
{
if (dof == 1)
{
NODE_Y(Ncylinder) += delta_y;
}
if (dof == 2)
{
NODE_X(Ncylinder) += delta_x;
NODE_Y(Ncylinder) += delta_y;
}
}
NODE_POS_UPDATED(Ncylinder);
}
}
}
end_f_loop(fm,t)
#endif
}

/*Impose cylinder displacement*/
DEFINE_GRID_MOTION(grid_motion_oring_RK4_NB14, domain3, dt3, time3,
    dtime3)
{
/*Transfer result to the dynamic mesh*/
real NTsel = RP_Get_Real("rk4_or_nb14"); /*RK4 = 1; NB14 = 2*/
real dof = RP_Get_Real("dof"); /*one dof = 1; two dof = 2*/

#if RP_NODE
Thread *t3;
t3 = DT_THREAD(dt3);
face_t fm3;
Node *Ncylinder3;
int n3;

SET_DEFORMING_THREAD_FLAG(THREAD_T1(t3));
```

```
begin_f_loop(fm3,t3)
{
f_node_loop(fm3,t3,n3)
{
Ncylinder3 = F_NODE(fm3,t3,n3);

if (NODE_POS_NEED_UPDATE(Ncylinder3))
{
if (NTsel == 1)
{
if (dof == 1)
{
NODE_Y(Ncylinder3) += delta_yRK;
}
if (dof == 2)
{
NODE_X(Ncylinder3) += delta_xRK;
NODE_Y(Ncylinder3) += delta_yRK;
}
}

if (NTsel == 2)
{
if (dof == 1)
{
NODE_Y(Ncylinder3) += delta_y;
}
if (dof == 2)
{
NODE_X(Ncylinder3) += delta_x;
NODE_Y(Ncylinder3) += delta_y;
}
}
NODE_POS_UPDATED(Ncylinder3);
}
}
}
end_f_loop(fm3,t3)
#endif
}

/*Save data from .cas.gz file*/
DEFINE_RW_FILE(writer_RK4_NB14,fp)
{
#if !RP_NODE
```

```
fprintf(fp,"%.12f␣%.12f␣%.12f␣%.12f␣%.12f␣%.12f␣%.12f␣%.12f␣%.12f␣%.12f
    ␣%.12f␣%.12f␣%.12f␣%.12f␣%.12f␣%.12f␣%.12f␣%.12f", x, vx, ax, y, vy
    , ay, xRK, vxRK, yRK, vyRK, fx_prev, fy_prev, delta_x, delta_y,
    delta_xRK, delta_yRK, vxRK_prev, vyRK_prev);
Message("WRITER:␣%.12f␣%.12f␣%.12f␣%.12f␣%.12f␣%.12f␣%.12f␣%.12f␣%.12f␣
    %.12f␣%.12f␣%.12f␣%.12f␣%.12f␣%.12f␣%.12f␣%.12f␣%.12f\n",x, vx, ax,
     y, vy, ay, xRK, vxRK, yRK, vyRK, fx_prev, fy_prev, delta_x,
    delta_y, delta_xRK, delta_yRK, vxRK_prev, vyRK_prev);
#endif
}
```

Bibliography

[1] Amalia, E., Moelyadi, M.A., Ihsan, M., 2018. Effects of Turbulence Model and Numerical Time Steps on Von Karman Flow Behavior and Drag Accuracy of Circular Cylinder. Journal of Physics: Conference Series 1005, 012012. doi:`10.1088/1742-6596/1005/1/012012`.

[2] Balasubramanian, S., Skop, R., Haan, F., Szewczyk, A., 2000. Vortex-excited Vibration of Uniform Pivoted Cylinders in Uniform and Shear Flow. Journal of Fluids and Structures 14, 65–85. doi:`10.1006/jfls.1999.0255`.

[3] Bearman, P.W., 1984. Vortex shedding from oscillating bluff bodies. Annual review of fluid mechanics 16, 195–222. doi:`10.1146/annurev.fl.16.010184.001211`.

[4] Bearman, P.W., 2011. Circular cylinder wakes and vortex-induced vibrations. Journal of Fluids and Structures 27, 648–658. doi:`10.1016/j.jfluidstructs.2011.03.021`.

[5] Beg, M.N.A., Carvalho, R.F., Tait, S., Brevis, W., Rubinato, M., Schellart, A., Leandro, J., 2018. A comparative study of manhole hydraulics using stereoscopic PIV and different RANS models. Water Science and Technology 1, 87–98. doi:`10.2166/wst.2018.089`.

[6] Berkooz, G., Holmes, P., Lumley, J., 1993. The Proper Orthogonal Decomposition in the Analysis of Turbulent Flows. Annual Review of Fluid Mechanics 25, 539–575. doi:`10.1146/annurev.fl.25.010193.002543`.

[7] Bishop, R.E.D., Hassan, A., 1964. The lift and drag forces on a circular cylinder oscillating in a flowing fluid. Proceedings of the Royal Society of London. Series A. Mathematical and Physical Sciences 277, 51–75. doi:`10.1098/rspa.1964.0005`.

[8] Bouguet, J.Y., 2001. Pyramidal implementation of the affine lucas kanade feature tracker—description of the algorithm. Intel Corporation 5, 1–10.

[9] Bourguet, R., Em Karniadakis, G., Triantafyllou, M.S., 2015. On the validity of the independence principle applied to the vortex-induced vibrations of a flexible cylinder inclined at 60°. Journal of Fluids and Structures 53, 58–69. doi:`10.1016/j.jfluidstructs.2014.09.005`.

[10] Bourguet, R., Karniadakis, G.E., Triantafyllou, M.S., 2011. Lock-in of the vortex-induced vibrations of a long tensioned beam in shear flow. Journal of Fluids and Structures 27, 838–847. doi:`10.1016/j.jfluidstructs.2011.03.008`.

[11] Brevis, W., García-Villalba, M., 2011. Shallow-flow visualization analysis by proper orthogonal decomposition. Journal of Hydraulic Research 49, 586–594. doi:`10.1080/00221686.2011.585012`.

[12] Brika, D., Laneville, A., 1993. Vortex-induced vibrations of a long flexible circular cylinder. Journal of Fluid Mechanics 250, 481–508. doi:`10.1017/S0022112093001533`.

[13] Chatterjee, A., 2000. An introduction to the proper orthogonal decomposition. Current Science 78, 808–817.

[14] Chow, V., 1959. Open-Channel Hydraulics. 1st ed., McGraw-Hill, New York.

[15] Daniels, S.J., Castro, I.P., Xie, Z.T., 2013. Peak loading and surface pressure fluctuations of a tall model building. Journal of Wind Engineering and Industrial Aerodynamics 120, 19–28. doi:`10.1016/j.jweia.2013.06.014`.

[16] Daniels, S.J., Castro, I.P., Xie, Z.T., 2016. Numerical analysis of freestream turbulence effects on the vortex-induced vibrations of a rectangular cylinder. Journal of Wind Engineering and Industrial Aerodynamics 153, 13–25. doi:`10.1016/j.jweia.2016.03.007`.

[17] Dong, P., Benaroya, H., Wei, T., 2004. Integrating experiments into an energy-based reduced-order model for vortex-induced-vibrations of a cylinder mounted as an inverted pendulum. Journal of Sound and Vibration 276, 45–63. doi:`10.1016/j.jsv.2003.07.041`.

[18] Duranay, A., Kinaci, O.K., 2020. Enhancing two-dimensional computational approach for vortex-induced vibrations by scaling lift force. Ocean Engineering 217, 107620. doi:`10.1016/j.oceaneng.2020.107620`.

[19] Étienne, S., Pelletier, D., 2012. The low Reynolds number limit of vortex-induced vibrations. Journal of Fluids and Structures 31, 18–29. doi:`10.1016/J.JFLUIDSTRUCTS.2012.02.006`.

[20] Feng, C.C., 1968. The measurement of vortex induced effects in flow past stationary and oscillating circular and D-section cylinders. Ph.D. thesis. University of British Columbia. doi:`http://dx.doi.org/10.14288/1.0104049`.

[21] Flemming, F., Williamson, C., 2005. Vortex-induced vibrations of a pivoted cylinder. Journal of Fluid Mechanics 522, 215–252. doi:`10.1017/S0022112004001831`.

[22] Fluent, A., 2018. Ansys Fluent Theory Guide .

[23] Franzini, G.R., Pesce, C.P., Gonçalves, R.T., Fujarra, A.L.C., Pereira, A.A.P., 2014. Concomitant vortex-induced vibration experiments: A cantilevered flexible cylinder and a rigid cylinder mounted on a leaf-spring apparatus. Journal of the Brazilian Society of Mechanical Sciences and Engineering 36, 547–558. doi:`10.1007/s40430-013-0095-x`.

[24] Gabbai, R.D., Benaroya, H., 2005. An overview of modeling and experiments of vortex-induced vibration of circular cylinders. Journal of Sound and Vibration 282, 575–616. doi:`10.1016/j.jsv.2004.04.017`.

[25] Gao, Y., Zong, Z., Zou, L., Takagi, S., Jiang, Z., 2018. Numerical simulation of vortex-induced vibration of a circular cylinder with different surface roughnesses. Marine Structures 57, 165–179. doi:`10.1016/j.marstruc.2017.10.007`.

[26] Gerrard, J.H., 1966. The mechanics of the formation region of vortices behind bluff bodies. Journal of Fluid Mechanics 25, 401–413. doi:`10.1017/S0022112066001721`.

[27] Gonçalves, R.T., Rosetti, G.F., Franzini, G.R., Meneghini, J.R., Fujarraa, A.L., 2013. Two-degree-of-freedom vortex-induced vibration of circular cylinders with very low aspect ratio and small mass ratio. Journal of Fluids and Structures 39, 237–257. doi:`10.1016/j.jfluidstructs.2013.02.004`.

[28] Govardhan, R., Williamson, C., 2000. Modes of vortex formation and frequency response of a freely vibrating cylinder. Journal of Fluid Mechanics 420, 85–130. doi:`10.1017/S0022112000001233`.

[29] Govardhan, R., Williamson, C., 2001. Mean and fluctuating velocity fields in the wake of a freely-vibrating cylinder. Journal of Fluids and Structures 15, 489–501. doi:`10.1006/jfls.2000.0350`.

[30] Govardhan, R., Williamson, C., 2002. Resonance forever: Existence of a critical mass and an infinite regime of resonance in vortex-induced vibration. Journal of Fluid Mechanics 473, 147–166. doi:`10.1017/S0022112002002318`.

[31] Govardhan, R., Williamson, C., 2006. Defining the 'modified Griffin plot' in vortex-induced vibration: Revealing the effect of Reynolds number using controlled damping. Journal of Fluid Mechanics 561, 147–180. doi:`10.1017/S0022112006000310`.

[32] Gsell, S., Bourguet, R., Braza, M., 2016. Two-degree-of-freedom vortex-induced vibrations of a circular cylinder at Re=3900. Journal of Fluids and Structures 85, 165–180. doi:`10.1016/j.jfluidstructs.2016.09.004`.

[33] Guilmineau, E., Queutey, P., 2004. Numerical simulation of vortex-induced vibration of a circular cylinder with low mass-damping in a turbulent flow. Journal of Fluids and Structures 19, 449–466. doi:`10.1016/j.jfluidstructs.2004.02.004`.

[34] Güven, O., Farell, C., Patel, V.C., 1980. Surface-roughness effects on the mean flow past circular cylinders. Journal of Fluid Mechanics 98, 673–701. doi:`10.1017/S0022112080000341`.

[35] Han, X., Lin, W., Wang, D., Qiu, A., Feng, Z., Tang, Y., Wu, J., 2018. Numerical simulation of super upper branch of a cylindrical structure with a low mass ratio. Ocean Engineering 168, 108–120. doi:`10.1016/j.oceaneng.2018.09.014`.

[36] Han, X., Lin, W., Zhang, X., Tang, Y., Zhao, C., 2016. Two degree of freedom flow-induced vibration of cylindrical structures in marine environments: frequency ratio effects. Journal of Marine Science and Technology (Japan) 21, 479–492. doi:`10.1007/s00773-016-0370-5`.

[37] Higham, J.E., Brevis, W., 2018. Modification of the modal characteristics of a square cylinder wake obstructed by a multi-scale array of obstacles. Experimental Thermal and Fluid Science 90, 212–219. doi:`10.1016/j.expthermflusci.2017.09.019`.

[38] Hover, F.S., Techet, A.H., Triantafyllou, M.S., 1998. Forces on oscillating uniform and tapered cylinders in crossflow. Journal of Fluid Mechanics 363, 97–114. doi:`10.1017/S0022112098001074`.

[39] Hsieh, S.C., Low, Y.M., Chiew, Y.M., 2016. Flow characteristics around a circular cylinder subjected to vortex-induced vibration near a plane bound-

ary. Journal of Fluids and Structures 65, 257–277. doi:10.1016/j.jfluidstructs.2016.06.007.

[40] Humphries, J.A., Walker, D.H., 1988. Vortex-excited response of large-scale cylinders in sheared flow. Journal of Offshore Mechanics and Arctic Engineering 110, 272–277. doi:10.1115/1.3257061.

[41] Jauvtis, N., Williamson, C., 2004. The effect of two degrees of freedom on vortex-induced vibration at low mass and damping. Journal of Fluid Mechanics 509, 23–62. doi:10.1017/S0022112004008778.

[42] Johnstone, A.D., Stappenbelt, B., 2016. Flow-induced vibration characteristics of pivoted cylinders with splitter-plates. Australian Journal of Mechanical Engineering 14, 53–63. doi:10.1080/14484846.2015.1093219.

[43] Kalal, Z., Mikolajczyk, K., Matas, J., 2010. Forward-backward error: Automatic detection of tracking failures, in: International Conference on Pattern Recognition, pp. 2756–2759. doi:10.1109/ICPR.2010.675.

[44] Kang, Z., Jia, L., 2013. An experiment study of a cylinder's two degree of freedom VIV trajectories. Ocean Engineering 70, 129–140. doi:10.1016/j.oceaneng.2013.05.033.

[45] Kang, Z., Ni, W., Sun, L., 2017. A numerical investigation on capturing the maximum transverse amplitude in vortex induced vibration for low mass ratio. Marine Structures 52, 94–107. doi:10.1016/j.marstruc.2016.11.006.

[46] Keane, R.D., Adrian, R.J., 1992. Theory of cross-correlation analysis of PIV images. Applied Scientific Research 49, 191–215. doi:10.1007/BF00384623.

[47] Khalak, A., Williamson, C., 1996. Dynamics of a hydroelastic cylinder with very low mass and damping. Journal of Fluids and Structures 10, 455–472. doi:10.1006/jfls.1996.0031.

[48] Khalak, A., Williamson, C., 1997. Investigation of relative effects of mass and damping in vortex-induced vibration of a circular cylinder. Journal of Wind Engineering and Industrial Aerodynamics 37, 341–350. doi:10.1016/S0167-6105(97)00167-0.

[49] Khalak, A., Williamson, C., 1999. Motions, forces and mode transitions in vortex-induced vibrations at low mass-damping. Journal of Fluids and Structures 13, 813–851. doi:10.1006/jfls.1999.0236.

[50] Khan, N.B., Ibrahim, Z., 2019. Numerical investigation of vortex-induced vibration of an elastically mounted circular cylinder with One-degree of freedom at high Reynolds number using different turbulent models. Proceedings of the Institution of Mechanical Engineers Part M: Journal of Engineering for the Maritime Environment 233, 443–453. doi:`10.1177/1475090217751992`.

[51] Kheirkhah, S., Yarusevych, S., Narasimhan, S., 2012. Orbiting response in vortex-induced vibrations of a two-degree-of-freedom pivoted circular cylinder. Journal of Fluids and Structures 28, 343–358. doi:`10.1016/j.jfluidstructs.2011.08.014`.

[52] Kheirkhah, S., Yarusevych, S., Narasimhan, S., 2016. Wake Topology of a Cylinder Undergoing Vortex-Induced Vibrations With Elliptic Trajectories. Journal of Fluids Engineering 138, 054501. doi:`10.1115/1.4031971`.

[53] Klamo, J.T., Leonard, A., Roshko, A., 2005. On the maximum amplitude for a freely vibrating cylinder in cross-flow. Journal of Fluids and Structures 21, 429–434. doi:`10.1016/j.jfluidstructs.2005.07.010`.

[54] Konstantinidis, E., Zhao, J., Leontini, J., Lo Jacono, D., Sheridan, J., 2019. Excitation and damping fluid forces on a cylinder undergoing vortex-induced vibration. Frontiers in Physics 7, 185. doi:`10.3389/fphy.2019.00185`.

[55] Larsen, A., 1995. Vortex-Induced Vibration of Circular Cylinders. II: New Model. Journal of Engineering Mechanics 121, 350–353. doi:`10.1061/(asce)0733-9399(1995)121:2(350)`.

[56] LaVision, 2016. DaVis 8.3 - Software for intelligent imaging. Technical Report.

[57] Leong, C.M., Wei, T., 2008. Two-degree-of-freedom vortex-induced vibration of a pivoted cylinder below critical mass ratio. Proceedings of the Royal Society A: Mathematical, Physical and Engineering Sciences 464, 2907–2927. doi:`10.1098/rspa.2007.0166`.

[58] Lourenco, L., Krothapalli, A., 1995. On the accuracy of velocity and vorticity measurements with PIV. Experiments in Fluids 18, 421–428. doi:`10.1007/BF00208464`.

[59] Low, Y.M., Srinil, N., 2016. VIV fatigue reliability analysis of marine risers with uncertainties in the wake oscillator model. Engineering Structures 106, 96–108. doi:`10.1016/j.engstruct.2015.10.004`.

[60] Lucas, B.D., Kanade, T., 1981. An iterative image registration technique with an application to stereo vision, in: Proceedings of the DARPA Image Understanding Workshop, pp. 121–130.

[61] Marakkos, K., Turner, J.T., 2006. Vortex generation in the cross-flow around a cylinder attached to an end-wall. Optics and Laser Technology 38, 277–285. doi:`10.1016/J.OPTLASTEC.2005.06.014`.

[62] Marble, E., Morton, C., Yarusevych, S., 2018. Vortex dynamics in the wake of a pivoted cylinder undergoing vortex-induced vibrations with elliptic trajectories. Experiments in Fluids 59, 1–16. doi:`10.1007/s00348-018-2530-3`.

[63] Marsh, P., Ranmuthugala, D., Penesis, I., Thomas, G., 2017. The influence of turbulence model and two and three-dimensional domain selection on the simulated performance characteristics of vertical axis tidal turbines. Renewable Energy 105, 106–116. doi:`10.1016/J.RENENE.2016.11.063`.

[64] Mella, D., Brevis, W., Susmel, L., 2020a. Single cylinder subjected to vortex-induced vibrations: Estimating cyclic stresses for fatigue assessment. Procedia Structural Integrity 28, 511–516. doi:`10.1016/j.prostr.2020.10.060`.

[65] Mella, D., Brevis, W., Susmel, L., 2020b. Spanwise wake development of a bottom-fixed cylinder subjected to vortex-induced vibrations. Ocean Engineering 218, 108280. doi:`10.1016/j.oceaneng.2020.108280`.

[66] Mella, D.A., Brevis, W., Jonathan, H., Racic, V., Susmel, L., 2019. Image-based tracking technique assessment and application to a fluid-structure interaction experiment. Proceedings of the Institution of Mechanical Engineers, Part C: Journal of Mechanical Engineering 233, 5724–5734. doi:`10.1177/0954406219853852`.

[67] Menter, F.R., 1994. Two-equation eddy-viscosity turbulence models for engineering applications. AIAA Journal 32, 1598–1605. doi:`10.2514/3.12149`.

[68] Menter, F.R., Kuntz, M., Langtry, R., 2003. Ten Years of Industrial Experience with the SST Turbulence Model. Turbulence, Heat and Mass Transfer 4, 625–632.

[69] Modarres-Sadeghi, Y., Mukundan, H., Dahl, J.M., Hover, F.S., Triantafyllou, M.S., 2010. The effect of higher harmonic forces on fatigue life of marine risers. Journal of Sound and Vibration 329, 43–55. doi:`10.1016/j.jsv.2009.07.024`.

[70] Morenko, I.V., Fedyaev, V.L., 2017. Influence of turbulence intensity and turbulence length scale on the drag, lift and heat transfer of a circular cylinder. China Ocean Engineering 2017 31:3 31, 357–363. doi:`10.1007/S13344-017-0042-1`.

[71] Morse, T.L., Williamson, C., 2009. Fluid forcing, wake modes, and transitions for a cylinder undergoing controlled oscillations. Journal of Fluids and Structures 25, 697–712. doi:`10.1016/j.jfluidstructs.2008.12.003`.

[72] Newmark, N.M., 1959. A Method of Computation for Structural Dynamics. Journal of the Engineering Mechanics Division 85, 67–94. doi:`10.1061/JMCEA3.0000098`.

[73] Ni, W., Zhang, X., Xu, F., Zhang, W., Kang, Z., 2019. Numerical investigation of bifurcation characteristics under perturbations in vortex induced vibration of cylinder with two degrees of freedom. Ocean Engineering 188, 106318. doi:`10.1016/j.oceaneng.2019.106318`.

[74] Norberg, C., 1994. An experimental investigation of the flow around a circular cylinder: Influence of aspect ratio. Journal of Fluid Mechanics 258, 287–316. doi:`10.1017/S0022112094003332`.

[75] Norberg, C., 2003. Fluctuating lift on a circular cylinder: Review and new measurements. Journal of Fluids and Structures 17, 57–96. doi:`10.1016/S0889-9746(02)00099-3`.

[76] Oviedo-Tolentino, F., Pérez-Gutiérrez, F.G., Romero-Méndez, R., Hernández-Guerrero, A., 2014. Vortex-induced vibration of a bottom fixed flexible circular beam. Ocean Engineering 88, 463–471. doi:`10.1016/j.oceaneng.2014.07.012`.

[77] Pan, Z.Y., Cui, W.C., Miao, Q.M., 2007. Numerical simulation of vortex-induced vibration of a circular cylinder at low mass-damping using RANS code. Journal of Fluids and Structures 23, 23–27. doi:`10.1016/j.jfluidstructs.2006.07.007`.

[78] Paul, I., Prakash, K.A., Vengadesan, S., 2014. Onset of laminar separation and vortex shedding in flow past unconfined elliptic cylinders. Physics of Fluids 26, 23601. doi:`10.1063/1.4866454`.

[79] Prasad, A.K., Adrian, R.J., Landreth, C.C., Offutt, P.W., 1992. Effect of resolution on the speed and accuracy of particle image velocimetry interrogation. Experiments in Fluids 13, 105–116. doi:`10.1007/BF00218156`.

[80] Prasanth, T.K., Behara, S., Singh, S.P., Kumar, R., Mittal, S., 2006. Effect of blockage on vortex-induced vibrations at low Reynolds numbers. Journal of Fluids and Structures 22, 865–876. doi:`10.1016/j.jfluidstructs.2006.04.011`.

[81] Prasanth, T.K., Premchandran, V., Mittal, S., 2011. Hysteresis in vortex-induced vibrations: Critical blockage and effect of m*. Journal of Fluid Mechanics 671, 207–225. doi:`10.1017/S0022112010005537`.

[82] Raghavan, K., Bernitsas, M.M., 2011. Experimental investigation of Reynolds number effect on vortex induced vibration of rigid circular cylinder on elastic supports. Ocean Engineering 38, 719–731. doi:`10.1016/j.oceaneng.2010.09.003`.

[83] Rhie, C.M., Chow, W.L., 1983. Numerical study of the turbulent flow past an airfoil with trailing edge separation. AIAA Journal 21, 1525–1532. doi:`10.2514/3.8284`.

[84] Riches, G., Martinuzzi, R., Morton, C., 2018. Proper orthogonal decomposition analysis of a circular cylinder undergoing vortex-induced vibrations. Physics of Fluids 30, 105103. doi:`10.1063/1.5046090`.

[85] Rodi, W., Scheuerer, G., 1986. Scrutinizing the κ-ϵ turbulence model under adverse pressure gradient conditions. Journal of Fluids Engineering, Transactions of the ASME 108, 174–179. doi:`10.1115/1.3242559`.

[86] Roshko, A., 1954. On the Development of Turbulent Wakes from Vortex Streets. Technical Report. National Advisory Committee for Aeronautics. Washington D.C.

[87] Roshko, A., 1993. Perspectives on bluff body aerodynamics. Journal of Wind Engineering and Industrial Aerodynamics 49, 79–100. doi:`10.1016/0167-6105(93)90007-B`.

[88] Ryan, K., Thompson, M.C., Hourigan, K., 2007. The effect of mass ratio and tether length on the flow around a tethered cylinder. Journal of Fluid Mechanics 591, 117–144. doi:`10.1017/S002211200700780X`.

[89] Sarpkaya, T., 2004. A critical review of the intrinsic nature of vortex-induced vibrations. Journal of Fluids and Structures 19, 389–447. doi:`10.1016/j.jfluidstructs.2004.02.005`.

[90] Scarano, F., Riethmuller, M.L., 2000. Advances in iterative multigrid PIV image processing. Experiments in Fluids 29, S051–S060. doi:`10.1007/s003480070007`.

[91] Schmitt, F.G., 2007. About Boussinesq's turbulent viscosity hypothesis: historical remarks and a direct evaluation of its validity. Comptes Rendus Mecanique 335, 617–627. doi:`10.1016/j.crme.2007.08.004`.

[92] Singh, S.P., Mittal, S., 2005. Vortex-induced oscillations at low reynolds numbers: Hysteresis and vortex-shedding modes. Journal of Fluids and Structures 20, 1085–1104. doi:`10.1016/j.jfluidstructs.2005.05.011`.

[93] Sirovich, L., 1987. Turbulence and the dynamics of coherent structures. I. Coherent structures. Quarterly of Applied Mathematics 45, 561–571. doi:`10.1090/qam/910462`.

[94] Soti, A.K., De, A., 2020. Vortex-induced vibrations of a confined circular cylinder for efficient flow power extraction. Physics of Fluids 32, 033603. doi:`10.1063/1.5131334`.

[95] Spiteri, R.J., Ruuth, S.J., 2006. A new class of optimal high-order strong-stability-preserving Time Discretization Methods. SIAM Journal of Numerical Analysis 40, 469–491. doi:`10.1137/S0036142901389025`.

[96] Srinil, N., Ma, B., Zhang, L., 2018. Experimental investigation on in-plane/out-of-plane vortex-induced vibrations of curved cylinder in parallel and perpendicular flows. Journal of Sound and Vibration 421, 275–299. doi:`10.1016/j.jsv.2018.02.021`.

[97] Szepessy, S., Bearman, P.W., 1992. Aspect ratio and end plate effects on vortex shedding from a circular cylinder. Journal of Fluid Mechanics 234, 191–217. doi:`10.1017/S0022112092000752`.

[98] Ünal, U.O., Atlar, M., Gören, Ö., 2010. Effect of turbulence modelling on the computation of the near-wake flow of a circular cylinder. Ocean Engineering 37, 387–399. doi:`10.1016/j.oceaneng.2009.12.007`.

[99] Vandiver, J.K., 1993. Dimensionless parameters important to the prediction of vortex-induced vibration of long, flexible cylinders in ocean currents. Journal of Fluids and Structures 7, 423–455. doi:`10.1006/jfls.1993.1028`.

[100] Vandiver, J.K., Jong, J.Y., 1987. The relationship between in-line and cross-flow vortex-induced vibration of cylinders. Journal of Fluids and Structures 1, 381–399. doi:`10.1016/S0889-9746(87)90279-9`.

[101] Versteeg, K., Malalasekera, W., 2006. An introduction to Computational Fluid Dynamics: The Finite Volume Method. 2nd ed., Pearson Education. doi:`10.2514/1.22547`.

[102] Vikestad, K., Vandiver, J.K., Larsen, C.M., 2000. Added mass and oscillation frequency for a circular cylinder subjected to vortex-induced vibrations and external disturbance. Journal of Fluids and Structures 14, 1071–1088. doi:`10.1006/jfls.2000.0308`.

[103] Voorhees, A., Dong, P., Atsavapranee, P., Benaroya, H., Wei, T., 2008. Beating of a circular cylinder mounted as an inverted pendulum. Journal of Fluid Mechanics doi:`10.1017/S0022112008002383`.

[104] Wanderley, J.B., Soares, L.F.N., 2015. Vortex-induced vibration on a two-dimensional circular cylinder with low Reynolds number and low mass-damping parameter. Ocean Engineering 97, 156–164. doi:`10.1016/j.oceaneng.2015.01.012`.

[105] Wang, K., Chi, Q., 2019. Numerical simulation of the two-degree-of-freedom vortex induced vibration of a circular cylinder at Reynolds number of O(104-105). Journal of Marine Engineering and Technology 1, 1–10. doi:`10.1080/20464177.2019.1633222`.

[106] Wang, K., Ji, C., Chi, Q., Wu, H., 2018. Hydrodynamic force investigation of a rigid cylinder under the coupling CF and IL motion. Journal of Fluids and Structures 81, 598–616. doi:`10.1016/j.jfluidstructs.2018.06.004`.

[107] Wang, Y., Chen, X., Li, Y., 2020. Nonlinear self-excited forces and aerodynamic damping associated with vortex-induced vibration and flutter of long span bridges. Journal of Wind Engineering and Industrial Aerodynamics 204, 104207. doi:`10.1016/j.jweia.2020.104207`.

[108] Westerweel, J., Scarano, F., 2005. Universal outlier detection for PIV data. Experiments in Fluids 39, 1096–1100. doi:`10.1007/s00348-005-0016-6`.

[109] Wieneke, B., 2015. PIV uncertainty quantification from correlation statistics. Measurement Science and Technology 26, 074002. doi:`10.1088/0957-0233/26/7/074002`.

[110] Williamson, C., 1996. Vortex dynamics in the cylinder wake. Annual Review of Fluid Mechanics 28, 477–539. doi:`10.1146/ANNUREV.FL.28.010196.002401`.

[111] Williamson, C., Govardhan, R., 2004. Vortex-Induced Vibrations. Annual Review of Fluid Mechanics 36, 413–455. doi:`10.1146/annurev.fluid.36.050802.122128`.

[112] Williamson, C., Roshko, A., 1988. Vortex formation in the wake of an oscillating cylinder. Journal of Fluids and Structures 2, 355–381. doi:`10.1016/S0889-9746(88)90058-8`.

[113] Zdravkovich, M.M., 1997. Flow Around Circular Cylinders. Volume 1: Fundamentals. First ed., Oxford University Press. doi:`10.1115/1.2819655`.

[114] Zhao, M., 2015. The validity of the independence principle applied to the vortex-induced vibration of an inclined cylinder in steady flow. Applied Ocean Research 53, 155–160. doi:`10.1016/j.apor.2015.08.005`.

[115] Zhao, M., Cheng, L., 2011. Numerical simulation of two-degree-of-freedom vortex-induced vibration of a circular cylinder close to a plane boundary. Journal of Fluids and Structures 27, 1097–1110. doi:`10.1016/j.jfluidstructs.2011.07.001`.

[116] Zhao, M., Tong, F., Cheng, L., 2012. Numerical simulation of two-degree-of-freedom vortex-induced vibration of a circular cylinder between two lateral plane walls in steady currents. Journal of Fluids Engineering 134, 104501. doi:`10.1115/1.4007426`.

[117] Zhu, H., Yao, J., 2015. Numerical evaluation of passive control of VIV by small control rods. Applied Ocean Research 51, 93–116. doi:`10.1016/j.apor.2015.03.003`.

[118] Zou, L., Lin, Y.f., Lam, K., 2008. Large-Eddy Simulation of Flow Around Cylinder Arrays at a Subcritical Reynolds Number. Journal of Hydrodynamics 2008 20, 403–413. doi:`10.1016/S1001-6058(08)60074-8`.